ISSN 0912-1803

PHOTON FACTORY ACTIVITY REPORT

1991

#9

NATIONAL LABORATORY FOR HIGH ENERGY PHYSICS, KEK

Photon Factory Activity Report 1991

Staff members and visitors of the Photon Factory gathered in front of the PF office building.

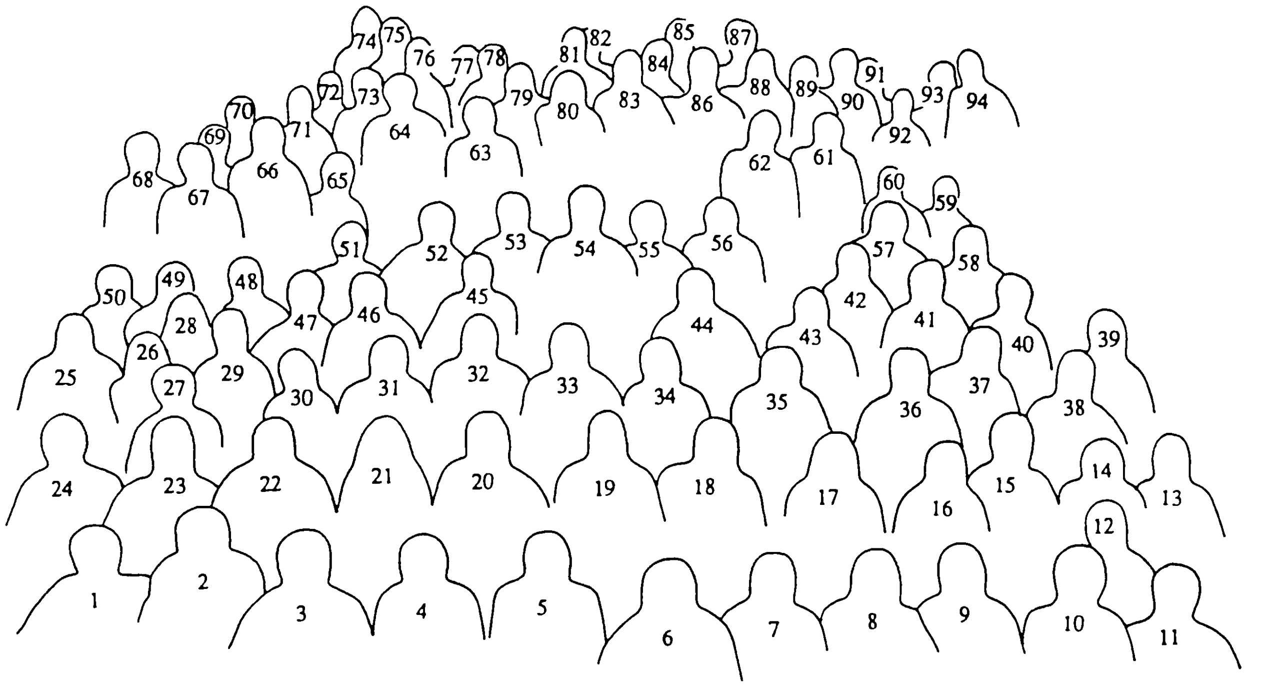

1. Y. Kagoshima
2. R. Matsuda
3. T. Kamitani
4. H. Kobayakawa
5. H. Iwasaki
6. T. Kosuge
7. A. Mikuni
8. T. Urano
9. S. Iwata
10. T. Koide
11. A. Yagishita
12. K. Furukawa
13. J. D. Wang
14. Y. Ogawa
15. K. Mori
16. H. Kitamura
17. M. Isawa
18. T. Iwazumi
19. A. Asami
20. T. Matsushita
21. H. Ando
22. T. Suwada
23. K. Tsuchiya
24. Y. Amemiya
25. A. Higuchi
26. M. Kimura
27. H. Nakamura
28. Y. Hakuta
29. T. Kikuchi
30. R. Watanabe
31. S. Fukuda
32. S. Ohsawa
33. N. Nakamura
34. T. Kikegawa
35. H. Kato
36. S. Muto
37. K. Tanaka
38. E. Shigemasa
39. K. Ohmi
40. Y. Sato
41. T. Noma
42. J. H. Chen
43. T. Shimura
44. Y. Kitajima
45. T. Yamakawa
46. K. Ito
47. H. Kimura
48. Y. Uchida
49. H. Honma
50. T. Kurihara
51. K. Kobayashi
52. A. Ueda
53. C. O. Pak
54. H. Kawata
55. N. Watanabe
56. S. Kishimoto
57. K. Hyodo
58. Y. Takiyama
59. S. Sakanaka
60. K. Nishimura
61. N. Kanaya
62. H. Aizawa
63. Y. Kobayashi
64. T. Katsura
65. T. Nogami
66. H. Maezawa
67. M. Nomura
68. K. Takeshita
69. S. Asaoka
70. S. Tokumoto
71. M. Yokota
72. H. Hanaki
73. A. Toyoshima
74. I. Abe
75. A. Mishina
76. K. R. Bauchspieß
77. T. Hori
78. K. Q. Lu
79. T. Shioya
80. S. Kojima
81. W. Möhling
82. H. Iijima
83. H. Siwaku
84. A. Koyama
85.
86. T. Shidara
87. M. Ando
88. T. Miyahara
89. S. Yamamoto
90. K. Ohsumi
91. T. Mori
92. N. Usami
93. T. Sasaki
94. P. Rehse

PREFACE

Professor H. Iwasaki
Director of the Photon Factory

It is a pleasure to publish a new volume of the Photon Factory Activity Report in which the present status and the progress achieved in fiscal year 1991 are described.

At the beginning of the year Professor J. Chikawa retired from his post as Director of the Photon Factory and I succeeded to his position. At the same time Professor T. Matsushita was appointed Director of the Instrumentation Division. Several new staff members have joined the Photon Factory and the total number of staff has reached 98.

A new project called "Super Light Source Project" was launched. It aims at converting the TRISTAN Main Ring to an ultra-high-brilliance and high-coherence radiation source. Theoretical estimates predict a brilliance of radiation three orders of magnitude higher than expected from this 3rd generation ring if a 4000-pole undulator is installed in the Main Ring and it is operated at an accelerating energy of 10 GeV. Professor M. Ando has been appointed Leader of the project team.

A new attempt was made at the 2.5 GeV storage ring: the accelerating energy was shifted up to 3 GeV, resulting in an increase in the intensity of radiation from the bending magnets by a factor of 20 at a photon energy of 30 keV. This has given beneficial effects to users in the fields of high pressure x-ray crystallography, heavy atom x-ray absorption spectroscopy etc. The increase in the accelerating energy has also resulted in a suppression of some kinds of beam instability of the ring. We are going to have special machine operation periods, several days each, in which the ring is operated at 3 GeV. The lifetime of the positron beam in the ring is still increasing and recently the product of ring current and lifetime has reached 1400 A min, which is nine times larger than that in the year 1985.

With a highly brilliant x-ray beam from the vacuum-shield undulator installed at the TRISTAN Accumulation Ring nuclear resonant Bragg scattering experiments were carried out on a hematite single crystal containing the isotope iron 57 and the quantum beat phenomenon could be observed with an appreciably higher counting rate. The curve showing the beat was so clear that fine structures could be recognized. Utilization of intense circularly polarized radiation from the insertion devices at BL-ARNE1 and BL-28U yielded remarkable results on x-ray magnetic Compton scattering and magnetic circular dichroism.

An agreement on collaborative research in synchrotron radiation science and technology was signed on July 1st between KEK and the Australian Nuclear Science and Technology Organization. Under the agreement a new branch beamline will be constructed at BL-20B in the 2.5 GeV ring which will be dedicated to x-ray diffraction experiments for materials science and macromolecular crystallography.

Professor H. Kitamura was awarded the Nishina Memorial Prize for his outstanding contribution to the development of novel insertion devices for synchrotron radiation.

Acknowledgments

The editors would like to thank Mss. Miyako Kimura and Chika Kawamata for their help in editing this issue. One of the editors (A. Y.) is grateful to Dr. Karl Rudolf Bauchspieß, visiting scientist at PF, for his careful reading of the manuscript of Instrumentation Division.

KEK Progress Report 91-2 A/M

KEK Reports are available from:

Technical Information & Library
National Laboratory for High Energy Physics
1-1 Oho, Tsukuba-shi
Ibaraki-ken, 305
JAPAN

Phone: 0298-64-1171
Telex: 3652-534 (Domestic)
(0)3562-534 (International)
Fax: 0298-64-2801
Cable: KEKOHO

CONTENTS

OUTLINE OF THE PHOTON FACTORY

INTRODUCTION

The Photon Factory (PF) is a national synchrotron radiation research facility affiliated with the National Laboratory for High Energy Physics (KEK) supervised by the Ministry of Education, Science and Culture. It is located at the northern end of Tsukuba Science City, which is about 60 km north-east of Tokyo. The PF consists of a 2.5-GeV electron/positron linear accelerator, a 2.5-GeV electron/positron storage ring as a dedicated light source, and beamlines and experimental stations for exploiting synchrotron radiation in studies involving such research fields as physics, chemistry, biology, medical sciences, pharmacology, earth sciences and lithography. All of the facilities for synchrotron radiation research are open to scientists of universities and research institutes belonging to the government, public organizations, private enterprises and those of foreign countries. The members of institutions affiliated with the Ministry of Education, Science and Culture are given the highest priority among all users. Applications from other organizations are also admitted.

OVERVIEW OF THE FACILITY

The plan view of the facility is shown in Fig. 1. The 2.5-GeV linac housed in a 450 m long enclosure is used as an injector for both the PF storage ring and the accumulation ring (AR) of TRISTAN main ring. The PF storage ring was already equipped with the flexibility of storing positrons in place of electrons. A part of the AR has been used as a high energy synchrotron radiation source producing radiation from its bending magnet and two insertion devices. One of the insertion devices produces elliptically polarized radiation, and the other highly brilliant radiation in the X-ray region. The AR has been operated for synchrotron radiation users with an energy range from 5.8 to 6.5 GeV.

ORGANIZATION AND STAFF

The organization of KEK is shown in Fig. 2. The PF is composed of three divisions: Injector Linac, Light Source and Instrumentation. A working group has been organized for the design study of the use of the TRISTAN Main Ring for synchrotron radiation science. The organization of the PF including its personnel is shown in Fig. 3. The Advisory Council for the PF was established to discuss scientific programs and management of the PF. The council consists of twenty one senior scientists including ten non-KEK members (Table 1). The term of membership is two years. The Program Advisory Committee (PAC) consisting of the members listed in Table 2 receives proposals of users and decides priorities for the experiments.

In Table 3 the names of the staff members are listed in alphabetical order to help make direct contact. Also, the numbers of staff members and visiting scientists are summarized in Table 4.

BUDGET AND OPERATION TIME

The budget of the PF is supplied by the Ministry of Education, Science and Culture. The annual budget after commissioning of the facilities is shown in Table 5. The numbers of beam channels in each year are shown in Table 6.

The machine operation time is divided into three terms per year. Summary and timetable of the machine operation in FY 1991 are shown in Tables 7 and 8, respectively.

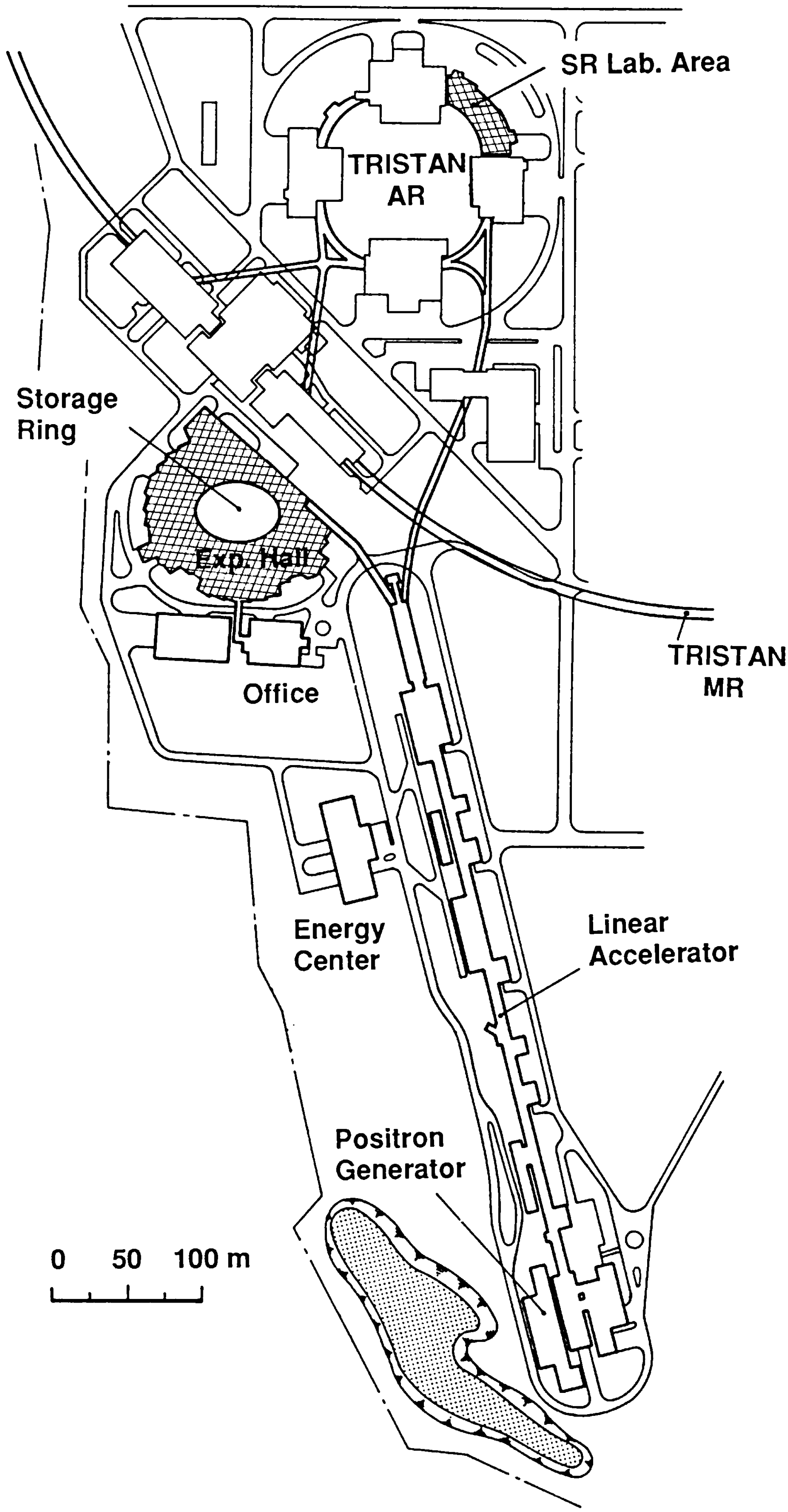

Fig. 1 Plan view of the Photon Factory

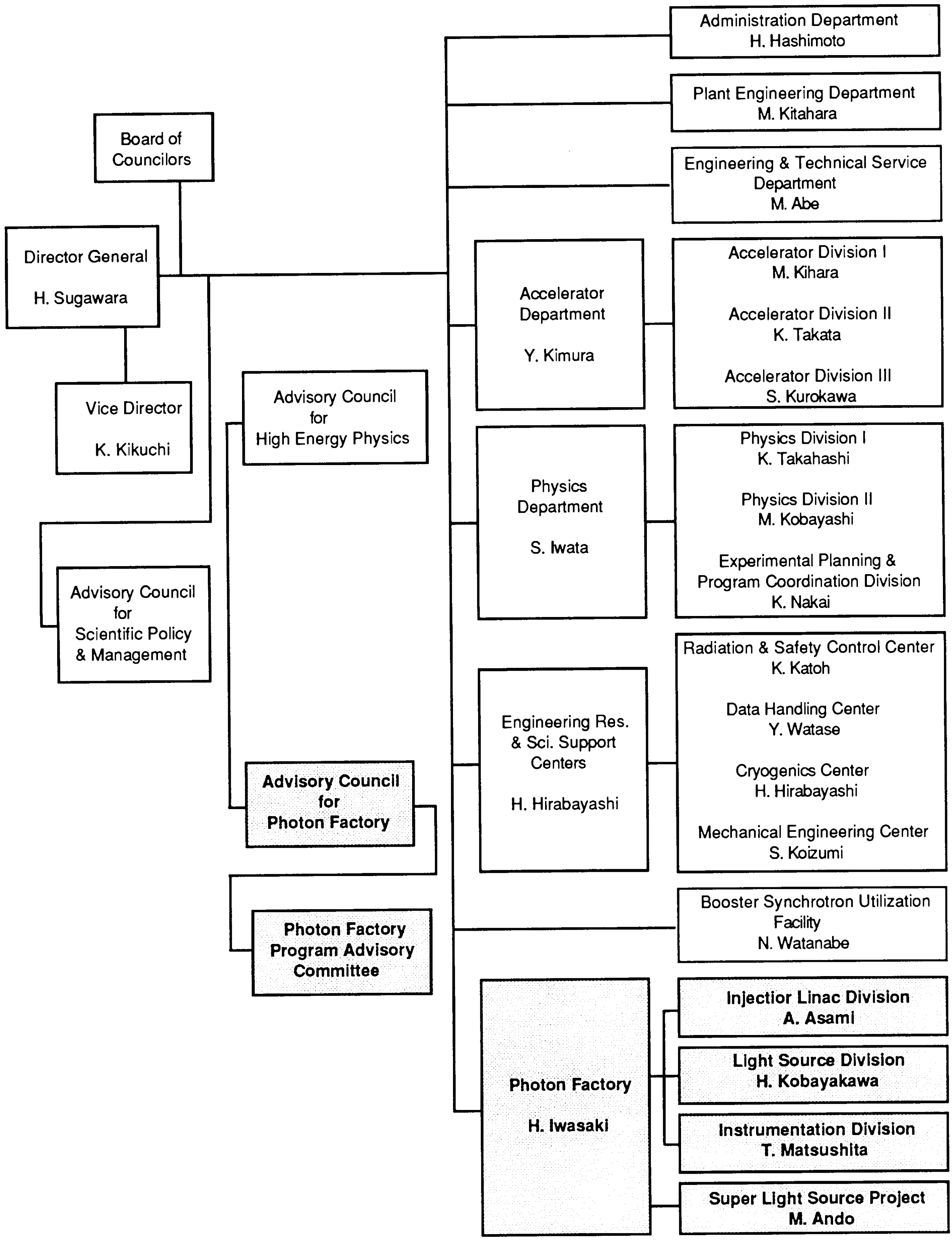

Fig. 2 Organization of KEK

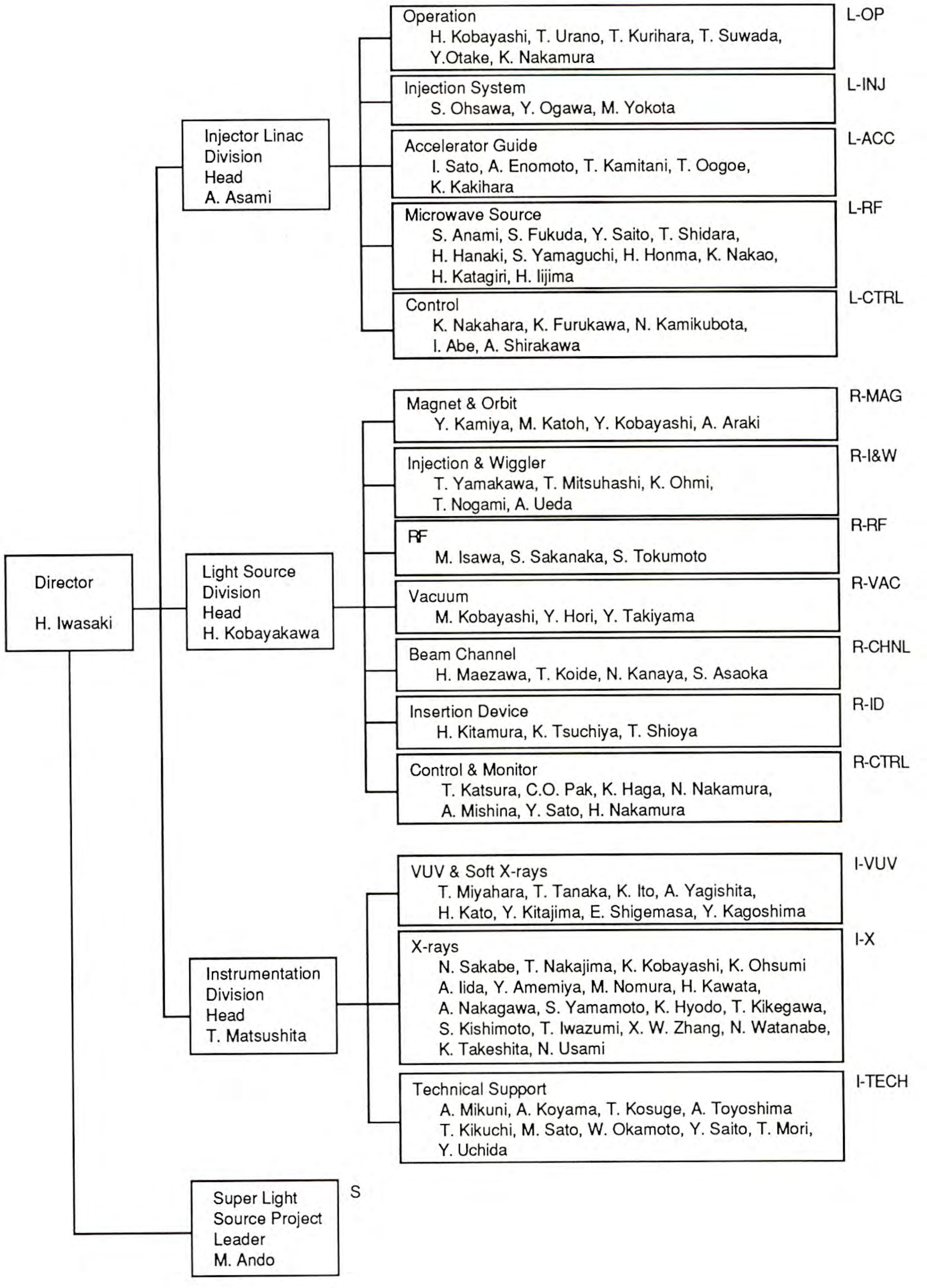

Fig. 3 Organization of the Phton Factory

Table 1 Members of Advisory Council

**Chairman * Vice-Chairman

ANDO, Masami	Instrumentation Division, PF, KEK
ASAMI, Akira**	Injector Linac Division, PF, KEK
FUJII, Yasuhiko	Institute of Materials Science, University of Tsukuba
HIEDA, Kotaro	Faculty of Science, Rikkyo University
IIJIMA, Takao	Faculty of Science, Gakushuin University
ISHII, Takehiko	Institute for Solid State Physics, University of Tokyo
KATSUBE, Yukiteru	Institute for Protein Research, Osaka University
KOBAYAKAWA, Hisashi	Light Source Division, PF, KEK
KOBAYASHI, Masanori	Light Source Division, PF, KEK
KURODA, Haruo*	Faculty of Science, University of Tokyo
MAEZAWA, Hideki	Light Source Division, PF, KEK
MATSUSHITA, Tadashi	Instrumentation Division, PF, KEK
MIYAHARA, Tsuneaki	Instrumentation Division, PF, KEK
NAKAHARA, Kazuo	Injector Linac Division, PF, KEK
OHTA, Toshiaki	Faculty of Science, Hiroshima University
SAKABE, Noriyoshi	Instrumentation Division, PF, KEK
SATO, Isamu	Injector Linac Division, PF, KEK
SUZUKI, Kenji	Institute for Materials Research, Tohoku University
TOKONAMI, Masayasu	Faculty of Science, University of Tokyo
YAMAKAWA, Tatsuya	Light Source Division, PF, KEK
WAKO, Shinya	Faculty of Library and Information Science, University of Library and Information Science

Table 2 Members of Program Advisory Committee

* Chairman

ASAMI, Akira	Injector Linac Division, PF, KEK
HASHIZUME, Hiroo	Research Laboratory of Egineering Materials, Tokyo Institute of Technology
IWASAWA, Yasuhiro	Faculty of Sciecne, University of Tokyo
KOBAYAKAWA, Hisashi	Light Source Division, PF, KEK
KOMA, Atsushi	Faculty of Sciecne, University of Tokyo
KOTANI, Akio	Institute of Solid State Physics, University of Tokyo
MATSUAHITA, Tadashi*	Instrumentation Division, PF, KEK
MIYAHARA, Tsuneaki	Instrumentation Division, PF, KEK
MURATA, Takatoshi	Department of Physics, Kyoto University of Education
NIHEI, Toshimasa	Institute of Industrial Science, University of Tokyo
SAKABE, Noriyoshi	Instrumentation Division, PF, KEK
SATO, Yukinori	Research Institute for Scientific Measurements, Tohoku Unisersity
SATOW, Yoshinori	Faculty of Pharmaceutical Sciences, University of Tokyo
UEKI, Tatsuo	The Institute of Physical and Chemical Research
WASEDA, Yoshio	Research Institute of Mineral Dressing and Metallurgy, Tohoku University

Table 3 Staff members of the Photon Factory

Name	Position	Responsibility(*)	Bitnet address
ABE, Isamu	Tech.	L-CTRL	ABEI@JPNKEKVM
AMEMIYA, Yoshiyuki	Assoc. Prof.	I-X	AMEMIYA@JPNKEKVX
ANAMI, Shozo	Assoc. Prof.	L-RF	
ANDO, Masami	Prof.	S	ANDO@JPNKEKVX
ARAKI, Akira	Tech.	R-MAG	
ASAMI, Akira	Prof.	L-Director	
ASAOKA, Seiji	Tech.	R-CHNL	
ENOMOTO, Atsushi	Assoc. Prof.	L-ACC	ENOMOTOA@JPNKEKVX
FUKUDA, Shigeki	Assoc. Pocrof.	L-RF	
FURUKAWA, Kazuro	Res. Assoc.	L-CTRL	FURUKAWA@JPNKEKVX
HAGA, Kaiichi	Res. Assoc.	R-CTRL	HAGA@JPNKEKVM
HANAKI, Hirofumi	Res. Assoc.	L-RF	HANAKI@JPNKEKVX
HONMA, Hiroyuki	Tech.	L-RF	HONMA@JPNKEKVM
HORI, Yoichiro	Res. Assoc.	R-VAC	
HYODO, Kazuyuki	Res. Assoc.	I-X	HYODO@JPNKEKVX
IIDA, Atsuo	Assoc. Prof.	I-X	
IIJIMA, Hitoshi	Tech.	L-RF	
ISAWA, Masaaki	Assoc. Prof.	R-RF	ISAWA@JPNKEKVM
ITO, Kenji	Assoc. Prof.	I-VUV	ITO@JPNKEKVM
IWASAKI, Hiroshi	Prof.	Chife Director	
IWAZUMI, Toshiaki	Res. Assoc.	I-X	IWAZUMI@JPNKEKVX
KAGOSHIMA, Yasushi	Res. Assoc.	I-VUV	KAGOSIMA@JPNKEKVX
KAKIHARA, Kazuhisa	Tech.	L-ACC	KAKIHARA@JPNKEKVX
KAMIKUBOTA, Norihiko	Res. Assoc.	L-CTRL	KAMI@JPNKEKVX
KAMITANI, Takuya	Res. Assoc.	L-ACC	KAMITANI@JPNKEKVX
KAMIYA, Yukihide	Assoc. Prof.	L-MAG	KAMIYA@JPNKEKVM
KANAYA, Noriichi	Res. Assoc.	R-CHNL	KANAYA@JPNKEKVX
KATAGIRI, Hiroaki	Tech.	L-RF	
KATSURA, Tomotaro	Assoc. Prof.	R-CTRL	KATSURA@JPNKEKVM
KATO, Hiroo	Res. Assoc.	I-VUV	
KATOH, Masahiro	Res. Assoc.	R-MAG	
KAWATA, Hiroshi	Res. Assoc.	I-X	
KIKEGAWA, Takumi	Res. Assoc.	I-X	KIKEGAWA@JPNKEKVX
KIKUCHI, Takashi	Tech.	I-TECH	
KISHIMOTO, Syunji	Res. Assoc.	I-X	KISHIMOTO@JPNKEKVM
KITAJIMA, Yoshinori	Res. Assoc.	I-VUV	
KITAMURA, Hideo	Prof.	R-ID	KITAMURA@JPNKEKVM
KOBAYAKAWA, Hisashi	Prof.	R-Director	
KOBAYASHI, Hitoshi	Assoc. Prof.	L-OP	
KOBAYASHI, Katsumi	Assoc. Prof.	I-X	KOBAYASI@JPNKEKVM
KOBAYASHI, Masanori	Prof.	R-VAC	
KOBAYASHI, Yukinori	Res. Assoc.	R-MAG	
KOIDE, Tsuneharu	Res. Assoc.	R-CHNL	
KOSUGE, Takashi	Tech	I-TECH	
KOYAMA, Atsushi	Tech.	I-TECH	
KURIHARA, Toshikazu	Res. Assoc.	L-OP	
MAEZAWA, Hideki	Prof.	R-CHNL	MAEZAWAH@JPNKEKVX
MATSUSHITA, Tadashi	Prof.	I-Director	MATSUS@JPNKEKVM
MIKUNI, Akira	Tech.	I-TECH	
MISHINA, Atsushi	Tech.	R-CTRL	MISHINA@JPNKEKVM

Name	Position	Responsibility(*)	Bitnet address
MITSUHASHI, Toshiyuki	Res. Assoc.	R-I&W	MITSUHAS@JPNKEKVX
MIYAHARA, Tsuneaki	Prof.	I-VUV	MIYAHARA@JPNKEKVM
MORI, Takeharu	Tech.	I-TECH	
NAKAGAWA, Atsushi	Res. Assoc.	I-X	NAKAGAWA@JPNKEKVX
NAKAHARA, Kazuo	Prof.	L-CTRL	
NAKAJIMA, Tetsuo	Assoc. Prof.	I-X	NAKATETS@JPNKEKVM
NAKAMURA, Kie	Tech.	L-OP	
NAKAMURA, Hajime	Tech.	R-CTRL	NAKAMUR@JPNKEKVM
NAKAMURA, Norio	Res. Assoc.	R-CTRL	NAKAN@JPNKEKVM
NAKAO, Katsumi	Tech.	L-RF	
NOGAMI, Takashi	Tech.	R-I&W	NOGAMI@JPNKEKVX
NOMURA, Masaharu	Assoc. Prof.	I-X	
OGAWA, Yujiro	Res. Assoc.	L-INJ	OGAWAYJ@JPNKEKVX
OHMI, Kazuhito	Res. Assoc.	R-I&W	OHMI@JPNKEKVX
OHSAWA, Satoshi	Assoc. Prof.	L-INJ	OHSAWA@JPNKEKVX
OHSUMI, Kazumasa	Assoc. Prof.	I-X	
OKAMOTO, Wataru	Tech.	I-TECH	
OOGOE, Takao	Tech.	L-ACC	
OTAKE, Yuji	Tech.	L-OP	OTAKE@JPNKEKVM
PAK, Cheol On	Assoc. Prof.	R-CTRL	PAK@JPNKEKVM
SAITO, Yoshio	Assoc. Prof.	L-RF	
SAITO, Yuuki	Tech.	I-TECH	
SAKABE, Noriyoshi	Prof.	I-X	SAKABE@JPNKEKVM
SAKANAKA, Shyogo	Res. Assoc.	R-RF	SAKANAKA@JPNKEKVM
SATO, Isamu	Prof.	L-ACC	
SATO, Masato	Tech.	I-TECH	
SATO, Yoshihiro	Tech.	R-CTRL	YOSHIHIR@JPNKEKVM
SHIDARA, Tetsuo	Assoc. Prof.	L-RF	SHIDARA@JPNKEKVM
SHIGEMASA, Eiji	Ress. Assoc.	I-VUV	
SHIOYA, Tatsuro	Tech.	R-ID	SHIOYA@JPNKEKVX
SHIRAKAWA, Akihiro	Tech.	L-CTRL	
SUWADA, Tsuyoshi	Res. Assoc.	L-OP	
TAKESHITA, Kunikazu	Res. Assoc.	I-X	TAKESHIT@JENKEKVX
TAKIYAMA, Youichi	Tech.	R-VAC	
TANAKA, Ken"ichiro	Assoc. Prof.	I-VUV	TANAKA@JPNKEKVM
TOKUMOTO, Shuichi	Tech.	R-RF	
TOYOSHIMA, Akio	Tech.	I-TECH	
TUCHIYA, Kimichika	Res. Assoc.	R-ID	TSUCHIYA@JPNKEKVX
UCHIDA, Yoshinori	Tech	I-TECH	
UEDA, Akira	Tech.	R-I&W	
URANO, Takao	Res. Assoc.	L-OP	URANO@JPNKEKVX
USAMI, Noriko	Res. Assoc.	I-X	
WATANABE, Nobuhisa	Res. Assoc.	I-X	NOBUHISA@JPNKEKVX
YAGISHITA, Akira	Assoc. Prof.	I-VUV	
YAMAGUCHI, Seiya	Res. Assoc.	L-RF	
YAMAKAWA, Tatsuya	Prof.	R-I&W	
YAMAMOTO, Shigeru	Res. Assoc.	I-X	SHIGERU@JPNKEKVX
YOKOTA, Mitsuhiro	Tech.	L-INJ	
ZHANG, Xiao Wei	Res. Assoc.	I-X	

(*) Refer to Fig. 3 for abbreviations

Table 4 Annual numbers of staff & visiting scientists

Position	Department	1978	1979	1980	1981	1982	1983	1984	1985	1986	1987	1988	1989	1990	1991
Chief Director		1	1	1	1	1	1	1	1	1	1	1	1	1	1
	Injector Linac	1	2	3	3	3	3	3	3	4	4	4	3	3	4
Professor	Light Source	1	4	4	4	4	4	4	3	4	4	4	4	5	5
	Instrumentation	0	0	0	1	1	1	1	2	3	4	5	5	5	6
Associate	Injector Linac	0	1	1	1	2	2	2	2	1	2	3	5	7	6
Professor	Light Source	1	5	4	4	4	3	5	5	3	3	3	5	4	3
	Instrumentation	0	0	1	3	4	5	5	8	7	9	7	10	9	8
Research	Injector Linac	1	3	4	6	7	8	9	10	11	10	10	9	8	9
Associate	Light Source	0	1	4	6	7	7	6	8	9	12	12	9	11	11
	Instrumentation	0	0	3	2	7	10	10	10	13	13	14	11	15	15
Technical	Injector Linac	0	0	2	3	5	5	6	6	7	8	9	10	11	11
Staff	Light Source	3	3	3	4	6	6	6	6	7	7	8	10	10	10
	Instrumentation	0	0	0	0	1	2	4	4	8	9	11	10	9	10
Visiting	Injector Linac	2	2	2	2	2	2	2	2	2	2	2	2	2	2
Scientist	Light Source	2	6	4	4	4	4	4	4	4	4	4	4	4	4
	Instrumentation	0	0	6	6	6	6	6	6	6	6	6	6	6	7
Total		12	28	42	51	64	69	74	80	90	97	103	104	110	112

Table 5 PF budget in each fiscal year (in million yen)

Item	1982	1983	1984	1985	1986	1987	1988	1989	1990	1991
Salary	402	474	484	510	561	561	642	757	764	859
PF Storage Ring (channel, insertion device, etc.)	0	0	0	153	131	647	0	0	196	103
PF Experiments	140	153	134	184	190	196	237	341	367	399
PF Operation & Maintenance	412	477	552	653	820	907	962	1,078	1,107	1,107
Computer Rentals	136	135	135	135	136	136	141	145	145	145
Positron Source & Electric Plant Operation	0	0	0	41	138	208	258	300	308	300
Cooling System & Electric Operation	120	111	124	180	211	214	217	231	235	240
Electricity	209	226	257	338	381	331	355	425	423	423
PF-Industrial Cooperative Experiments	0	94	84	95	185	166	302	219	171	174
AR Construction and Experiments						398	267	387	250	260
Miscellaneous	115	134	115	127	162	120	301	243	287	388
Total	1,534	1,804	1,885	2,397	2,864	3,884	3,682	4,126	4,253	4,398

Table 6 Yearly account of beam channels

Fiscal	1981	1982	1983	1984	1985	1986	1987	1988	1989	1990	1991
PF	6	8	8	8	10	12	13	13	15	15	17
Institutes	0	0	0	1	1	1	3	4	4	4	4
Industry	0	0	1	2	4	4	4	4	4	4	4
Total	6	8	9	11	15	17	20	21	23	23	25

Table 7 Summary of operation in FY 1991 (April 1991 - March 1992) (hours)

Cycle	Linac	PF Ring	Users' time	AR	Dedicated to SR at AR
1	2305	2278	1548	2163	1458
2	1889	1704	1224	1824	1396
3	1080	960	648	1008	756
Total	5274	4942	3420	4995	3610

Table 8 Timetable of the Machine Operation in FY 1991.
PF : PF ring, AR : Accumulation ring

Machine Tuning
Photobaking of Beamline
Users Beam Time
Parasitic SR Use of AR
Users Bonus Time
Machine Study
Lectures for Students
Dedicated SR Use of AR
Machine Tuning / Photobaking

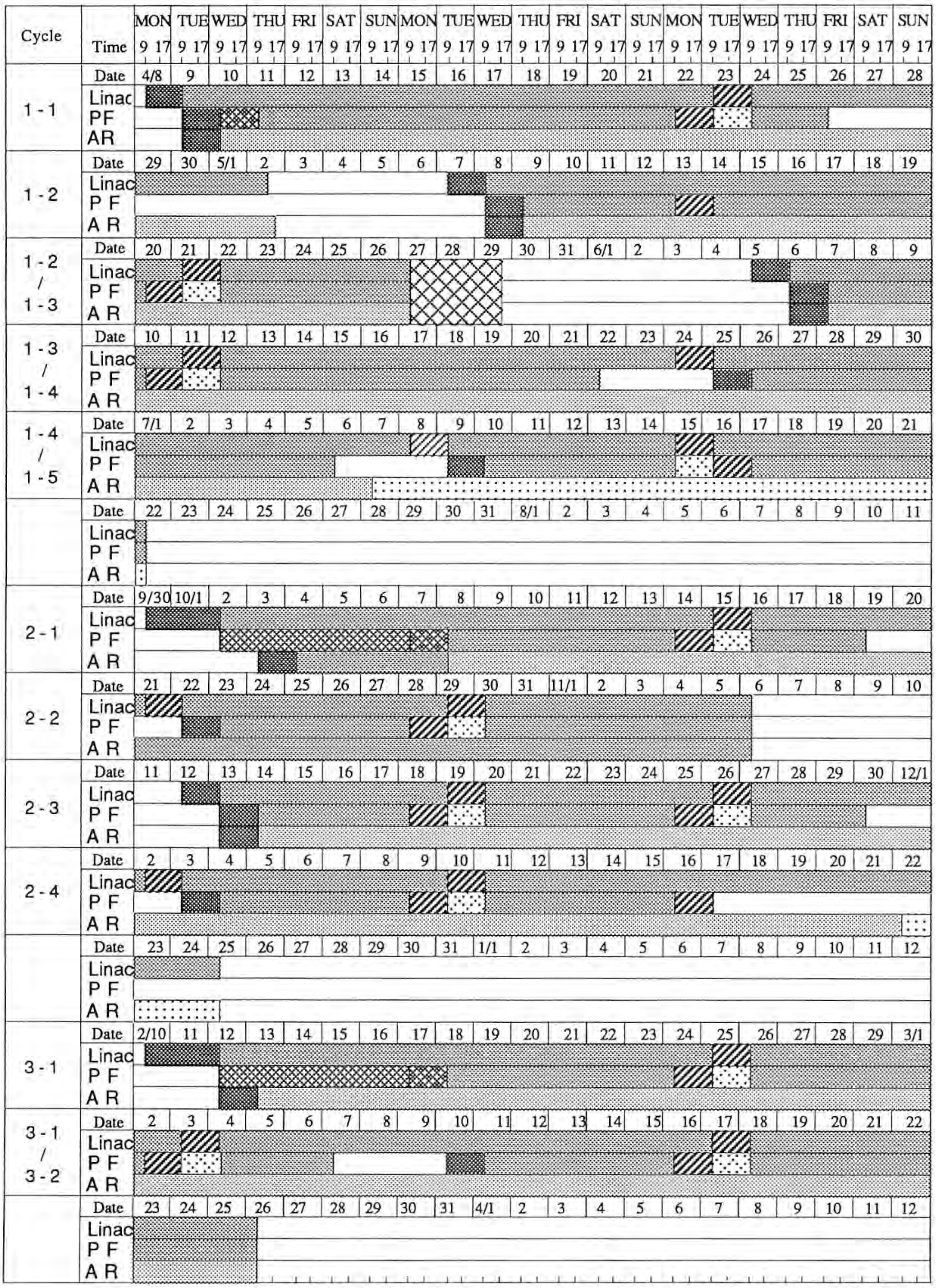

SEMINARS, MEETINGS AND PUBLICATIONS

Twenty one seminars were given by scientists who visited the PF in 1991. Three users' meetings were held in FY 1991, including the annual PF symposium. The PF publishes its quarterly "PHOTON FACTORY NEWS" in Japanese for communication between users and staff.

PF seminars

Zhu, F. Q. (IHEP)
Status of BEPC Injector -1.1/1.4 GeV Electron Linac — January 18, 1991

Stankevitch, V. (Institute of Atomic Energy, USSR)
Optical Properties of High Tc Materials — February 5, 1991

Akimoto, K. (NEC Corp.)
Metal/GaAs Interface Structure Studied by Anomalous X-ray Scattering — March 1, 1991

Wong, J. (Lawrence Livermore National Laboratory)
YB_{66}: A New Soft X-ray Monochromator for Synchrotron Radiation — March 5, 1991

Quinn, P. (SERC Daresbury Laboratory)
SRS Status, Operations and Beam Stability — April 26, 1991

Ryu, C. M. (POSTECH)
Current Status of the Pohang Linear Accelerator Project — April 18, 1991

Kawasaki, S. (Saitama Univ.)
Unconventional FEL — April 26, 1991

Connerade, J. P. (Imperial College of Science, Technology and Medicine, Univ. of London)
Giant Resonances in Atoms, Molecules, Clusters and Solids — May 29, 1991

Connerade, J. P. (Imperial College of Science, Technology and Medicine, Univ. of London)
Magneto-optical Spectroscopy with Synchrotron and Lasers — May 30, 1991

Connerade, J. P. (Imperial College of Science, Technology and Medicine, Univ. of London)
The Experimental Programme in VUV and in Strong Laser Fields at the Blackett Laboratory — May 31, 1991

Feiters, M. (Katholieke Universiteit, The Netherlands)
X-ray Absorption (EXAFS and XANES) Studies of Iron in Soybean Lipoxygenase-1 — June 5, 1991

Attwood, D. (Center for X-ray Optics, Lawrence Berkeley Laboratory)
Undulators, Coherence and Optics for X-ray Microscopy — May 21, 1991

Kulikov, A. P. (Institute of Chem., Vladivostok)
Short-range Order in Fluorozirconate Glasses — June 28, 1991

Chung, J. W. (Pohang Institute and Science College)
Silicon-O Bond Structure in Slow-ion Deposited SiO_2 Films — June 28, 1991

Sawatzky, G. A. (Applied and Solid State Physics Laboratory)
X-ray Absoption Spectroscopy and Magnetic Dichroism of Highly Correlated Systems — August 5, 1991

Siddons, P. D. (NSLS, Brookhaven National Laboratory) Recent Scientific Topics of the R&D Group at NSLS	September 24, 1991
Xie, J. L. (Institute of High Energy Physics, China) 1. An RF Linac FEL at the Institute of High Energy Physics, China 2. The BNL Accelerator Test Facility	October 11, 1991
Kawata, H. (Photon Factory, KEK) First Observation of Magnetic Compton	November 7, 1991
Kiefer, J. (Justus-Liebig-University, Germany) Heavy Ion Effects on Cellular Systems	November 11, 1991
Sutherland, B. M. (BNL. Biology Dept.) DNA Damage and Repair *in Vitro* and in Human Skin *in Situ*	November 27, 1991
Collins, S. P. (Daresbury Laboratory) X-ray Magnetic Bragg Scattering from Ferromagnetic Materials	December 17, 1991

Users' Meetings

Medical Applications of Synchrotron Radiation–I	January 10-11, 1991
Medical Applications of Synchrotron Radiation–II	June 21-22, 1991
The 9th Photon Factory Symposium (Annual Users' Meeting)	January 9-10, 1992

Publications

PHOTON FACTORY NEWS ISSN 0916-0604 Vol.9, No.1-4

GRADUATE UNIVERSITY FOR ADVANCED STUDIES

The National Graduate University was established in 1988. It has the following three schools:

School of Cultural Studies
School of Mathematical and Physical Sciences
School of Life Sciences.

KEK has participated in the University to form the Department of Synchrotron Radiation Science and the Department of Accelerator Science, both of which belong to the School of Mathematical and Physical Sciences.

Students in the Department of Synchrotron Radiation Science are expected to study the basic theory of emission of synchrotron radiation, its characteristics, and interaction of radiation with matter, and then engage in research by using various facilities at the PF. The research field includes the development of radiation sources, optical elements, and instruments for diffraction, scattering, spectroscopy, and irradiation experiments as well as exploration of new areas of applying synchrotron radiation to science and technology.

PROPOSALS FOR EXPERIMENTS

The PF receives proposals for beam time on the PF storage ring and the AR. The proposals are reviewed and rated on the basis of scientific and technological merit by the PAC. The detailed procedure for submitting a proposal is described below. The number of proposals approved by the PAC since commissioning of the PF is listed in Table 9.

Beam time at the PF is also available for a fee to researchers of private corporations. No approval by the PAC is required. Scientific programs in collaboration between PF staff members and scientists of private corporations are also in progress; no fees and no approval by the PAC are required. The programs are renewed every fiscal year starting in April.

All proposals approved during FY 1991 are listed at the end of this capter.

GUIDELINES FOR PROPOSALS

Application form

The PF is open to everybody in scientific research. A proposal should be filed on an application form, which is available on request from the Research Cooperation Section of the Administration Department of KEK. An applicant should carefully read the guide before filing an application. A spokesperson should get the agreement of the members to join the team.

An overseas applicant is requested to find an appropriate "contact person in Japan" (CPJ), who will mediate between the applicant and KEK.* Please contact the person in charge of the experimental station that you wish to use, if you do not know any appropriate CPJ. He/she will select the person appropriate for the applicant's research plan. A list of the people in charge of the experimental stations can be found in this report.

All experimental proposals are subject to approval of the Program Advisory Committee (PAC). The CPJ will be informed about the decision.

Note that the procedure has been changed since April 1992. Therefore an applicant should use the new application forms: old ones cannot be accepted.

* *The contact person in Japan will help you translate Japanese and English and assist with visa applications and your experiments. In order to assure his/her agreement the signature or seal imprint of the CPJ is required.*

Category of proposals

There are four categories of proposals: G(eneral), S(pecial), P(reliminary) and U(rgent). The character, process of approval and terms of validity are different among those categories.

G(eneral) is the category for general experiments using synchrotron radiation. Deadlines of application and valid terms are as follows:

Deadlines:
July 10, 1992 (a) and January 8, 1993 (b)
Valid terms:
from October, 1992 to September, 1994 for (a)
from April, 1993 to March, 1995 for (b).

P(reliminary) is the category for preliminary experiments in order to determine the feasibility of proposals for categories G or S. There are some limitations as listed below.

1) the maximum beamtime for one project is less than about 72 hours.
2) One spokesperson can have only one project at a time.
3) More than three proposals of this category cannot be approved for an experimental station by the PAC.

Deadlines:
July 10, 1992 (a) and January 8, 1993 (b)
Valid terms:
from October, 1992 to September, 1993 for (a)
from April, 1993 to March 1994 for (b).

S(pecial) is the special category for those experiments that may be difficult to do but may have extremely high scientific value. Among those could be experiments for the development of a difficult technique or those requiring special operation of the storage ring. The PF supports the projects of this category financially within certain limits; the funds cannot be used for travel expenses or salary. At least one Japanese scientist should be included in a team. The process of judgement is different from other categories. An applicant has to express his/her plan at the "Photon Factory Symposium" and at the PAC. The progress report should be presented at the "Photon Factory Symposium" which takes place every year.

Deadline: late September, 1992
Valid term: from April, 1993 to March, 1996.

U(rgent) is the category for urgent proposals which cannot be postponed unity the next deadline and which are of extremely high scientific value. Once approved, these projects may exclude already assigned beamtime for other projects. Applicants can apply at any time but the valid terms are limited. Results of a project should be reported at the "Photon Factory Symposium".

Valid term:

end of March, for a project approved between October and March.

end of September, for a project approved between April and September.

Accommodation

KEK provides guest houses at low cost for visiting scientists. In the case of domestic experimenters, please contact the person in charge of your experimental station. Overseas experimenters should ask the CPJ to book rooms. KEK supports travel and living expenses for domestic experimenters within certain limits but does not do so for overseas experimenters.

Others

(1) Experimenters must obey the safety rules at KEK and the PF.

(2) Further procedures may be requested in order to carry out an experiment.

(3) If there are questions regarding procedures, please contact the

Research Cooperation Section,
Administration Department,
National Laboratory for High Energy Physics.
Oho, Tsukuba 305, Japan
FAX: 81-298-64-4602

Table 9 Number of proposals approved by the PAC.

Research Field	1983	1984	1985	1986	1987	1988	1989	1990	1991
(A) EXAFS	42	26	35	40	61	66	57	71	69
(B) Biology	18	18	28	28	32	38	57	61	75
(C) X-Ray	24	29	75	54	73	65	61	80	92
(D) VUV & Soft X-Ray	19	12	27	26	28	28	36	27	45
Total	103	85	165	148	194	197	211	239	281

区分 category	G型、P型、S型、U型

高エネルギー物理学研究所放射光実験施設共同利用実験申請書

Application form for synchrotron radiation experiments at Photon Factory (PF)

高エネルギー物理学研究所長殿

申請日 (Date)

実験責任者 Spokesperson

氏名 (Name) 印 (Signature)

所属、職名 Affiliation Position

連絡先住所 Mailing Address 〒

下記の通り申請します

Tel. FAX E-mail

実験課題名 Proposal title	(日本語)
	(英訳)

I. 実験組織 team

ローマ字 氏名 Name	所属 Affiliation[1] (大学、学部、学科)	職名[2] Position	電話番号[3] Tel.	PFの利用経験[4] Experience at PF	分担事項 Role in the team

1.大学院生は所属大学、研究科、専攻 2.大学院生は課程、学年 3.内線を含む 4.ステーション名及び習熟度 (excellent, good, fair, poor, none)
欄が不足する場合は同寸別紙に記入の上5枚目に添付

II. 希望ビームタイム schedule

ステーション Station	希望時期 year/month	希望時間[5] beam time
総計 total		

5.時間または日単位で記入 in units of hours or days

III. 希望ステーションとその理由
(Name of stations and why you chose them)

第1希望

第2希望

第3希望

For overseas applications, describe the contact person in Japan (Name, mailing address, tel. and FAX)

氏名 印 Tel. FAX

所属、職名

連絡先住所 〒

Office use

受理年月日	※
受理番号	※

List of proposals accepted in fiscal 1991

Proposal Number	Spokesperson	Title
91-001	M. Abe Faculty of Science, Tokyo Institute of Technology	EXAFS study of Nb (Ta) in Li ion-exchanged niobic acid (tantalic acid)
91-002	H. Kanai Faculty of Living Science, Kyoto Prefectural Univ.	An EXAFS study in the structures of composite titanium oxides prepared by a CVD method
91-003	I. Nakai Department of Chemistry, Univ. of Tsukuba	Characterization of metallic elements and biominerals unusually accumulated in animal tissues
91-004	K. Ozutsumi Department of Chemistry, Univ. of Tsukuba	Solvation structure of cobalt(II), nickel(II), copper(II) and zinc(II) ions in pyridine and its derivatives
91-005	K. Ozutsumi Department of Chemistry, Univ. of Tsukuba	Solvation structure of metal ions in tetramethylurea and N, N-dimethyformamide
91-007	A. Yamagishi College of Arts and Sciences, Univ. of Tokyo	Coordination structure of alternately layered zirconium-hafnium phosphonate on silicon wafer
91-008	K. Oki Graduate School of Engineering Science, Kyushu Univ.	Crystal structure changes and valence fluctuations of Ce in Pd-Ce ordering alloys
91-009	N. Yasuoka Faculty of Science, Himeji Institute of Technology	EXAFS study of hydrogenase from Desulfovibrio vulgaris Miyazaki F
91-010	R. F. Howe Department of Physical Chemistry, Univ. of New South Wales	Fe bimetallic clusters in Zeolites derived from the absorbed $Fe(CO)_5$
91-011	H. Kuroda Faculty of Science, Univ. of Tokyo	EXAFS study about the photoproduct of $H_2Ru_4(CO)_{13}$ physisorbed on the surface
91-012	Y. Iwasawa Faculty of Science, Univ. of Tokyo	EXAFS analysis for the catalytic active structures of attached carbide anion clusters of Fe, Co, Ru, Rh and Os
91-013	N. Toshima Faculty of Engineering, Univ. of Tokyo	The structure of polymer-protected bimetallic cluster
91-015	M. Kawai Research Lab. of Engineering Materials, Tokyo Institute of Technology	Studies on geometric and electronic structure of the high Tc superconductor oxides by XAFS
91-016	H. Endo Faculty of Science, Kyoto Univ.	Liquid-liquid critical phenomena in liquid chalcogenides

Proposal Number	Spokesperson	Title
91-017	F. Kanamaru Institute of Scien. and Indus. Research, Osaka Univ.	EXAFS study on reduction process of nickel double oxides
91-019	T. Tanase Faculty of Science, Toho Univ.	An XAFS study of transition metal complexes (Cu, Ni, Pd, and Pt) containing sugar ligands which catalyze some asymmetric reactions
91-020	T. Yamamura Faculty of Science, The Science Univ. of Tokyo	XAS and distance geometry of metallo peptides: models for DNA binding proteins
91-021	K. Sakurai National Research Institute for Metals	XAFS study on the amorphous $Cu_{30}Ta_{70}$ alloy synthesized by mechanical alloying
91-022	N. Kamijou Government Industrial Research Institute, Osaka	Temperature dependent EXAFS Debye-Waller factor in amorphous ionic conductors
91-023	K. Kadono Government Industrial Research Institute, Osaka	XAFS analysis of halide glass structure
91-024	L. Kunquan Institute of Physics, Academia Sinica	The EXAFS study of some bromide and selenite molten states
91-025	T. Ohta Faculty of Science, Hiroshima Univ.	The process of silicon nitride formation studied with XANES
91-026	T. Ohta Faculty of Science, Hiroshima Univ.	The decay processes of L core holes of the fifth row element compounds
91-027	A. Nishijima National Chemical Laboratory for Industry	Study of functional materials containing SiC and SiN by Si K-edge XAFS
91-028	A. Nishijima National Chemical Laboratory for Industry	Study on the inner shell photoelectron and high resolution fuluorecent X-ray spectra
91-029	H. Oyanagi Electrotechnical Laboratory	"In-situ" structure study of surfaces and interfaces using intense SR X- ray beam
91-030	A. Nishijima National Chemical Laboratory for Industry	Study on a high resolution monochromator for soft X-ray
91-032	T. Murata Department of Physics, Kyoto Univ. of Education	EXAFS studies on the local lattice structure around impurity ion in ionic crystals
91-033	G. A. Williams Australian Radiation Laboratory	EXAFS studies of monomeric/dimeric equilibria of nitrido-technetium complexes in solution
91-034	K. Tomita Faculty of Pharmaceutical Sciences, Osaka Univ.	X-ray crystallographic studies of recombinant cytokines

Proposal Number	Spokesperson	Title
91-035	S. Harada Faculty of Engineering, Osaka Univ.	High resolution X-ray diffraction data collection of neutral protease from strepoomyces caespitosus
91-036	I. Tanaka Faculty of Science, Hokkaido Univ.	High resolution X-ray structure analysis of Ca binding lysozyme
91-037	K. Takahashi Faculty of Science, Univ. of Tokyo	X-ray crystallography of acid proteinase A from Aspergillus niger var. macrosporus
91-038	M. Konno Faculty of Science, Ochanomizu Univ.	The three dimensional structure of manganese superoxide dismutase
91-039	K. Fukuyama Faculty of Science, Osaka Univ.	X-ray crystallographic analysis of cytochrome bc, complex
91-040	H. Morimoto Faculty of Engineering Science, Osaka Univ.	X-ray crystallographic analysis of the conformation change of metal substituted hybrid hemoglobins
91-041	Y. Kai Faculty of Engineering, Osaka Univ.	X-ray crystal structure analysis of carboxylases
91-042	Y. Katsube Institute for Protein Research, Osaka Univ.	X-ray crystal structure analysis of function of glutathione synthetase
91-043	T. Tsukihara Faculty of Engineering, Tokushima Univ.	Intensity data collection by still photographs
91-044	T. Tsukihara Faculty of Engineering, Tokushima Univ.	X-ray crystal structural analysis of a single strand DNA binding protein
91-045	T. Tsukihara Faculty of Engineering, Tokushima Univ.	X-ray crystal structural analysis of tobacco necrosis virus
91-046	N. Sakabe Photon Factory, KEK	Evaluation and novel application study with newly constructed protein data collection system using multi-purpose Weissenberg camera III
91-047	N. Sakabe Photon Factory, KEK	X-ray crystal structure analysis of insulin derivative; big C2 DPI
91-048	N. Sakabe Photon Factory, KEK	Development of data collection system with newly developed Laue camera for time-resolved protein crystallography
91-049	N. Yasuoka Faculty of Science, Himeji Institute of Technology	X-ray study of hydrogenase and related proteins from sulfate reducing bacteria

Proposal Number	Spokesperson	Title
91-050	S. Yoshikawa Faculty of Science, Himeji Institute of Technology	X-ray structural analysis of cytochrome coxidase from bovine heart
91-051	H. Hotani Faculty of Science and Technology, Teikyo Univ	X-ray structure analysis of bacterial flagellar filaments
91-052	N. Kamiya The Institute of Physical and Chemical Research	Crystal structure analysis of nitrile hydratase
91-053	E. F. Pai Medical Research, MAX-Plank Institute	Very high resolution structure of HA-ras p21
91-054	E. N. Baker Dept. of Chem. and Biochem., Massey Univ.	Determination of the 3D structure of lactoferrin, aldehyde dehydrogenase and aspartyl proteinase by X-ray crystallography
91-055	A. Mondragon Mol. Biol. and Cell Biol., Dept. of Biochem., Northwestern Univ.	Structural studies of Escherichia coli, DNA topoisomerase I
91-056	D. Ollis Mol. Biol. and Cell Biol., Dept. of Biochem., Northwestern Univ.	Structural studies of the E. coli, single strand binding protein
91-057	A. Yonath Hamburg & Weizmann Institute, MAX-Plank Research Unit	Crystallography of ribosomes
91-058	G.G. Dodson Dept. of Chemistry, Univ. of York	Crystal structure of rat CD4: fab complex
91-059	N. Sosfenov Inst. of Crystall. of Academy of Science of the USSR	Nitrogen ficsation problem
91-060	N. Sasaki Faculty of Engineering, Muroran Institute of Technology	Time resolved X-ray diffraction from tendon collagen under creep
91-061	M. Hirai Faculty of Engineering, Kanagawa Institute of Technology	Development of solution scattering method by using ferrofluid
91-062	T. Fujisawa The Institute of Physical and Chemical Research	Structural change of the protein during the hydrolysis of ATP or GTP
91-063	D.M. Engelman Dept. of Mol. Biophys. and Biochem., Yale Univ.	Conformation of an unfolded protein under physiological conditions: Truncated Staphylococcal nuclease

Proposal Number	Spokesperson	Title
91-064	N. Yagi School of Medicine, Tohoku Univ.	X-ray diffraction of frog skeletal muscle during unloaded shortening
91-065	N. Yagi School of Medicine, Tohoku Univ.	Structure analysis of frog skeletal muscle in rigor
91-066	A. Ikai Faculty of Biosci. and Biotech., Tokyo Institute of Technology	Time resolved X-ray small angle scattering applied to the mechanistic study of trapping function of α 2-macroglobulins
91-067	I. Hatta Faculty of Engineering, Nagoya Univ.	Microscopic structural changes during the phase transitions of phospholipids
91-068	K. Wakabayashi Faculty of Engineering Science, Osaka Univ.	X-ray diffraction studies on structural changes of thin (actin) filaments during contraction of striated muscles
91-069	T. Hamanaka Faculty of Engineering Science, Osaka Univ.	X-ray diffraction studies on light induced structural change of cephalopodes visual cell outer segments
91-070	M. Sato Institute for Protein Research, Osaka Univ.	Time-resolved small-angle X-ray scattering study of F1-ATPase
91-071	K. Horiuchi Medical College of Oita	Structural study of myosin-actin interaction using caged ATP
91-072	S. Takemori The Jikei Univ. School of Medicine	X-ray diffraction study of an isolated mechanically-skinned skeletal muscle fiber (during contraction and after stretching)
91-073	S. Kikuta Faculty of Engineering, Univ. of Tokyo	Structural analysis of metal-silicon interface by X-ray
91-074	K. Sakurai National Research Institute for Metals	Characterization of thin films by grazing incidence X-ray fluorescence using SR
91-075	M. Miyamoto College of Arts and Sciences, Univ. of Tokyo	Structure and texture of micro-sized diamonds by chemical vapor deposition
91-076	Y. Ohashi Faculty of Engineering, Tokyo Institute of Technology	Dynamical structure analysis of desolvation process in cobaloxime complex crystal
91-077	N. Ishizawa Research Lab. of Engi. Materials, Tokyo Institute of Technology	Size effect on the phase transition of barium titanate by the micro crystal X-ray diffraction technique
91-078	H. Toraya Ceramic Engineering Research Lab., Nagoya Institute of Technology	The precise measurement of unit cell parameters and the structure determination by using powder diffraction method and synchrotron X-ray radiation
91-079	K. Ohsumi Photon Factory, KEK	Structure refinement of the microcrystal and microtexture based on the analysis of composite X-ray diffraction pattern

Proposal Number	Spokesperson	Title
91-080	N. Haga Faculty of Science, Himeji Institute of Technology	Structural study of commensurate-incommensurate transition of Co-åkermanite
91-081	R. Uno College of Humanities and Science, Nihon Univ.	Independent determination of the temperature factor of an atom in a powder sample
91-083	Y. Matsuo Faculty of Science, Nara Women's Univ.	X-ray diffuse scattering study of quasicrystal
91-084	H. Mashiyama Faculty of Science, Yamaguchi Univ.	New structures and phase transitions in A_2BX_4-type dielectric materials
91-085	K. Ishida Faculty of Science and Technology, The Science Univ. of Tokyo	X-ray magnetic diffraction study on hexagonal ferrite
91-086	T. R. Finlayson Department of Physics, Monash Univ.	Studies of diffuse scattering from martensitic indium-thallium alloys
91-087	A. M. Mathieson Chemistry Dept., La Trobe Univ.	Detailed investigation of Bragg single-crystal reflections by the Δw, $\Delta 2\theta$ method
91-088	Y. Noda Faculty of Science, Chiba Univ.	Hydrogen bond length of $K_3(H, D)(SO_4)_2$ under high pressure
91-089	T. Yagi Institute for Solid State Physics, Univ. of Tokyo	In situ observations of phase transformations of silicates at very high pressures and high temperatures
91-090	A. Onodera Faculty of Engineering Science, Osaka Univ.	Structural phase transition of boron nitride at high pressures and room temperature
91-091	K. Takemura National Institute for Research in Inorganic Materials	Pressure-induced structural phase transition of indium
91-092	R. J. Nelmes Dept. of Physics, Univ. of Edinburgh	Development of rietveld profile refinement and application to high-pressure structural studies of III-V type semiconductors
91-093	T. Nakajima Photon Factory, KEK	Study of structural transformations of Ho-elpasolite ($Cs_2NaHoCl_6$) at ultra and very low temperatures
91-094	T. Izumi Faculty of Engineering, Chubu Univ.	Effects of SR irradiation of superconductors Bi and Y system
91-095	C. Masuda National Research Institute for Metals	Fracture analysis of composite materials under loading condition by X-ray CT using synchrotron radiation

Proposal Number	Spokesperson	Title
91-096	Y. Kuroiwa Faculty of Science, Chiba Univ.	Atomic correlations of transition metals intercalated in layered compounds TiS_2
91-097	M. Tokonami Faculty of Science, Univ. of Tokyo	The study on site preference of a small amount of ion in olivin
91-098	T. Ohba Faculty of Science and Technology, Teikyo Univ.	Incommensurability in a composite crystal Nd-Fe-B
91-099	T. Takahashi Institute for Solid State Physics, Univ. of Tokyo	Structural studies on semiconductor surfaces by X-ray diffraction
91-100	Y. Muroga Faculty of Engineering, Nagoya Univ.	Analysis of aggregation-state of solid ionomers by wide angle range X-ray scattering
91-101	K. Nakayama National Research Laboratory of Metrology	Precision measurement of lattice spacing on standard crystals
91-102	O. Shimomura National Institute for Research in Inorganic Materials	Phase relation on boron nitride at high pressure and high temperature
91-103	Y. Noda Faculty of Science, Chiba Univ.	Structure analysis of $K_3H(SO_4)_2$ by high energy X-ray diffractometry
91-104	F. Marumo Research Lab. of Engi. Materials, Tokyo Institute of Technology	A study of electron distributions in crystals of transition-metal compounds with a micro-single-crystal X-ray diffraction technique
91-105	S. Kikuta Faculty of Engineering, Univ. of Tokyo	Nuclear resonant Bragg scattering by synchrotron radiation
91-106	K. Ishida Faculty of Engineering Science, The Science Univ. of Tokyo	Study of the high-Tc superconductors by X-ray resonant raman scattering
91-107	K. Ishida Faculty of Engineering Science, The Science Univ. of Tokyo	Wave length dependence of X-ray rocking curves from distorted crystal surfaces
91-108	S. Nanao Institute of Industrial Science, Univ. of Tokyo	Structural analysis of single quasi-crystals by anomalous X-ray scattering
91-109	Y. Sugita Faculty of Science, Toyama Univ.	Study of micro strain fields in silicon crystals by X-ray topography with high-order reflection
91-110	K. Kojima Faculty of Literature and Science, Yokohama City Univ.	Dislocation structure and motion in organic crystals

Proposal Number	Spokesperson	Title
91-111	H. Ino Faculty of Engineering, Univ. of Tokyo	Medium range atomic order and magnetism of melt-quanched RE-Fe alloys
91-112	T. Hondo Faculty of Engineering, Hokkaido Univ.	Behavior of lattice defects in ice under high pressure
91-113	K. Namikawa Department of Physics, Tokyo Gakugei Univ.	Polarization on analysis of resonant magnetic X-ray scattering
91-114	T. Ishikawa Faculty of Engineering, Univ. of Tokyo	Ultra precision triple-crystal topography
91-115	T. Ishikawa Faculty of Engineering, Univ. of Tokyo	Development of X-ray quarter-wave plates and its application
91-116	K. Namikawa Department of Physics, Tokyo Gakugei Univ.	X-ray parametric frequency conversion
91-117	J. Chikawa Faculty of Science, Himeji Institute of Technology	Impurity incorporation during crystal growth by X-ray irradiation
91-118	T. Matsushita Photon Factory, KEK	Study of two dimensional structure of Langmuir and Langmuir-Blodgett films
91-119	H. Arashi Research Institute for Scien. Meas., Tohoku Univ.	Compressibility measurements of β and β"- alumina
91-120	T.Yagi Institute for Solid State Physics, Univ. of Tokyo	Phase relations in the system silicate-metal-water under high pressure
91-121	O. Gendo Faculty of General Education, Kumamoto Univ.	Development of compton scattering technique at high pressure
91-122	S. Hasegawa Faculty of Electro-Communications, Univ. of Electro-Communication	Development of large field X-ray television system for energy subtraction and its application to coronary angiography
91-123	F. Takasaki Physics Department, KEK	Measurement of absolute sensitivity of photoemissive material by synchrotron light
91-124	T. Kikegawa Photon Factory, KEK	Development of the structural study of materials at high pressure and high temperature with high-energy monochromatic SR and MAX 80 system
91-125	S. Be The Institute of Physical and Chemical Research	Study of photodesorption using high energy photon beam

Proposal Number	Spokesperson	Title
91-126	K. Takikawa Institute of Physics, Univ. of Tsukuba	Radiation hardness test of scintillation calorimetry
91-128	M. Sakurai National Institute for Fusion Science	Generation and storage of multiply-charged rare gass ions using synchrotron radiation
91-129	H. Hashizume Research Lab. of Engineering Materials, Tokyo Institute of Technology	Epitaxial structures of perovskite-related oxides
91-130	Y. Nannichi Institute of Materials Science, Univ. of Tsukuba	Structural and chemical properties at VI/III-V compound semiconductor interfaces
91-131	Y. Kagoshima Photon Factory, KEK	Characterization of transmission diffractive elements for soft X-ray optics
91-132	Y. Kagoshima Photon Factory, KEK	Application of a 400 Å-resolution zone plate to a soft X-ray microscope
91-133	T. Nagata Faculty of Science and Technology, Meisei Univ.	Multiple photoionization of rare earth atoms due to photoexcitation of 4d-shell electron
91-134	Y. Sato Research Institute for Scien. Meas., Tohoku Univ.	Dissociation dynamics of BF_3 and SiF_4 by inner-shell photoexcitation
19-135	K. Ueda Research Institute for Scien. Meas., Tohoku Univ.	Ionic fragmentation following L-shell photoexcitation of PH_3, PF_3, and PCl_3
91-136	T. Hayaishi Institute of Applied Physics, Univ. of Tsukuba	Decay channels following inner-shell photoionization in Kr and Xe
91-137	T. Hayaishi Institute of Applied Physics, Univ. of Tsukuba	Ne 1s conjugate shake-up spectrum in threshold electron spectroscopy
91-138	S. Nagaoka Faculty of Science, Ehime Univ.	Photodissociation of organometallic molecules by core-level excitation
91-139	K. Okuno Faculty of Science, Tokyo Metropolitan Univ.	Electron-correlation in inner-shell photoionization of atoms
91-140	T. Miyahara Photon Factory, KEK	Study on characterization of surface roughness using glancing-angle photoemission
91-141	H. Kihara School of Nursing, Jichi Medical School	Evaluation of photoemission surface characteristics
91-142	F. Iga Electrotechnical Laboratory	Study of the electronic structure of ABO_3 type conducting oxides by photoemission spectroscopy

Proposal Number	Spokesperson	Title
91-143	E. Miyazaki Faculty of Science, Tokyo Institute of Technology	Angle-resolved photoemission study of Si nitride films grown on the Si (111) surface
91-144	M. Taniguchi Faculty of Science, Hiroshima Univ.	Co 3d partial density of states and p-d hybridization in $Cd_{1-x}Co_xSe$
91-145	K. Obi Faculty of Science, Tokyo Institute of Technology	Study of photochemical surface reactions by optical emission spectroscopy
91-146	N. Kouchi Faculty of Science, Tokyo Institute of Technology	Absolute measurements of the photoabsorption, ionization, and dissociation cross sections for halogenated and organic silicon compound molecules
91-148	K. Yoshino Harvard-Smithonian Center for Astrophysics	Determination of spectroscopic properties of atmospheric molecules from vacuum ultraviolet cross sections, the schumann-runge continuum of O_2
91-149	K. Yoshino Harvard-Smithonian Center for Astrophysics	High resolution spectroscopic study and measurement of absolute photoabsorption coefficients of molecules of astrophysical and atmospheric importance
91-150	S. Suga Faculty of Engineering Science, Osaka Univ.	Resonant photoemission and 2-dimensional photoelectron spectroscopy of Cu_2Sb-type compounds
91-151	S. Sato Faculty of Science, Tohoku Univ.	Angle-resolved resonant photoemission from Ni single crystal
91-152	S. Kono Faculty of Science, Tohoku Univ.	Angle-resolved high-energy-resolution photoemission study of alkali-metal/Si(001) surfaces
91-153	T. Takahashi Faculty of Science, Tohoku Univ.	High-energy-resolved angle-resolved photoemission of Bi-high-Tc superconductor
91-154	S. Suzuki Faculty of Science, Tohoku Univ.	Determination of the polarization character of synchrotron radiation in VUV region
91-155	T. Ishii Institute for Solid State Physics, Univ. of Tokyo	High resolution photoemission of RB_6 (R=Lu, Ce, Pr, Nd, Sm)
91-156	A. Kakizaki Institute of Solid State Physics, Univ. of Tokyo	High resolution photoelectron spectra of Ce-Ni-Al compounds
91-157	T. Kinoshita Institute of Solid State Physics Univ. of Tokyo	Photoelectron spectroscopy study of rare earth metals/Ni(100) surfaces
91-159	M. Ando Photon Factory, KEK	An attempt at MR emittance measurement using X-ray optics

Proposal Number	Spokesperson	Title
91-160	K. Nishimura Saitama Medical College	Development of high speed acquision system for energy subtraction image of coronary arteries
91-161	S. Hasegawa Department of Chemistry, Tokyo Gakugei Univ.	XAFS study on the structure of surface species of Mn/MgO
91-162	K. Suzuki Institute for Materials Research, Tohoku Univ.	EXAFS study on pair correlation of Cu-Au alloys
91-163	K. Hyodo Photon Factory, KEK	Development of a new monochromator system for K-edge subtraction angiography
91-164	M. Ichikawa Catalysis Research Center, Hokkaido Univ.	Synthesis of dinuclear Mo sites inside zeolite and investigation of their thermal and photo activation process using dynamic EXAFS spectroscopy
91-165	M. Ichikawa Catalysis Research Center, Hokkaido Univ.	Synthesis of Pt_6-Pt_{15} carbonyl clusters inside NaY zeolite and interlayer nyobium oxide and their EXAFS characterization
91-166	N. Yoshida Faculty of Science, Hokkaido Univ.	XAFS studies on the axial-equatorial interactions in (dimethylgly oximato) cobalt (III) complexes
91-167	O. Terasaki Faculty of Science, Tohoku Univ.	Structures of PbI_2 clusters confined in the spaces of LTA
91-168	M. Sakurai Institute for Materials Research, Tohoku Univ.	Roles of the small additives in the formation of nanocrystalline growth from amorphous matrix
91-169	M. Matsuura Miyagi National College of Technology	Local structures of pseudo binary laves phase alloys
91-170	K. Ozutsumi Department of Chemistry, Univ. of Tsukuba	Structure of lanthanide (III) ion and its chloro and bromo complexes in N, N-dimethyformamide
91-171	Y. Iwasawa Faculty of Science, Univ. of Tokyo	XAFS studies on the dependence of d-densities of Pt and Ir catalysts on the particle size and the alloy formation with 11-group hetals, and the relation with the hydrogenation of C=C band
91-172	M. Misono Faculty of Engineering, Univ. of Tokyo	EXAFS of supported perovskite thin films with high catalytic activity for oxidation
91-173	H. Yoshitake Faculty of Engineering, Yokohama National Univ.	XAS study on metal trimer-attached electrodes — structure and dynamic behavior
91-174	H. Yoshitake Faculty of Engineering, Yokohama National Univ.	XANES study on the d-electronic state of electrode surface perturbed by the field of the electrical double layer during redox reactions

Proposal Number	Spokesperson	Title
91-175	T. Tanaka Faculty of Engineering, Kyoto Univ.	Yb L-edge XAFS study of valence variation of Yb in Zeolite
91-178	T. Murata Department of Physics, Kyoto Univ. of Education	Site selective analysis of local structure through optical XAFS and mechanism of X-ray excited optical luminescence in ionic crystals
91-179	I. Watanabe Faculty of Science, Osaka Univ.	Solvent parameters and EXAFS parameters for solvated bromide ion
91-180	I. Watanabe Faculty of Science, Osaka Univ.	Study of structures of $[CuN_4]$-type imide-amine complexes in solution by XAFS
91-181	H. Sakane Faculty of Science, Osaka Univ.	XAFS study of the Jahn-Teller effect on hexanitro complexes of Cu(II) and Co(II)
91-182	H. Sakane Faculty of Science, Osaka Univ.	Studies on the structures of coordination sites and electronic state of metal glycerate complexes
91-183	Y. Okamoto Faculty of Engineering Science, Osaka Univ.	EXAFS analysis of the structure of active species on supported $PdCl_2$-$CuCl_2$ composite catalysts
91-184	S. Emura Institute of Scien. and Indus. Research, Osaka Univ.	Research on correlation between host-guest complementarity and coloration
91-185	H. Terauchi Faculty of Science, Kwansei Gakuin Univ.	Local structure analysis of the ferroelectric $Cd_{1-x} Zn_x Te$ mixed crystals
91-186	H. Yamazaki Faculty of Science, Okayama Univ.	Local structure and spin electronic states in amorphous R-Fe alloys
91-187	Y. Nishihata Faculty of Science, Okayama Univ.	EXAFS study on local structures near the displactive phase transition of perovskites
91-188	T. Ohta Faculty of Science, Hiroshima Univ.	Temperature dependent EXAFS study of bromine and krypton-adsorbed systems
91-189	K. Tamura Faculty of Integrated Arts and Sciences, Hiroshima Univ.	EXAFS studies of liquid chalcogenide semiconductors
91-190	I. Ouchi Faculty of General Education, Tottori Univ.	Local distribution of Cr atoms in Co-Cr thin films
91-192	T. Yamaguchi Faculty of Science, Fukuoka Univ.	XAFS study on oxygen-evolving complex (photosystem II) and model compounds

Proposal Number	Spokesperson	Title
91-194	L. Ma Center of Analysis and Measurement, Fudan Univ.	Structure research for ionomers and catalysts of transition metal
91-195	Y. Kou Lanzhou Institute of Chem. Phys., Chinese Academy of Science	XAFS study of immobilized carbonyl cluster
91-196	J. M. Webb Mudoch Univ.	EXAFS studies of biological iron oxide particles
91-197	M. Itoh Institute of Atomic Energy, Kyoto Univ.	Application of EXFAS on the structure analysis of ultrafine particles of binary compounds (BiCu, BiTe, Pd-H)
91-198	K. Seki Faculty of Science, Nagoya Univ.	XANES studies of resonance structures and tautomerism of organic compounds
91-199	A. Fujishima Faculty of Engineering, Univ. of Tokyo	Investigation of the photochromic behaviors of oxidized transition metal thin films by the X-ray absorption spectroscopy
91-200	Y. Kondo Faculty of Engineering, Tohoku Univ.	Effects of core excitation on the defect-formation yield: Br-ls excitation in KBr single crystals
91-201	K. Hirotsu Faculty of Science, Osaka City Univ.	Structure and function of aspartate aminotransferase
91-202	A. Takenaka Faculty of Biosci. and Biotech., Tokyo Institute of Technology	Structural studies on functional nucleic acid fragments
91-203	K. Miki Research Lab. of Resources Utilization, Tokyo Institute of Technology	X-ray crystallographic analysis of NADH-cytochrome b_5 reductase
91-204	S. Iwata Photon Factory, KEK	X-ray crystallography of L-lactate dehydrogenase from Bifidobacterium longum
91-205	A. Nakagawa Photon Factory, KEK	Development of wavelength selecting system at BL-6A2
91-206	K. Nakamura Faculty of Engineering, Nagaoka Univ. of Technology	Crystal structure analysis of site-directed mutants of ribonuclease Rh
91-207	E. Ohtsuka Faculty of Pharmaceutical Sciences, Hokkaido Univ.	X-ray structural analysis of T_4 endonuclease V by synchrotron orbit radiation
91-208	B. W. Matthew Institute of Molecular Biology, Univ. of Oregon	Weissenberg data collection of beta-galactosidase from E. coli
91-209	J. L. Smith Department of Biological Science, Purdue Univ.	Collection of diffraction data from crystals of glutamine amidotransferase

Proposal Number	Spokesperson	Title
91-210	J. T. Bolin Department of Biological Science, Purdue Univ.	Measurement of high resolution diffraction data from crystals of nitrogenase MoFe protein
91-211	F. A. Quiocho Howard Hughes Medical Institute	Crystallographic study of antibody Fab fragments; gp 120
91-212	J. Varghese CSIRO	Antigen-antibody structure; influenzavirus antigens complexed with antibody FAB fragments
91-213	J. Varghese CSIRO	Seed storage protein structure
91-214	T. L. Blundell Dept. of Crystallography, Birkbeck College	Collection of high resolution X-ray diffraction data using Weissenberg camera from crystals of the aspartic proteinases
91-215	W. H. Hunter Department of Chemistry, Univ. of Manchester	Structural characterisation of trypanothione reductasce
91-216	D. C. Wilev Dept. of Biochem. and Biophys., Harvard Univ.	Crystallographic studies of influenza C virus glvcoprotein at the Photon Factory
91-217	K. Kajiwara Faculty of Engineering and Design, Kyoto Institute of Technology	Dynamic aspect of thermoreversible gelation of tamarind gum
91-218	S. Sakurai Faculty of Textile Science, Kyoto Institute of Technology	Structural investigation on fatigue mechanism of segmented polyurethanes containing polydimethylsiloxane
91-219	Y. Inoko Faculty of Engineering Science, Osaka Univ.	X-ray solution scattering study of the packing of subunits in polynucleosomes
91-220	H. Yoshida Faculty of Engineering, Tokyo Institute of Technology	Small angle X-ray study on super-structure formation of the water-polysaccharide systems
91-221	Y. Izumi Faculty of Engineering, Yamagata Univ.	Structure of calmodulin-target protein complex and expression of function
91-222	N. Matsushima School of Allied Health Professions, Sapporo Medical College	Structure of S100 proteins as studied by solution X-ray scattering
91-223	T. Yamaguchi Faculty of Science, Fukuoka Univ.	Small-angle X-ray scattering from solution of bile salt
91-224	H. Sugi School of Medicine, Teikyo Univ.	Determination of the actomyosin-ATP reaction step coupled with force generation in skeletal muscle
91-225	M. Watanabe Department of Physiology, The Jikei Univ. School of Medicine	X-ray diffraction study of the guinea-pig Taenea coli

Proposal Number	Spokesperson	Title
91-226	T. Ohnishi Department of Biology, Nara Medical Univ.	Killing effects of soft X-ray on the spores of dictyostelium discoideum
91-227	N. Munakata National Cancer Center Research Institute	Action spectroscopy for inactivation and mutagenesis of bacterial spores in ultrasoft-X wavelengths
91-228	K. Hieda Faculty of Science, Rikkyo Univ.	Effects of K-shell X-ray absorption of carbon, phosphorus and bromine on strand breaks of oligonucleotides
91-229	A, Yokoya Japan Atomic Energy Research Institute	Characteristics of degradation of biological molecules with inner-shell photoabsorption in solutions
91-230	K. Kobayashi Photon Factory, KEK	Study on the type of genetic changes induced by monochromatic soft X-rays in yeast cells
91-231	T. Takeda Institute of Clinical Medicine, Univ. of Tsukuba	Coronary angiography by filter method
91-232	H. Mori School of Medicine, Tokai Univ.	Applications of SR-excited X-ray fluorescent spectrometry in medical fields
91-233	H. Mori School of Medicine, Tokai Univ.	Attempt at diagnosis using table heavy trace element by imaging technique with synchrotron radiation
91-234	Y. Gohshi Faculty of Engineering, Univ. of Tokyo	Development of hard X-ray aspherical mirrors
91-235	A. Iida Photon Factory, KEK	Wavelength dispersive X-ray fluorescence analysis
91-236	I. Nakai Department of Chemistry, Univ. of Tsukuba	Characterization of light-elements in earth and planetary minerals by SR-XRF microanalysis
91-238	O. Terasaki Faculty of Science, Tohoku Univ.	Structures of zeolites and materials confined in them
91-239	J. Plevert Research Lab. of Engineering Materials, Tokyo Institute of Technology	Polymorphic crystal structures of $Co(NO_3)_2 \cdot 6H_2O$ and phase transformations at low temperatures
91-240	K. Toriumi Faculty of Science, Himeji Institute of Technology	X-ray structural analysis of C_{60} and the related carbon fullerens
91-241	Y. Kashiwase College of Education, Nagoya Univ.	Correlation between X-ray inelastic scattering and dynamical diffraction
91-242	T. Fukamachi Saitama Institute of Technology	Determination of anomalous scattering factors used by Pendellösung fringes due to X-ray resonant scattering

Proposal Number	Spokesperson	Title
91-243	T. Fukamachi Saitama Institute of Technology	Diffraction due to imaginaring atomic scattering factors from absorbing perfect crystal
91-244	M. Sakata Faculty of Engineering, Nagoya Univ.	X-ray powder diffraction by specimens of light elements
91-245	S. Nojima Faculty of Engineering, Nagoya Univ.	Morphology formation in PCL/PCL-b-PB polymer alloys
91-246	K. Osamura Faculty of Science, Kyoto Univ.	Synchrotron radiation SAXS analysis of III-V epitaxial layers and their interfaces
91-247	K. Osamura Faculty of Science, Kyoto Univ.	Dynamical structure change of Al-based alloys during phase decomposition and reversion
91-248	M. Izumi Tokyo Univ. of Mercantile Marine	Study of molecular conformation of I_3-ions in layered Langmuir-Blodgett films of charge-transfer salt based on TTF derivative
91-250	Y. Kashihara Japan Atomic Energy Research Institute	Study of step structures on the declined surface
91-251	Y. Kudo Faculty of Science Tohoku Univ.	Single crystal X-ray study on pressure-induced phase transition of CaF_2
91-252	N. Kojima Faculty of Science, Kyoto Univ.	High temperature and high pressure X-ray study on the crystal structure of Au mixed-valence compounds $M_2Au_2X_6$ (M=Rb, Cs; X=Cl, Br, I)
91-253	S. Urakawa Japan Atomic Energy Research Institute	Precise determination of the phase relations of $KAlSi_3O_8$ under high pressure
91-254	K. Takemura National Institute for Research in Inorganic Materials	Structure determination of the high-pressure phase (IV) of Ba
91-255	M. Imai National Research Institute for Metals	Pressure-induced phase transition of calcium silicide and barium silicide
91-256	K. Kawamura Faculty of Science, Hokkaido Univ.	Pressure induced structure change of binary alkali silicate liquids
91-257	H. Kawamura Faculty of Science, Himeji Institute of Technology	Structural phase transformation induced by electronic transition under pressure
91-258	T. Yokoo The Institute for Chemical Research, Kyoto Univ.	Role of heavy metal oxide in functional glasses on the basis of anomalous X-ray
91-259	E. Matsubara Re. In. of Min. Dressing and Metallurgy, Tohoku Univ.	Structural analysis of colloidal particles in aqueous solution by anomalous X-ray scattering

Proposal Number	Spokesperson	Title
91-260	H. Tsunemi Faculty of Science, Osaka Univ.	Performance test for the direct X-ray detection CCD at soft X-ray region
91-261	H. Yamazaki Faculty of Science, Okayama Univ.	5d- and 4f-electronic states of $R_2Fe_{14}B$ compounds by X-ray resonance exchange scattering
91-262	Y. Chikaura Faculty of Engineering, Kyushu Institute of Technology	Instrumentation research on X-ray scattering topography using SR
91-263	T. Chikaura Faculty of Engineering, Kyushu Institute of Technology	Observation of thermal behavior of microdefects in thinned silicon wafers by means of plane-wave SR topography
91-264	N. Yamaguchi Plasma Science Center, Univ. of Tsukuba	Calibration of radiation measurement instruments for plasma diagnostics
91-265	H. Iwasaki Photon Factory, KEK	Development of dynamic measurement method of pole figures using synchrotron radiation and its application to recrystallization process of silicon steel
91-266	A. Goto Faculty of Engineering, Hokkaido Univ.	Photon counting method using synchrotron-radiation X-rays and its applications
91-267	Y. Amemiya Photon Factory, KEK	Test of the X-ray polarimeter and its application to optical activity measurement
91-268	A. Matsumuro Faculty of Engineering, Nagoya Univ.	Structure and properties of quasicrystal under high pressure
91-269	A. Matsumuro Faculty of Engineering, Nagoya Univ.	Determination of high pressure phase diagram and P-V relation of Al-Li alloy
91-270	S. Nakai Faculty of Engineering, Utsunomiya Univ.	XAS measurement with a PPAC detector
91-271	M. Okusawa Faculty of Education, Gunma Univ.	Resonant-photoemission studies of satellites accompanying shallow-core-level lines in transition-metal compounds
91-272	S. Yasumi Teikyo Univ.	Studies on the M-shell of the dysprosium atom using monochromatic X-rays of determining the mass of the electron neutrino
91-273	T. Ohta Faculty of Science, Hiroshima Univ.	Polarized XAFS study on the dissociation process of silane and disilane adsorbed on Ni single crystals
91-274	K. Shinohara The Toyko Metropolitan Institute of Medical Science	Biological application of X-ray microscopy with zooming tube

Proposal Number	Spokesperson	Title
91-275	Y. Kitajima Photon Factory, KEK	Study on surface reconstruction induced by sulfur adsorption on silver and cupper single crystal
91-276	T. Sasaki Japan Atomic Energy Research Institute	Electronic-structure analysis of ion-implanted layers by XANES
91-277	H. Kihara School of Nursing, Jichi Medical School	Observation of Au-colloid-labeled biospecimen by contact X-ray microscopy
91-278	M. Yanagihara Research Institute for Scien. Meas., Tohoku Univ.	Developments and applications of short-spacing multilayers for soft X-rays
91-280	H. Fukutani Institute of Physics, Univ. of Tsukuba	Development, characterization and applications of polarizers in VUV, SX
91-281	T. Koide Photon Factory, KEK	Magnetic-circular-dichroism study of the electronic states of transition metals, rare earths and their compounds. II
91-282	N. Ueno Faculty of Engineering, Chiba Univ.	Photochemical decomposition of organic solids in VUV and soft X-ray region
91-283	K. Ito Photon Factory, KEK	High-resolution Stark spectroscopy of rare gases
91-284	M. Ukai Faculty of Science, Tokyo Institute of Technology	Perfect focusing TOF magnetic bottle photoelectron spectrometer
91-285	I. Honma Faculty of Engineering, Univ. of Tokyo	A synthesis of diamond films by SR-photochemical vapour deposition
91-286	A. Kakizaki Institute for Solid State Physics, Univ. of Tokyo	Core level photoelectron spectra of alkalimetals
91-287	C. Y. Park Dept. of Physics, Sung Kyun Kwan Univ.	ARUPS study of reconstructional phase transition Mo(100) surface
91-288	M. Kusunoki Institute for Protein Research, Osaka Univ.	X-ray crystal structure analysis of UDP-glucose pyrophosphorylase
91-289	R. M. Stroud Dept. of Biochemistry, Univ. of California	Crystal structure of transmembrane ion channels: colicin Ia, nicotinic acetylcholine receptor, and Bacillus thuringiensis toxin
91-290	X. M. Huang Photon Factory, KEK	Study of pressure effects on amorphous formation of $Pd_{40}Ni_{40}P_{20}$ alloy
91-293	H. Takei Institute for Solid State Physics, Univ. of Tokyo	Clustering of V^{3+} ions in $LiVO_2$ single crystals

Proposal Number	Spokesperson	Title
91-Y001	M. Oshiro Fujitsu Laboratories Ltd.	Exposure test by synchrotron radiation in BL-17A, BL-17B, and BL-17C
91-Y002	K. Kato Mitsui Petrochemical Industries, Ltd.,	EXAFS studies on the structure of the zirconocene derivative catalyst in solution
91-Y003	Y. Goto Fundamental Research Lab., NEC Corp.	X-ray optics, X-ray lithography and photo-chemical reaction experiments
91-Y004	K. Miyauchi Center Research Laboratory, Hitachi Ltd.	A study of semi-conductor etching reactions by synchrotron radiation
91-Y005	K. Miyauchi Center Research Laboratory, Hitachi Ltd.	BL-8A; soft X-ray diffractometry, XPS. B; silicon EXAFS experiments, total reflection measurement. C; digital radiography, lithography, microprobe experiments, CT, and micro X-ray diffractometry.
91-Y006	Y. Ishii Applied Electronics Laboratory, NTT	Materials analysis, lithography and photo-reaction using SR
91-Y007	S. Saeda Center Research Laboratory, Showa Denko K.K.	Micro-analysis of contaminants on a silicon wafer by X-ray fluorescence
91-Y008	K. Yoshida Research Center, Mitsubishi Chemical Industries Ltd.	The structural analysis of Co complexes in solution by XAFS
91-Y009	S. Suzuki Polymer Research Laboratory, Idemitsu Petrochemical. Co., Ltd.	Structure determination of organometallic compounds by EXAFS
91-Y010	K. Ohshima Central Research Institute, Mitsui Toatsu Chemicals, Inc.	XAFS analysis of metallic copper catalyst
91-Y011	K. Ohshima Central Research Institute, Mitsui Toatsu Chemicals, Inc.	XAFS analysis of metallic silver catalyst
91-Y012	Y. Goto Fundamental Research Lab., NEC Corp.	X-ray optics, X-ray lithography and photo-chemical reaction experiments
91-Y013	A. Hyugaji Central Research Institute, Mitsui Toatsu Chemicals, Inc.	EXAFS analysis of modified metallic copper catalysts
91-Y014	M. Miyao Center Research Laboratory, Hitachi Ltd.	BL-8A; soft X-ray diffractometry, XPS. B; silicon EXAFS experiments, total reflection measurement. C; digital radiography, lithography, microprobe experiments, CT, and micro X-ray diffractometry.
91-Y015	M. Ohtsuki Fujitsu Laboratories Ltd.	Exposure tests by synchrotron radiation in BL-17A, BL-17B, and BL-17C

Proposal Number	Spokesperson	Title
91-C001	K. Akimoto Fundamental Research Laboratories, NEC Corp.	Characterization of semiconductor materials by high precision X-ray goniometer system
91-C002	Y. Ohishi Tsukuba Research Laboratory, Sumitomo Chemical Co., Ltd.	Small Angle X-ray shattering study for dynamical structural Change of polymers
91-C003	N. Yoshioka LSI R&D Laboratory, Mitsubishi Electronic Corp.	Application of high-efficiency monochromator for soft X-ray
91-C004	H. Morikawa Nippon Steel Corp.	Dynamic observation of materials processing using synchrotron radiation
91-C005	Y. Yasuami ULSI Research Center, Toshiba Corp.	Diffuse X-ray scattering study on sublattice ordering
91-C006	S. Suzuki Tsukuba Research Center, Sanyo Electric Co., Ltd.	Microfabrication technique using synchrotron radiation
91-C007	A. Aoki Technical Research Center, NKK Corp.	Structure analysis of materials bombarded with particle beams
91-C008	T. Takigawa ULSI Research Center, Toshiba Corp.	Metal film deposition by SOR light irradiation
91-C009	K. Hayashi Nippon Steel Corp.	Quantitative Materials evaluation by monochromatic X-ray CT using synchrotron radiation
91-C010	M. Matsumoto Mechanical Research Laboratory Hitachi Ltd.	Study on surface cleaning and purification of materials using synchrotron radiation
91-C011	S. Kawado Research Center Sony Corp.	Characterization of Si crystal and process-related materials
91-C012	K. Kinoshita Hamamatsu Photonic K.K.	Development of a Photoemission microscope with synchrotron radiation
91-C013	Y. Yoshinaga Technical Research Center, NKK Corp.	Design study on the advanced SR beamline
91-C014	H. Nagata Nikon Corp.	Reflectivity measurement of Mo/Si Multilayers
91-C015	H. Yamada Sumitomo Heavy Industries Ltd.	Study for the development of ultra high brightness insertion device
91-C016	H. Hoshino Development Center, Konika Corp.	Study on structure of photographic silver halide microcrystals using high resolution X-ray powder diffraction

Proposal Number	Spokesperson	Title
91-C017	Y. Himeno Power Reactor and Nuclear Fuel development Cor.	The basic study of the development for high intensity CW Electron liner accelerator
91-C018	Y. Fukuda Cannon Inc.	Reflectivity measurements of Mo-Si multilayer mirrors
91-C019	K. Kondo Petroleum Energy Center	EXAFS study on hydrodesulfurization catalysts for ultra low sulfur distillate
91-C020	S. Suzuki Nuclear Power Division, Shimizu Corp.	Study on the effect of the building distortion to the beam orbit in the Photon Factory storage ring
91-C021	M. Koeda Shimazu Corp.	Development of SiC grating for soft X-ray
91-C022	H. Ohno Japan Atomic Energy Research	Analysis of Electronic states and atomic structures of radiation damaged materials
91-C023	H. Hashimoto Toray Research Center	Study of the dispersive XAFS spectrometer for time resolved measurements
91-C024	K. Usuda Research & Development Center, Toshiba Corp.	Characterization of Ga, As, Al crystals by means of X-ray diffraction
91-C025	M. Jinno Shimazu Corp.	Characterization of high spatial resolution soft X-ray recording material and its application by using undulator radiation

Y: approved for charged beam time,
C: Collaborations between the Photon Factory and institutes of private companies.

Injector Linac Division

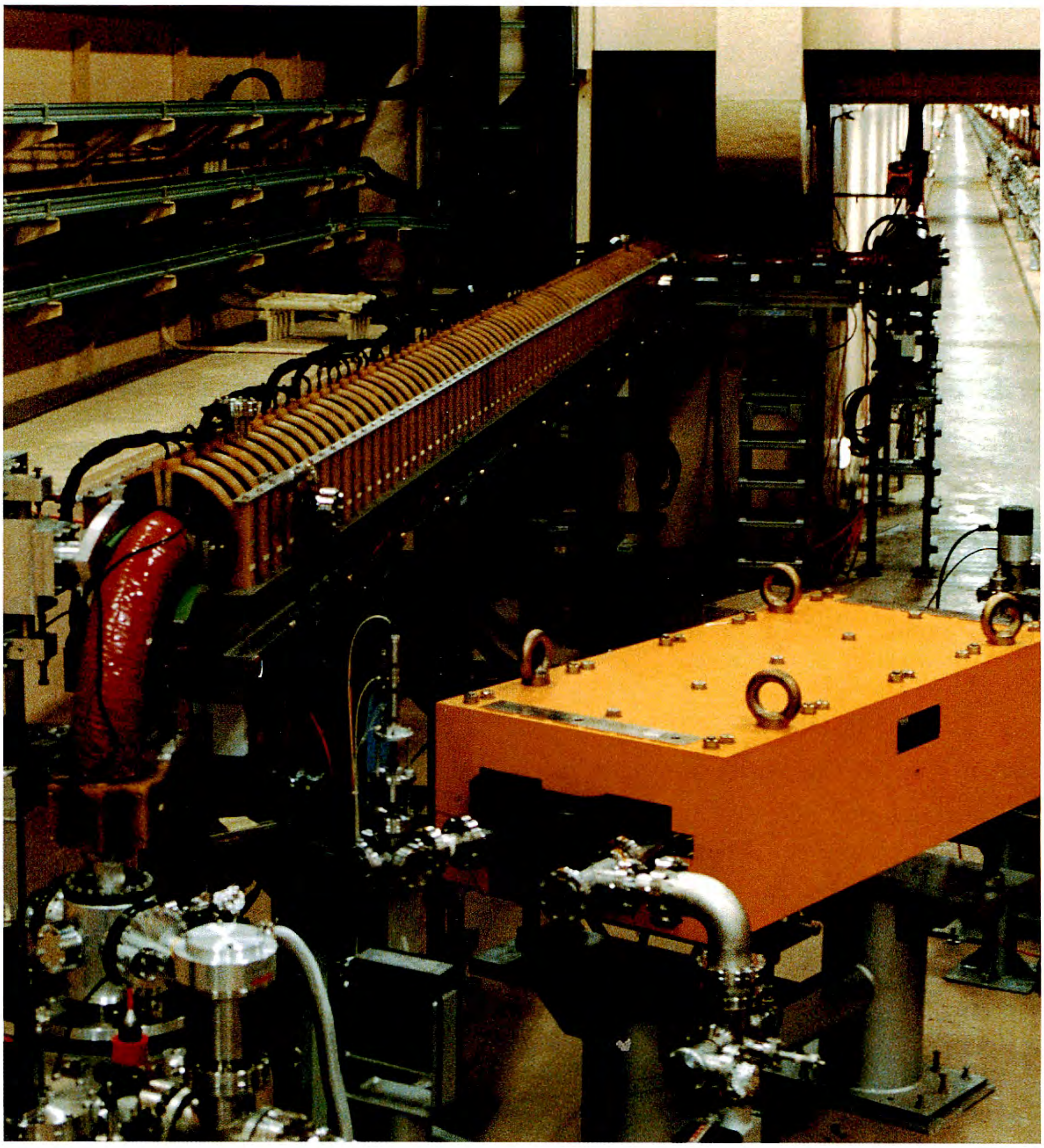

*Slow-positron beamline under construction
at the end of the PF 2.5-GeV electron/position linac.*

You can jump to the article by clicking its title.

CONTENTS

INJECTOR LINAC DIVISION

A. INTRODUCTION

Operation of the linac this year has also been satisfactorily performed on the whole. There were a few problems, such as an rf window breakdown and a dummy load failure, for which it took a somewhat long time to recover, because a vacuum leak was caused.

Although almost all klystrons presently being used have barium-impregnated cathodes, all of them have old-type rf windows. A few klystrons were recently made which have improved windows with a Ti-N coating, and will be test used very soon. It seems probable that in the near future a demand to increase the rf power will be made on the linac in connection with KEK's future plans. A test operation of a SLAC-5045 klystron has started in order to meet such a demand. The control system of the linac has been used for nearly ten years; various improvements have been made and successfully used. However, it will become necessary to upgrade the system drastically within a few years; we thus already started studies of a new system.

Following the previous year, the following reinforcements have continued on the positron-focusing system: new DC solenoids, sixteen quadrupoles, and an electron-positron separator. As a result, the positron intensity was almost doubled at the end of the generator. An improvement of the pulsed coil system was slightly delayed; however, the power supply of the system was completed and has undergone test use.

Regarding research, the following programs are now either in progress or have been completed: (1) high-brightness beam production, (2) a slow-positron source, (3) BBU experiments, (4) radiation-hardness tests of a detector for the SSC, (5) a plasma wake-field accelerator and (6) channeling radiation experiments.

High-brightness beam production has been studied with a cathode of 1 mm in diameter, and a new emittance measurement system is under development.

Fundamental research concerning a slow-positron sources was financially approved and construction of the source was undertaken in the beam switchyard.

A B-Factory project is one of the major future plans of KEK; in this project our linac is expected to produce high-intensity positrons that are more than ten times as strong as those being produced at present. For this purpose a study has been undertaken in order to accelerate a high-intensity electron beam up to 2 GeV. An extensive investigation of wake-field effects is planned.

One of the candidates to be used as a detector in the SSC is a tile/fiber calorimeter; one problem with this detector involves radiation damage. Therefore, the radiation hardness was investigated using 2.5-GeV electron beams by a group from the University of Tsukuba and KEK. As a result, it was shown that this detector could be an appropriate design under the expected radiation circumstances.

A study of a plasma wake-field accelerator has been continued with a new plasma chamber. The chamber is capable of producing a more intense plasma with a density range of $2\text{-}8\times10^{12}$ cm^{-3}; the experiment showed good agreement with calculations.

The channeling radiation experiment was further carried out with a 2.5-GeV positron beam, and succeeded to directly detect radiation with a NaI (Tl) detector system.

Finally, it is worth mentioning that a group in our division received the 16th Technical Prize from the Vacuum Society of Japan for research concerning "Breakdown Phenomena of Alumina-Ceramics RF Window and Its Suppression."

A. Asami

B. OPERATION

During the period from October, 1990, to September, 1991, the linac was stably operated with a total operation time of 5,125 hours and an operation rate of 97.7%. The operation statistics for this period are listed in Table 1. Several failures which involved comparatively long recovering times during this run were as follows: a puncture of the capacitor of a klystron modulator (Feb. 14, '91); a vacuum leak of a microwave window (Feb. 19, '91) and a vacuum leak of a dummy load for an accelerating waveguide (June 24, '91). Frequent internal arching of the accelerating structure (P-4) which is installed immediately after the position target occurred during this period; it was subsequently replaced during the summer shutdown (August, '91).

The cumulative usage hours and the averaged fault rate with the averaged applied anode voltage during these nine years are shown in Tables 2 and 3, respectively. Klystrons with barium-impregnated (BI) cathodes were introduced into the linac from 1987, and

41 out of the 48 klystrons were replaced with them at the end of July, 1991. A very low fault rate of the BI tubes at a comparatively higher anode voltage was obtained, as was also true last year. Owing to the higher averaged anode voltage, four klystrons have usually been able to stand by under 2.5 GeV operation.

H. Kobayashi

Table 1. Operation and failure time of each cycle.

	Date	Operation time (hrs)	Failure time (hrs)	Operation rate (percent)
FY 1990				
	Oct. 16 - Nov. 14	688	2.4	99.7
	Nov. 20 - Dec. 25	828	15.7	98.1
	Jan. 29 - Feb. 27	692	49.4	92.9
	Mar. 4 - Mar. 30	612	4	99.3
FY 1991				
	Apr. 8 - May 2	569	4	99.3
	May 7 - May 29	528	10.1	98.1
	June 5 - June 30	604	28.2	95.3
	June 1 - July 26	604	2.8	99.5
total		5,125	116.6	97.7

Table 2. Cumulative usage hours of klystrons during the past years.

Period	Total	Unused	Failed		Living		MTBF
	No. of tubes	No. of tubes	No. of tubes	Mean age (hours)	No. of tubes	Av.op.time (hours)	(hours)
up to 1985/7	79	2	28	3,600	49	6,200	13,400
up to 1986/7	91	3	39	4,400	49	7,400	13,100
up to 1987/7	106	4	52	4,400	50	9,600	13,600
up to 1988/7	120	2	67	4,500	51	11,400	13,500
up to 1989/7	140	5	82	6,400	53	12,400	14,400
up to 1990/7	158	6	98	8,500	54	11,200	14,700
up to 1991/7	176	14	107	10,100	55	11,100	15,800

Table 3. Averaged fault rate and averaged applied voltage to klystrons.

Period	Fault rate (/day·tube)	Applied voltage (kV)	Total operation (tube-days)
1982/8 - 1983/7	2.5	238	4,470
1983/8 - 1984/7	1.6	242	4,150
1984/8 - 1985/7	1.2	240	4,420
1985/8 - 1986/7	1.0	238	5,600
1986/8 - 1987/7	1.0	239	7,740
1987/8 - 1988/7	1.0	240	9,990
1988/8 - 1989/7	0.6	241	10,510
1989/8 - 1990/7	0.3	244	10,690
1990/8 - 1991/7	0.2	246	10,750

C. PROGRESS AND IMPROVEMENTS

1. INJECTION SYSTEM

1.1 Optical Trigger-Pulse Transmission System with Monitors

The optical trigger-pulse transmission system (Fig. 1) is utilized to transmit beam-requiring trigger pulses to an electron-gun grid pulser on the gun high-voltage potential level. In order to simplify trouble-shooting, this system has been improved so as to be able to monitor the output pulses of the relevant circuits at the high-potential level. This system consists of three module circuits, and the optical fibers connecting them: E/O and monitor modules on the ground level and a O/E module on the high-potential level. Trigger pulses which require electron beams are transmitted to a grid pulser through E/O and O/E modules. The monitor pulses of the O/E and the grid pulser are transmitted to the monitor module and switch its LED indicators. These pulses can be observed by using an oscilloscope to examine the circuit status. This new system enables us to quickly detect any problems in the relevant circuits, if any exist.

S. Ohsawa

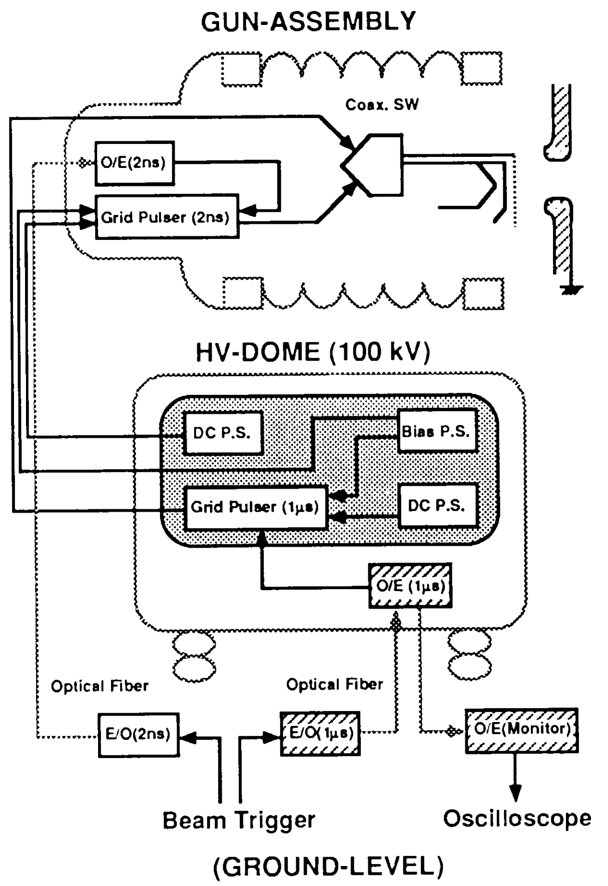

Fig. 1 Block diagram of the improved gun-trigger and the micro-second grid-pulser system.

1.2 New Micro-Second Grid Pulser and DC Power Supplies for the Electron Gun

A new micro-second grid pulser and DC power supplies for electron guns have been developed in order to meet the requirements of computer controlling and monitoring. All of the old ones were replaced by new ones. They are all fabricated compactly in NIM units (2 or 3 spans in case size) and installed in the high-voltage (HV) dome. Through a HV-dome control system their operational states can be obtained in a computer frame at a long distance through a CATV. They are also connected through a controller to an Expert System which has been developed for both diagnosis and operational support of the electron guns.

M. Yokota

2. MICROWAVE SOURCE

2.1 Operational Performance of Klystrons

The use of a barium-impregnated (BI) cathode instead of an oxide cathode in a klystron for an electron gun was the most effective method found to suppress internal arcing of the klystron, due to less electrode contamination. Up to July, 1991, as shown in Table 4, 46 klystrons with a BI cathode were operating in the linac klystron gallery, where 48 sockets and modulators are installed. They indicate a much longer MTBF (mean time between failures) of 100,000 hours than that of the oxide cathode type. Table 5 shows the operational performance of the klystrons. During these four years, the contribution of the BI cathode tubes to the total operation time increases by up to 87%, and their fault rate was 0.19/day-tube; this has resulted in a stable operation of the klystrons with an averaged applied voltage of 246 kV. More detailed statistics concerning operation shows that the rate of klystron down trips due to internal arcing in the BI cathode tubes has been 0.06/day-tube, which is much smaller than that in the oxide cathode type.

Table 4. Cumulative status of klystrons up to July 1991 corresponding to the year of production. Unused tubes are those which have never been used in the klystron gallery. STB(stand-by) tubes are those which have been used in the gallery and can be used there again.

Year of production	Cathode	Total No.of tubes	Unused No.of tubes	Living No.of tubes	Living (STB	Living Working) e-	Living e+	Living Av.op.time (hours)	Failed No.of tubes	Failed Causes (arcing	Failed Causes windows	Failed Causes others)	Failed Mean age (hours)	Cumulative operation (tube-hours)	MTBF (hours)
1979	oxide	4	0	0	0	0	0	------	4	2	1	1	3,902	15,608	3,902
1980	oxide	20	0	1	1	0	0	3,657	19	13	5	1	9,050	175,606	9,242
1981	oxide	20	0	1	1	0	0	11,227	19	11	2	6	15,965	314,611	16,588
1982	oxide	9	0	1	1	0	0	2,120	8	5	2	1	10,054	82,549	10,317
1983	oxide	13	0	1	1	0	0	14,170	12	6	2	4	18,753	239,205	19,934
1984	oxide	13	1	1	0	1	0	25,984	11	10	0	1	8,492	119,401	10,855
1985	oxide	12	1	3	0	3	0	25,449	8	7	0	1	8,409	143,618	17,952
1986	oxide	15	0	1	1	0	0	11,568	14	13	0	1	3,524	60,910	4,351
1987	oxide	7	0	0	0	0	0	------	7	5	1	1	4,342	30,393	4,342
1987	BI	7	0	6	0	6	0	17,496	1	0	1	0	10,219	115,194	115,194
1988	BI	20	1	17	2	12	3	12,065	2	0	2	0	9,031	223,163	111,582
1989	BI	18	1	15	0	13	2	8,367	2	0	1	1	5,185	135,880	67,940
1990	BI	18	10	8	0	6	2	4,025	0	0	0	0	-----	32,197	------
	oxide	113	2	9	5	4	0	16,125	102	72	13	17	10,164	1,181,901	11,587
	BI	63	12	46	2	37	7	10,169	5	0	4	1	7,730	506,434	101,287
	total	176	14	55	7	41	7	11,144	107	72	17	18	10,051	1,688,335	15,779

Table 5. Fault rate and applied voltage of oxide-cathode and BI cathode tubes during each one-year operation period.

Period	Fault rate (/day·tube) oxide	Fault rate (/day·tube) BI	Applied voltage (kV) oxide	Applied voltage (kV) BI	Total operation (tube-days) oxi	Total operation (tube-days) BI
1982/8 - 1983/7	2.5	---	238	---	4,470	---
1983/8 - 1984/7	1.6	---	242	---	4,150	---
1984/8 - 1985/7	1.2	---	240	---	4,420	---
1985/8 - 1986/7	1.0	---	238	---	5,600	---
1986/8 - 1987/7	1.0	---	239	---	7,740	---
1987/8 - 1988/7	1.03	0.28	238	239	9,290	710
1988/8 - 1989/7	0.79	0.27	238	244	6,460	4,060
1989/8 - 1990/7	0.42	0.25	242	245	3,440	7,250
1990/8 - 1991/7	0.19	0.19	244	246	1,380	9,370
total (up to 1991/7)	1.12	0.23	239	245	46,850	21,390

A breakdown phenomena in the output window of the klystrons, which is another serious problem involving high-power microwave sources, has been studied the last several years. The durability of the alumina ceramic materials used for windows has been examined at higher power (200 MW) using a resonant ring; a thickness optimization of the TiN coatings on the alumina window disks was also performed in order to suppress the multipactor effect. During FY 1991, newly developed alumina disks were mounted in the klystron output window; these will be tested under practical operation in the klystron gallery.

Y. Saito

2.2 60-MW Test Operation with the 5045 Klystron

As future projects at KEK, a B-factory asymmetry-rings positron-electron collider and the 3-GeV energy upgrade of the PF storage ring are now under investigation, both of which require an energy upgrade of the PF linac. In order to increase the linac accelerating energy, it is necessary to upgrade the rf source; we are planning to replace the existing 30-MW klystron stations with 60-MW class ones. Thus, for both preparation and experience regarding this power upgrade, we have carried out high-power tests using the SLAC-5045 klystron with associated components, as well as the existing modulator modified for matching the klystron characteristics.

The 5045 klystron parameters are shown in Table 6, together with the existing klystron (MELCO PV-3030) for a comparison. A doubling of the klystron output power requires a modification of the klystron modulator. In order to reduce the modification cost, the output voltage and average power of the modulator maintain present values, while an increase from 270 kV to 350 kV in klystron beam voltage is compensated for by increasing the pulse transformer step-up ratio from the present 1:12 to 1:15. As a consequence, the impedance and pulse width of the pulse-forming network (PFN) become 3.6 Ω and 2.2 μs, respectively, because the total capacitance remains unchanged (0.0146μF×20). The specifications of both the original and modified modulators are shown in Table 7.

In order to evaluate the modifications mentioned above, a preliminary test was carried out in the klystron test building. The klystron was set 10 m apart from the modulator in order not to interfere with routine tests of the 30-MW klystron unit; thus, 12 10-m-long 50-Ω coaxial cables in parallel were used to connect the PFN and the pulse transformer. The much lower impedance of the PFN required a modification of the number of PFN cells, from 20 to 10, by connecting the 2 capacitors and inductors in parallel. Figure 2 shows the beam current and output power versus the beam voltage of the 5045 klystrons. An rf output power of 58 MW with a pulse width of 1 μs was obtained at 345 kV; the rf conversion efficiency was 44%. The pulse shapes of the rf output power and the beam voltage are shown in Fig. 3. The ripple of the pulse top in the beam voltage is considered to be due to the effect of the length of the long coaxial cables combined with the leakage inductance of the pulse transformer. In addition, adjustment of the pulse shaping by the PFN inductors could not be sufficiently carried out, due to the limited variable range of the inductors.

A PFN reusing the existing capacitors is being fabricated in order to make pulse-shape adjustments easy and to obtain pulses that are more wide and flat. In order to examine the long-term reliability as a system, including the waveguide and the accelerating structure, preparations of more practical tests at the klystron gallery are presently under way.

Honma & Shidara

Table 6. Comparison of the original and upgraded klystron specifications.

	Original	Upgraded
Model designation	Mitsubishi PV-3030	5045
PF peak output power (MW)	30	65
Beam voltage (kV)	270	350
RF pulse width (μs)	3.5	2.2
Repetition rates (pps)	50	50
RF gain (dB)	51	50
Micro-perveance	2	2
Efficiency (%)	40	45

Table 7. Comparison of the original and modified modulator specifications.

	Original	modified
Maximum peak power (MW)	84	145
Maximum average power (kW)	14.7	14.7
Transformer step-up ratio	1:12	1:15
Output pulse voltage (kV)	23.5	23.5
Output pulse current (A)	3600	6150
PFN impedance (Ω)	6.0	3.6
PFN total capacitance (μF)	0.3	0.3
Pulse width (μs)	3.5	2.2
Rise time (μs)	0.7	0.8
Fall time(μs)	1.2	1.5
Pulse repetition rate (pps)	50	50
Maximum pulse height deviation from flatness (%)	0.3 (peak to peak)	0.5
Maximum pulse amplitude drift (%/hour)	0.3	0.5
Thyratron anode voltage (kV)	47	47

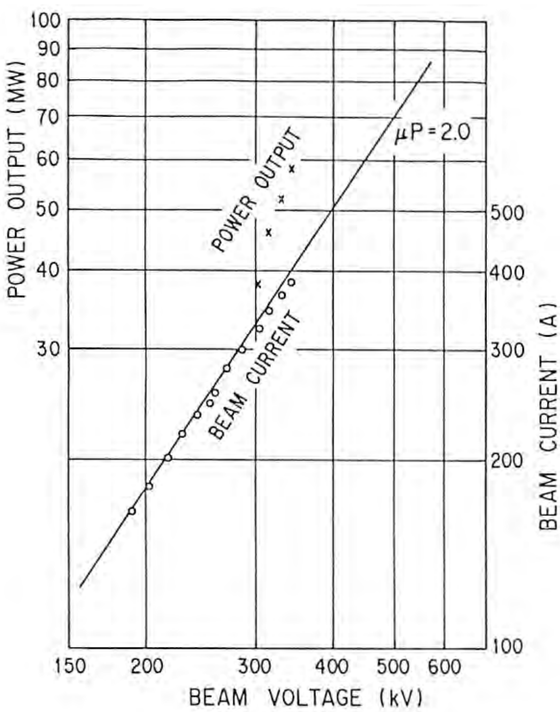

Fig. 2 Beam current and output power versus the beam voltage.

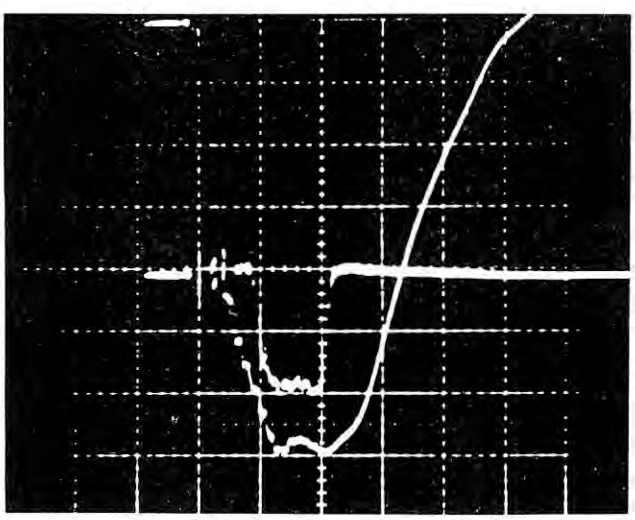

Fig. 3 Pulse shapes of the beam voltage (upper; vert. 50 kV/div, hor. 1 μs/div) and output power (lower; vert. 10 mV/div, hor. 1 μs/div).

3. CONTROL SYSTEM

3.1 Linac Control System Upgrade

The linac has been controlled with a distributed processor network, with which eight minicomputers (Mitsubishi MELCOM70/30), and hundreds of microcomputers are connected. However, the system resources have become inadequate for increasing demand. In addition, Mitsubishi will discontinue support for the MELCOM70/30 system over the next few years. We have therefore studied the possibility of a system rejuvenation based on a complete replacement of the minicomputers (MELCOM70/30) as well as its associated fiber-optic network (LOOP-I). The proposed control system is to comprise Unix-based workstations as a man-machine interface, an Ethernet as a high-speed communication network, and VME stations as front-end systems. Table 8 gives the correspondences between the components of the present and the proposed control systems.

We have introduced Unix-based workstations (a DECstation 5000/200 and a diskless DECstation 5000/125) and a VME station (68030-based with the OS9/68k operating system). The aim is to study software techniques needed in the next control system. A survey regarding X-windows and related tools has been used in a new study of the availability of X-window as a man-machine interface. The feasibility of RPC (Remote Procedure Calls) used as a network communication tool has also been investigated. These studies are still in progress.

A network communication library called "SCLIB", which is based on stream sockets (TCP/IP protocol), has been developed. This library shows high communication availability among different operating systems (Unix, VMS, and MS-DOS). It also shows a high source portability of application-level programs among computer systems provided by different vendors. The data-transfer times, including library overhead, are 0.2-30 ms for a data size of 1-1000 bytes, depending on the CPU power of the computers used. The SCLIB library is expected to be used in the next control system.

A replacement of the sub control stations requires a new I/O module which would connect the existing local-network (LOOP-II/III) with the new main-network (an Ethernet). A VME module for controlling the LOOP-III has been developed and is now being checked in the test phase. Another VME module for the LOOP-II is under development.

Table 8. Plan for the replacement of the present control system. The local-networks and the device controllers will be used successively in the next system.

Hardware	the present system	the next system
main-console station	MELCOM70/30 (two)	Unix-Workstations (many)
main-network	LOOP-I (5 Mbit/s)	Ethernet (TCP/IP) (10 Mbit/s)
sub control station	MELCOM70/30 & CAMAC (six)	VME stations (seven)
local-network	LOOP-II/III (500/48 kbit/s)	(do not change)
device-controller	microprocessor based board computers	(do not change)

Recently, application processes for the magnet power-supplies have been developed and are now under operation in the new workstations. These processes control/monitor the power-supplies through the gateway (Mitsubishi MX3000II) with the present system. Since these program sources call the SCLIB functions, they do not contain any vendor-dependent descriptions. These sources are thus expected to be available even in the next control system.

N. Kamikubota

3.2 Improvements in DS-Link

The DS-Link network has been operated stably as a human interface of the PF 2.5-GeV linac. Many programs involving linac operation are continuously being developed and improved, mainly using a structured BASIC language.

OS/2 multitask stations were linked to the existing MS-DOS station network (DS-Link) in 1990, and the OS/2 station (FMR70HX3, 386-CPU, 25 MHz, 16 MB, FUJITSU Co.) has been running as a monitor station for status checking. There has been many discussions concerning program productivity, reliability, flexibility, etc. We have thus been tried to build a so-called ACPP (Accelerator Control Program Package), which makes operation easy, and improves the reliability, flexibility and productivity of the program.

ACPP is a tool used for a non-programming type accelerator control which is graphically oriented, and easy-to-use by using flexible control and a monitor system. It has an alarm and report system and is supported by a simple expert system. ACPP is presently under operation for the magnet, klystron modulator.

I. Abe

3.3 Expert System

Many expert systems (ESs) have been developed in the PF linac. In 1991, a diagnostic and operation support ES for the injector system (electron gun) was developed and is now undergoing test operation.

The ES can now support linac operators, and even injector-system experts when they face various problems. Since the ES is on-lined with the conventional computer network, it would ask fewer questions to the users and suggest how to carry out operation and repairs. A knowledge base for many tasks in the accelerator domain was investigated during this project; what has been achieved was outlined in a presentation at ICALEPCS (International Conference on Accelerator and Large Experimental Physics Control Systems).

I. Abe

4. POSITRON GENERATOR

The KEK positron generator focusing system has been upgraded since FY 1990. By the end of January, 1991, the upgrade was completed except for the pulsed solenoid just after the positron production target. During the 1991 summer shutdown, the pulsed power supply was replaced by an upgraded (from 5 to 20 kA) one. A new pulsed solenoid producing much stronger field by this power supply, is presently under development.

4.1 Performance of the Upgraded Positron Focusing System

The following items were improved in the focusing system: (1) the magnetic field strength of the focusing solenoid after the target was doubled (2 kG -> 4 kG), (2) the length of the solenoid was doubled (4 m -> 8 m), and (3) the acceptance of the beam transport after the solenoid was also doubled by adding quadrupole magnets. It was expected from a theoretical estimation that the positron current would be doubled.

Another improvement was in the beam separator. Before this upgrade, we could not accurately measure the current of the positron beam until the bending magnet for the beam transport line, due to a cancellation involving electrons from the target. We have placed a set of four bending magnets and an electron absorber. Electrons and positrons are separated here, and only electrons are eliminated. This elimination of electrons enables us to measure the positron current just after the solenoid region. We can independently observe the performance of the focusing of positrons by a solenoid as well as the performance of the beam transport by quadrupole magnet system.

During a beam study after the upgrade, the beam transport system for electrons which hit the target and the solenoid focusing system were tuned by monitoring the positron current just after the separator. The positron beam transport system after the solenoid region was tuned with the monitoring positron current at the end of the positron linac. After careful tuning, the positron current was increased to 36 mA at the end of the positron linac. Since the ordinary current before the upgrade was around 19 mA, the improvement was almost twice as much.

An increase of the field strength of the focusing solenoid has resulted in an increase of the transverse acceptance, as well as a further increase in the energy acceptance. We have measured the dependence of the positron beam current and the spectrum for the solenoid field strength. They were measured at the end of the positron linac. Figure 4(a) shows the spectra of positrons with magnetic fields of (a) 2 kG and (b) 4 kG. It shows that the energy acceptance of the solenoid focusing system has been almost doubled, as was expected. The variation of the positron current with the magnetic field strength is shown in Fig. 4(b). An increase by more than a factor of two in the current was observed upon doubling the field strength.

T. Kamitani

(a)

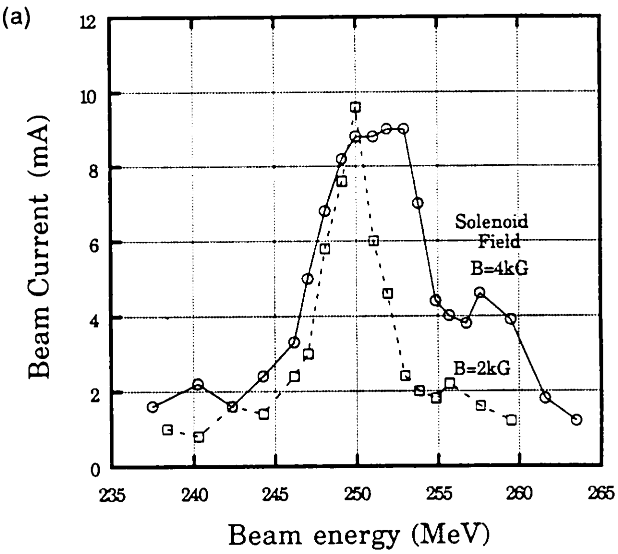

(b)

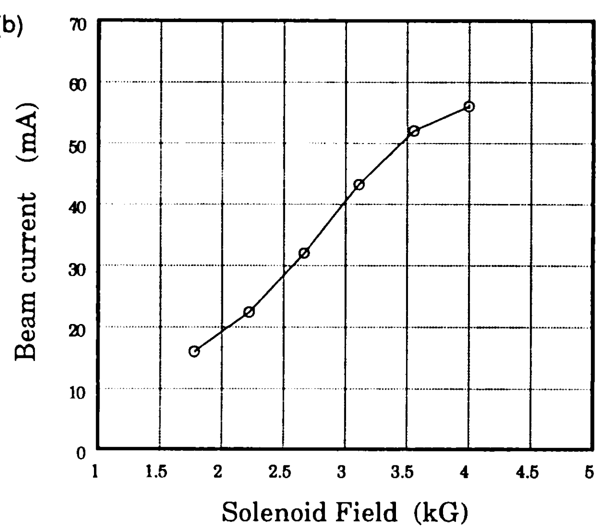

Fig. 4 Positron beam characteristics at the end of the positron generator (250 MeV): (a) spectrum, (b) positron beam current vs. solenoid field.

4.2 Newly Fabricated Pulsed Power Supply

As one of the improvements in the positron generator focusing system, a strong pulsed power supply was newly fabricated and installed for the pulsed focusing coil located just downstream the positron production target. This power supply was designed so as to produce half sine-wave pulses that are 100 μs wide with a 20-kA peak current, a 4-kV peak voltage and a 50-Hz repetition rate. Such a high-current performance was realized by utilizing the highest grade commercially available silicon controlled rectifiers (SCRs). The main switching part comprises four units connected in parallel, each of which is made of three serially connected SCRs. The main specifications of the pulsed power supply are listed in Table 9. They were determined so as to satisfy the requirements of a newly designed pulsed coil which is now under development.

With this power supply, the new pulsed coil is expected to produce a stronger and shorter axial field (20 kG and 5 cm), compared with the present one (~10 kG, ~8 cm effective length). This requirement results from the following considerations based on the "quarter-wave-transformer (QWT)" principle: (1) The pulsed coil, which has a strong field (B_i) and a short effective length (L), performs the phase-space matching function between the positron-target exit and the low-field region (B_f) following the pulsed coil. The matching condition is

$$B_i = B_f\ (\ a\ /\ r_i\ ),$$

where a the acceleration structure aperture and r_i the size of the positron beam emerging from the target. (2) The positron yield is approximately proportional to B_f/L; therefore, a stronger B_f and a shorter pulsed coil is effective. In this upgrade, we have increased B_f by a factor of two; the pulse coil length will be decreased from 8 to 5 cm. (3) It is preferable that the acceptable positron momentum, determined by B_iL, be lager, since it suppresses debunching effects. This requires a higher field. In order to satisfy the above mentioned requirements, the specifications of the pulsed power supply were determined.

S. Ohsawa & T. Oogoe

Table 9. Main specifications of the pulse-coil power supply.

Output pulse current (Max.)	20 kA	
Output pulse Voltage (Max.)	4 kV	
Pulse wave form	half sine	
	pulse width	100 μs
Load coil inductance	4~6 μH	
Pulse amplitude drift	less than 1 %	
Pulse repetition rate	50 Hz	

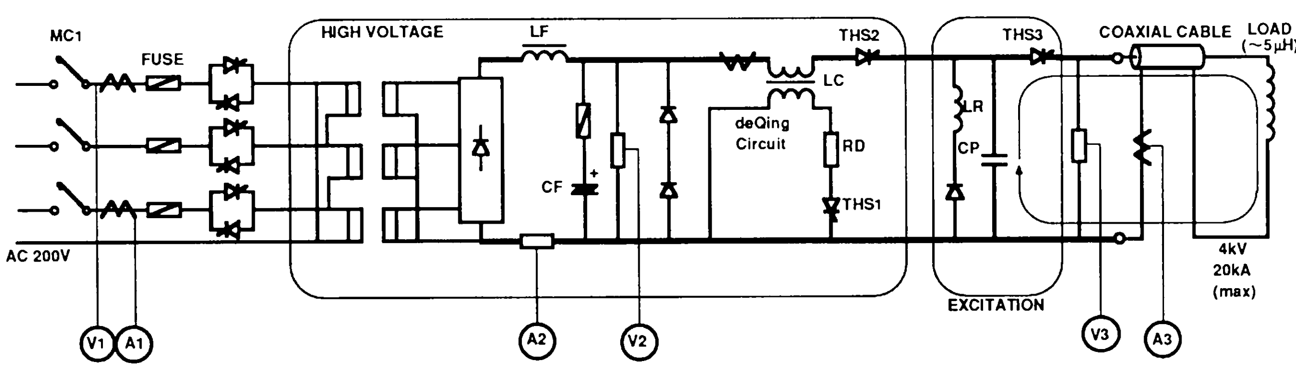

Fig. 5 Circuit diagram of the pulse-coil power supply.

D. RESEARCH

1. TEST LINAC

In the test linac facility, the first beam with an energy of 25 MeV and an average current of 1 μA was accelerated on April 17, 1991. After checking the radiation safety interlock system by the Radiation Safety Control Center of KEK , the use of the linac was permitted. Since then, an electron gun and an emittance measurement system for high-brightness electron sources have been investigated.

An electron gun with a 1-mmϕ cathode was fabricated on the basis of the design parameters described in the last issue. The output current versus the cathode temperature of the gun at an anode voltage of 150 kV was measured (Fig. 6). A maximum current of 430 mA (current density of 55A/cm^2) was obtained; this would be the limit of the cathode temperature.

The calculated emittance of this gun is around 1 πmm-mrad at the current of 600 mA (current density of 76 A/cm^2). An emittance measurement system for such a small value is being developed. We wanted to avoid any errors due to either an energy change during the rise and fall times or a pulse-to-pulse fluctuation of the anode voltage. To this end, the pepper-pot method with a time gate was adopted (Fig. 7). The beamlets passed by the pepper-pot mask drift and hit a 10-μm thin scintillator film located downstream. The pin-hole image on the scintillator is very small, and is measured by a long-distance microscope. An image intensifier with a gate width of 3 ns at minimum and a gain of 10^6 at maximum is used to amplify the image intensity of the long-distance microscope. A camera with an image analyzer follows the image intensifier.

The pinhole diameter for the pepper-pot is 30 μm and is spaced by 200 μm in order to measure a beam with a very small size and a small divergence angle.

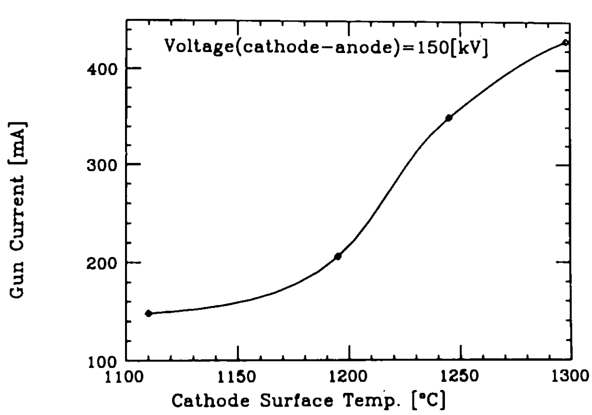

Fig. 6 Output current of the gun versus the cathode temperature of the gun.

The pin-hole on the pepper-pot and the pin-hole image on the scintillator film are shown in Figs. 8(a) and (b), respectively. The measured normalized emittance of the gun is about 0.8 πmm-mrad at a current of 200 mA. Thus a gun with small emittance will be used as a reference beam generator in investigations concerning the emittance growth in each component of the linac.

H. Kobayashi

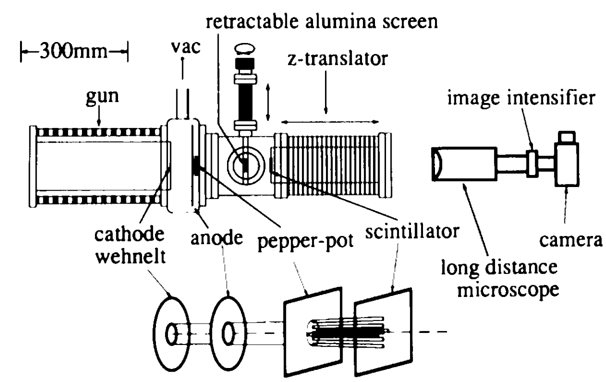

Fig. 7 Setup of the emittance measurement system. The arrangement is as follows: anode to pepper-pot 12.7 mm; pepper-pot to scintillator 172.4 mm.

(a)

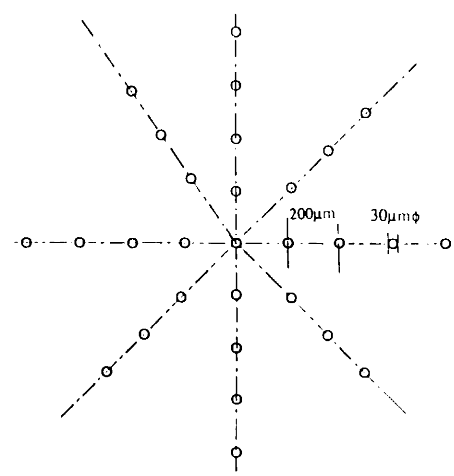

(b)

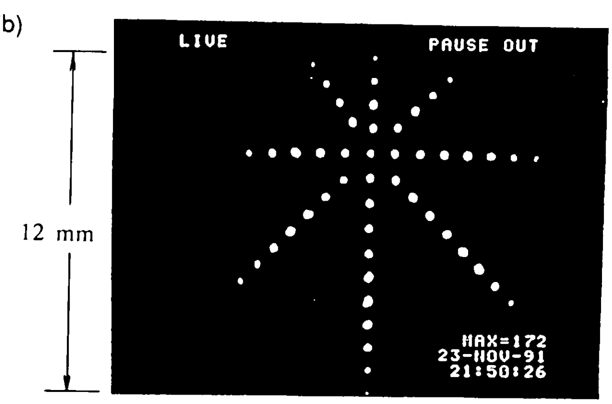

Fig. 8 Dimensions of the pepper-pot (a) and image of the pepper-pot on thin scintillator (b).

2. SLOW-POSITRON SOURCE

Recently, beams of monoenergetic positrons over an energy range from eV to keV (so-called slow positrons) have been used to study a variety of fields of solid state physics: surface, bulk and defect phenomena. Studies of the interactions of positrons with matter has received great acceleration due to a new technique based on an insight by Madansky and Rasetti in 1950; positrons do not necessarily annihilate in the same material in which they are slowed to thermal energies. Slow-positron reemission from a solid under β^+ bombardment was discovered by Cherry in 1958 and confirmed by Costello et al. 10 years later.

Since positrons have the same mass as electrons, they will exhibit similar diffraction effects when scattered from a single-crystal surface. The advantage of using positrons are that they interact with the solid in a simpler way, owing to the absence of any exchange forces or repulsion from the ion cores, in contrast to the attraction and strong influence for low-energy electrons. For example, the interpretation of low-energy electron diffraction (LEED) requires extensive computations; these simple aspects of the positron may be valuable. However, positron diffraction cannot be a practical method due to the lack of its intensity obtained from a radioactive-isotope-based positron source. Using a β^+ emission radioactive isotope, only about 10^5 -10^6 slow positrons per second can be obtained. This positron current of sub-pico ampere is too small compared to typical electron beam currents used for surface analysis. This is the reason why we have developed a slow-positron source. We may expect 4×10^8 positrons per second with a nominal beam power of the PF linac (6.25 kW), and 2×10^9 positrons per second with a full beam power of 30 kW.

Devices used for the slow-positron transport line (such as Helmholtz coils, coil-wound vacuum ducts as well as their power supplies) were fabricated. During the summer shutdown, most of these devices were installed in the beam switchyard at the end of the 2.5-GeV Linac. Reconstruction of the 2.5-GeV electron /positron beamline to the target-moderator assembly was also carried out during the summer shutdown. The 2.5-GeV electron beam was injected into the target-moderator assembly position through an achromatic beam transport line comprising two 18°-deflecting magnets and a quadrupole magnet, as shown in Fig. 9. Figure 10 shows the slow-positron beamline from the target-moderator assembly to the experimental area. The entire length of the beam line is about 30 m. The positrons will be detected by a channel electron multiplier (CEM).

T.Kurihara and A.Shirakawa

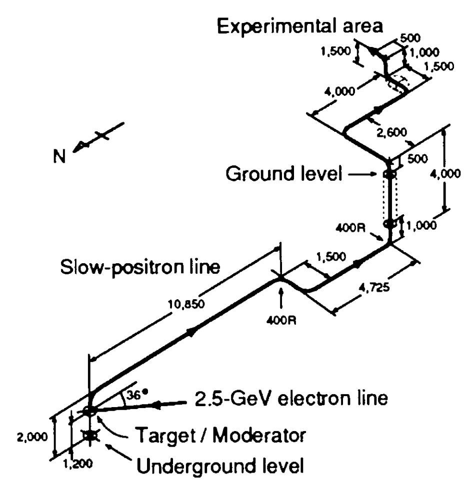

Fig. 10 Schematic layout of the slow-positron beam line.

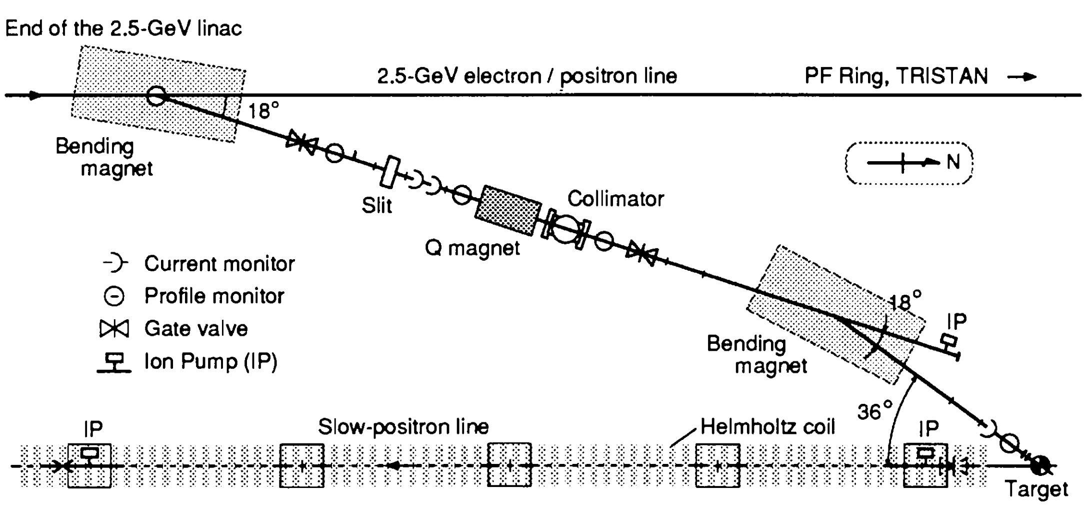

Fig. 9 Layout of the reconstructed beam lines in the switchyard at the end of the 2.5-GeV Linac.

3. BBU EXPERIMENTS ON A HIGH-CURRENT SHORT-PULSE BEAM

A fine investigation of the wake-field instability caused by an intense beam is one of the most indispensable items for the research and development of future accelerator designs: the Japan linear collider (JLC) and the injector linac of the proposed B-factory project at KEK. In both designs, emittance growth during acceleration must be prevented in order to obtain a large luminosity at the collision point (JLC) as well as a large positron yield at the target (B-factory).

We have carried out a series of experimental studies on the wake field characteristics of the KEK positron generator linac (a peak current of 10 A, a pulse width of 2 ns and a final energy of 250 MeV(a length of 23 m)) since 1989. The results have shown good agreement between experiments and theoretical predictions. For future large-scale, high-intensity accelerators, however, wake-field effects will be more complex, since the length of the accelerator becomes very long and, accordingly, many factors which can cause instabilities may appear. In this connection, we performed two experiments in order to clarify the distance dependence of the instability as a simple extension of our former experiments, and to study the long-acceleration characteristics of the intense beam: one was achieved by extending the acceleration region of the KEK positron generator linac (10 A, 2 ns and 250 MeV) from 250 MeV to 500 MeV; the other was performed by using the 2.5-GeV linac with a peak current of 1 A, a pulse width of 17 ns and a final energy of 2.5 GeV.

The distance dependence was clearly verified by comparing the results of 250- and 500-MeV experiments at the positron generator linac. On the other hand, the long-acceleration characteristics of the intense beam could not be investigated quantitatively at the 2.5-GeV linac, since it seemed that the wake-field instability easily occurred with a slight error in beam steering. Figure 11 shows a typical beam break-up (BBU) phenomenon observed at the end of the 2.5-GeV linac. The end part of the beam waveform was distorted by the wake-field instability. This phenomenon was confirmed by observing the beam profile at the 2.5-GeV energy-analyzing station; a transverse spread of the last part of the bunches was observed. We also measured the beam emittance at the end of the linac, which indicates enormous growth. Since the results still seem to be too complicated to say anything quantitative, we will continue the experiments.

Y. Ogawa

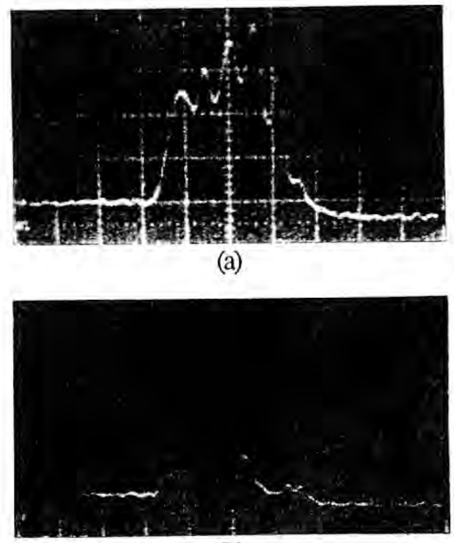

(a)

(b)

Fig. 11 Typical waveforms of the 2.5-GeV beam: (a) without an initial offset at the entrance of the first accelerating structure, (b) with an initial offset. The waveform distortion is caused by a transverse wake-field instability.

4. RADIATION-HARDNESS TESTS OF A SCINTILLATING TILE/FIBER CALORIMETER

The SSC (Super-conducting Super Collider) is a head-on-collider of 20-TeV protons, which is under construction in Texas, USA, and is scheduled to be commissioned in 1999. It is aimed at studying the standard model of electroweak theory as well as the mass-generation mechanism (Higgs mechanism). In addition, it is expected to explore novel phenomena in the TeV-region.

A general-purpose detector complex will be installed at one of the collision points by the SDC (Solenoidal Detector Collaboration) group, where many Japanese researchers participate. In the detector complex, calorimeters will play an important role, which requires a fast response time and a good position/energy resolution for high-multiplicity events.

At the University of Tsukuba, the feasibility of scintillating tile/fiber calorimeters has been studied. While they have good characteristics regarding response time and energy resolution, their radiation hardness was unknown. The luminosity of SSC is so high that detectors would be exposed to radiation up to several Mrad at the barrel part.

We, members of the University of Tsukuba and KEK, have collaborated to investigate radiation hardness of tile/fiber calorimeters. An electron beam of

2.5 GeV, which is adequate to simulate the real detector environment, was used.

The experiment was carried out at the beam dump of the PF 2.5-GeV linac from May to July, 1991. Figure 12 shows the experimental setup. Sample calorimeter modules, located on a movable table, were irradiated by the electron beam. The beam size and its position were controlled by newly designed quadrupole and steering magnets. Under various conditions eight modules were irradiated. The relation between the radiation dose and reduction of the signal outputs was examined with a test beam at the KEK proton synchrotron and with RI sources. The result shows that the reduction of the light outputs, measured in the range of 4 krad to 6.1 Mrad, increases roughly exponentially and reaches 25% at 0.44 Mrad.

Taking into account the result of an electron shower simulation, the characteristics change of the calorimeter in a real SSC experiment was estimated. The non-linearity of the calorimeter outputs at a radiation damage of 30% will be 5 to 2% for an electron shower in the 5 to 100-GeV range. This is not serious, since it can be calibrated with the decay events of W and Z bosons during the experiments. The energy resolution at radiation damage of 25% is estimated to be broadened by only 1% for a 100-GeV electron shower.

The present study suggests that the tile/fiber type calorimeters have sufficient radiation hardness for the barrel part of the SSC detector. The SDC group decided to employ the scintillating tile/fiber calorimeters as a barrel calorimeter in September, 1991.

K. Furukawa

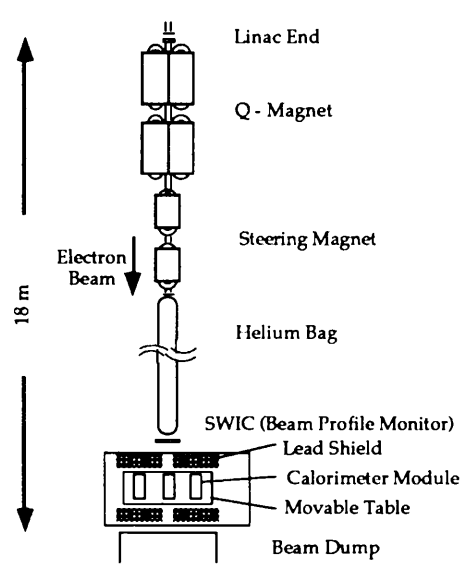

Fig.12 Experimental setup at the linac beam dump.

5. PLASMA WAKE-FIELD ACCELERATOR (PWFA) EXPERIMENTS

In the plasma wake-field accelerator (PWFA), a high-intensity driving bunch excites a large-amplitude plasma-wave which, in turn, accelerates a low-intensity trailing bunch. The plasma-wave is strongly excited when the distance between bunches coincides with a multiple of the plasma wavelength, determined by the plasma density. The amplitude of the wave depends on the driving bunch intensity, the size, the bunch train shape and the plasma density.

The KEK plasma wake-field experiment was initiated in 1989, utilizing an intense electron beam of the positron generator linac. At first, we used a 250-MeV, 7-A, 1-ns beam and a 1-m long, 300-mmϕ chamber with tungsten multi-filament cathodes in order to produce an argon-discharge plasma, and with permanent magnets to confine the plasma. In 1990 the cathodes were replaced by 4 lanthanum hexa-boride (LaB_6) cathodes, increasing the plasma density from approximately 10^{11} to 10^{12} cm^{-3}; by also solving a radiation safety problem, a 500-MeV beam became available. During this period (1991), the plasma chamber was renewed to a different type for further improvements of the plasma density. It has the same length (1 m), but a diameter of 50 mm with a 0.5-kG solenoid coil. The plasma is produced by ionizing argon gas with a helicon-wave excited by a 5-10 MHz, 0.5-1 kW rf wave fed into the chamber through a helical antenna. Thus, the plasma density ranged 2-8×10^{12} cm^{-3} within a rms radius of 5 mm along the beam axis.

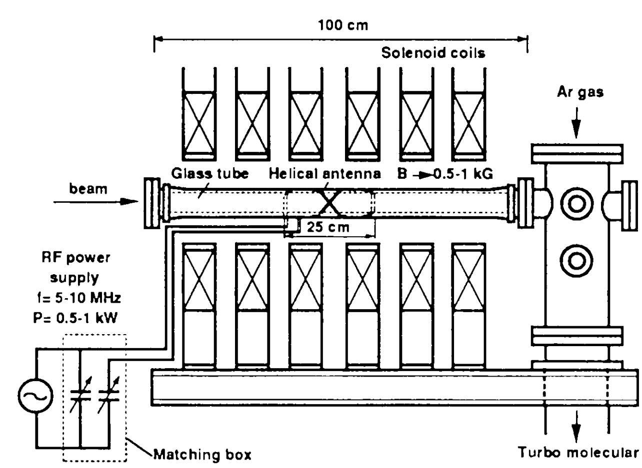

Fig. 13 Plasma generator with a helical antenna.

The energy spectrum of each bunch passing through the plasma chamber was measured with a bending magnet and a streak-camera system. In the 10^{12} cm^{-3} plasma density region the plasma wavelength is comparable with the bunch length. Therefore, the bunch may feel both an acceleration and a deceleration field along the bunch length; we obtained a rather low averaged energy shift of the bunch, compared with the last experiment. This result is reported in the user's report.

A. Enomoto

6. CHANNELING RADIATION EXPERIMENT

The channeling-radiation experiment group completed a two-year program using the linac 2.5-GeV positron beam. The experimental setup was the same as the previous one: a beamline with two lead collimators (2 mmϕ and 1 mmϕ) separated by 6.5 m, beam monitors (plastic scintillators, photodiodes), a 330-μm thick silicon crystal in a goniometer, and a NaI photon detector system.

After much effort to produce a highly collimated positron beam, in order to reduce the background noise and to align the NaI scintillator with the photon axis, a channeling photon spectrum was observed (Fig. 14). The photon peak energy was analyzed to be about 10 MeV by a pulse height analyzer (PHA), calibrated with Co^{60}.

A. Enomoto

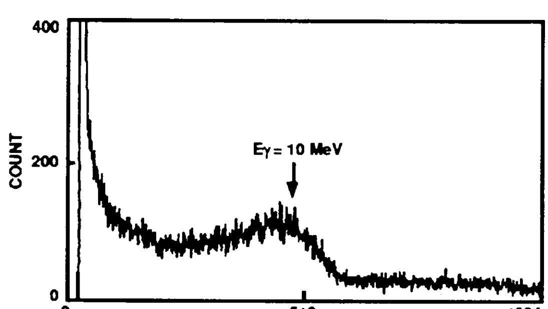

Fig. 14 Channeling radiation photon spectrum observed using a 2.5-GeV positron beam incident along the (110) plane of a 330-μm thick silicon target.

Light Source Division

The roof of the PF building was covered with polyethylene foam mats to suppress the thermal distortion of the building.

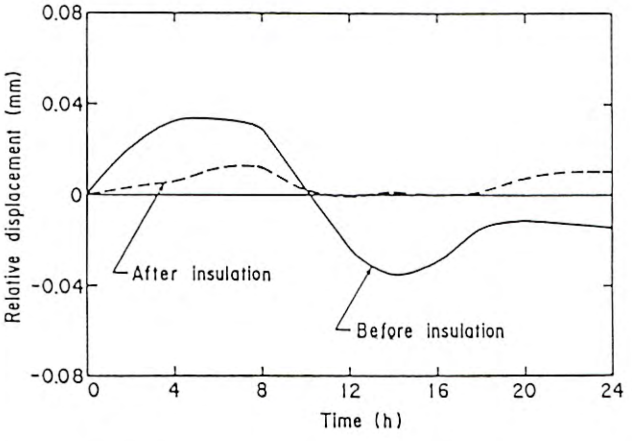

Diurnal vertical displacement of the PF building floor before and after thermal insulation.

You can jump to the article by clicking its title.

CONTENTS

LIGHT SOURCE DIVISION

A. INTRODUCTION

Single-bunch user-runs took place frequently during fiscal year 1990. This was the first trial at the Photon Factory, since the majority of users preferred high-current multi-bunch beams. Many problems concerning single-bunch operation were revealed, such as a local vacuum-pressure rise at the location of the isolation valves with no rf-shields. Single-bunch currents and lifetimes were largely limited through these vacuum conditions. During the scheduled shutdown from July 22 to October 2, 1991, a large modification related to the vacuum system was carried out. It involved a big venting of the storage-ring ducts; more than 2/3 of the vacuum ducts were opened. The isolation valves with no rf-shields, at which the pressure increased under single-bunch operation, were replaced by the valves with rf-shields.

Preparation for the FEL-project using the PF storage ring is underway; this project involves FEL research for developing a shorter-wavelength region. A gain measurement in the 177-nm region is our present goal. High-peak-current and high-quality beams under low-energy operation are essential for this project. In a preliminary study, a peak-current of 45 A was achieved with a beam energy of 0.75 GeV. For the FEL-project, we are planning to use beamline-2 (BL-02), where at present a 120-pole undulator is under operation as the most popularly used insertion device at the Photon Factory. This undulator is going to be replaced by an optical klystron next summer. The optical klystron, which is under construction, has a special structure in that the magnet configuration can be switched to the same configuration of the 120-pole undulator within two or three hours. During last summer, beam duct of B-01 was changed to a new duct which has an optical port at the opposite side of the synchrotron radiation port for the purpose of gain measurements and construction of an optical-cavity system.

Test runs under 3-GeV operation were carried out for users who require high-energy X-rays. We injected beams at 2.5 GeV, and then slowly boosted the beam energy up to 3 GeV. The stored current was 300 mA and the beam loss while boosting beam energy was quite small.

Tuning the magnet gaps of the insertion devices causes a small drift in the beam-orbit, and the photon axes move. Even such small drift disturbs user experiments. Independent tuning is carried out by carefully adjusting the beam orbit using the correction coils of each insertion device. At present, undulator #2, the undulator mode of MPW#16, multi-undulators #19A,C,and D and EMPW #28 are available for independent tuning. For MPW#13 and the wiggler mode of MPW#16, the gaps can be changed only during the beam-injection time.

SUMMARY OF STORAGE RING OPERATION

A summary of the operation times of the storage ring is given in Fig. 1. Table 1 shows the operation statistics between April 9 and December 16, 1991. The injection intervals and average currents are illustrated in Fig. 2. The initial stored current was 350 mA for the user-run, and the beam lifetime was in excess of 60 hours at 300 mA. The average stored current was about 300 mA during 24-hour operation. During fiscal year 1990, 296 hours (8.3% of the user time) was provided for single-bunch users. In fiscal year 1991, the single-bunch time was 208 hours, as listed in Table 1. At present, the maximum single-bunch current is limited to 104 mA due to a vacuum-pressure rise. The beam lifetime at 50 mA is 10 hours, which is mainly due to the Touschek effect. Therefore, the lifetime strongly depends upon the beam size, which was examined by using skew quadrupole magnets, as discussed later.

Progress has been made in cleaning the beams in neighboring buckets. This is very important for experiments using nuclear resonances, such as Mössbauer experiments. Vertical betatron-tunes vary with the bunch currents at a rate of about -2×10^{-4}/mA, which can be explained in terms of the transverse broadband impedances of the beam ducts. If there is a large difference in the beam population, a bunch with a low population, a low-current bunch, can be singly excited with an rf knock-out method which destroys it. The fraction in neighboring bunch to the center one was reduced to below 10^{-5} by using the rf knock-out method and vertical scrapers which were installed in a straight section between B4 and B5.

Figure 3 is a plot of $I\tau$ (beam current × lifetime). The values of $I\tau$ are almost constant during each run, and $I\tau$ is a good standard of the storage-ring performance. The value of 1400 A·min during 1991

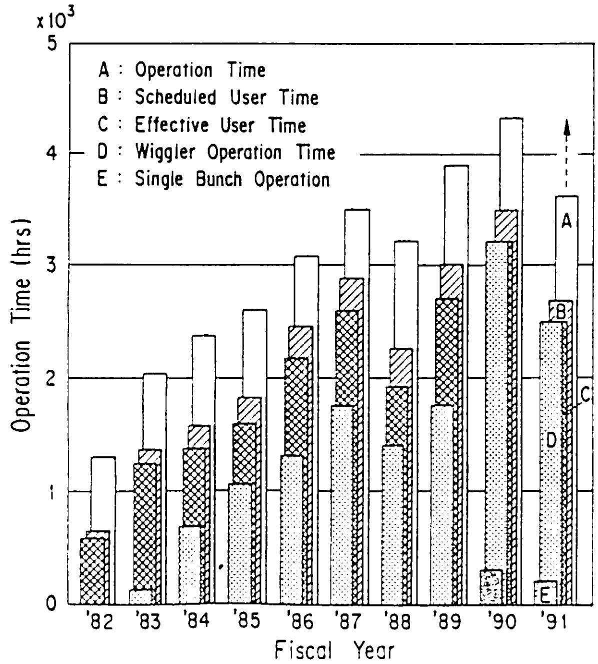

Fig. 1 Operation times of the storage ring from April 9 to December 16,1991.
A: Total operation time.
B: Scheduled user time.
C: Effective user time.
D: Wiggler operation time.
E: Single bunch operation.

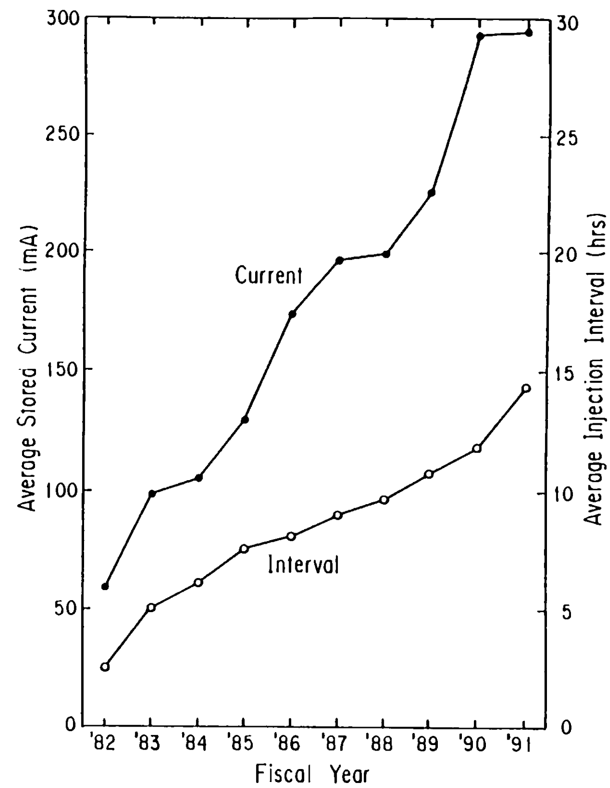

Fig. 2 Average stored currents and injection intervals.

Table 1. Statistics of storage ring operation between April 9 and December 16,1991

	Multi-bunch	Single-bunch	Total
Ring Operation Time (hours)	——	——	3595.5
Scheduled user time (hours)	2684.0	208.0	2892.0
Net user time T (hours)	2503.2	81.2	2584.4
Time used for injection (hours)	78.7	5.9	84.6
Integrated current in T (Ah)	722.0	2.1	724.1
Average current in T (mA)	288.5	25.5	——
Number of injection	175	11	186
Interval between injections (hours)	14.3	7.4	——

was very large and still appears to be increasing. $I\tau$ was 150 A·min in 1985, and it was already large. We usually vent 1/2 or 2/3 of the ring-ducts every summer shutdown for installation of insertion devices or other vacuum work. Immediately after every recommissioning, although the ring vacuum is usually very bad and so the lifetime was starting very badly, it gradually recovers.

A big increase of $I\tau$ during 1990 and 1991, as can be seen in Fig 3, can mainly be explained by following two reasons: (1) operation with low-β optics, and (2) single-bunch operation. The vertical beam aperture at the chamber of MPW#16 is 15 mm, which is the narrowest in the storage ring. Because the present beam lifetime is mainly given by the Coulomb scattering with residual gas, this chamber showed its lifetime limit. We changed the lattice parameters in order to optimize the lifetime due to gas scattering; we lowered the vertical betatron function from 12.7 m to 5 m at MPW#16 in April, 1990. With this optics (we call it the low-β optics) the beam lifetime went up by a factor of about two (see Activity Report 1990).

The increase of $I\tau$ shows that the ring-ducts are still becoming clean. Under single-bunch operation, the vacuum was usually very bad at the location of the isolation valves, since single-bunch beams generate high-frequency wake-fields inside the valves if their inner surfaces are not smooth. The lifetime was becoming increasingly better after repeating single-bunch operation. This suggests that strong wake-fields forced an outgassing of the heavy element components, and cleaned the beam ducts.

H. Kobayakawa

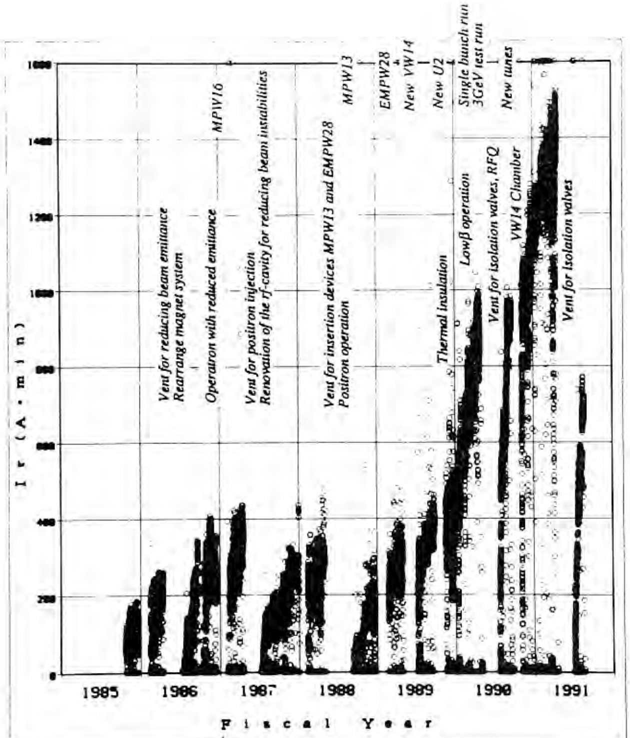

Fig. 3 Plot of Iτ (beam current times lifetime).

B. OPERATION

1. 3-GeV OPERATION

1.1 Magnet

During FY 1990~1991, the power supplies for the quadrupole magnets were reinforced in order to realize 3GeV operation (see Section 4.1). A positron beam of 300 mA has been successfully accelerated up to 3GeV. Thus, 3GeV operation is now ready for user's experiment.

Procedures for acceleration and deceleration

Since the positron beam from the injector linac has an energy of 2.5 GeV, it is necessary to accelerate and decelerate the stored beam without any beam loss under routine operation. We determined the optimum exciting current of the magnets every 0.1GeV in the range from 2.5 to 3 GeV in order to avoid any large tune shift or large COD (Closed-Orbit-Distortion). As a result, acceleration/deceleration has been carried out within about 10 minutes without any beam loss.

Before 3GeV operation, we initialize all of magnets by sweeping the exciting current corresponding to the beam energy from 2.5 to 3GeV in order to avoid any magnetic hysteresis effect. This procedure allows us to repeat acceleration/ deceleration of the beam in the above mentioned energy range by keeping the tune shift and COD fixed.

Beta function at 3 GeV

The beta functions at 3 GeV are shown in Fig. 4. The vertical beta functions at each straight section for undulator #2 and MPW #16 were 1.8 time as large as that at 2.5 GeV; in other sections they were almost the same.

Correction of the tune shift caused by the wigglers

The tune shift due to the strong focusing forces of the wigglers (VW#14,MPW#13,#16,and #28) are compensated for by changing the exciting current in a few quadrupole magnets nearby each wiggler.[1] Since the focusing force of the wigglers decreases in proportion to $1/\gamma^2$, where γ is a Lorentz energy factor, the correction, Δk (the kick), by the quadrupole magnets must also decrease in proportion to $1/\gamma^2$. Δk is represented by

$$\Delta k = \frac{\Delta B' l}{B\rho},$$

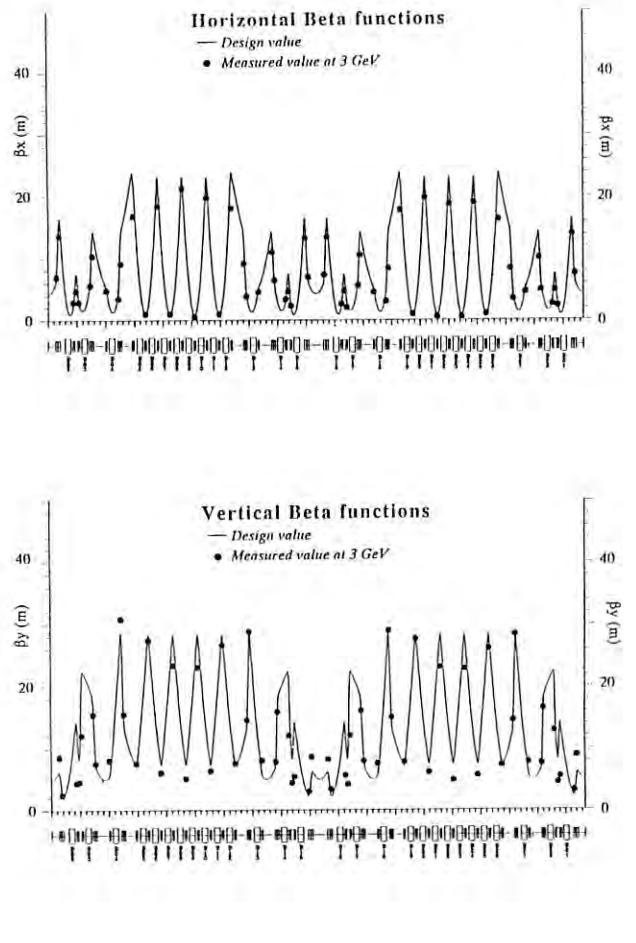

Fig. 4 Beta functions at 3.0 GeV. The open circles represent the measured value and the solid line the calculated values.

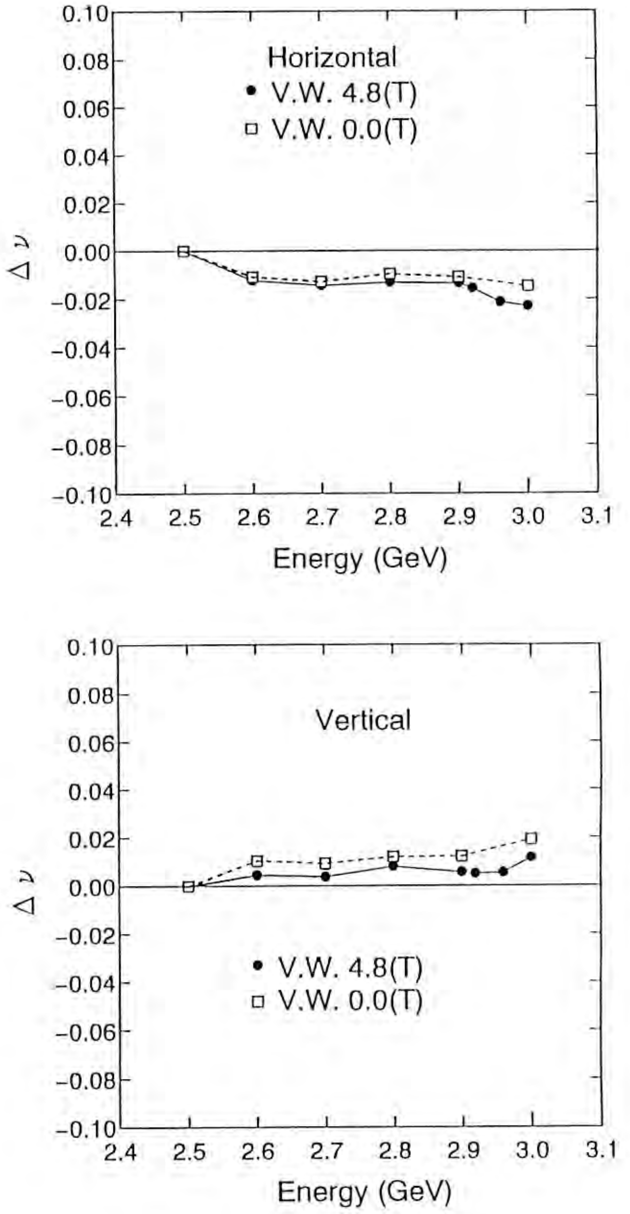

Fig. 5 Tune shifts during acceleration. The closed and open circles represent the tune shift without and with exciting VW#14 at 4.8 T.

where $B\rho$ is the magnetic rigidity, $\Delta B'$ the correction field gradient and l the length of the quadrupole magnet. Since $B\rho$ is proportional to γ, $\Delta B'$ must be proportional to $1/\gamma$. Thus, if the saturation of the magnetic field is negligibly small, the correction currents to be supplied to the quadrupole magnets should be proportional to $1/\gamma$. Figure 5 shows an example of the tune shift correction. The tune is sufficiently corrected, as expected.

Correction of the vertical COD

After acceleration, it was observed that the COD gradually rose in the vertical plane for several hours. The cause of such vertical COD has not yet been explained. However, this vertical COD can be suppressed using the digital feedback system (DFB),[2] as shown in Fig. 6.

Y. Kobayashi

References

1) PF Activity Report, #4,p.83,1986.
2) PF Activity Report, #6,pp.R-11-12,1988.

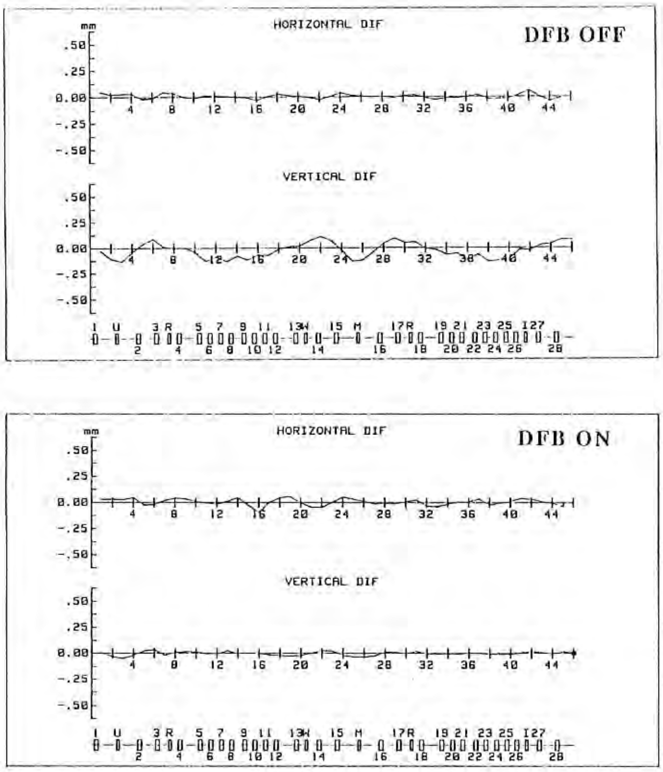

Fig. 6 Difference of the beam orbits: (upper) without DFB, and (lower) with DFB.

1.2 RF

The dominant radiation sources in the PF ring are the bending magnets, superconducting wiggler VW#14 (5 Tesla, 3 poles) and multipole wiggler MPW#16 (1.5 Tesla). A cavity gap voltage of 2.02 MV is required for 3 GeV operation with these sources in order to obtain a quantum lifetime of 48 h. The gap voltage is obtained by driving four single-cell cavities with a dissipation power of 32 kW/cavity. This value is sufficiently below the maximum dissipation power of 110 kW/cavity.

The total particle energy loss due to synchrotron radiation is 910 keV/turn at 3 GeV. Taking into account the reflection power from the cavities, the total generator power is calculated as a function of the stored current, as shown in Fig. 7.[1]. From the point of rf power capacity of the existing PF accelerating system, a current of 360 mA can be stored at 3 GeV with all insertion devices in operation.

M.Isawa

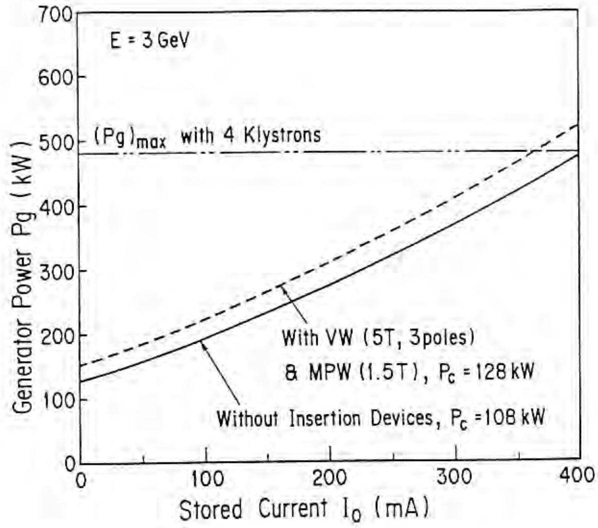

Fig. 7 Calculated total generator power as a function of the stored current under 3GeV operation.

Reference

1) S.Sakanaka, M.Izawa, H.Kobayakawa, S.Tokumoto and T.Kiuchi, KEK Report 91-7.

1.3 Vacuum

One of the important mechanisms of outgassing by SR irradiation is desorption by secondary photoelectrons. The outgassing rate by photoelectrons is proportional to the yield of photoelectrons. The yield depends upon the irradiation angle and beam energy (E_b). It is proportional to $E_b^{1.76}$ at the bending-magnet section in the PF ring.

On the other hand, thermal outgassing due to heating of the duct components is another important mechanism. Since the SR power increases in proportion to E_b^4, the outgassing increases abruptly with E_b in this case.

The beam-energy dependence of the average pressure at all bending magnet sections was measured in the beam energy range of 2.5 to 3 GeV (Fig. 8). The pressure normalized to the beam current increased rapidly with E_b, and at 3 GeV it was 2.5 times as high as that at 2.5 GeV. The energy dependence is much larger than $E_b^{1.76}$. Therefore, the dominant mechanism of outgassing is considered to be thermal desorption. There seems to be a hysteresis curve in the Fig. 8 caused by a time delay in the temperature rise (fall) of ducts during acceleration (deceleration).

The beam lifetime was also measured at a beam current of 200 mA, as shown in Fig. 9. The calculated cross section of scattering with residual gas was reduced to 95% of that at 2.5 GeV. Considering the pressure rise at 3 GeV, the lifetime is expected to be ~40% (=95/2.5) of that at 2.5 GeV. However, the observed lifetime was ~80% of that at 2.5 GeV. The reason has not yet been explained clearly.

Y.Hori

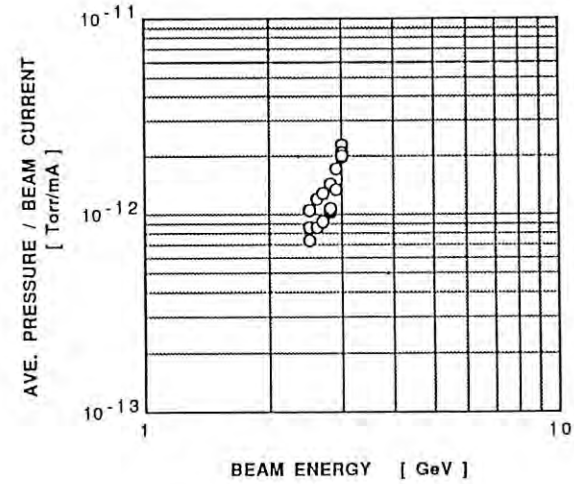

Fig. 8 Change of the ring pressure as a function of the beam energy. The stored current is 200 mA. The ring pressure is normalized to the stored current (Pav/I).

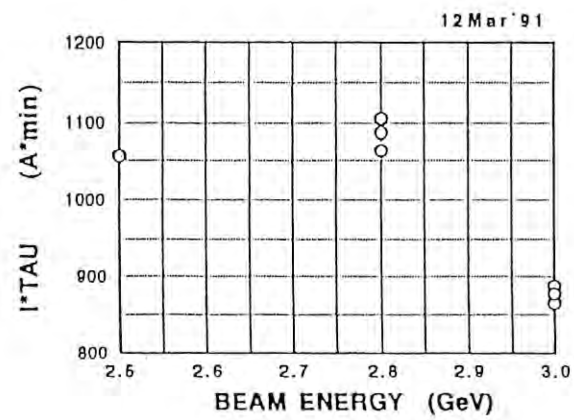

Fig. 9 Beam lifetime(Iτ) as a function of the beam energy.

1.4 Spectra of Synchrotron Radiation

The spectra of the synchrotron radiations from the various sources in the ring will be changed by an increase in the beam energy from 2.5 to 3.0 GeV. Since the critical photon energy depends on the beam energy as E^3 for the bend sources or E^2 for wigglers, the available photon energy range will be extended to the higher-energy side by a factor of 1.73 (bend) or 1.44 (wigglers). In case of the undulators, however, the photon energy of each harmonic is shifted to the higher-energy side by a factor of 1.44, so that the photon energy region which is available at 2.5 GeV cannot be covered at 3.0 GeV. Figure 10 shows the spectral brilliance obtained from the typical sources (B05, MPW#16 and VW#14, U#02) for beam energies of 2.5 GeV (solid curves) and 3.0 GeV (dashed curves). As described above, the spectra of the sources, except for the undulator (U#02), is found to be extended to the higher-energy side by an increase of the beam energy. On the other hand, the lower limit

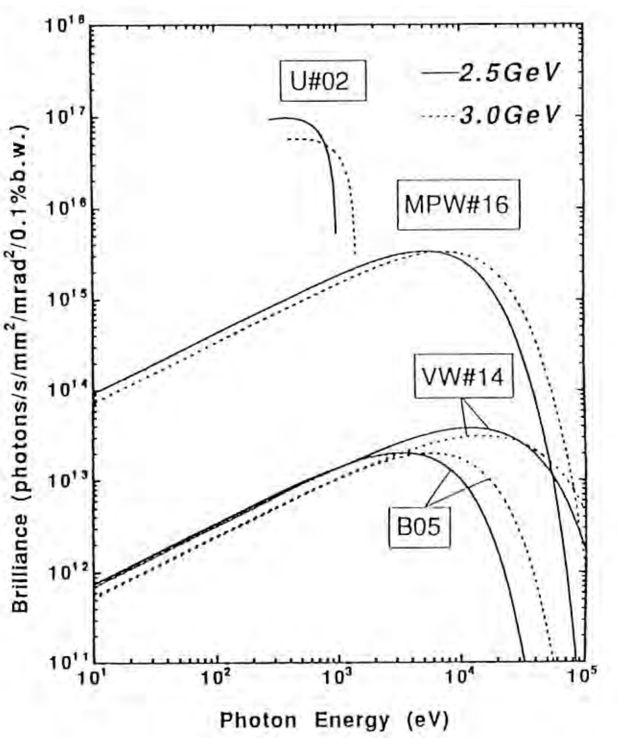

Fig. 10 Spectral brilliance obtained from typical sources (B05, MPW#16 and VW#14, U#02) for beam energies of 2.5 GeV (solid curves) and 3.0 GeV (dashed curves). Each curve for U#02 is a locus of the peak brilliance of the first harmonic when the K value is changed up to the maximum value of 2.25.

of the available photon energy range of U#02 is increased from 280 eV to 400 eV, although the upper limit is extended from 900 eV to 1300 eV. It should be noted that the brilliance of U#02 is decreased by a factor of about 2, since the beam emittance is increased from 125 nm·rad to 180 nm·rad.

Roughly speaking, the angular power density of the synchrotron radiation depends on the beam energy as E^5 for bend sources, and E^4 for insertion devices. Figure 11 shows the vertical angular distribution of the power density of the bend source (B05) and MPW#16 for a beam energy of 2.5 GeV (solid curves) or 3.0 GeV (dashed curves). The maximum power density is found to increase by a factor of 2.5 (B05) or 2.1 (MPW#16).

H.Kitamura

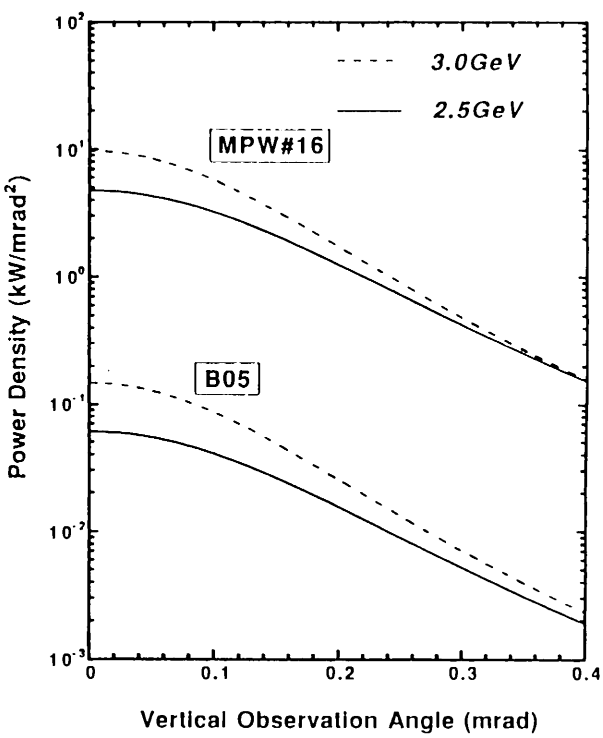

Fig. 11 Vertical angular distribution of the power density of B05 and MPW#16 for a beam energy of 2.5 GeV (solid curves) or 3.0 GeV (dashed curves).

2. SINGLE-BUNCH OPERATION

2.1 Lifetime and Current Limit

Lifetime

The major processes of beam loss in the PF ring are the Touschek effect and scattering with residual gases. Considering the above two processes, the beam lifetime (τ) is represented by

$$1/\tau = 1/\tau_t + 1/\tau_s \tag{1}$$

where $1/\tau_t = I_b\sigma_t/n_b$ and $1/\tau_s = P_{av}\sigma$; P_{av} is the average pressure of the ring, n_b the bunch number, I_b the average beam current, and σ_τ and σ_v are factors which determine the beam loss cross sections caused by the Touschek effect and scattering, respectively.

The Touschek lifetime (τ_t) depends on the acceptance imposed by the rf bucket height or by the transverse aperture. The rf acceptance is dominant in the PF ring. The Touschek lifetime (τ_t) can be calculated as a function of the cavity gap voltage (Fig. 12). As shown in the figure, $I_b\tau_t$ is 14 Amin at the normal cavity gap voltage of 1.7 MV. Therefore, σ_t is 0.071 $A^{-1}min^{-1}$.

The σ_v depends upon the composition of residual gas and machine parameters. Assuming that the component of the residual gas is only CO, σ_v is calculated to be 6×10^5 $Torr^{-1}min^{-1}$. Using B-A gauges, the normalized pressure (P_{av}/I_b) under single-bunch operation was measured, and was found to be 1.2×10^{-8} Torr/A. However, this measured value should be multiplied by 3 to obtain the actual value at the beam orbit, i.e., $P_{av}/I_b = 3.6\times10^{-8}$ Torr/A.

Substituting the above values into Eq. (1), we obtain $I_b\tau$ =11 Amin. This value agrees well with the observed values (11~12 Amin) reported in a previous activity report.

Although the lifetime can be improved by increasing the cavity gap voltage, it is not a realistic solution. However, it is possible to reduce the Touschek effect by, for example, increasing the bunch volume, as shown in Fig. 13. An increase in the bunch volume was made by exciting a skew quadrupole magnet. The figure shows that the lifetime can be improved by up to 5 times as long as the bunch volume is not increased. The larger the bunch volume, the less is the brilliance of the light. We therefore determined the operating point for user runs as shown in the figure. At that operating point the lifetime is improved by about a factor of three.

Current limit

The maximum beam current in user runs was limited to 35 mA, since the lifetime was considerably shortened beyond this current limit due to a pressure rise, as shown in Fig. 14. The pressure rise was caused by heating of duct components, especially at the gate valves in the ring, due to a wakefield induced by the single-bunch beam.

During the summer shutdown, some of the gate valves were replaced with ones with rf shields. Then, a maximum beam current of 104 mA was achieved.

Y. Hori

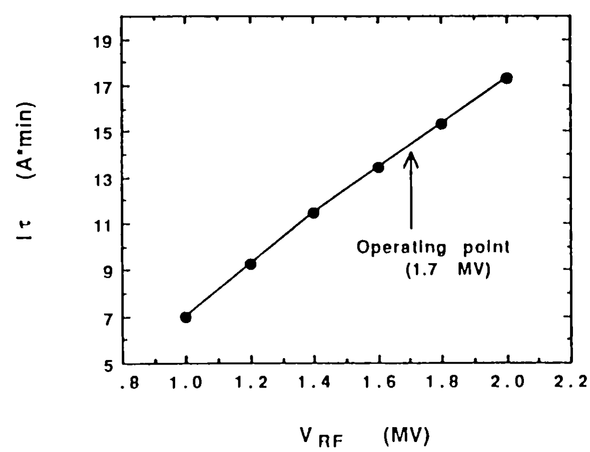

Fig. 12 Touschek lifetime of single-bunch operation in the Photon Factory as a function of the cavity voltage. The lifetime is represented by the product of the beam current and the lifetime.

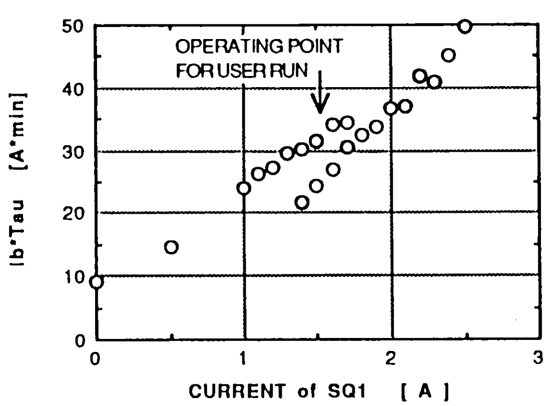

Fig. 13 Beam lifetime as a function of the exciting current of a skew quadrupole magnet (SQ1).

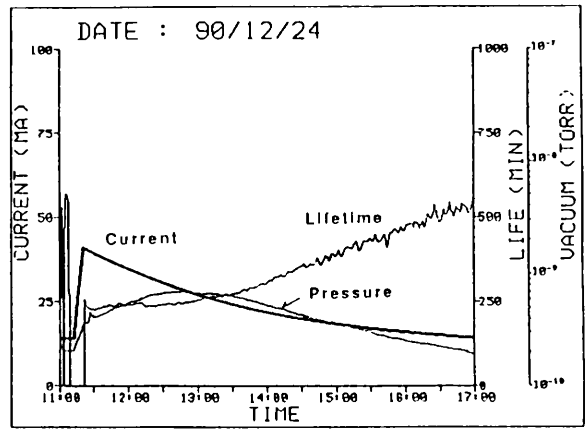

Fig. 14 Change of the beam current, the averaged ring pressure and the beam lifetime in a single-bunch user run.

2.2 Bunch-Length and Tune-Shift Measurements

The bunch length under single-bunch operation was measured with a streak camera[1)] for three different cases of the beam energy (E) and RF voltage (V_{RF}): (1) E=2.5 GeV and V_{RF}=1.7 MV, (2) E=2.5 GeV and V_{RF}=1.1 MV, (3) E=1.8 GeV and V_{RF}=1.1 MV. The results are shown in Fig. 15. At very low currents, the bunch length (σ_l) was nearly equal to the natural bunch length. As the bunch current (I_b) increased, the bunch length significantly increased. The bunch-length data at low currents is well fitted with a potential-well distortion model. The fitted curve is indicated by the solid line in Fig. 15. In the higher current region, however, the bunch length began to deviate from the fitted curve. In addition, the bunch length could be expressed as a function of only one parameter (ξ) defined by $\alpha I_b/E\nu_{s0}^2$ (α:momentum compaction factor, ν_{s0}: synchrotron tune at zero current). This suggests that the microwave instability occurred. As shown in Fig. 16, all bunch-length data above the microwave instability threshold were well fitted to a power-law curve,

$$\sigma_l(\text{cm}) = 0.337\xi^{0.336}(\text{mA/GeV})\,. \qquad (1)$$

From the potential-well distortion model and the Boussard criterion, the longitudinal effective impedance was estimated to be about 2 Ω. This value

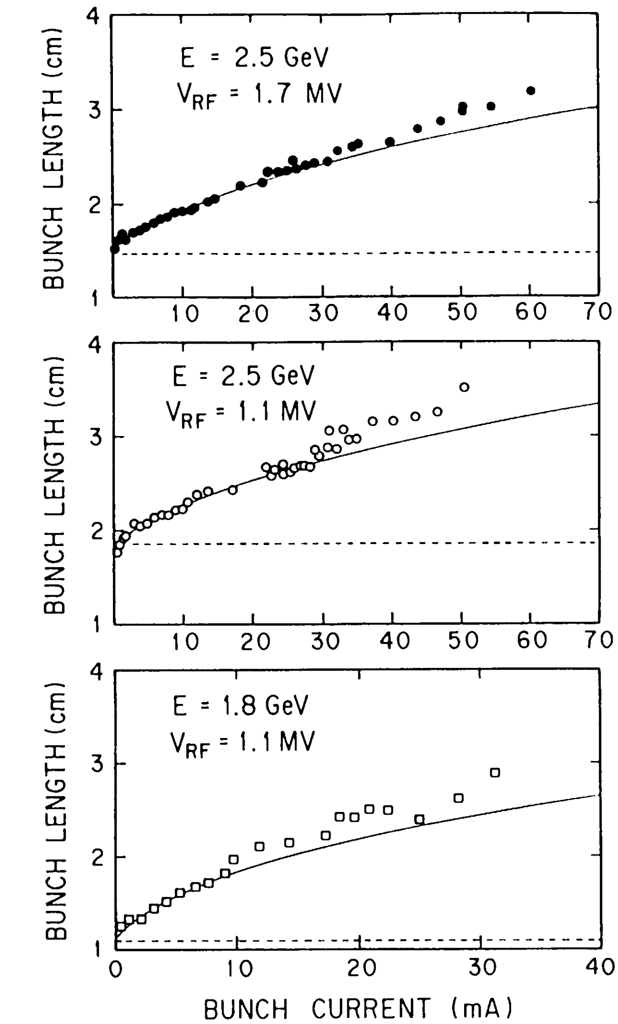

Fig. 15 Current dependence of the bunch length for three different cases. For each case, the natural bunch length is indicated by a broken line. The solid line shows the best-fit curve of the potential well distortion model for the low-current data.

comparatively agrees with the result of an impedance measurement and a calculation (see section 3.1).

Horizontal and vertical betatron tune shifts were also measured for E=2.5 GeV and V_{RF}=1.7 MV. The tune-shift data were fitted to the values corresponding to the lowest head-tail mode, which has the following fom:

$$\Delta\nu_{x,y} = -\frac{e\beta_{x,y}}{E}\frac{R}{4\sqrt{\pi}\sigma_l}Z_{x,y}I_b \, . \qquad (2)$$

Here, $Z_{x,y}$ are the horizontal and vertical effective impedances, $\beta_{x,y}$ the average horizontal and vertical

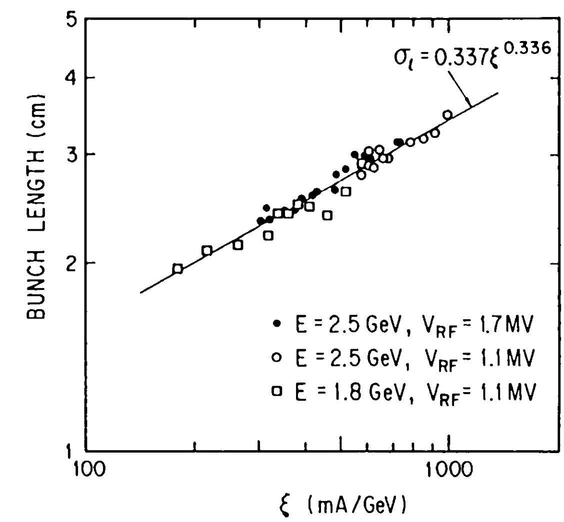

Fig. 16 Bunch-length data above the threshold as a function of the scaling parameter, $\xi=\alpha I_b/E\nu_{s0}^2$. The solid line represents the best-fit power-law curve.

betatron functions, and R the ring average radius. The potential-well distortion model and Eq. (1) was used for calculating the bunch length. The fitting results are shown in Fig. 17. The fitted values of the horizontal and vertical impedances were 34 and 178 kΩ/m. The vertical impedance are five times as large as the horizontal impedance. This can be qualitatively understood by the fact that the aperture of the vacuum chamber is narrower in the vertical direction than that in the horizontal direction.

N. Nakamura

Reference

1) N. Nakamura, S. Sakanaka, K. Haga, M. Izawa and T. Katsura, *Proceedings of the 1991 IEEE Particle Accelerator Conference*, San Francisco, 1991.; KEK Preprint 91-41.

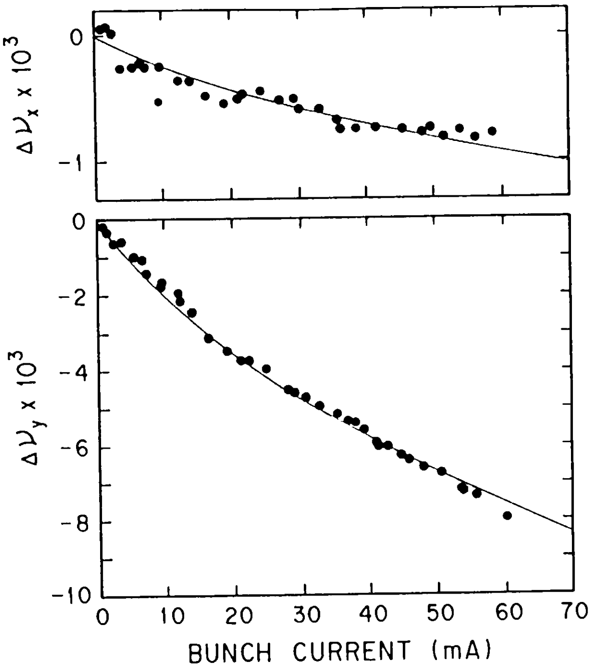

Fig. 17 Current dependence of the horizontal and vertical betatron tune shifts. The best-fit curves of Eq. (2) are shown by solid lines.

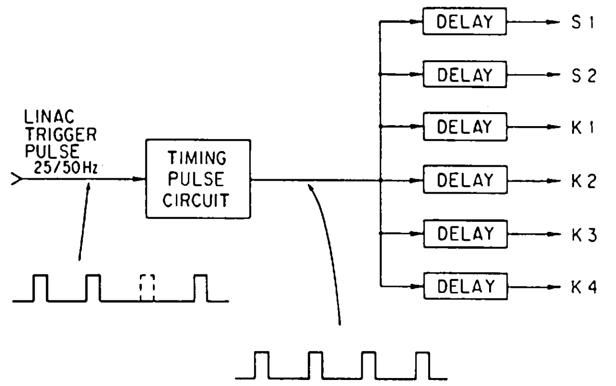

Fig. 18 Trigger pulse circuit for injection magnets

C. IMPROVEMENTS AND DEVELOPMENTS

1. INJECTION

1.1 Improvement of the Trigger System for Pulse Magnets

A trigger pulse train from the Linac has a quasi repetition rate of 25 or 50 Hz, and is used for synchronizing the timing of an injection beam pulse with that of the bucket in the ring. This pulse train is not completely periodic, since one of these pulses may be lost due to the modulus relationship between Linac and Ring rf signals (2856 and 500 MHz).

A trigger-pulse circuit was added to the existing trigger system (Fig.18) in order to provide a completely periodic pulse train, by making supplemental pulses for the power supplies of two septums and four kickers. As a result, these power supplies can periodically recharge their high voltage to improve the injection efficiency during single-bunch operation.

A.Ueda

2. RF

2.1 Effects of the RF Quadrupole Magnet on Beam Instabilities

An RF Quadrupole Magnet (RFQM) was installed in the ring in order to produce a bunch-to-bunch tune spread which decouples the transverse coupled-bunch oscillations.

The effect of the RFQM was first studied on a horizontal coupled-bunch instability caused by the TM111-mode of accelerating cavities.[1] The horizontal instability was induced by adjusting the tuning-plunger position of a cavity which was not powered. Then, the threshold currents of the horizontal instability were measured with and without exciting the RFQM, as shown in Fig. 19. Without exciting the RFQM, the behavior of the threshold current suggested a resonance having a resonance frequency of $(669-\delta v_x)f_r$ at which the threshold had its minimum value of 9.0 mA, where δv_x is a fractional betatron tune and f_r is the revolution frequency. At the resonance frequency, the threshold current was increased by a factor of 2.7 by introducing a tune spread of 2.5×10^{-4} (peak value). This result shows that the RFQM is effective to increase the threshold current of the transverse coupled-bunch instability. Note that the increase in the threshold became small as the resonance frequency was slightly shifted from a frequency of $(669-\delta v_x)f_r$. This behavior seems to be qualitatively in agreement with the theoretical prediction.[2]

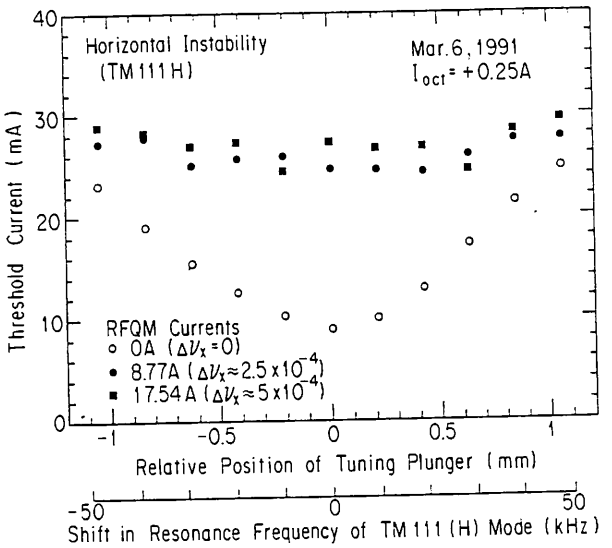

Fig. 19 Measured threshold currents of the TM111(H) instability for three exciting currents of the RFQM. The data are shown as a function of the shift in the resonance frequency of TM111(H) mode. The center of the horizontal abscissa corresponds to 1071.62 MHz (~(669-$\delta\nu_x$)f_r). The ring was uniformly filled.

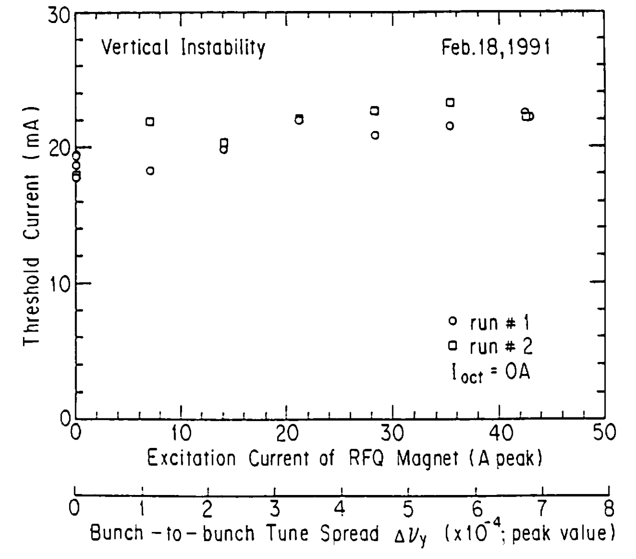

Fig. 20 Measured threshold currents of the vertical instability as a function of the exciting current of the RFQM. The ring was uniformly filled.

The effect of exciting the RFQM on a vertical instability[3] was also studied. This instability appears above a threshold current of ~18 mA (with octupoles off), leading to an increase of the beam size at high currents. The threshold current of the vertical instability was measured as a function of the exciting current of the RFQM (Fig. 20). It was found that the threshold current also increased by a factor of only 1.2 with the maximum exciting current.

S. Sakanaka

References

1) S. Sakanaka and T. Mitsuhashi, to be published in the Proc. of the 1991 IEEE Particle Accelerator Conference, and also KEK Preprint 91-40.
2) Y.H. Chin and K. Yokoya, DESY 86-097 (1986).
3) PHOTON FACTORY ACTIVITY REPORT #8 (1990) p. R-5.

3. VACUUM

3.1 Measurements of the Loss Parameters of the Duct Components

The loss parameters of the duct components were measured[1] using the wire method. A block diagram of the measurement set-up is shown in Fig. 21. The equipment comprised two taper sections, two straight sections, a reference duct or measurement object, an inner wire (3 mm in diameter) and two inner-wire supporters. A pulse simulating a single bunch was obtained by using the synthetic pulse function of the network analyzer (HP8510B) . Using this function, the frequency responses of the object and reference ducts were converted to synthetic pulses using inverse FFT. The synthetic pulses obtained were close to a Gaussian shape with a standard deviation (σ) ranging from 26.7 to 78.3 ps.

As for the duct components having an axial symmetric or approximately symmetric, the code TBCI[2] was used to calculate their loss parameters. The results are shown in Table 2. The dominant contribution to the total loss parameter comes from the bellows in the quadrupole magnet ducts (Q-bellows) and the gate valve sections. The ring impedance was estimated to be $|Z/n|$=3.2 Ω by using the broadband impedance model.

During the 1991 summer shutdown most of these gate valves were replaced by ones with an rf shield and the large gaps of flanges were filled so that each gap width became within 0.5 mm.

Y.Hori

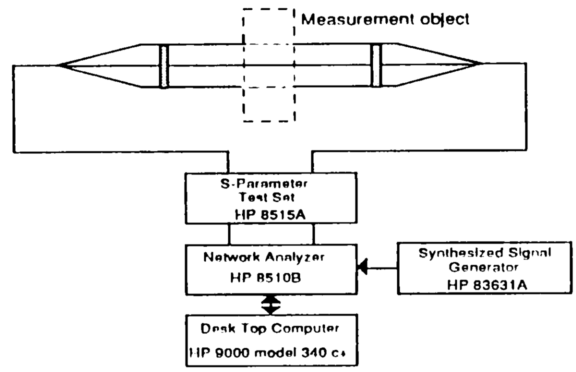

Fig. 21 Block diagram of the measurement setup

References

1) M. Izawa, T. Kikuchi, S. Tokumoto, Y. Hori, S. Sakanaka, M. Kobayashi, and H. Kobayakawa, Proceedings of the 4-th international conference on Synchrotron Radiation Instrumentation, Chester, 1991.
2) T. Weiland, NIM **212**(1983)13

Table 2 Loss parameters of the PF ring duct components

Bunch length (ps)		**26.7**	**31.7**	**45.2**	**53.0**	**63.6**	**78.3**
Component	Quantity						
RF Cavity *	4	1.74	1.54	1.11	0.94	0.78	0.61
Flange Gap							
Q-Q	59	2.96	2.79	1.92	1.61	1.30	1.00
R-R	8	1.24	1.13	0.82	0.66	0.47	0.29
subtotal		4.20	3.92	2.74	2.27	1.77	1.29
Bellows							
R-Bellows	11	1.84	1.42	0.61	0.36	0.17	0.06
Q-Bellows	98	23.70	19.55	5.88	3.12	2.07	1.15
subtotal		25.54	20.97	6.49	3.48	2.24	1.21
SR Absorber							
Q-Abs	46	0.80	0.73	0.42	0.46	0.26	0.15
R-Abs	6	0.27	0.25	0.17	0.14	0.11	0.08
subtotal		1.07	0.98	0.59	0.60	0.37	0.23
Gate Valve	15	5.44	4.56	3.17	2.63	2.09	1.54
Taper Transition	12	0.89	1.50	1.13	0.82	0.50	0.27
Position Monitor	45	2.35	1.50	1.13	0.82	0.50	0.27
Total (V/pC)		**40.00**	**34.20**	**15.70**	**11.10**	**8.00**	**5.32**

*Not included K_0=0.18. 'R-' indicates 'Round duct' and 'Q-' 'duct for Quadrupole magnet'

4. MAGNET

4.1 Reinforcement of the Quadrupole Magnet Power Supply

A reinforcement of three power supplies for the QMs was carried out during fiscal years 1990-1991 in order to realize 3-GeV operation. The power supply was designed to use thyristors and filters (passive and active filter -61dB at 600 Hz). The specifications of the power supplies are listed in Table 3. After reinforcement, the beam has been successfully accelerated to 3.0 GeV.

Table 3 Specification of new power supplies for the quadrupole magnets

Name	PAS	PBS	PCS
Max current (A)	620	470	760
Max voltage (V)	180	100	180
Power (kW)	116.6	47.0	136.8
Current stability		$< 2\times10^{-4}$	
Linearity		$< 2\times10^{-4}$	
Ripple and Noise		$< 1\times10^{4}$	
Setting resolution		2×10^{-4}	

4.2 New Method for a Sextupole Correction

It is known that the sextupole magnets (SX) may sometimes cause non-linear phenomena (narrow dynamic aperture, tune shift etc), especially in the low-emittance ring.

Since low-emittance operation started, we have intensely studied the chromaticity correction using 22 SXs, which are installed in the dispersion sections of normal cells.

A new method of chromaticity correction[1] was investigated for the following three cases:

(1) Chromaticity correction using two families of SXs (two group of SXs and each group has the same exciting current) (normal correction).

(2) Chromaticity correction without an amplitude-dependent tune shift.

(3) Chromaticity correction with a vertical amplitude-dependent tune shift.

Case (2) and (3) were carried out using eleven families of SXs. For cases (2) and (3), the strength of the SXs were optimized by an improved EKHARM program.[2]

The dynamic aperture and the amplitude-dependent tune shift for three cases were simulated using a modified version of PATRICIA[3] (a particle tracking code). The results are shown in Figs. 22 and 23.

Figure 23 shows that the horizontal amplitude-dependent tune shift is also different for cases (1) and (3). As can be seen in Fig. 23 the tune shift in case (1) is larger than that in case (3). Therefore, the horizontal damping rate in case (1) is larger than that in case (3). The difference of the tune shift between the two cases can thus be observed by measuring the threshold current of the horizontal instability. The thresholds of the horizontal instability due to TM111 were measured and the values were 5 mA in case (3) and 15 mA in case (1), as expected from Fig. 23. The power supplies for SXs are now being reinforced. A further investigation is in progress.

Y. Kobayashi

References

1) Y. Kamiya, M. Katoh and I. Honjo, Proc. of IEEE Part. Accl. Conf., p.1310 1987; Y. Kobayashi and Y. Kamiya, Proc. of the 4th SRI Conf., England, 1991(to be published)

2) M. Donald, PEP note-331, 1973; also see the program EKHARM.

3) H. Wiedemann, PEP Note-220, 1976; also see the program PATRICIA.

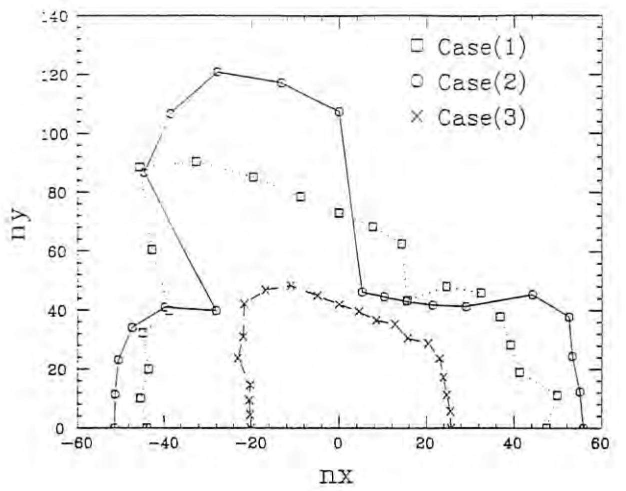

Fig. 22 Dynamic aperture calculated by a computer simulation (particle tracking).

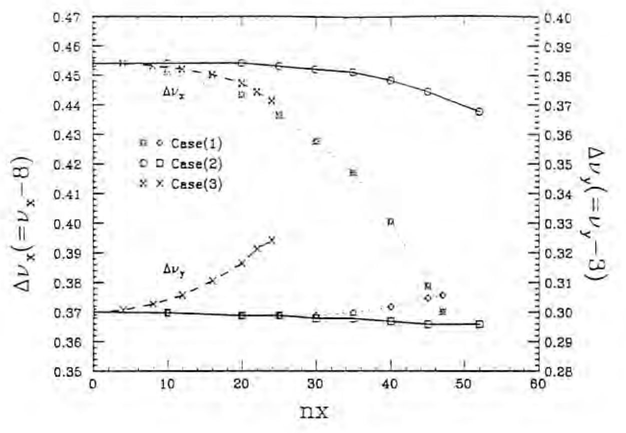

Fig. 23 The amplitude-dependent tune shifts

5. INSERTION DEVICES

5.1 Independent Tuning During Insertion Device Operation

The photon energy of the undulator radiation can be chosen by changing the magnetic gap of the insertion device. However, the closed orbit in the storage ring is sometimes affected by a change of the gap, unless an adjustment of the device is made over the entire operating range of the gap, which causes a fluctuation of the photon beam axis during the SR experiments at all of the beam lines equipped with the ring. If this fluctuation, especially in the vertical direction, is so large that the SR experiments cannot be performed, a change of the gap is allowed only just after the injection of an electron/positron beam into the ring, which may spoil the capability of the insertion devices; it is very important to freely vary the photon energy of undulator radiation during SR experiments in order to operate the scanning monochromator together with the undulator.

In the PF ring, adjustments of the insertion devices for independent tuning have been carried out using the correction magnet systems located in both ends of each insertion device. The optimum exciting currents in those magnet systems can be obtained over the entire operating range of the gap, so as to fit the closed orbit to the standard one authorized for synchrotron radiation use by using the beam-position monitor for the horizontal correction and the synchrotron radiation monitor for the vertical. In the case of PF, the maximum permissible deviations of the gradients of the photon beam axis are 10 μrad for the horizontal direction and 2 μrad for the vertical.

Figure 24 shows a typical design for the correction magnet which can generate an integrated magnetic field up to 2000 Gauss·cm either in the vertical or horizontal direction. In order to obtain good reproducibility, the remnant field of the correction magnets should be made as low as possible. A magnetic alloy (permalloy) with high permeability of 10^5 and low coercive force of 0.01 Örsted has been adopted for core material.

Figure 25 shows the optimum currents in the correction magnets as a function of the gap of EMPW#28 (Helical undulator mode). A personal computer system is used for controlling the gap and correction magnets simultaneously. As shown in Fig. 26, the resulting vertical deviations of the gradients of the photon beam axes observed at beamlines BL04 and BL06 are found to be within the maximum permissible value (2 μrad). The maximum horizontal deviation is estimated to be as small as 5 μrad from beam-position measurements.

In the PF ring, the four insertion devices (U#02 and Revolver#19, MPW#16 and EMPW#28) have been adjusted for independent tuning. The adjustment of the other insertion device (MPW#13) will be completed by the end of FY1992.

H.Kitamura

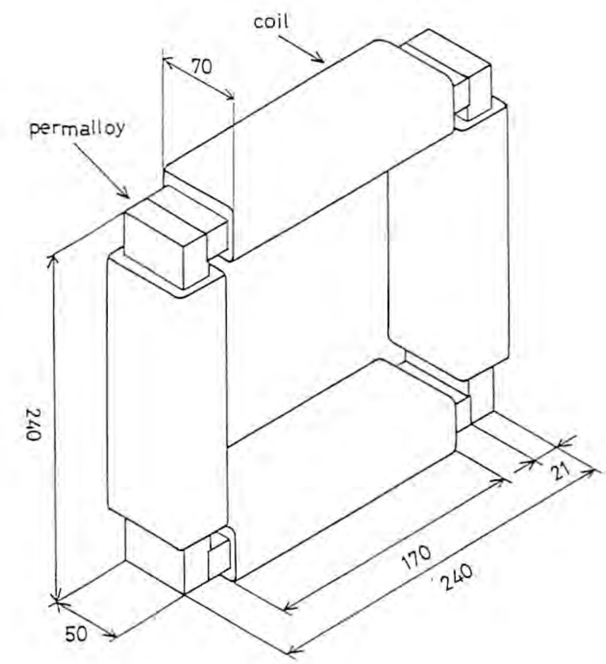

Fig. 24 Typical design for the correction magnet.

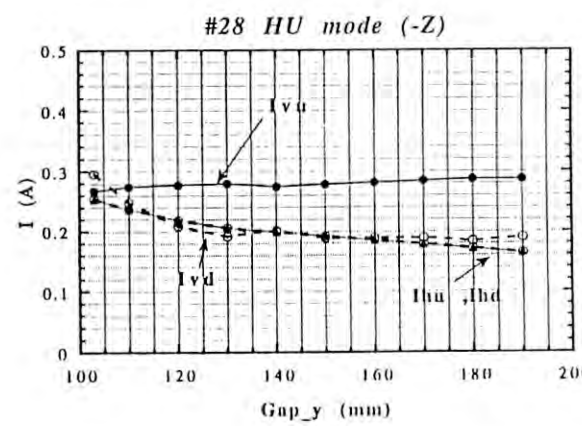

Fig. 25 Gap dependences of the current in the correction magnet system. I_{hu}/I_{vu} or I_{hd}/I_{vd} denotes the current in the horizontal/vertical-correction magnet located in the up- or downstream side of EMPW#28, respectively.

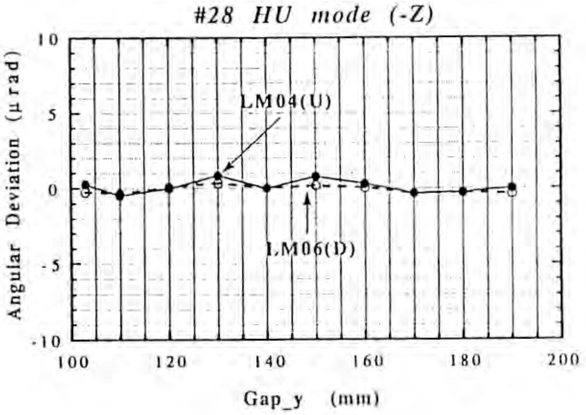

Fig. 26 Vertical deviations of the gradients of the photon beam axes observed at the beamlines, BL04 and BL06,

5.2 Status of the Superconducting Wiggler

The wiggler has five superconducting magnets. At present, three of them are in operation. The field strength of the wiggler was limited to 4 T because the x-rays generated from the wiggler pass through the aluminum duct of the wiggler, and then reach the inner helium vessel, thus warming up the cryostat of the wiggler. The wiggler duct was shielded by a tungsten membrane with a thickness of 1mm using a plasma-deposit method. As a result, the consumption rate of liquid helium became 0.12±0.02 L/h in the permanent-current mode. The wiggler can be successfully operated at a field strength of 4.8 T.

Under permanent-current operation, the magnetic field of three coils gradually decrease, since the currents in the coils decrease due to the resistance of junctions between the coils and the permanent current switches. The damping rates of three coils were $0.918\times10^{-5}\,h^{-1}$, $1.318\times10^{-5}\,h^{-1}$ and $1.014\times10^{-5}\cdot h^{-1}$, respectively. The difference of these values produces a momentum kick which causes an orbit distortion.

The change rate of the field integral in the wiggler is given as

$$\Delta\int_{wig} Bdl/\Delta t = 2.04\times10^{-6}\cdot Tm/h.$$

Since the lineality of the damping rate is good enough to correct any obit distortion (Fig. 27), a field correction can be made with an open-loop control. Thus, by driving two steering magnets installed at both sides of the wiggler, a personal computer automatically corrects the orbit distortion every 18 minutes with a minimum field strength correction of 0.61×10^{-6} Tm .

K.Ohmi

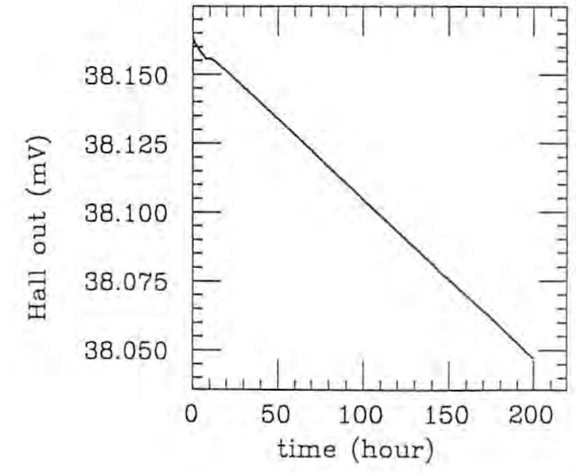

Fig. 27 Damping rate of the magnetic field of the wiggler.

6. MONITOR

6.1 Photon Beam Position Monitors for Insertion Devices

Several types of photon beam position monitors are operating in more than fourteen beamlines, as listed in Chapter D.

For insertion device beamlines, two sets of split photoemission monitors (Dual SPM), shown in Fig. 28, are used: one on the left and the other on the right edge of the beam to measure both the vertical and horizontal photon beam positions.[1,2] Each set has a pair of blades housed in an individual water-cooled field box and is made adjustable for horizontal positioning with respect to the photon beam.

The monitor was tested at beamline NE1 in the AR for different gap sizes of the 42-pole multipole wiggler. The response of the monitor is shown in Fig. 29 as a function of the K-value of the wiggler. The vertical position signal showed an unreal drift of more than 200 μm when the gap was changed from 30 mm (K=14.6) to 50 mm (K=9.51). The response of the monitor for various gap sizes was simulated based on the assumption that a photon beam with a 2-dimensional Gaussian-like power distribution falls on a set of electrode pairs which are arranged asymmetrical between left and right with respect to the monitor

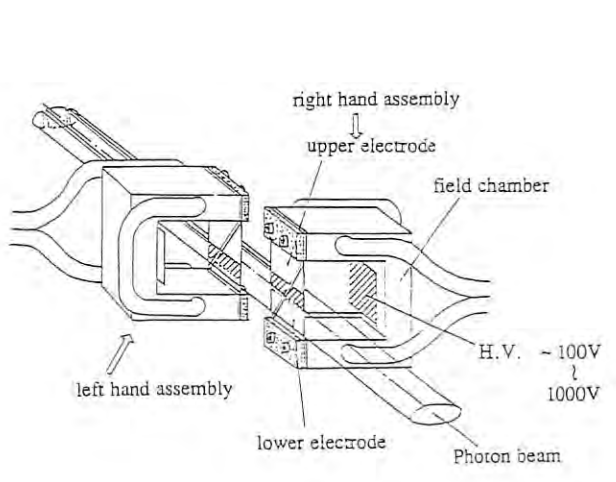

Fig. 28 Dual split photoemission monitor (DSPM) for insertion device beamlines

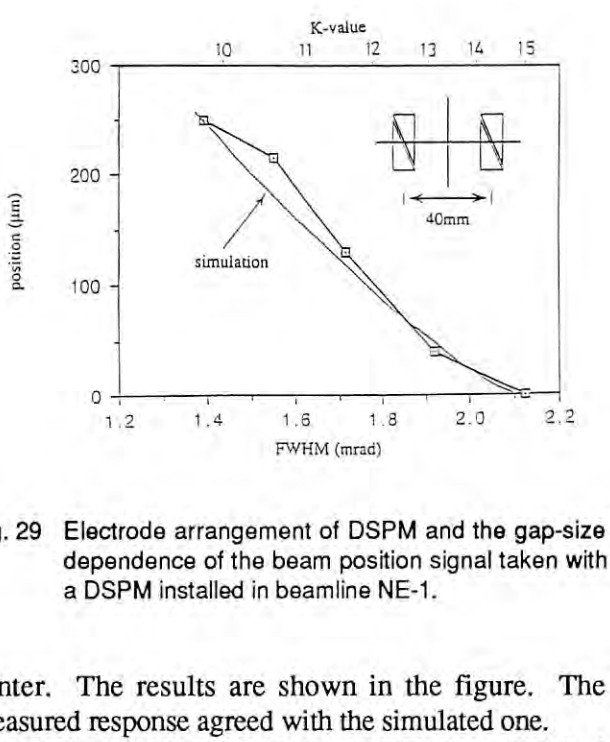

Fig. 29 Electrode arrangement of DSPM and the gap-size dependence of the beam position signal taken with a DSPM installed in beamline NE-1.

center. The results are shown in the figure. The measured response agreed with the simulated one.

To reduce this kind of unreal drift, a symmetrical arrangement of the blades was chosen (shown in the insert of Fig. 30) and tested at beamline BL-16 with the MPW#16. The results are shown in the figure for gap sizes from 19 mm (K=16.8) to 27 mm (K=12.9). The unreal drift in the vertical position was reduced to less than ± 20 μm.

T.Mitsuhashi

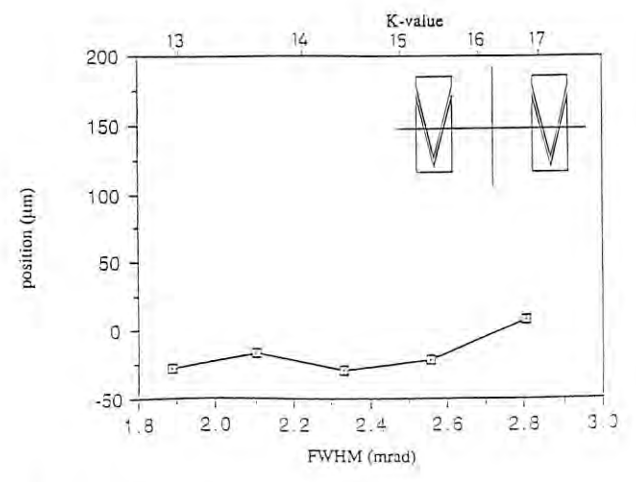

Fig. 30 Improved electrode arrangement and gap dependence measured at BL-16 with the MPW#16

6.2 Improved Split Ion Chamber for High-Brilliance Sources

For future high-brilliance sources, the deficiency of the photoemission monitor used above is that its blades, being immersed in the beam, can very rapidly melt down due to heat concentration, even with a water-cooled structure. A new type of monitor, called a split ionization monitor, has been designed to avoid having such heat problems. As shown in Fig. 31, the basic electrode arrangement of the monitor is almost the same as that of the split ion chamber; however, being filled with no gas, it collects only a minute ion current from ionized residual gas in the high vacuum. A pair of right-triangluar ion collectors (70 mm long and 100mm high) are fixed at one side of the field box, and a bias electrode is fixed at the other side. The aperture between the collector and the bias electrode is 80 mm wide. Two masks are added at the entrance and exit of the field box to eliminate both parasitic background around the photon beam and backshine from downstream. Test results were obtained in the 42-pole multipole wiggler beamline (NE1) with K=14.6 and a vacuum pressure of about 2×10^{-4} Pa. An ion current of about 30 nA was obtained with the bias voltage set at 500 V.

Because this new split ionization monitor has an advantage over the heat problem, we can observe the center of gravity of the beam power distribution, the while other type of monitors mentioned earlier can observe the beam center by sensing the beam density distribution only at the edge. A further test is awaited to improve its signal-to-background ratio.

T. Katsura

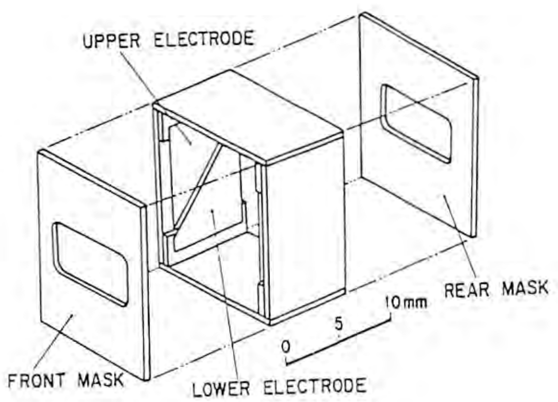

Fig. 31 Structure of the new split ionization monitor

References
1) T. Mitsuhashi, A. Ueda, and T. Katsura : Proceedings of the 4-th international conference on Synchrotron Radiation Instrumentation, Chester, 1991.
2) Photon Factory Activity Report No.8, R-15 (1990).

6.3 Streak Camera with a Cross-Sweep Option

A streak-camera system has been developed with a cross-sweep option in order to display multi-streak images on the CCD screen. A block diagram of this system is shown in Fig. 32. A synchrotron light pulse from a circulating bunch produces electrons at a photocathode in the streak tube. These electrons are vertically swept by a voltage across a pair of electrodes, converting the temporal picture into a spatial one. Then, a temporal profile of the light pulse is displayed on the CCD screen. The image of an SR pulse can be simultaneously displayed on the CCD screen at given time intervals by a horizontal deflector. The cross-sweep streak camera system can, thus, record either specified bunch every N-th revolution, or several different bunches during a revolution period (624 ns). The horizontal sweep time can be selected over a range of 130 ns to 170 ms in full scale, and a vertical sweep time from 0.54 to 1.24 ns.

A frequency of 125 MHz, required for the vertical sweep, was obtained by dividing an accelerating frequency of 500 MHz, so that the vertical sweep could be synchronized with light pulses from a bunch. In order to select a light pulse from the specified bunch, the streak tube's high voltage was gated with the logical AND signal between the horizontal sweep signal and the signal of Beam Position Monitor (BPM), which is masked by the 1/N divider and a pulse generator (DG535).

Figure 33 shows a CCD image of synchrotron light pulses from a bunch at every 45-th turn during single-bunch operation. The horizontal interval between pulses corresponds to 45 revolution periods (28 μs).

N. Nakamura

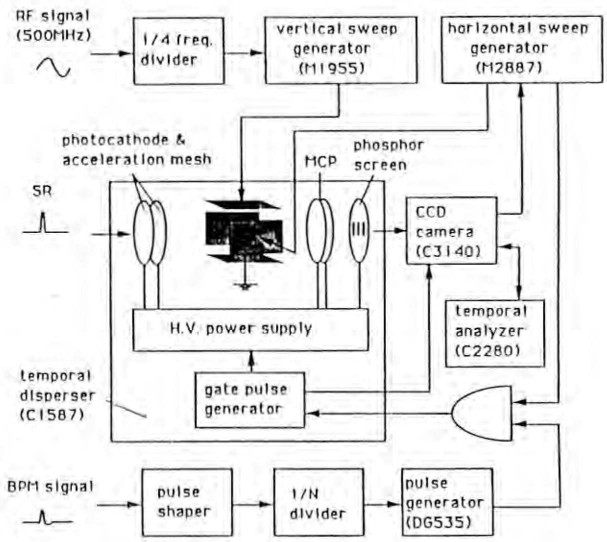

Fig. 32 Block diagram of the cross-sweep streak camera system.

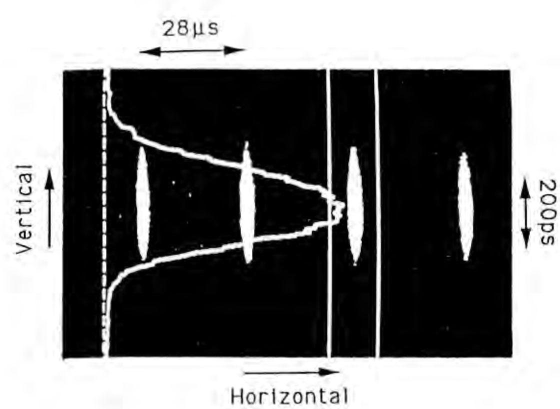

Fig. 33 Streak camera picture of a bunch at every 45-th turn.

6.4 Measurement of the Vertical Displacement Along Beamline 5

A building distortion, which is caused by its thermal stress from solar irradiation, has affected the beam position stability, since the low-emittance operation was started. In order to reduce the distortion, the PF building was insulated from solar irradiation with polyethlene-foam mats placed on the roof in January, 1990. The floor displacement near beamline 5 was measured both before and after insulation. A simulation model (finite element method) made by Shimizu Corporation[1)] showed the amount of distortion, which was compared with the amount of measured distortion.

The vertical displacement of the BL-5 floor was measured with a hydrostatic leveling system comprising three tanks connected in series with pipes. The water level was measured with laser displacement sensor mounted on the top cover of each tank. Each sensor's signal was sent to the computer system, which analyzed the data. Figure 34 shows the locations of three tanks (B05, 5A, and 5B). Figure 35 shows some typical diurnal relative displacements (5B-5A) as well as the temperatures of the ceiling surface on fine days before and after insulation. The mean peak-to-peak relative displacement on fine days before insulation was 173 μm, and that after insulation was 105 μm. Before insulation the displacement had a close correlation with the temperature. After insulation the temperature variation became about one-fifth as large as that before insulation, and the relative displacement became about half. The reason for this difference is considered to be because the heat from the building's wall, which was not insulated, somewhat affected the displacement. Figure 36 shows the measured and calculated displacements. The agreement between the measured and the calculated displacements is good.

H.Nakamura

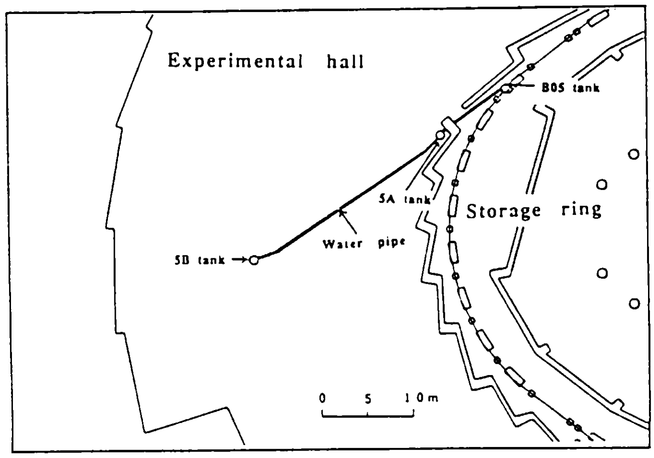

Fig. 34 Locations of the three tanks.

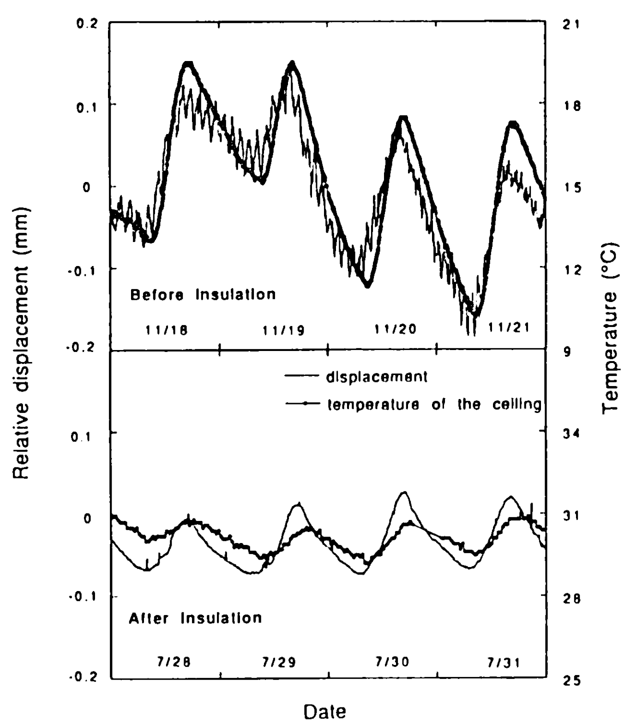

Fig. 35 Diurnal relative displacements (5B-5A) and temperatures of the ceiling surface before and after insulation.

Reference
1) PF ACTIVITY REPORT 1988 R-12

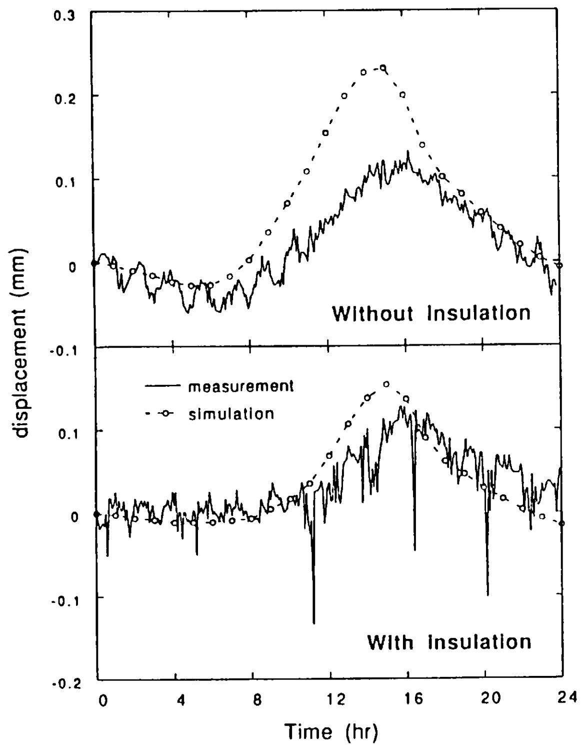

Fig. 36 Measured and calculated displacements before and after insulation.

6.5 Photon Counting System for Bunch-Length and Purity Measurements

A photon counting system was installed at beamline 21 for precise measurements of the time-structure of bunches under the single-bunch condition. The system is shown schematically in Fig. 37. Visible light is reflected by a SiC mirror and reaches a microchannel-plate photomultiplier (PMT) through an ICF-70 view port, a 22-mm thick Pb-acrylic glass, ND-filters and a precise horizontal slit. The number of photons is reduced so that one photon is detected during about a few hundred revolutions of a bunch. Pulses from the PMT are amplified by two sets of wideband amplifiers, and shaped with a constant fraction discriminator (CFD, Ortec 583). The time interval between the shaped signal and a signal synchronized to a bunch is converted to a pulse height. The distribution of the pulse height corresponding to the time-structure of bunches is analyzed by a multichannel analyzer (MCA).

The bunch lengthening was also measured with the system.[1] The measured threshold current was 28 mA,

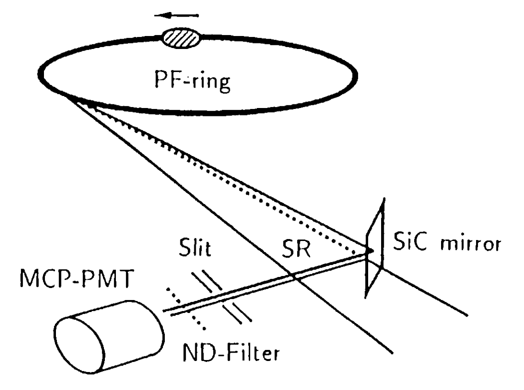

Fig. 37 Photon counting system. MCP-PMT: Hamamatsu R2809U microchannel plate photomultiplier.

agreeing well with the threshold current measured by means of the streak camera.

In addition, the single-bunch impurity, which is the ratio of positrons in unwanted bunches to those in the main one, could be successfully measured, since the system has an excellent dynamic range. Figure 38 shows an example of the time-structure of a bunch on the log scale at a beam current of 10 mA. The abscissa shows the MCA channels corresponding to the time interval. Three peaks are clearly recognizable in addition to the main bunch. The single bunch impurity was about 1% in this case.

Positrons gaining momenta greater than the bucket height by the Touschek effect may be captured by some other following buckets. This makes the single-bunch purity worse. The resolution of the impurity measurement of the system was of the order of 10^{-5}, which is sufficient for measuring the change in the impurity. The deterioration of bunch purity was clearly observed with this system. The bunch purity of the PF ring becomes worse at a rate of 10^{-4} per hour without any cure.[2]

This study was carried out in collaboration with Hiroshima University.

M. Tobiyama (Univ. of Hiroshima) and T. Katsura (PF)

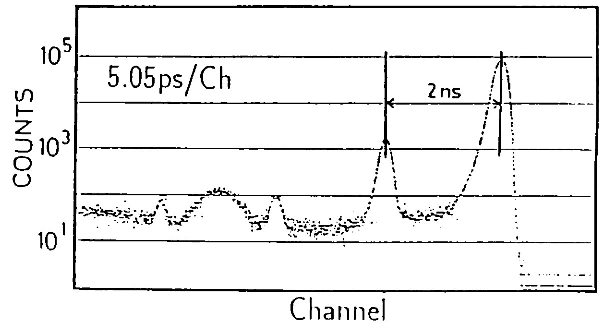

Fig. 38 Time structure of bunches on the log scale.

References

1) M. Tobiyama, T. Kasuga, T. Obita, T. Takeo and T. Katsura, "Measurement of Bunch Time-Structure in KEK PF" to be published in Proceedings of the IEEE Particle Accelerator Conference, San Francisco, 1991
2) T. Obina, T.Takeo, M. Tobiyama, T. Kasuga and T.Katsura, "Bunch Lengthening and Purity Measurements of Single-Bunch Beam by Photon Counting Method in KEK-PF" to be published in Proceedings of the 7th Symposium on Accelerator Science and Technology, RIKEN, Japan 1991

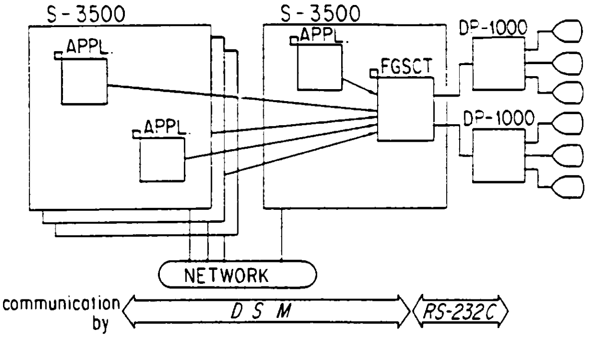

Fig. 39 Schematic diagram of the FGS.
APPL.: Application Task
FGSCT: FGS Control Task
DSM: Data Stream Manager (Inter-task communication based on token ring network)

An intelligent graphic display station (DP-1000, Digital Electronic Co.) receives commands from FGSCT and draws pictures. DP-1000 is a VME computer system that was specially made for graphics processing. It has 4 Mbyte screen memories and drives three independent 20" CRT, each with a resolution of 1280 (horizontal) by 1024 (vertical) dots and 64 colors. The link between S-3500 and DP-1000 is RS-232C.

7. CONTROL

7.1 Development of a Flexible Graphic Display System

We have developed a flexible graphics display system (FGS) for storage ring control. A schematic of the FGS architecture is shown in Fig. 39. The control system uses four minicomputers (FACOM S-3500 from Fujitsu) linked to each other by a token ring-type network.[1] The FGS control task (FGSCT) resides in one of the control computers. Many application tasks for control are distributed over four control computers. The application task sends a request to display a necessary graphic picture to FGSCT by DSM (Data Stream Manager, inter-task communication utility based on network.[1] FGSCT manages those requests from various application tasks. When it accepts a display request, it establishes a connection between the application task and a display monitor. Hereafter, the application task is able to make modifications on a displayed picture.

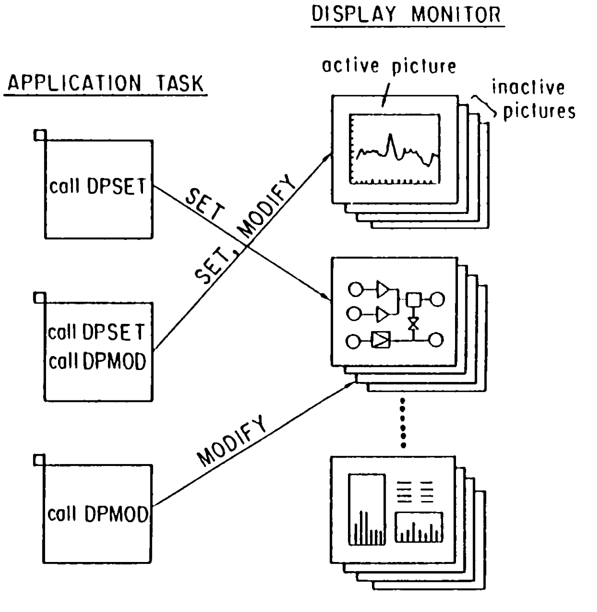

Fig. 40 Schematic diagram of command flow from an application task to a graphic display.

Logically, the application tasks have only to send short command strings to the graphic display, as shown in Fig.40. Actually, FGSCT accepts the request for a new picture from the application task, and sends a display command to the display station. FGSCT has a stack-like structure for display commands. Although the old picture is pushed into the stack, it can still be modified by commands from the application task. In addition, FGSCT automatically assigns the nearest display monitor to the touch screen, which initiated the application task.

7.2 Refined Control of the Accelerating Frequency

We refined the control of the accelerating frequency. In the old system, a workstation (HP-310), which is used for the beam-position monitor system,[2] directly manipulated a master oscillator of the rf system in order to correct the horizontal COD (Closed Orbit Distortion). In addition, the frequency was also changed by manual operation of the master oscillator.

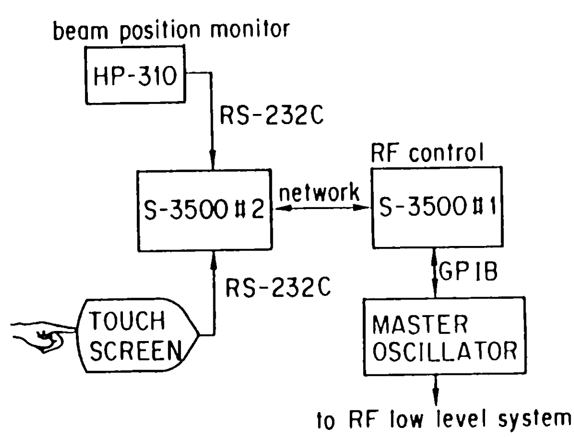

Fig. 41 Refined frequency control of the rf system.

In the refined system, the frequency is always manipulated by a control computer (FACOM S-3500 #1), as shown in Fig. 41. Another control computer (S-3500 #2) accepts requests for frequency changes from HP-310 and/or from touch screens. It then transfers those requests to an rf control computer through a network. The new frequency value after a change is sent back. The control computer (S-3500 #1) watches the requested frequency value and prevents any illegal changes which could cause a beam loss.

C. O. Pak

References
1) C. O. Pak, Nucl. Instr. Meth. A277 (1989) 501.
2) Photon Factory Activity Report #7, R-19,(1989)

8. BEAM CHANNEL

8.1 New Beam Channels

Front ends of beamlines BL-20 and BL 27 were installed in 1990 and completed in 1991 for exploiting residual bending magnet sources B20 and B27. A branch beamline of BL-20 is for a bright and high resolution VUV spectroscopy and another X-ray branch is assigned to Australian national beamline facility. The BL-27 was commissioned in a collaboration with Japan Atomic Energy Research Institute (JAERI) to promote researches concerning to radioactive materials such as radiation biology using tracer elements, inner-shell spectroscopy of actinide compounds etc.

In designing the new front-ends, special efforts were made to improve cooling capability of the beam absorber, shutters, masks and diaphragms since further power-up of radiation is persistently contemplated in the facility. In the BL-27, all diaphragms were made vacuum-tight so as to protect the ring donut and other beam channels from radioactive pollution in any kind of failure as tightly as possible.

Figure 42 is an optical path diagram of the front end BL-20 schematically showing acceptance of the masks and diaphragms. As for the BL-27, it will be reported elsewhere.

8.2 Vertical Wiggler Beamline

Front end of the vertical wiggler beamline BL-14 was totally reconstructed in response to installation of the new wiggler[1]. Radiation power of the wiggler can be as about three times higher than that of the old one[2] when operated with 5 poles at 5 T. All water-cooled components were redesigned to withstand the heat load, beryllium windows were replaced by newly designed ones[3], and the 1 mm thick beryllium plate heat absorber[4] for protection of the beryllium windows was replaced by a 0.42 mm thick graphite foil. The fast closing valve was replaced by a new type[5], and an additional pneumatic isolation gate valve was installed according to other PF front-end standard.

Figure 43 is the optical path diagram of the front end of BL-14. A care must be taken not to confuse the vertical and horizontal plans.

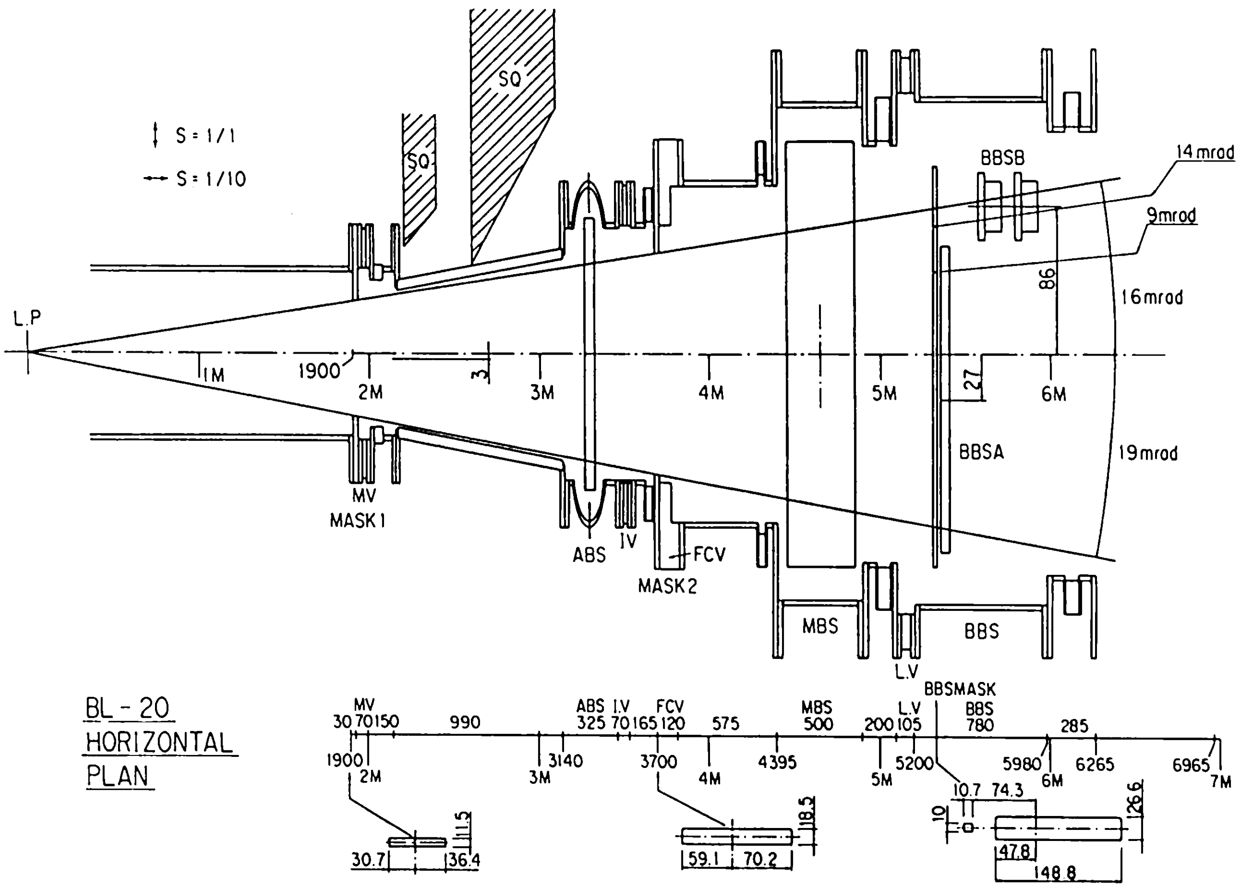

Fig. 42 The optical path diagram of BL-20 front-end. Vertical acceptance is 5 mrad for the branch A and 2 mrad for B. The pure numerics are in unit of mm.

8.3 Direct Irradiation Experiment

A test apparatus[3] for direct irradiation of beamline components by undulator radiation was facilitated at a straight-through port of BL-28 and some irradiation experiments were made on beryllium windows, graphite foils, silicon-carbide mirrors, and silicon-carbide-based multilayer mirrors[6].

<u>Calorimetric measurement of undulator power</u>

Prior to the irradiation experiments, total power and spatial power distribution of undulator radiation were measured with Faraday-cup type calorimetric devices[6] made of copper. It was confirmed that the total power and spatial power distribution were strictly represented by Kim's formula[7] when taking into account the finite beam emittance.

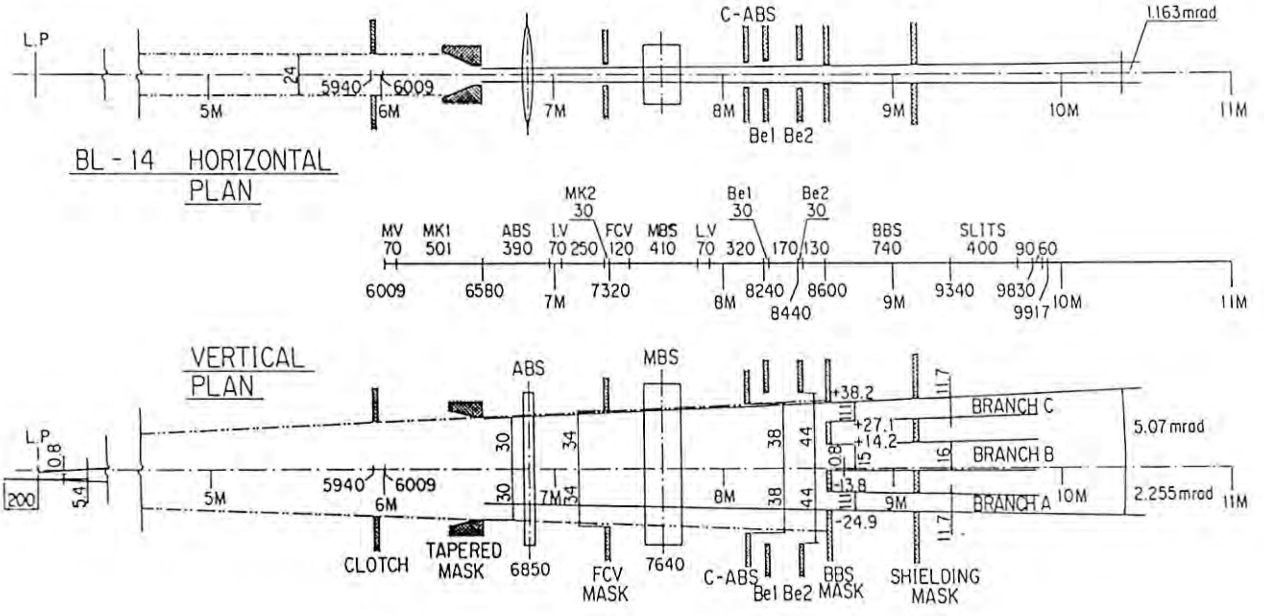

Fig. 43 The optical path diagram of BL-14 front-end.

<u>Beryllium windows and graphite foil heat absorbers</u>

A new type of beryllium window[3] was developed for high heat load wiggler beamlines. A copper disk with a race-track type aperture was clad in stainless steel rings by explosion bonding to form a double sided conflat flange. A 0.3 mm thick beryllium foil was brazed to the aperture along which cooling water channels were drilled as nearly as possible. The new type of windows was firstly applied to high power wiggler beamlines BL-16[8] and BL-14[4].

It was confirmed from the direct irradiation experiments that a thermo-mechanical breakdown of the beryllium window foil such as cracked and meltdown failure occurred well in accordance with a simple failure theory concerning to the maximum shearing stress.

Graphite foil absorber is, therefore, indispensable for protecting beryllium windows in high heat flux X-ray beamlines. A graphite foil was also tested in the irradiation port using un-filtered multipole wiggler radiation[9].

H. Maezawa

References

1) K.Ohmi et.al., to be published in Rev. Sci. Instrum.
2) T.Yamakawa et.al., Nucl. Instrum. Meth. A246 (1986) 32
3) S.Asaoka et.al., to be published in Rev. Sci. Instrum.
4) S.Sato et.al., Nucl.Instrum.Meth.A246(1986)177
5) N.Kanaya et.al., IEEE Trans.NS-36(1989)1391.
6) M.Yanagihara et.al., Proceedings of a satellite meeting to SRI-91 held 20 July 1991, Chester College, UK
7) K.J.Kim, Nucl.Instrum.Meth.A246(1986)67
8) S.Sato et.al., Rev.Sci.Instrum.60(1989)1965
9) to be reported elswhere in detail.

D. LIGHT SOURCE SPECIFICATIONS

This section contains major specifications of the PF ring to provide quick and handy information for users and machine physicists.

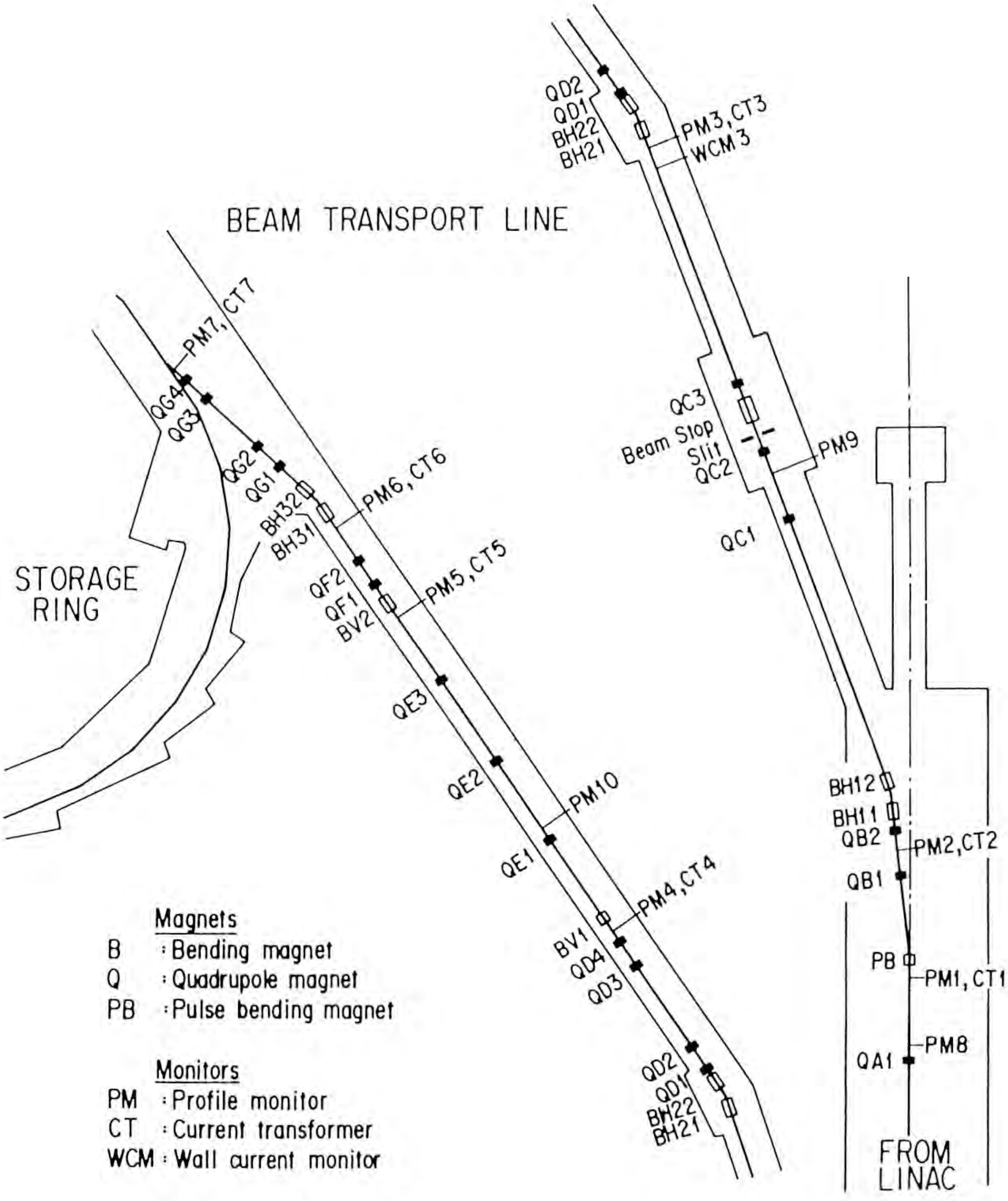

Fig. D-1. Beam transport line.

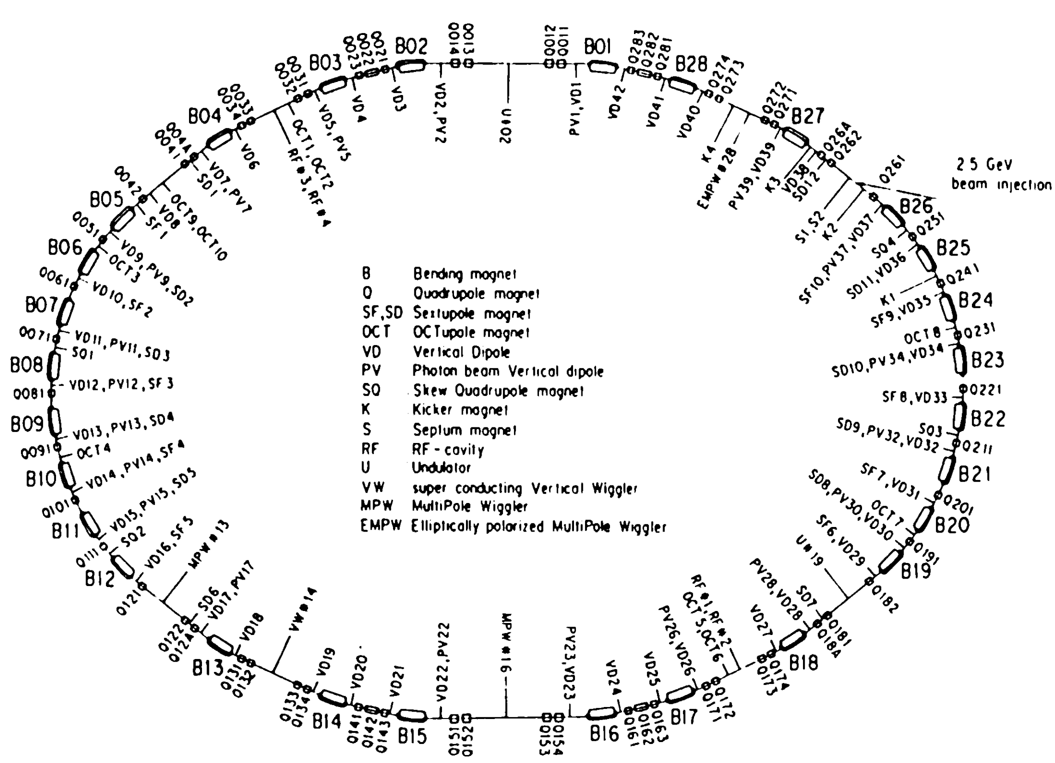

Fig. D-2. Ring lattice components.

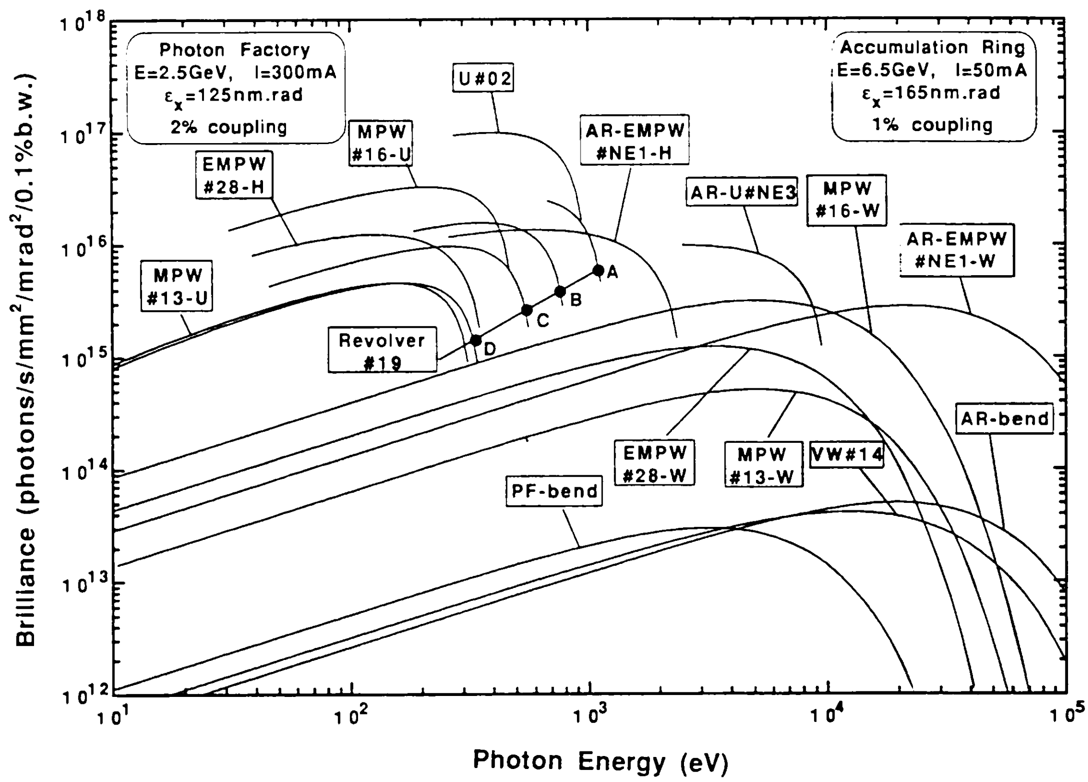

Fig. D-3. Synchrotron radiation spectra.
Brilliance of radiation vs. photon energy for the insertion devices (U#02, MPW#13, VW#14, MPW#16, Revolver#19 and EMPW#28) and the bending magnet (Bend) of the PF, and for the insertion device (EMPW#NE1) of the AR. The name of each source is assigned in Table D-4. Several insertion devices have both undulator and wiggler modes, which are denoted by U or W, respectively. The spectral curve of each undulator (or undulator mode of multipole wiggler) is a locus of the peak of the first harmonic within the allowable range of K-parameter. Spectra of Revolver#19 are shown for four kinds of period lengths.

Table D-4 Insertion devices

Calculated spectral performances of the bend source and 6 insertion devices at the Photon Factory. E/I: beam energy and current, λ_u: period length, N: number of periods, L: length of undulator or wiggler, $G_y(G_x)$: minimum vertical (horizontal) gap height, $B_y(B_x)$: maximum vertical (horizontal) magnetic field, P: pure configuration, H: hybrid configuration, S.C.: superconducting magnet, $\sigma_{x,y}$: horizontal or vertical beam size, $\sigma_{x',y'}$: horizontal or vertical beam divergence, $K_h(K_v)$: horizontal(vertical) deflection parameter, $\varepsilon_1/\varepsilon_c$: photon energy of the first harmonic(critical energy in the case of bend source or wiggler), $\Delta\varepsilon/\varepsilon$: relative bandwidth, Pc: degree of circular polarization, $\mathcal{D}$: photon flux in unit solid angle (photons /s ·mrad^2 ·0.1%b.w.), $\mathcal{B}$: brilliance (photons /s ·mm^2 ·mrad^2 ·0.1%b.w.), P_T: total radiated power, $dP/d\Omega$: power in unit solid angle. Different operating modes of undulator and wiggler are denoted by -U and -W, respectively.

Name	E/I GeV/mA	λ_u cm	N	L m	$G_y(G_x)$ cm	$B_y(B_x)$ T	Type of magnet	σ_x mm	σ_y mm	$\sigma_{x'}$ mrad	$\sigma_{y'}$ mrad	$K_h(K_v)$	$\varepsilon_1/\varepsilon_c$ keV	$\Delta\varepsilon/\varepsilon$	$\mathcal{D}$	$\mathcal{B}$	P_T kW	$dP/d\Omega$ kW/mrad^2
Bend	2.5/300							0.74	0.26	0.38	0.037		4.0		3.5E13	2.9E13		0.060
U#02		6.0	60	3.6	2.8	0.4	H(NdFeB)	0.78	0.11	0.16	0.022	2.25	0.28	0.029	5.2E16	9.7E16	0.68	2.7
MPW#13-W -U		18.0	13	2.5	2.7	1.5	H(NdFeB)	1.66	0.17	0.15	0.019	25.0 2.0	6.2 0.108	 0.086	9.7E14 5.7E15	4.9E14 3.2E15	6.7 .042	2.6 0.19
VW#14					5.0	5.0	S.C.	1.05	.096	0.16	0.025		20.8		2.2E13	3.4E13		0.18
MPW#16-W -U		12.0	26	3.1	1.9	1.5	H(NdFeB)	0.78	0.11	0.16	0.022	16.8 2.0	6.2 0.162	 0.050	1.8E15 1.6E16	3.1E15 2.8E16	8.3 0.12	4.9 0.52
Revolver #19		5.0 7.2 10.0 16.4	46 32 23 14	2.3	3.0	0.28 0.41 0.53 0.62	H(NdFeB) H(NdFeB) H(NdFeB) P(NdFeB)	1.66	0.17	0.15	0.019	1.3 2.7 5.0 9.5	0.637 0.176 0.0436 0.0078	0.021 0.039 0.047 0.066	4.1E16 2.1E16 6.9E15 1.2E15	2.3E16 1.2E16 3.8E15 6.3E14	0.21 0.44 0.78 1.05	1.27 1.54 1.53 1.09
EMPW#28 -W -U		16.0	12	1.9	3(11)	1(0.2)	P(NdFeB)	1.05	.096	0.16	0.025	 15(1) 1(1)	 4.2(Pc=89%) .18(Pc=99%)	 0.11	 2.5E14 6.3E15	 3.4E14 9.8E15	 2.3 0.02	 0.38 0.058

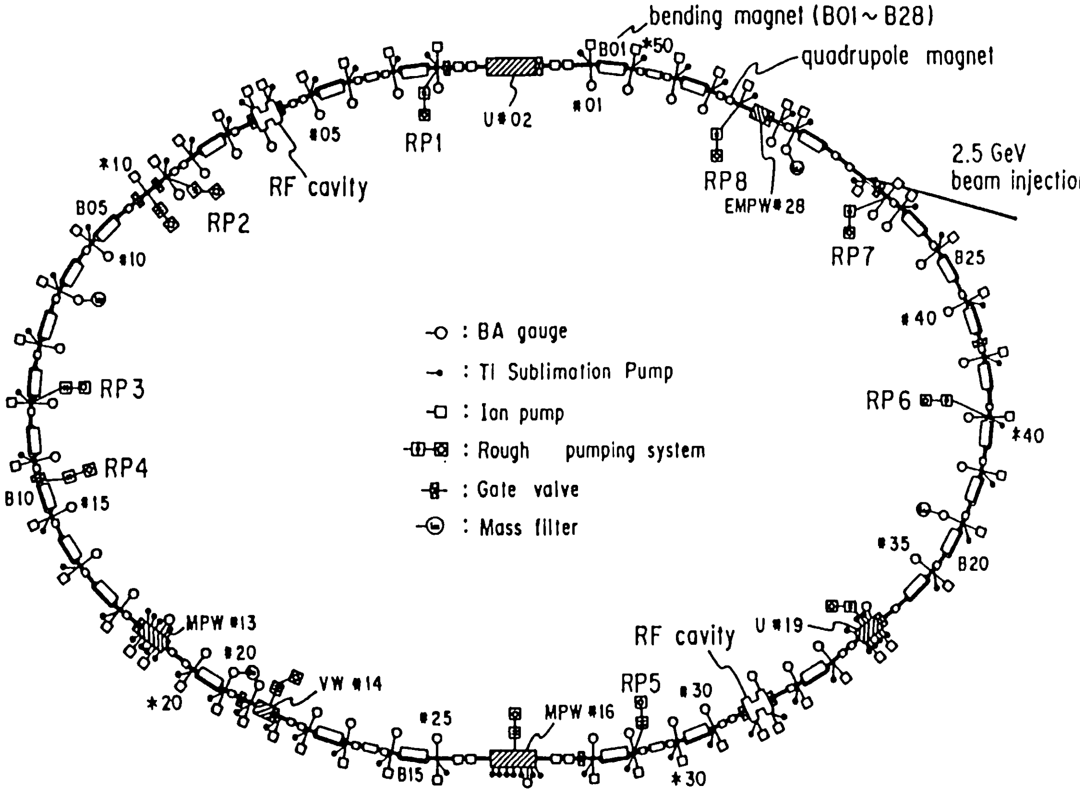

Fig. D-5. Vacuum system components.

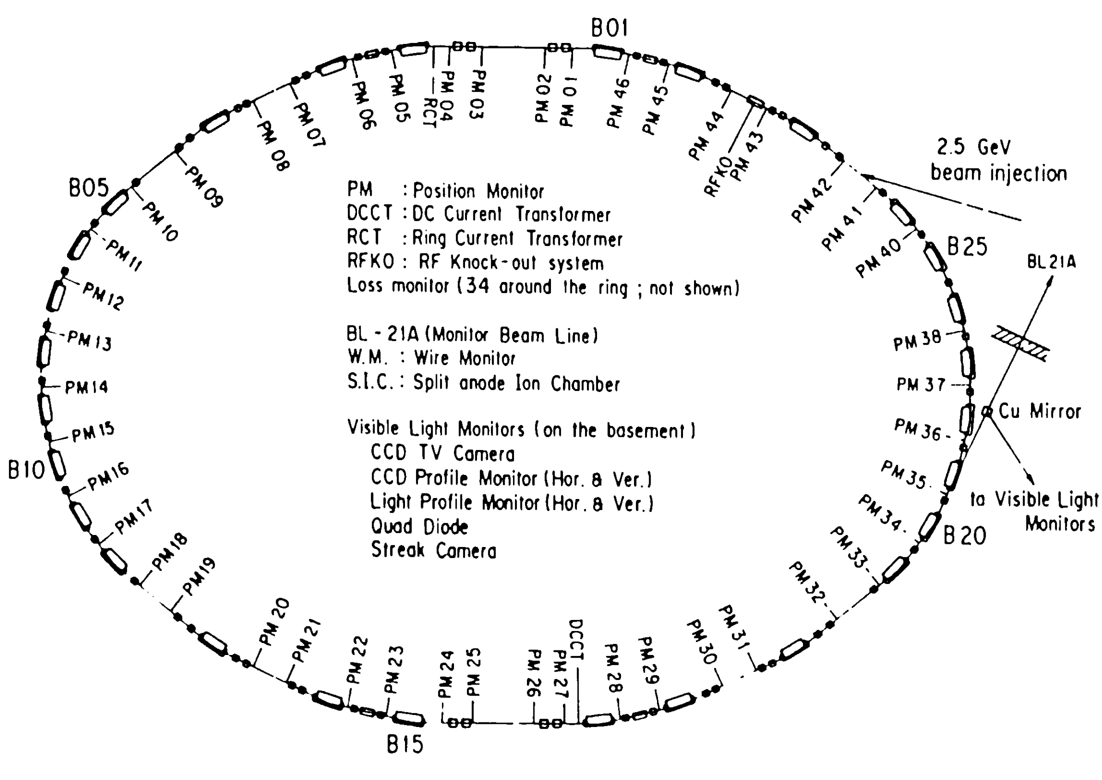

Fig. D-6. Beam monitors.

Table D-7. General parameters of the storage ring.

Energy	2.5 GeV	(0.75 GeV to 3 GeV)
Initial stored current (multi-bunch)	350 mA	(max 500 mA)
(single bunch)	40 mA	(max 104 mA)
Emittance	130nm·rad(horizontal) ~2nm·rad(vertical)	
Circumference	187m	(bending radius=8.66m)
RF frequency	500MHz	(harmonic number=312)
Injection	2.5GeV Linac	(positron/electron)
Beam lifetime	60 h (at 300 mA)	I·τ ≳ 18 A·h (at ~250 mA ~ 350 mA)
Vacuum pressure	$\lesssim 3\times10^{-10}$ Torr (at 300mA) P/I ~ 8×10^{-10} Torr/A (at ~250 mA ~ 350 mA) ~ 3×10^{-11} Torr (at 0 mA)	
Insertion devices	Superconducting vertical wiggler 5T 60 period undulator K=1.78~0.1 26 period multipole wiggler/undulator 1.5T~0.04T Four way revolver type undulator 14 period multipole wiggler Elliptically polarized multipole wiggler	
SR channels	SR experiment 22 (1 under installation) Beam diagnosis 3	

Table D-8. Beam parameters.

Horizontal tune n_x	8.45
Vertical tune n_y	3.30
Compaction factor α	0.015
Natural chromaticity ξ_x	-15.8
ξ_y	-8.6
Bunch length σ_z	1.5cm
Transverse damping time	7.8msec
Longitudinal damping time	3.9msec
Energy spread	7.3×10^{-4}
Radiation loss	400keV

Table D-9. Principal parameters of the accelerator system.

Magnet system

	number of magnets	number of power supplies
Bending	28	1
Quadrupole	58	12
Sextupole	22	2
Octupole	11	10
Skew quadrupole	4	4
Dodecapole	6	6
Vertical steering	42	42
Photon beam steering	20	20
Others		
Backleg winding of bending magnet	28	
Electric shunt for tune compensation	12	

RF system

Number of RF stations	4
Number of klystrons	4 (180kW/klystron)
Number of RF cavities	4 (single cell cavity)
Shunt impedance	32MΩ (four cavities)
Unloaded Q	39000
Total power dissipated in cavity wall	89kW
Total cavity gap voltage	1.7MV
Synchrotron frequency	37kHz

Vacuum system

main pumping system

pump	pumping speed	number
SIP (Sputter Ion Pump)	128 l/sec	54
DIP (Distributed Ion Pump)	150 l/sec	26
Ti sublimation	-----------	71
NEG (Non-Evaporable Getter)	-----------	2

total effective pumping speed = 2×10^4 l/sec (for CO)

Rough pumping system

	pumping speed	number
TMP (Turbo Molecular Pump)	300 l/sec	12

Measurement

	number
B-A gauge	48
mass filter	4
cold cathode gauge	16 (for baking)

Sector gate valve

	number
all metal with RF shield	5
all metal without RF shield	1
Viton seal with RF shield	10

Injection system

Septum magnet

name	Septum I (S1)	Septum II (S2)
core material	laminated silicon steel (passive type)	
length [mm]	1500	1000
maximum current [A]	6000	6000
deflection angle [degree]	7.0	5.0
pulse width [msec]	88	60

Kicker magnet

name	K1 , K2 , K3 , K4
core material	ferrite (window frame type)
core length [mm]	300
maximum current [A]	3500
maximum deflection angle [mrad]	4.4
pulse width [msec]	5

Superconducting vertical wiggler

Maximum field strength on the beam orbit	5 Tesla
Magnet gap	66 mm
Magnet pole size (widthxhight)	40 mm × 260 mm
Number of magnetic poles	5 poles arranged every 200 mm
Rated exciting current	220 A at 5 Tesla
Superconducting wire	NbTi : Cu 1 : 1 size 1.70 × 0.85 mm^2
Cross section of coils	65 mm × 70 mm
Number of turn	2520
Liquid helium consumption in the permanent current mode	0.1 L/h
Damping rate of the permanent current	1.4×10^{-5}/h
Inductance	1.31 H/coil

Monitor system

I Orbiting Beam Monitors

PM(Position Monitor)	45
RCT(Ring Current Transformer)	1
DCCT(Direct Current Current Transformer)	1
RFKO(Radio Frequency Knock-Out system	1
WCM(Wall Current Monitor)	1
Visible Light Monitor	
CCD TV camera	1
CCD Profile Monitor (H &V)	1
Light Profile Monitor (H & V)	1
Quad Diode	1

II Photon beam position monitors installed in beamlines of PF and AR rings.

Beamline	Source	Upstream	Downstream	Ver./Hor.
BL 2	U	DSPM	DSPM	V, H
BL 3A	B	SPM		V
BL 3C	B	SPM	SPM	V
BL 4C	B	SPM	SPM	V
BL 6B	B	SLIT		V
BL 6C	B	SLIT		V
BL 6C	B	SPM	SPM	V
BL 7C	B	SLIT	SPM	V
BL 10A	B	SIC		V
BL 10B	B	SLIT		V
BL 12A	B	WM	WM	V
BL 14C	SVW	SPM	SPM	H
BL 15A	B	SPM		V
BL 15B	MPW			V
BL 16	MPW	DSPM		V, H
BL 21	B	WM		V
BL 27	B	Under constr.		
BL 28	EMPW	Under constr.		
NE 1	EMPW	DSPM		V, H
NE 5	B	SPM	SPM	V

Note:
SPM : Split photoemission monitor
SIC : Split ion chamber
WM: Wire monitor
DSPM: Dual SPM for insertion device line

B: Bending magnet
U: Undulator
SVW: Superconducting vertical wiggler
MPW: Multipole wiggler
EMPW: Elliptical MPW

Control system

		number	memory
Control computers	FACOM S-3500	4	16 Mbyte
Library computer	FACOM M-780/10R	1	32 Mbyte
Computer network (type : optical token ring)			
number of nodes = 5 (max. 256)			

Table D-10. Beam size and divergence at source point.

location	σ_x [mm]	σ_y [mm]	σ'_x [mrad]	σ'_y [mrad]
B15&B01	0.34	0.16	0.41	0.033
B02&B16	0.60	0.13	0.38	0.033
B03&B17	0.43	0.22	0.32	0.018
B04&B18	0.52	0.18	0.29	0.045
B05&B19	1.26	0.21	0.39	0.037
B06&B20	0.85	0.25	0.38	0.037
B07&B21	1.26	0.21	0.39	0.037
B08&B22	0.85	0.25	0.38	0.037
B09&B23	1.26	0.21	0.39	0.037
B10&B24	0.85	0.25	0.38	0.037
B11&B25	1.26	0.21	0.39	0.037
B12&B26	0.85	0.25	0.38	0.037
B13&B27	0.44	0.23	0.31	0.045
B14&B28	0.50	0.20	0.30	0.018

Table D-11Summary of Beamline in FY 1991.

Beamline	Affiliation	Source	Spectral range	Status
BL-1	NTT	bending magnet (B1)	VUV and soft X-ray	in operation
BL-2	KEK-PF	60-period permanent magnet undulator	Soft-X-ray	in operation
BL-3	KEK-PF	bending magnet (B2 & B3)	VUV and X-ray	in operation
BL-4	KEK-PF	bending magnet (B2)	X-ray	in operation
BL-5	KEK-PF	permanent magnet wiggler/undulator (under design)	-	under installation
BL-6	KEK-PF	bending magnet (B6)	X-ray	in operation
BL-7	University of Tokyo	bending magnet (B7)	VUV and X-ray	in operation
BL-8	Hitachi Ltd.	bending magnet (B8)	VUV and X-ray	in operation
BL-9	Nippon Electrical Co. (NEC)	bending magnet (B9)	VUV and X-ray	in operation
BL-10	KEK-PF	bending magnet (B10)	X-ray	in operation
BL-11	KEK-PF	bending magnet (B11)	VUV and soft X-ray	in operation
BL-12	KEK-PF	bending magnet (B12)	VUV	in operation
BL-13	Research Team for advanced materials*)	27-pole wiggler	Soft and hard X-ray	in operation
BL-14	KEK-PF	superconducting vertical wiggler	Hard X-ray	in operation
BL-15	KEK-PF	bending magnet (B15)	X-ray	in operation
BL-16	KEK-PF	53-pole permanent magnet wiggler/undulator	Soft and hard X-ray	in operation
BL-17	Fujitsu Ltd.	bending magnet (B16 & B17)	VUV and X-ray	in operation
BL-18	ISSP and KEK-PF	bending magnet (B18)	VUV	in operation
BL-19	ISSP and KEK-PF	permanent magnet multi-undulator	VUV	in operation
BL-20	KEK-PF	bending magnet (B20)	VUV and X-ray	in operation
BL-21	KEK-PF	bending magnet (B21)	White, visible, and X-ray	in operation
BL-27	KEK-PF	bending magnet (B27)	Soft X-ray and X-ray	in operation
BL-28	KEK-PF	25-pole permanent magnet wiggler/undulator	Circularly polarized VUV and soft X-ray	in operation
AR-NE-5	KEK-PF	bending magnet of Accumulation Ring (AR)	Hard X-ray	in operation
AR-NE-1	KEK-PF	41-pole wiggler	Circularly polarized hard X-ray and soft X-ray	in operation

*) National Research Laboratory of Metrology, National Institute of Researches in Inorganic Materials, Electrotechnical Laboratory, and National Chemical Laboratory for Industry

Instrumentation Division

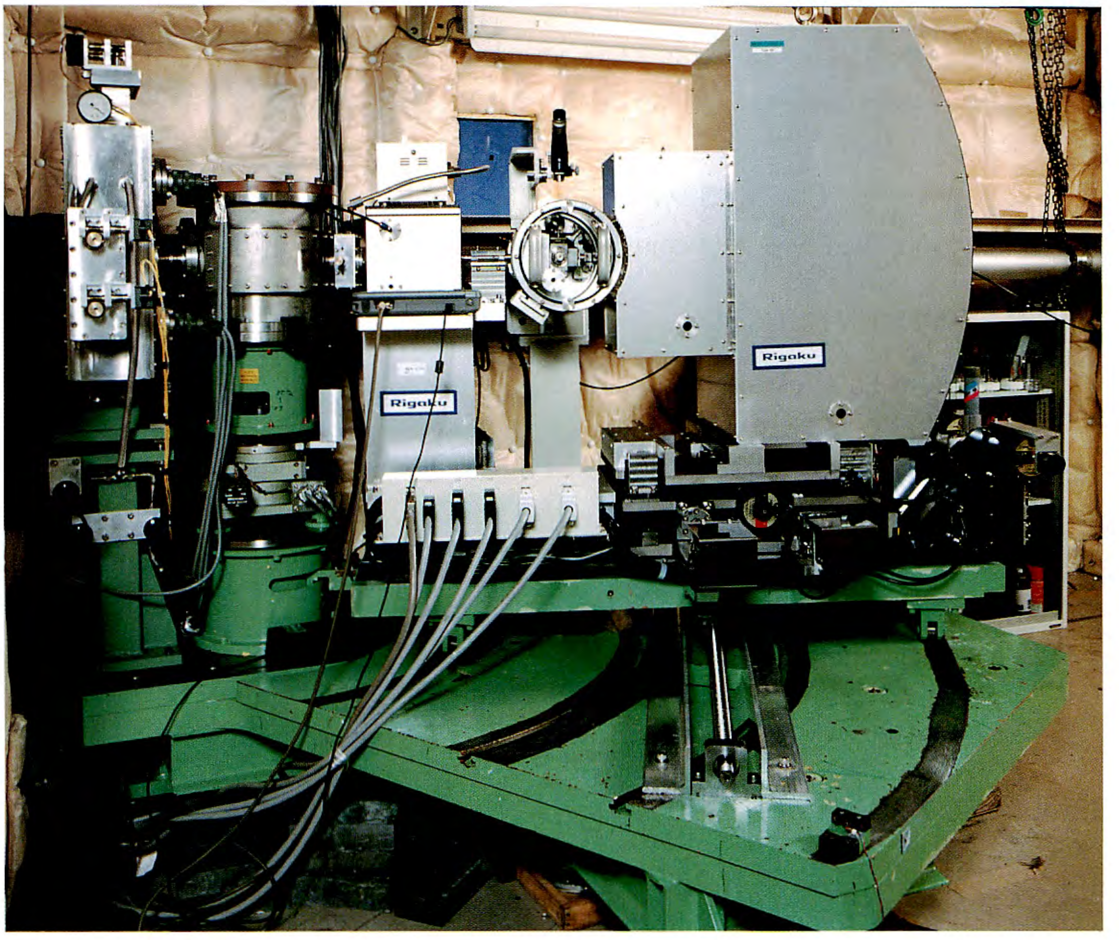

The Weissenberg Camera for Macromolecular Crystallography (type III) installed at BL-6A2 (see article on page I-11.)

You can jump to the article by clicking its title.

CONTENTS

INSTRUMENTATION DIVISION

A. INTRODUCTION

Owing to our continual efforts in the last few years, three insertion device beamlines have become operational in the year of 1991. Construction of new beamline is also being continued to increase experimental opportunities.

Three new insertion device beamlines now in operation are BL-16U, BL-19 and BL-28U. Beamline 16U covers the photon energy range of 40 - 600 eV. This is the beamline on which the first test of the SiC grating was carried out as described later in this section. Beamline 19 has been built by Institute of Solid State Physics, University of Tokyo in collaboration with the Photon Factory. This beamline is equipped with a so-called revolver type undulator which has 4 pairs of magnet arrays and covers the energy range of 30 -1200 eV. On Beamline 28U, circularly polarized light in the energy range of 5 - 300 eV is emitted from a crossed undulator. Magnetic circular dichroism of Ni and Gd thin films has already been measured on this beamline.

Six branch beamlines are under construction. Users at the Weissenberg camera station on BL-6A_2 has almost tripled in these two years. To meet such increasing demands of protein crystallographers, Beamline 18B now under construction will be equipped with another Weissenberg camera for macromolecular crystallography. Beamline 20A has been designed to obtain a high flux ($\sim 10^{12}$/sec) photon beam in an energy range of 10 - 40 eV by using a normal incidence monochromator. Upon completion of this beamline, most of experiments on BL-12A which covers almost the same energy range will be moved to this new beamline. BL-20B is an X-ray branch line which is being built as the Australian National Beamline. We expect to have the first beam on this beamline in summer of 1992. Beamline 27 has two branches each covering soft X-ray and hard X-ray regions and both branches are designed for use of radioactive samples. Special care was taken in the design of this beamline to meet the Japanese regulation on handling radioactive materials. By operating the insertion device on BL-28 in a wiggler mode, circularly or elliptically polarized synchrotron light is obtained in the energy range of 2 - 10 keV. A mirror-crystal-mirror optics is being constructed on this beamline. This beamline will be used for measurement of magnetic circular dichroism in such energy range and other kinds of experiments.

Some modifications of existing beamlines have been made. In particular, Beamline 14 has been modified to handle radiation emitted by a new 5-pole superconducting magnet wiggler.

Besides constructing new beamlines, instrumental developments are also important for creating new experimental opportunities for users. Some of such developments made in the year of 1991 are optics to measure and control circular polarization of synchrotron radiation, various instruments and techniques to measure secondary photons or particles and new detectors. Among these, the development of the avalanche photodiode detector is very timely and useful. It has a time resolution of 0.23 ns and is extensively used in the Nuclear Bragg Scattering experiment. The X-ray phase retarder using Bragg case diffraction is very effective in the fast switching of helicity of the X-ray beam. The combination of an intense linearly polarized light source and such a phase retarder will be a useful tool in the high accuracy scattering and spectroscopic studies of magnetic materials.

Several experimental results are also given in section D. The high resolution photoabsorption spectra at the oxygen K-edge demonstrates the unique performance of the spectrometer on the undulator Beamline 2B. Users' demands for beam time on this beamline is increasing. The result of microcrystal diffraction is encouraging. The Laue diffraction data were obtained and analyzed for the smallest crystal ($0.27\mu m^3$) ever studied.

We expect to complete construction and commissioning of 6 branch beamlines described above in these 2 years. After that, we shall have only one completely empty beamline (BL-5) and one empty branch beamline (19C) on the 2.5 GeV ring for installation of new experimental instruments. It is to be noted that BL-5 is connected to the last empty straight section left of the 2.5 GeV ring. Discussion on the design of these beamlines will be made in 1992.

T. Matsushita

B. BEAMLINES

1. NEW BEAMLINES IN OPERATION

BL-16U VUV and Soft X-ray Undulator Beamline

A 2-m grazing-incidence VUV/soft X-ray monochromator with a SiC-based master grating for undulator radiation has been equipped and installed on a 26-period multipole wiggler/undulator (MPW/U) beamline, BL-16U.[1] This monochromator was designed to cover the photon energy range 40 - 600eV using 1200 and 2400-mm^{-1} SiC based master gratings.[2] Its performance using a 1200-mm^{-1}grating was previously evaluated and a resolving power of 2200 at 244.4eV and a photon flux in the order of 10^{12} photons/s were achieved.[3] Here the performance using a 2400-mm^{-1} grating is evaluated and the groove profile of the grating exposed to the undulator radiation is also analyzed.

The spectral response of the monochromator was measured with a gold mesh photocathode. Figure 1 shows the spectral distribution of the undulator radiation for typical MPW/U operation with a field parameter K=2.4. The first to third harmonic peaks were clearly observed. This spectral response was stable and could always be reproduced during long-term operation. However, the photocurrent intensity of the first harmonic peak was about two orders of magnitude less than that of the peak measured with the 1200-mm^{-1} grating.[3]

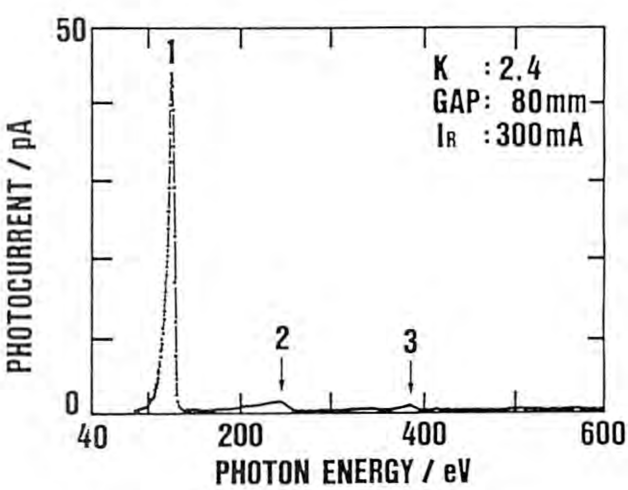

Fig. 1 Spectral response of the monochromator measured with a gold mesh photocathode. The numbers in the figure indicate the harmonic order of the respective peaks.

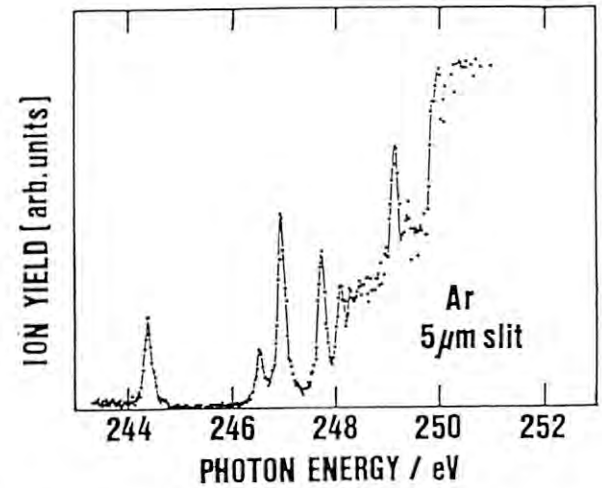

Fig. 2 Total ion yield spectrum of Ar $^2P_{3/2,1/2} \rightarrow nl$ Rydberg series.

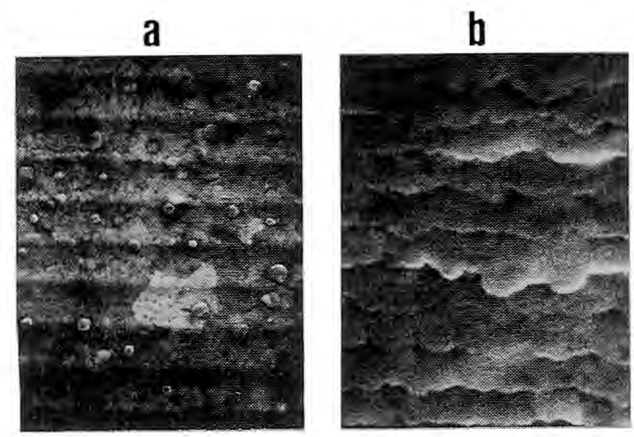

Fig. 3 SEM images of the grating surface exposed to undulator radiation for about 100 hours.

The resolving power was evaluated by measuring the total ion yields of rare gases. Figure 2 shows the Ar-$L_{2,3}$ spectrum obtained with the narrowest slit (5μm). The full width at half maximum of the $2p^5(^2P_{3/2})4s^1$ peak at 244.4 eV was 140meV. Taking into account a natural width of 121 meV, deconvolution showed that a resolving power of more than 4000 was achieved, which was in good agreement with the expected value derived from the grating dispersion.

Thermal degradation of the grating surface was observed by means of Scanning Electron Microscopy (SEM). Figure 3 shows the SEM images of the grating surface exposed to undulator radiation for about 100 hours. Many grain-like objects in Fig. 3(a), which were the same as those formed on the irradiated 1200-mm^{-1} grating [3], were observed in the irradiated area. In addition, vigorous degradation shown in Fig.3(b) was observed locally in the irradiated area. However, the periodicity of the groove structure was well preserved. The above-mentioned performance with the lower diffraction efficiency and the high resolving power of the 2400-mm^{-1} grating may be explained by the vigorous degradation of the grooves and the preserved periodicity of the groove structure.

H. Kato & Y. Muramatsu

1) Y. Muramatsu and H. Maezawa; Rev. Sci. Instrum., **60**(7), 2078(1989).
2) T. Kita et al.; Rev. Sci. Instrum., (in press).
3) Y. Muramatsu et al.; Rev. Sci. Instrum., (in press).

BL-19B Revolver Undulator Beamline

Beamline 19B is specially designed to accept radiation from a revolver undulator and dedicated to photoelectron spectroscopic studies on phase transitions of solids.[1] The beamline consists of a front end, a mirror system and a plane grating monochromator (PGM). The PGM was designed so that its output photon energy ranges from 30 to 1200 eV. The optical layout of the PGM is shown in Fig. 4. The undulator radiation is reflected at 88.5° by a SiC cylindrical mirror (M_B) in a water cooled adjustable mirror holder. The radiation passes through a diaphragm chamber equipped with vertical and horizontal apertures as well as wire monitors, and guided to a water cooled long SiC plane mirror with a length of 500 mm. The monochromator has no entrance slit. The PGM is equipped with two varied-space plane gratings (VSPG), recently developed by Harada et al.[2] The gratings are located 19.0 m from the center of the undulator. An energy range from 100 to 1200 eV is covered by the VSPG with 2400/mm. The groove separation of this VSPG is optimized for 5 Å at an incidence angle of 89.0°. Another VSPG is used to cover the output photon energy from 30 to 400 eV. The exit slit is set at 1000 mm from the grating. Assuming a beam size of $\sigma_z = 0.6$ mm and $\sigma_x = 2.0$ mm, an energy resolution $\Delta E/E$, smaller than 1/1500, is attainable by ray tracing in the energy region between 30 and 1200 eV with a 20 μm exit slit. In order to scan the photon energy, both the incidence angle and the deviation angle of the grating are properly changed. For this purpose, numerical control of the rotations of the grating and the long plane mirror (LPM) is required.

Monochromatic light emerging from the exit slit is focussed by a toroidal mirror onto a spot of 0.7×0.5 mm^2 on a sample in an analyzing chamber equipped with a hemispherical electron energy analyzer with a spin LEED detector and a liquid He cryostat. The characterization of the PGM has been achieved by employing simultaneous scanning of undulator magnet gap and monochromator since 1990. In fiscal year 1991 it was found that an output photon energy range from 30 to 1170 eV could be covered by the fundamental radiation from the revolver undulator.

Photoelectron spectra of solids at low temperature will be measured using this system and the temperature dependences of the electronic states of solids accompanying phase transitions, such as electric and magnetic transitions, will be studied.

M. Fujisawa and A. Kakizaki

1) A.Kakizaki et al.; Rev. Sci. Instrum. **60**,1893 (1989).
2) T.Harada et al.; Soc. Photo-Opt. Instrum. Eng. **503**, 114 (1984).

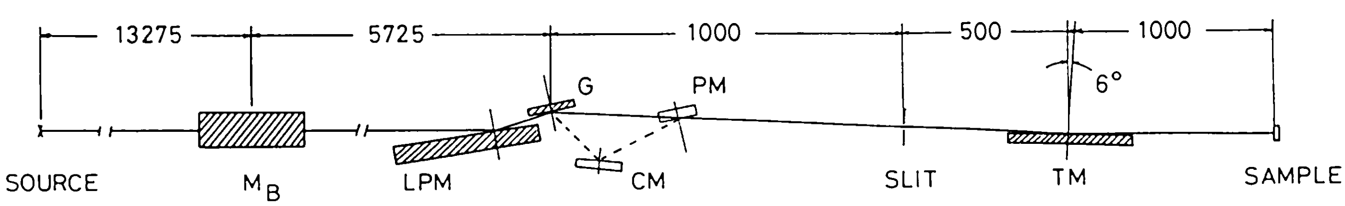

Fig. 4 Optical layout of PGM. Rotation of the large plane mirror (LPM) and the grating (G) are numerically controlled. Output light is focussed by means of a toroidal post-focussing mirror(TM). (MB: SiC cylindrical mirror; PM: Plane mirror; CM: Curved mirror)

BL-28U Beamline for Circularly Polarized VUV

The first test operation of the beamline was performed in December 1990, when the magnetic circular dichroism of thin Ni films was measured in the photon energy region associated with 3p-3d photoexcitations. The comparison between a theoretical calculation and the experimental results suggested that the degree of polarization was better than 70 % in the above photon energy region, which is below the photon energy of the first harmonic peak of the undulator radiation. Figure 5 shows a typical example of the undulator radiation measured with the grating monochromator where the intensity of the first harmonic is much reduced because the incidence angle of the grating used was very close to 90 degrees. Although some efforts to determine the Stokes parameters were made using a polarimetric method, they were not successful due to some movement of the output beam which was dependent on the wavelength scanning of the grating monochromator.

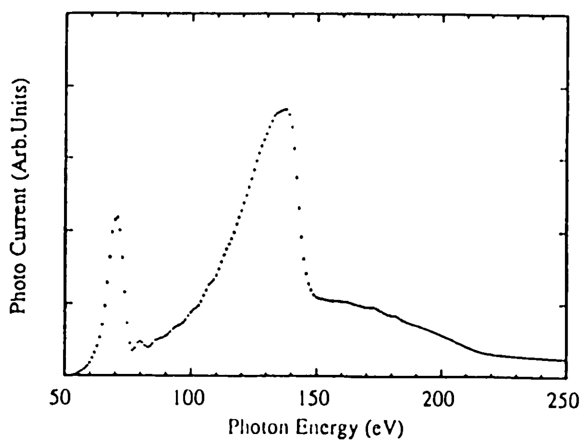

Fig. 5 Typical spectrum of undulator radiation.

This movement seems to be caused by some misalignment of the optical components of the monochromator, but the detailed cause is still unknown and should be identified and removed.

Figure 6 shows a schematic optical layout of the beamline including a post-focusing mirror system. The optical components of the monochromator are located between the entrance slit, S1, and the exit slit, S2. The optics is rather complicated because the monochromator should cover photon energies of both the normal incidence region and the glancing-incidence region, namely from 5 eV to 300 eV. In fact, M3 and M4 work as the glancing-incidence optics with deviation angles of 170 and 160 degrees, respectively, while M5 works as the normal-incidence optics. The glancing optics covers photon energies higher than 20 eV using one of the four gratings G1, G2, G3, and G4, while the normal-incidence optics covers those below 20 eV using G5.

The quality of the three gratings G1, G3, and G4 used for the glancing-incidence optics has been found not to be satisfactory in terms of higher-order diffraction and scattering background. Therefore new gratings made of SiC with rectangular grooves are now being fabricated and will be mounted in the monochromator in the near future. The degradation of the degree of circular polarization caused by a grating is an important subject which will be studied more extensively. The study will be carried out using two pieces of apparatus that are now being constructed to measure the Stokes parameters. One employs a polarizer and an analyzer consisting of three mirrors and the other employs those consisting of multilayer mirrors.

T. Miyahara

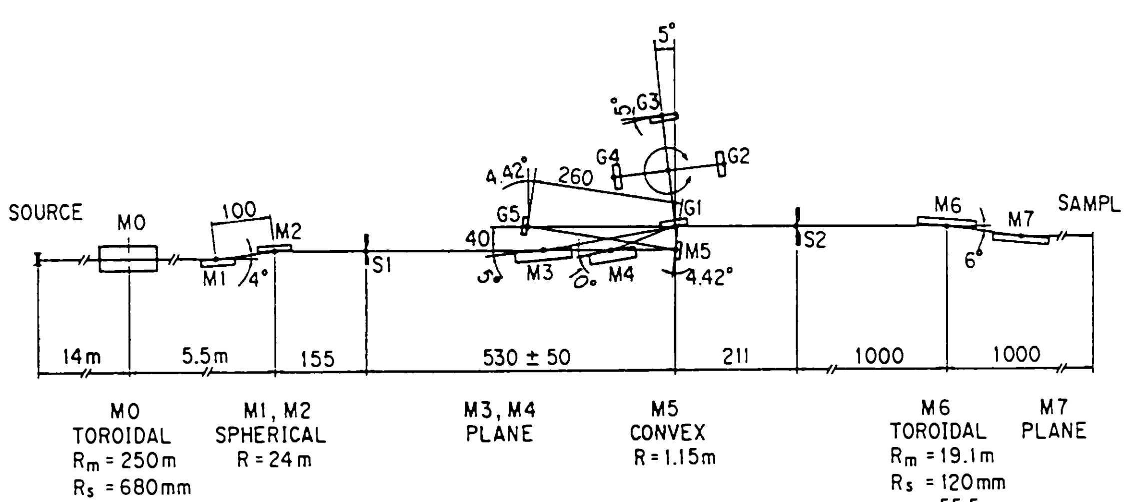

Fig. 6 Schematic layout of BL-28U

2. BEAMLINES UNDER CONSTRUCTION

BL-18B Beamline for Macromolecular Crystallography

On beamline 18, BL-18A had already been constructed in 1989 and is in operation for photoemission experiments of surfaces and interfaces. BL-18B for macromolecular crystallography has been newly designed and is under construction. BL-18B is an end station so that there is enough space for installing a larger camera for macromolecular crystallography. The design of the optical alignment of BL-18B is constrained by the presence of BL-18A and BL-18C and the future use of BL-18C has also been taken into account. A layout of the beamline is shown in Fig. 7. A water cooled mask for BL-18B and 18C was newly designed and installed behind the mirror chamber of BL-18A.
7Branch beamlines 18B and 18C receive 3.0 and 2.0 mrad of radiation, respectively. BL-18B and BL-18C are separated from the UHV section of BL-18A by Be windows behind the mask. BL-18B will be equipped with a 1m long fused quartz bent cylindrical mirror with 1:1 focusing, located 13.7m from the source, and a double-crystal monochromator using silicon (111) or germanium (111) crystals, located 23.1m from the source.

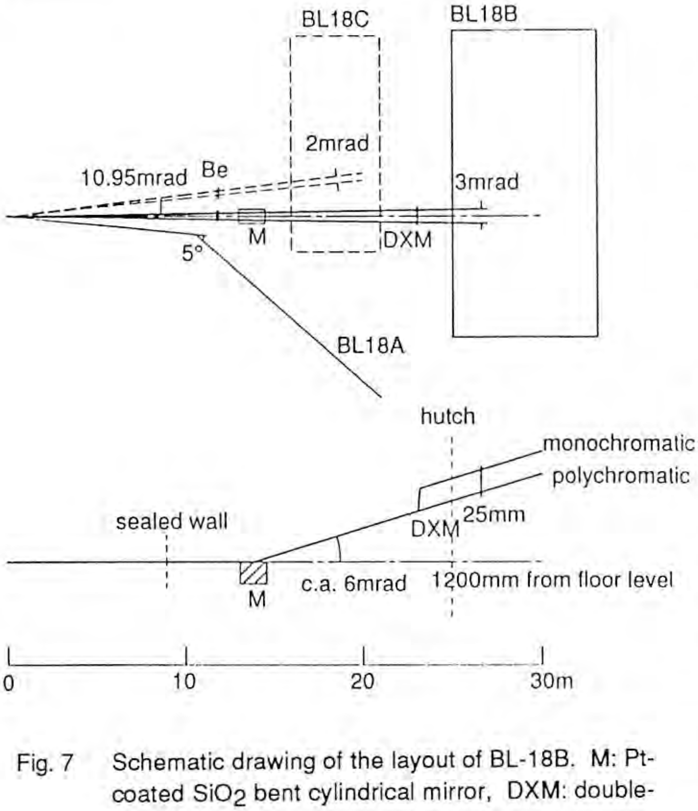

Fig. 7 Schematic drawing of the layout of BL-18B. M: Pt-coated SiO_2 bent cylindrical mirror, DXM: double-crystal monochromator, Be: Be windows.

The surface of the focusing mirror is cylindrically polished with a radius of ca. 41mm and platinum coated. It will be bent to a radius of ca. 4,500m. The glancing angle of the X-ray beam with the mirror will be set to about 3mrad, which yields a cut-off wavelength of approximately 0.4Å. Flat crystals will be used as the first and second crystals of the monochromator. Two kinds of crystals, Si and Ge, will be interchangeable without opening the vacuum chamber. BL-18B is designed for monochromatic protein crystallography but will also be useable as a white X-ray beamline for polychromatic (Laue) crystallography. The station will be operational in October 1992.

N. Watanabe

BL-20A High Flux 3-m NIM Beamline

The installation of a high-flux 3-m normal-incidence monochromator (3-m NIM) was completed at BL-20A during the 1991 summer shutdown. The first photons came out from the exit slit of the monochromator in the beginning of October 1991. The horizontal acceptance of the first toroidal mirror is 28 mrad in order to obtain a high photon flux in the energy region of 10 - 40 eV. The photon flux at 550Å was estimated to be 3×10^{11} photons/sec/Å by measuring the photoemission current from a gold-coated photocathode. At present, there is a problem with the vertical focussing by the first mirror resulting in a significant loss of photon flux. It is assumed that the photon flux will be increased several times by repolishing of the first mirror. The resolving power, $\lambda/\Delta\lambda$, was estimated from the width of the ns' autoionization line of Ar and Kr atoms and found to be $\approx 10^4$ at 800 Å, which was aimed at in the design stage of the monochromator. Further improvements are now underway.

K. Ito

BL-20B Australian National Beamline

A double-crystal X-ray monochromator and multi-configuration diffractometer are being built at BL-20B by a consortium of Australian institutes and universities. The beamline is designed to deliver white beam or monochromatic beam in the 5-20keV range. The layout of the beamline is shown in Fig. 8. Initially the primary optics will consist of a simple Si(111) channel-cut monochromator.

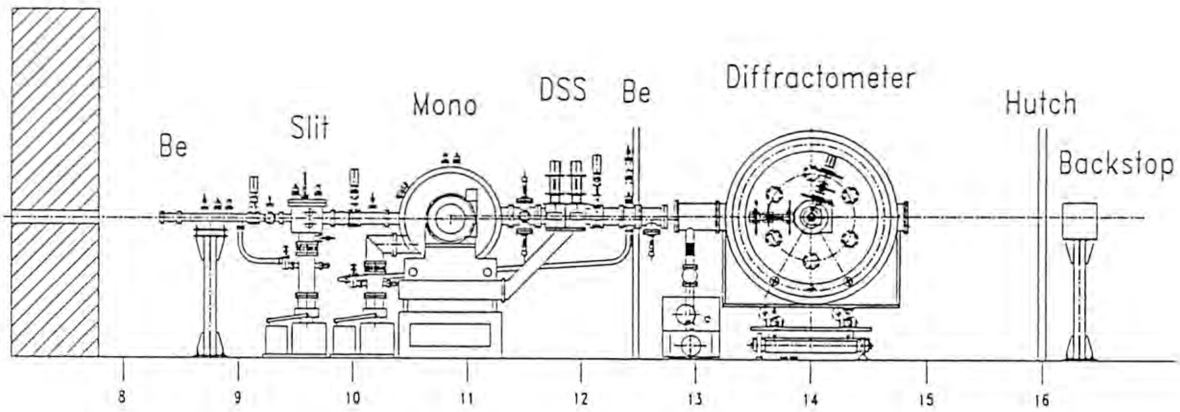

Fig. 8 Layout of the Australian National Beamline

This will be replaced later by a sagittally focusing double-crystal monochromator of the type developed by Matsushita.[1] The two-circle diffractometer is housed in a large vacuum vessel, and both vacuum and helium operation modes will be available. The diffractometer will be optimized for powder diffraction, small-angle scattering and protein crystallography, and will operate as a 570 mm radius Weissenberg camera using image plates as the detection system. Alternatively other detectors can be mounted on the two-theta arm. A vertically condensing channel-cut secondary monochromator will be an option in the diffractometer.

The beamline components, monochromator and diffractometer are being fabricated and tested in Australia. The beamline will be installed in early 1992 and will be available for white-beam experiments. The monochromator and diffractometer will be shipped to Japan for installation at the beamline in the late summer of 1992. The sagittally focusing monochromator will follow, as will further refinements including a vertical beam position feedback system.

R.F. Garrett

1) Photon Factory Activity Report #4 (1986) p.93.

BL-27 Beamlines for Radioactive Materials

A beamline, BL-27, designed for experiments using radioactive materials, is now under construction. As reported earlier, this beamline consists of two branch beamlines, BL-27A for soft X-rays(1-6 keV) and BL-27B for hard X-rays(4-20 keV). A cylindrical pre-mirror installed at BL-27A is one of the largest SiC mirrors ever made, 70 cm long and 12 cm wide, and bent mechanically to form a quasi-toroidal mirror. It is water cooled to avoid thermal distortion. Double-crystal monochromators are used in both branch beamlines. The one in BL-27A is of ultra-high vacuum type and a heat pipe is used to cool the first crystal in the ultra-high vacuum. In order to prevent the intrusion of radioactive materials into the beamline upstream and the storage ring, special precautions are taken into as to the apertures of slits and masks and the design of an adsorption chamber. Apparatus for checking the contamination of the isotopes inside the beam pipe is also installed in the beamline. The maximum amount of radioactive isotopes per day will be 1 mCi (37 MBq), normalized to the fourth group in the radioisotope regulation rules.

Experiments using radioisotopes will start in April of 1992 as scheduled.

K. Kobayashi

BL-28X Beamline for Circularly Polarized X-rays

At Photon Factory there are two insertion devices, EMPW#28 and EMPW#NE1, to generate intense circularly polarized synchrotron radiation. Both devices are complementary to each other with respect to their energy ranges. Beamlines NE1A2 (6 ~ 100 keV), NE1B (240 ~ 1500 eV), and 28A (5 ~ 300 eV) are already commissioned. Using the EMPW#28 in multipole-wiggler mode one can get intense circularly polarized X-rays in the energy range between those of NE1A2 and NE1B.

A design study of BL-28X for experiments using the EMPW#28 in the multipole-wiggler mode has been started in the spring of 1991. The deflection parameters of the EMPW#28 are fixed at K_x=1.0 and K_y=15.0 to obtain intense circularly polarized X-rays in the energy range of 2 ~ 10 keV. Under these conditions, the radiated power becomes 2.2 kW. Design values of the horizontal and vertical acceptances are 4.0 mrad and 0.2 mrad, respectively. The fundamental optical elements are as follows:

Pre-Mirror:
- 18.8 m from source point
- 16 mrad reflection
- Pt-coated Si, Ni-coated Si
- Bent cylinder
- Horizontal focusing
- Vertical focusing or collimating
- Indirect water cooling

Double-Crystal Monochromator:
- 29.0 m from source point
- Fixed exit beam position
- No sagittal focusing mechanism
- Several kinds of crystals
- Indirect cooling (water, liquid metal, etc.)

Post-Mirror:
- 30.5 m from source point
- 16 mrad reflection
- Pt-coated SiO_2, Ni-coated SiO_2
- Bent plane
- Vertical focusing

Focusing Point:
- 34.5 m from source point.

Because of the soft X-ray region all the optical components will be installed in ultra-high vacuum and there will be no beryllium window to separate the storage ring vacuum from the beamline vacuum.

Design of the pre-mirror and the double-crystal monochromator is now in progress. The beamline construction will be finished by the end of March, 1993.

T. Iwazumi

3. IMPROVEMENT OF BEAMLINES

BL-2A Crystal Cooling System of the Undulator Beamline

A double-crystal monochromator was used without any crystal-cooling system at BL-2A in order to obtain 1.7-4.0keV photons from a 60-period soft x-ray undulator. With the replaced undulator and the increased maximum stored current, the maximum power density on the first crystal has become 5.24W/mm^2 and various problems caused by the heat load have emerged. Thus, a cooling system for the first crystal was designed and installed in the spring of 1991.

The double-crystal monochromator with the new crystal-cooling system is shown in Fig. 9, which is a view from upstream of the beamline. A few drops of liquid metal are put between the first crystal (A) of 30×30×1mm size and the copper holder (B). In the holder (B) and a fan-shaped block (C), several heat pipes are embedded. The block (C) is partly immersed in a liquid-metal bath (D), consisting of a eutectic of 77 wt.% gallium and 23 wt.% indium. The main heat pipe (E) of 22.22mm in diameter is attached to the bath. (F) are air-cooled radiative plates. An angle scan can be performed by means of a goniometer (G) and a stepping motor (H) connected to a rotation table (I). A stage and cam mechanism (J) keeps the exit beam height constant and a pair of plates (K) with a ball and springs, and dc motors are used to adjust the parallelism between the two crystals. All the components of the monochromator stand on a large flange (L), which can be withdrawn along a rail (M) if neccesary. Utilization of heat pipes and a liquid-metal bath result in good thermal conductivity and smooth movements for scanning and adjustment of the crystals in the high-vacuum chamber.

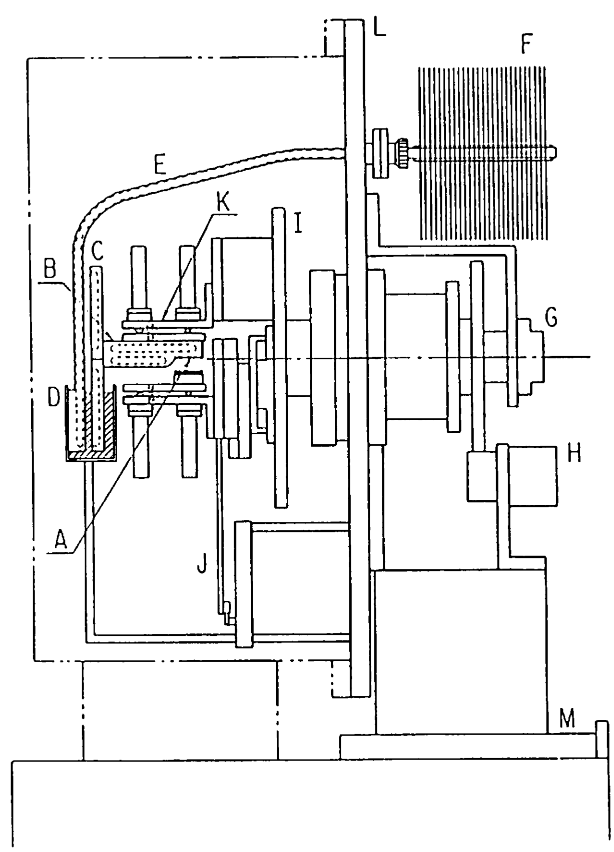

Fig. 9 A schematic drawing of the monochromator with the crystal-cooling system. See text for details of A-M.

For a Si(111) crystal the temperature rise due to irradiation is measured to be only 6°C or less, instead of about 100°C before, so that the beam position instability and the undesirable degradation of the energy resolution have now disappeared. Now about 10^{10} photons/s of 2.1-4.0keV in a 2×2mm area with an energy resolution (E/ΔE) of more than 5000 are available at this station.

Y. Kitajima

BL-14 Vertical-wiggler Beamline

BL-14 is the only beamline providing vertically polarized hard X-rays. The vertical wiggler had been replaced by a new 5-pole superconducting one in September 1989. In order to cope with 5-pole 5 Tesla operation of the new wiggler, the beamline was also modified during this summer shutdown. A water-cooled mask, beam shutters and X-Y slits were replaced with new ones. The efficiency of the water cooling of the beamline assembly was improved. The upper and lower limits of vertical beam acceptance of the three branch beamlines are summarized in Table 1. Presently, the wiggler is usually operated in 3-pole 5 Tesla mode. A study of the 5-pole operation is in progress.

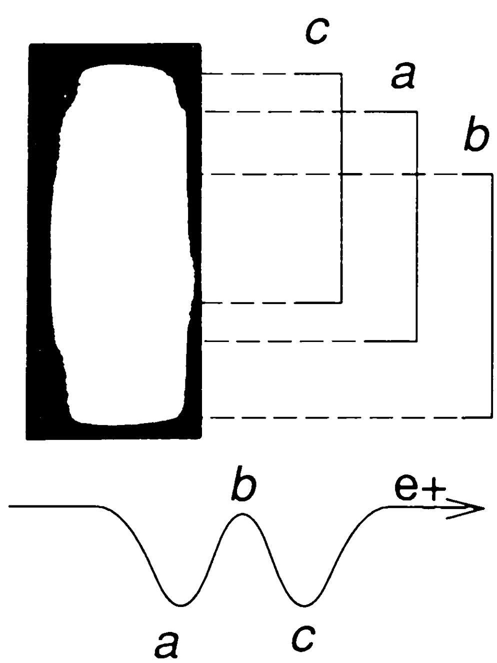

Fig.10 Image of X-rays from 5-pole vertical wiggler observed at BL-14C when the wiggler was operated in 5-pole 4.5 Tesla mode. *a, b* and *c* indicate source points from which the X-rays are emerging.

Fig.10 shows the observed image of X-rays from the wiggler, operated in 5-pole 4.5 Tesla mode, at BL-14C. The incoming X-rays have an intensity profile produced by a superposition of X-rays from the three source points. In the center of the beam the intensity of hard X-rays is three times higher than normal.

N. Watanabe & S. Kishimoto

Table 1 Upper and lower limits of vertical acceptance of three branch beamline at BL-14.
Source points *a, b* and *c* are defined in Fig. 10.

Source point	BL-14A (mrad)	BL-14B (mrad)	BL-14C (mrad)
5-pole *a*	-1.0 -2.2	1.7 -0.2	4.7 3.4
5-pole *b*	-1.5 -2.8	1.7 0.0	4.5 3.2
5-pole *c*	-1.0 -2.3	1.8 0.0	4.9 3.6
3-pole	-1.0 -2.3	2.3 0.5	5.1 3.8

C. NEW INSTRUMENTATION

Apparatus for Polarimetric Measurements of Circular Polarization

Two pieces of apparatus for polarimetric measurements of the Stokes parameters of polarized synchrotron radiation have been constructed and are now being assembled and adjusted. One employs a polarizer and an analyzer consisting of three reflecting mirrors, while the other employs a polarizer and analyzer made of a multilayer mirror.

The former covers the photon energy range below 100 eV which is limited by the optical characteristics of the constituent gold-coated mirrors. Using three mirrors either for the polarizer or the analyzer the optics assumes a geometry such that the analyzer and the polarizer can rotate around a common axis which coincides with the direction of the incoming light. Therefore, ideally, this apparatus works without changing the direction of the optical layout of a beamline. Because the apparatus also has a mechanism for linear motion of the mirrors for the incident light to go through, any apparatus connected after this apparatus can use the incident light without being affected by this apparatus.

The latter apparatus with multilayer mirrors covers photon energies from 70 eV to several hundred eV but actually the upper limit of photon energy depends on the optical characteristics of the multilayer mirrors. We hope to cover the energy up to 250 eV, which is the lower limit of the 10 m glancing-incidence monochromator located at beamline NE1C of the TRISTAN accumulation ring (AR).

Because in the apparatus both the polarizer and the analyzer consist of a single multilayer mirror, the direction of the reflected light is not the same as the direction of the incident light. Therefore the polarizer can rotate around the direction of the incident light and the analyzer can rotate around the direction of the light reflected by the polarizer. The incidence angle of the polarizer can be varied from 0 to 60 degrees and that of the analyzer can be changed from 0 to 70 degrees. A microchannel plate is used for the detector which accurately follows the direction of the light reflected by the analyzer. The holder of the polarizer has a mechanism to flip the mirror off the axis of the incident light, so that any apparatus connected after this apparatus can accept the incoming light directly.

The above requirements make the mechanism of the apparatus rather complicated but will allow us to perform versatile measurements of the polarization characteristics of synchrotron radiation.

T. Miyahara

Photoelectron Spectrometer at BL-28U

An apparatus for measuring circular dichroism appearing in photoelectron spectra of solids has been designed and constructed. The whole system is now being assembled and adjusted. The apparatus consists of an analysis chamber, a sample preparation chamber and a vacuum system. It is also equipped with a double cylindrical mirror electron energy analyzer (DCMA), a hemispherical electron energy analyzer (HA) for angle-resolved experiments, LEED optics, an ion gun, and an airlock system. The DCMA will be mainly used for partial or total photoyield measurements to obtain the signals of magnetic circular dichroism, while the HA will be used for studies of circular dichroism of the angle dependence of photoemission. The HA is mounted on a two-axis rotating mechanism for angle-resolved measurements. When the HA is used the DCMA retreats into a vacuum tube by a linear motion mechanism. The HA can also be used for conventional angle-resolved photoelectron spectroscopy to determine band dispersions of solids or surfaces, where the linear undulator mode can be selected to use horizontal polarization.

A sample manipulator to adjust the sample position along the X, Y, and Z directions can be attached to the apparatus. A cryostat which can cool the sample down to 20 K is mounted on the manipulator. In the test operation the temperature of the surface of the sample holder was found to be below 25 K.

The voltages applied to the retarding grid, the inner and outer cylinders of the DCMA, are controlled by a microcomputer system with a GPIB interface through remote controllable power supplies. Because the computer also controls the scanning of the grating monochromator at BL-28, constant initial state spectroscopy can be easily performed by simultaneous control of the electron analyzer and the monochromator.

The airlock system has a sample bank which can contain five sample holders. Any one of the sample holders can be transferred to the sample preparation chamber or the analysis chamber using two linear-motion feedthroughs. In the sample preparation chamber the surface of a sample can be filed or some metals can be deposited on the surface by an electron gun.

The surface of a sample can be checked in the analysis chamber by Auger spectroscopy using an electron gun mounted in the DCMA and by the LEED system where the surface can be sputtered by the ion gun.

T. Miyahara

Spin-Polarized Photoelectron Spectrometer at BL-19A

A spin-, angle- and energy-resolved photoelectron spectrometer was installed at the revolver undulator beamline, BL-19A. Figure 11 shows a schematic view of the apparatus. It consists of a sample preparation chamber, an energy-analyzer chamber and an electron-lense chamber and Mott detector as spin analyzer. The sample preparation chamber is equipped with a sample manipulator, low-energy electron diffraction (LEED) optics, a cylindrical mirror analyzer (CMA) for Auger electron spectroscopy, a sputter ion gun, a gas inlet valve and others. The analyzer chamber is equipped with an angle-integrated electron energy analyzer for normal photoemission spectroscopy and an angle-resolved electron energy analyzer for spin-polarized photoemission spectroscopy. The energy-(ΔE) and angle-($\Delta\theta$) resolutions of the latter one are $E/\Delta E \sim 80$ and $\Delta\theta \sim \pm 2°$, respectively. (E is the pass energy of the hemispherical analyzer, its mean radius being 40mm.)

Angle- and energy-resolved photoelectrons are accelerated up to ~100keV in the Mott scattering chamber, which is installed in a tank filled with SF_6 gas to prevent discharge. The accelerated electrons are scattered by a thin film of gold and detected by five surface barrier detectors (SBD) around the film, one for the forward scattered electrons through the film and the others for the backscattered electrons (scattering angle 120°). The normal photoemission spectra can be obtained by counting the foward scattered electrons.

If the incoming electrons are spin-polarized, the backscattered electrons should show right-left or top-bottom asymmetry. The relationship between the asymmetry and the counting rate at each SBD is determined by the following equations:

$$A_{rl}(t)=(N_r(t)-N_l(t))/(N_r(t)+N_l(t)) \quad (1)$$

and

$$A_{tb}(t)=(N_t(t)-N_b(t))/(N_t(t)+N_b(t)), \quad (2)$$

where $A_{rl}(t)$ and $A_{tb}(t)$ are the right-left and top-bottom asymmetries, respectively, as a function of the thickness t of the gold film. N_r, N_l, N_t and N_b denote the counting rates at the right, left, top and bottom detectors, respectively. Two components of the spin polarization vector, for example, spin parallel and perpendicular to the sample surface, can be measured simultaneously by measureing both the right-left and the top-bottom asymmetries. The spin polarization of the electrons is deduced as

$$P=(N_u-N_d)/(N_u+N_d)=A(t)/S(t), \quad (3)$$

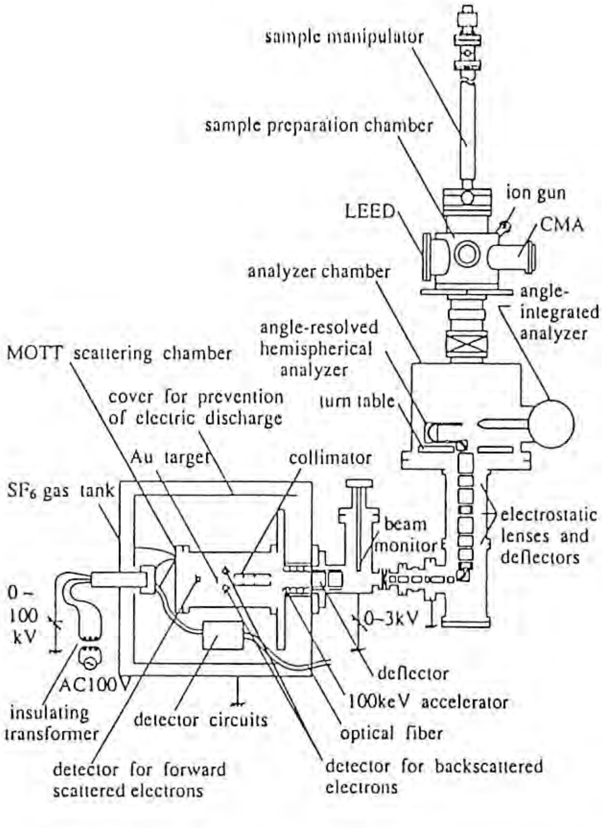

Fig. 11 Schematic view of the spin-polarized photoelectron spectrometer at BL-19A.

where N_u and N_d are the numbers of up and down-spin electrons, respectively, and S(t) is an effective Sherman function. The values of the effective Sherman function in our apparatus are S(400Å)=0.265, S(600Å)=0.258, S(800Å)=0.225 and S(1200Å)=0.174. Since the detector circuits, such as the pre-amplifier, are floated electrically on a 100kV level, the pulse signals are converted to optical signals and sent to the data acquisition system which is at ground.

Spin-polarized photoemission measurements for the ferromagnetic Ni(110) surface are now in progress.

T. Kinoshita

Apparatus for Surface Structure Analysis

A new ultra-high vacuum chamber (Fig. 12) has been designed and constructed for surface structure analysis with the back-reflection X-ray standing-wave method, surface XAFS, and XPS. It is equipped with a windowless Si(Li) solid state detector (HORIBA) and a UHV compatible gas-flow proportional counter to detect fluorescent soft X-rays, and a concentric hemispherical analyser (RIGAKU) for photoelectron spectroscopy and Auger electron spectroscopy. The SSD is specially designed as the detector faces upwards below the sample in order to detect grazing emission at any X-ray incidence angle. The sample manipulator consists of an XYZ-stage (VG), differentially-pumped rotary feedthrough (VG), and a liquid-nitrogen cryostat. It is also equipped with a 5kV ion gun (ANELVA), grazing-incidence electron gun (PHI), and LEED optics (VARIAN) for sample preparation and characterization.

The chamber is evacuated by a 300 l/s turbomolecular pump (SEIKO-SEIKI) with a 56 l/s backing turbomolecular pump (BALZERS), circularly arranged 5 STARCELL ion pumps (60 l/s, VARIAN), titanium sublimation pump with a liquid-nitrogen cooled shield (THERMIONICS), and non-evaporable getter pump (600 l/s for H_2, SAES getters). To minimize the area of the inner wall of the stainless steel chamber, it is mirror polished (R_{max}=0.1μm) by electro-chemical buffing (Ultra Finish Technology Co.). The achieved base pressure is 7×10^{-9}Pa.

Using this chamber on BL-2A, about 100cps of fluorescence signal from a half monolayer adsorbate of sulfur or chlorine atoms can be obtained and a fairly high S/B ratio is achieved for standing-wave absorption profile measurements.

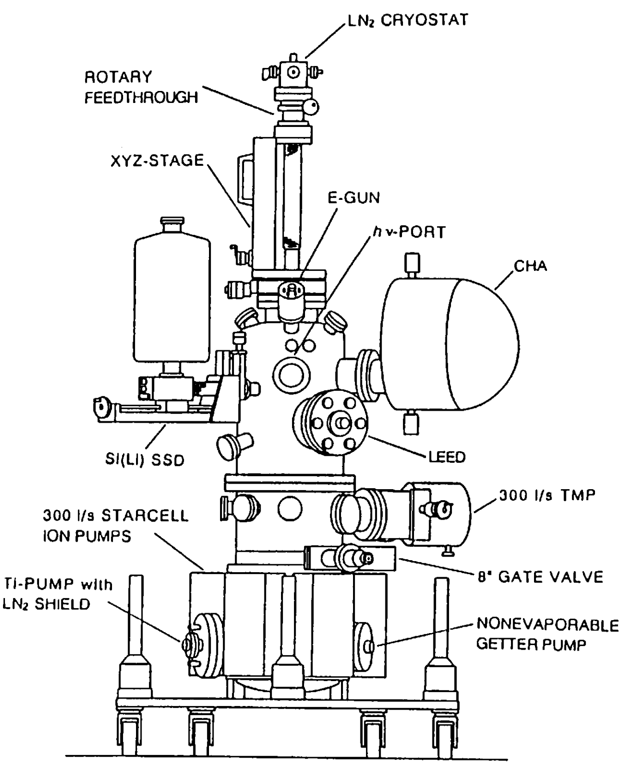

Fig. 12 Front view of the new apparatus for surface structure analysis.

As an example, the Cl/Ni(111) system and a surface XAFS study of a molecular adsorption system (CS_2/Ni(100)) are presented in the users' reports section of this issue.

Y. Kitajima

Weissenberg Camera for Macromolecular Crystallography (Type III)

A new Weissenberg camera for macromolecular crystallography has been constructed and opened to users at BL-6A2 from April in 1991. This camera was designed based on experience with a Weissenberg camera (Type II) at BL-6A2 during 5 years. The main improvements of the new camera are as follows: A film cassette of large radius (r=859.5mm) can be used for data collection from a crystal with large cell dimensions (1000Å) and cassettes can cover a large detector area with two or four sheets of imaging plates (IP) (200×400mm) as shown in the Table 2, and the operation of the camera has become very much simpler than for the Type II. The alignment of the crystal can be carried out by a Handy Terminal in the hutch. The helium chamber between the crystal and the film which is essential for the reduction of the background level through the displacement by helium gas is divided into two parts in order to speed up the helium exchange. A new eraser called KONISHIKI, which can erase 6 IP sheets at once, was installed beside the hutch. A brief characterization of the new camera is summarized in the table.

N. Sakabe

Table 2 Brief specification of the new camera.

a. Film cassette		
Radius of film cassette	No. of IP sheets that can be attached	Angular range (2θ)
1. 143.3 mm	1	-80° to 120°
2. 286.5 mm	1	-78° to 40°
	2	-78° to 40
3. 429.7 mm	1	-26° to 33
	4	-53° to 53
4. 573.0 mm	4	-40° to 40
5. 859.5 mm	4	-26.5° to 26.5°
b. Fuji Imaging Plate; 400×200 or 250×200mm Only these two types are available.		
c. Translation mechanism of the film cassette driven by a stepping motor:		
Moving range	+/- 100.0mm	
Step ratio	0.01mm/step	
Moving speed	max. 40mm/sec	
Reproducibility of position	<0.02mm	
d. Up/down mechanism of the film cassette driven by a stepping motor:		
Moving range	+/- 10.0mm.	
e. Rotation mechanism of the w-axis driven by a stepping motor or Handy Terminal:		
Rotation range	+/- 360	
Step ratio	0.001°/step	
Rotation speed	min. 0.005°/sec max. 10.0°/sec	
f. Collimator: 1.0×1.0, 0.5×0.5, 0.4×0.4, 0.3×0.3, 0.2×0.2, 0.1×0.1, 0.05×0.05 mm		
g. The crystal can be aligned by screws driven by hand:		
Rotation range	±20° (min. scale 0.05°)	
Translation range along ω axis	± 10mm (min. scale 0.01mm)	
h. Useable wave length range:	0.9 to 2.0Å	

An Avalanche Photodiode X-ray Detector with Subnanosecond Time Resolution

During single-bunch mode experiments of time-correlated photon counting in the X-ray region, for example the observation of quantum beats in the nuclear resonance of ^{57}Fe, can be performed. Thus, a fast timing detector for X-rays is needed to obtain an accurate timing of incident beams or photons emitted from a sample. The avalanche photodiode (APD) detector was developed as such a new timing detector with a subnanosecond time resolution. A silicon APD used in the present detector is commercially available (Hamamatsu S2384). A test pulse caused by a single X-ray photon was obtained with the APD and a fast amplifier which had a gain of 200.

The timing performance of the APD detector has been tested at BL-14A during single-bunch runs of the PF strage ring. The measured spectrum of 14.4-keV X-rays is shown in Fig. 13. The peak at t=0 was generated by positrons contained in a main RF bucket of the storage ring. The residual bunches were less than 10^{-5} of the main bunch in the run by purifying beam bunches with the RF-knockout method and scrapers. Therefore, the measured peak profile almost represents the response function of the detector in the time spectrum. The peak could be well fitted by a Gaussian distribution, shown by the dashed curve, although the peak was followed by a tail which contained about 10% of the total counts, shown by the shaded area. A time resolution of 0.28 ns (fwhm) was obtained from the width of the main peak, containing contributions from the detector system and from the width of the positron beam. When a Gaussian distribution was assumed for each shape of the observed peak and the bunch profile, the resolution of the detector system was determined as 0.23 ns (fwhm) since the beam width of the main bucket was known to be 0.16 ns (fwhm) from the results of the measurements observing visible light with a streak camera.

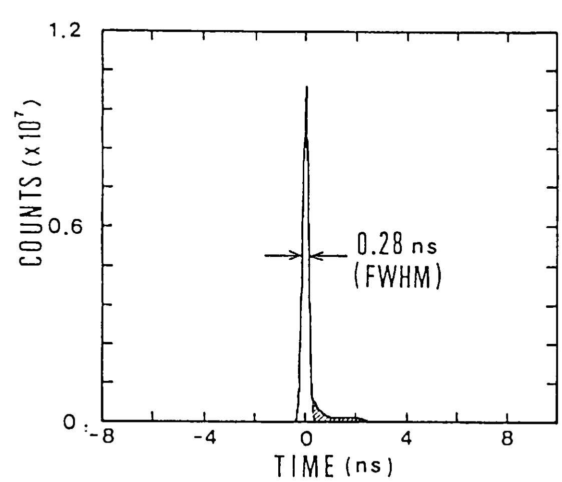

Fig. 13 Time spectrum of 14.4-keV X-rays during a single-bunch run of the PF strage ring. The dashed curve is the peak at a main RF bucket, fitted by a Gaussian distribution. The width (fwhm5) was 0.28 ns. The shaded area indicates a tail part after the peak.

In the spectrum the integral counts of the main peak reached to 4.7×10^7, while the total background at no incident beams was less than 3 counts at the same measuring time of 3200 s. If the tail after the peak can be ignored, this means that a peak-to-background ratio of more than 1.6×10^7 was achieved.

Moreover, the APD detector may be promising as a detector with a high-countrate capability, that is, a wide dynamic range to 10^7 cps and a short dead time of about 10 ns, as proved in our other experiments.

However, the thickness of the depletion layer of the APD device is only 30 μm of silicon so that the efficiency is at most 7% for 14.4 keV X-rays. The response function of the detector also was not satisfactory and depended on the structure of the APD device. New detectors using improved APD devices are now being built.

S. Kishimoto

X-ray Area Detector Based on CCD Readout for Diffraction Study

Although the imaging plate has excellent performance characteristics, it does not allow one to perform real-time measurements. Therefore, it is necessary to develop an area detector which has real-time capability with its other specifications kept as close as possible to those of the imaging plate system. With this in mind, we have started to develop an area detector system which is based on a charge coupled device (CCD) readout (Fig. 14).

In the system incident x-rays are converted to visible photons by a phosphor screen (Y_2O_2S or CsI(Na)) which is evaporated onto a fiberoptic plate. The fiberoptic plate is attached to the input surface of a large-aperture (100 mm in diameter) image intensifier. The image is intensified about 100 times and its linear dimension demagnified to one fourth by the image intensifier. The intensified visible image on the output phosphor screen of the image intensifier is viewed through a 1:1 optical lens system by the cooled CCD (Thomson:THX31156). The CCD has 1024 x 1024 pixels (pixel size : 19 μm x 19 μm), a pixel well-depth of 290,000 electrons, and a readout noise of 20 electrons. The detector has the following characteristics:

The active area is 78 mm x 78 mm. The spatial resolution is 120 μm x 120 μm (fwhm). The detective quantum efficiency is about 60 % for 8 keV, and the dynamic range is more than 10^4.

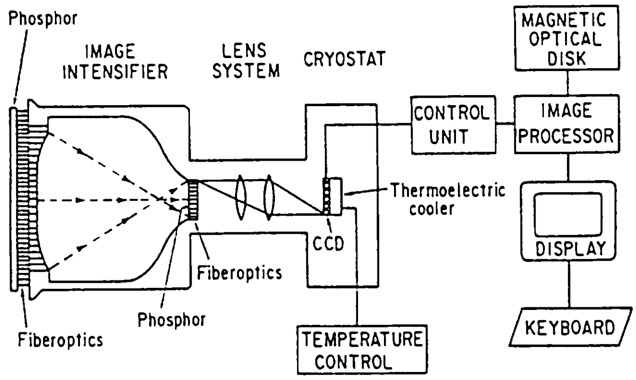

Fig. 14 Schematic of X-ray area detector with CCD (charge coupled device) readout.

The readout time is 4sec. The uniformity of response is not good enough at present: the intensity response at the peripheral is about 20 % of that of the central part. This is due mainly to vignetting of the optical lens system which is used to view the output image of the image intensifier. The uniformity of the response is expected to be improved by optimizing the numerical aperture of the optical lens system. At present, the non-uniformity of response is corrected by using a shading pattern which is obtained by uniform irradiance from a radioactive isotope source. The CCD is cooled to –30 to –40°C to reduce the dark current during measurements. The background noise level of the detector system corresponds to less than 10 X-ray photons per pixel when the exposure time is a few tens of seconds. The detailed performance characteristics of the system are now being measured.

The system has been used preliminarily to measure small-angle x-ray diffraction patterns of collagen and of muscle. The exposure time required was almost the same as that required for the imaging plate. This system will also be applied to protein crystallography.

Y. Amemiya

D. SELECTED EXPERIMENTS

Stark Effect on Kr Rydberg States

Figure 15 shows some of the absorption spectra of Kr in the region of 111 600 - 112 500 cm^{-1} under an electric field strength of 0 - 2000 V/cm. The direction of the electric field was perpendicular to the linear polarization of the incident photons, so that an excitation into Rydberg states with M=±1 can contribute to the absorption spectra. At zero electric field, three Rydberg series can be clearly seen: the $ns[3/2]_1$, the $nd[1/2]_1$ and the $nd[3/2]_1$ converging to the first lower ionization limit $I_{3/2}$. New absorption lines appear on the longer wavelength side of the $nd[1/2]_1$ lines with increasing the electric field. These lines are probably caused by transitions from the ground state $^1S_0$ to energy levels which are strongly correlated with a certain Rydberg series with a fairly large quantum defect. They are probably the np Rydberg series with quantum defects of 2.5 - 2.7, converging to the ionization limit $I_{3/2}$ as the $nd[1/2]_1$ series. Several weak absorption lines can also be observed under a certain electric field strength at the shorter wavelength side of the $nd[1/2]_1$ absorption lines. The Stark correlation of these lines with the $nd[3/2]_1$ and nd[1/2] is smaller than that of the np series. In the case where the polarization direction of the incident photons is parallel to the applied electric field, where Rydberg states with M=0 can be excited, the np and nd series appear in ways different from the perpendicular case.

A typical feature in the Stark absorption spectra are hydrogenlike Stark manifolds caused by the mixing of l states with very small quantum defects (l=3 to n–l). With increasing of the field strength the manifolds expand first to the $ns[3/2]_1$ lines, and then to the $nd[3/2]_1$ lines. It should be pointed out that some of the spectral lines in the manifolds seem to consist of at least two absorption lines.

It is very important to simulate the Stark spectrum theoretically. We have to diagonalize the Stark energy matrix for the Rydberg series converging to the first lower ionization limit. In order to describe the Rydberg series of Kr, a jl-coupling basis set is used. The diagonalization of the Stark energy matrix was carried out separately for M=0 and M=±1. For n = 13 - 15 the Stark energy matrix requires 312 and 306 basis functions for M=0 and M=±1, respectively. Note that the Rydberg states with J=0 do not exist for M=±1.

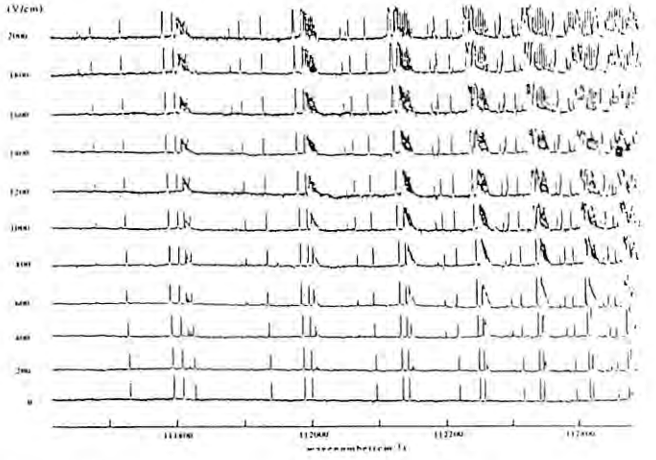

Fig.15 Densitometer traces of the photographed absorption spectra of krypton atoms under an electric field of 0 - 2000 V/cm. The direction of the electric field was perpendicular to the polarization of the incident photons.

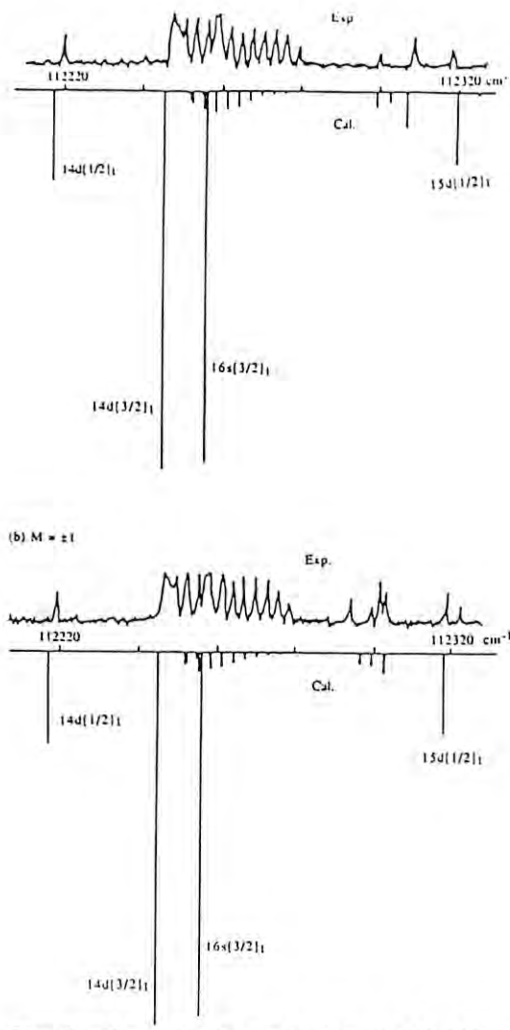

Fig. 16 Simulated spectra in the region of 112 220 - 122 320 cm^{-1} for (a) M=0 and (b) M=±1. The observed spectra are shown together with the simulated ones for each case.

The eigenfunctions obtained from diagonalization are represented by linear combinations of the basis set wave functions. The eigenstates which have significant coefficients of the ns$[3/2]_1$, nd$[1/2]_1$ and nd$[3/2]_1$ basis wave functions should appear in the Stark absorption spectra. The simulated spectra in the wavenumber region of 112 220 - 112320 cm^{-1} are shown in Fig. 16 for M=0 and M=±1, together with the observed spectra. The absorption line positions in the simulated spectra are qualitatively in good agreement with the measured ones.

However, the calculated absorption intensity does not reproduce the observed one very well. This is partly because no parameter for absorption profiles has been taken into account in the present simulation.

Further analysis of these spectra is now underway.

K. Ito

Auger-Electron—Photoion Coincidence Studies of Small Molecules

Recently, ionic fragmentation processes following inner-shell excitation in molecules have been a topic of much interest with developments of experimental techniques related to synchrotron radiation. Once an inner-shell electron of a molecule composed of light elements is ionized, Auger decay takes place replacing the inner-shell hole with two outer-shell holes. The doubly-charged molecular ion generated by the Auger decay dissociates into various products depending on the specific valence-hole configuration. To understand the dissociation processes of the core-excited molecules, it is therefore indispensable to elucidate the relation between the Auger decay process and the dissociation pathway.

As a typical example for Auger-electron—photoion coincidence (AEPICO) measurements, the results for SiF_4 are presented here. Figure 17 shows the Si-*LVV* Auger spectrum of SiF_4 excited by 130 eV photons. The peaks A and B in Fig. 17 correspond to Auger transitions, the final states of which have two holes in the inner valence orbitals. The peaks D and C are caused by Auger transitions to the two-hole final states, with one of the holes being in the inner valence and the other in the outer valence orbital. The peaks E and F are attributable to Auger transitions to the outer-valence two-hole states. The double structure of each group is caused by hole-hole interaction. The peaks A, C, and E correspond to final states, having two holes in the same Si-F bond (localized-hole states), while the peaks B, D, and F correspond to final states having two holes in different Si-F bonds (delocalized-hole states). In the present work, the localized-hole and delocalized-hole states were not sufficiently resolved for measuring coincidence spectra.

Figure 18 shows TOF mass spectra of SiF_4 taken in coincidence with the Auger electrons. The top spectrum (a) in Fig. 18 was obtained in coincidence with the peaks A and B in Fig. 17. The middle spectrum (b) was taken in coincidence with the peaks C and D, and the bottom one (c) in coincidence with the peaks E and F. A photon energy of 145 eV was selected for obtaining the spectra (b) and (c).

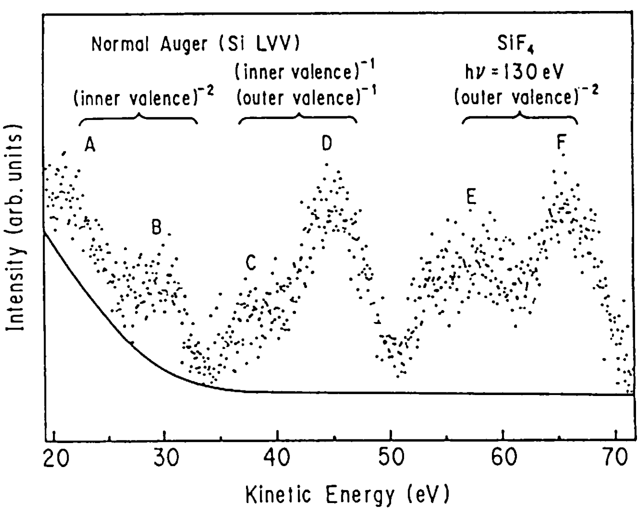

Fig. 17 Si-LVV Auger spectrum of SiF_4 excited by 130 eV photons. Dots and solid line represent data points and background, respectively.

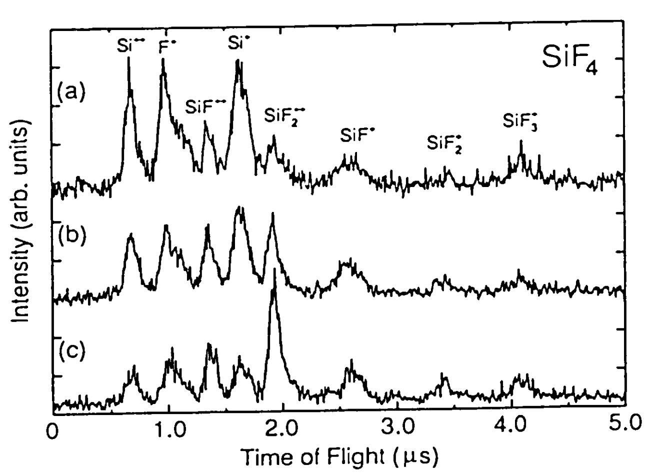

Fig. 18 Fragment ion spectra of SiF_4 taken in coincidence with Auger electrons having kinetic energies ranging from 18 to 34 eV (a), 35 to 50 eV (b), and 52 to 68 eV (c).

To avoid overlap of the Si 2p photolines and Auger lines, a photon energy of 180 eV was used for spectrum (a). These spectra are normalized to each other at the peak of the SiF^+ ions in order to see the differences of the fragmentation patterns. As is clearly seen from Fig. 18, the fragmentation patterns strongly depend on the Auger final states.

Spectrum (c) indicates that fragmentation from the outer-valence two-hole states considerably yields the molecular ions, while spectrum (b) indicates that additional dissociation channels generating the atomic ions open in the fragmentation from the outer-valence one-hole, inner-valence one-hole states. In contrast to spectrum (b), the strong enhancement of the atomic ions of Si^+, F^+, and Si^{2+} are clearly observed in spectrum (a). Spectrum (a) may suggest that the binding energy of the inner-valence two-hole states is above the threshold energy for triple ionization.

E. Shigemasa

High-Resolution Soft X-ray Spectroscopy of Free Molecules

The inner-shell spectra of free molecules have been intensively studied over the past twenty years. However, the inner-shell spectra have not been thoroughly investigated due to a limited energy resolution. The development of soft X-ray synchrotron monochromators promises to revitalize this research field.

We have measured K-shell photoabsorption spectra of small molecules, including carbon, nitrogen and oxygen at BL-2B. This beamline has a 10-m grazing-incidence monochromator (10-m GIM) combined with a 60-period soft X-ray undulator. It is difficult to determine the resolution of the monochromator, because the natural linewidth of the O K-shell is not known. However, a comparison with all the available high-resolution spectra of the oxygen molecule reveals that the achieved resolving power of the 10-m GIM is more than 10000 at the O K-edge. The rich structure of the spectra, which were revealed by the high-resolution 10-m GIM, have been identified with the help of *ab intio* SCF-CI and frozen-core calculations. As a typical example from a lot of experimental data, Fig. 19 shows the oxygen molecule absorption spectrum in the region of the O 1s → Rydberg excitation.

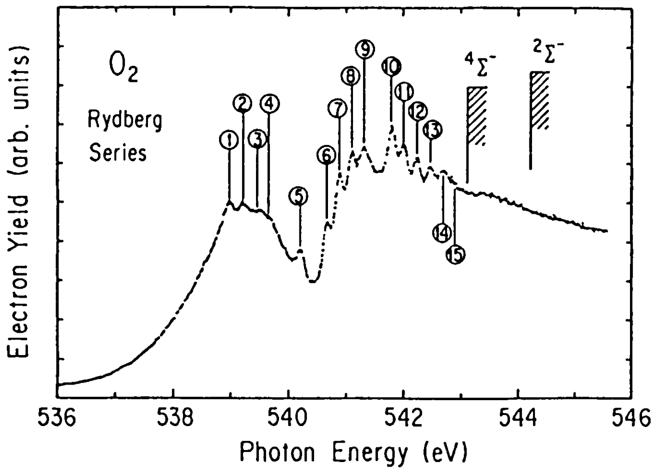

Fig. 19 High-resolution electron-yield spectrum at the O K-edge of O_2. The Rydberg transitions are observed in the 1s $\rightarrow$ 2pσ^* resonance region.

Many Rydberg transitions 1-15 converging to the $^4\Sigma^-$ and $^2\Sigma^-$ ionization thresholds are found on the 1s $\rightarrow \sigma^*$ resonance, but above the $^4\Sigma^-$ threshold the Rydberg series converging to the $^2\Sigma^-$ shows only a broad band. The 1s $\rightarrow$ 3sσ, 1s $\rightarrow$ 3pπ and 1s $\rightarrow$ npσ (n=3,4...) Rydberg series are predominatly observed. In contrast to the core-to-Rydberg transitions, the core-to-valence (1s $\rightarrow \sigma^*$) excited state at ~ 539.5eV related to the $^2\Sigma^-$ spin coupling is lower in energy than the 1s $\rightarrow \sigma^*$ state at ~542eV related to the $^4\Sigma^-$ one.

This result on oxygen molecules will appear in a journal. The other results of the series of high-resolution spectra will be published next year.

A. Yagishita

Surface Structure Analysis by the Back-reflection X-ray Standing-Wave Method

At Photon Factory, the structure of metal surfaces with adsorbates has been studied by surface XAFS and the back-reflection x-ray standing wave (BRXSW) method. In the BRXSW experiments, standing wave (SW) absorption profiles are measured in back reflection (normal incidence) geometry using soft X-rays of several Å, and the position of adsorbate atoms relative to lattice planes can be determined. Recently, a new apparatus for BRXSW has been constructed where a windowless Si(Li) solid state detector measures soft x-rays emitted under grazing conditions. We have applied this apparatus to structure studies of metal surfaces using highly-monochromatized soft x rays at the undulator beamline BL-2A.

Figure 20 shows typical pulse-height spectra of the SSD for the soft x-ray yield from c(2×2)S/Ni(100). For the normal-incidence 200 reflection (upper half), a spectrum measured previously with a gas-flow proportional counter (PC) at BL-11B is also shown for comparison. The energy resolution is much improved so that the sulfur K fluorescence can be separated completely from other fluorescent or scattered X-rays. Scattered X-rays are mostly suppressed by the grazing-emission geometry at any incidence angles. The lower half of Fig. 20 shows a pulse-height spectrum for the normal incidence onto the 111 reflection plane which is inclined by 55° with respect to the (100) crystal planes. We have measured SW absorption profiles of the sulfur fluorescence from c(2×2)S/Ni(100) at the two Bragg conditions and confirmed the surface structure studied before, which demonstrates the high reliability of the BRXSW method. The detailed description of another application to the study of adsorption site selectivity in the system of chlorine on Ni(111) is also reported in this volume.

Y. Kitajima

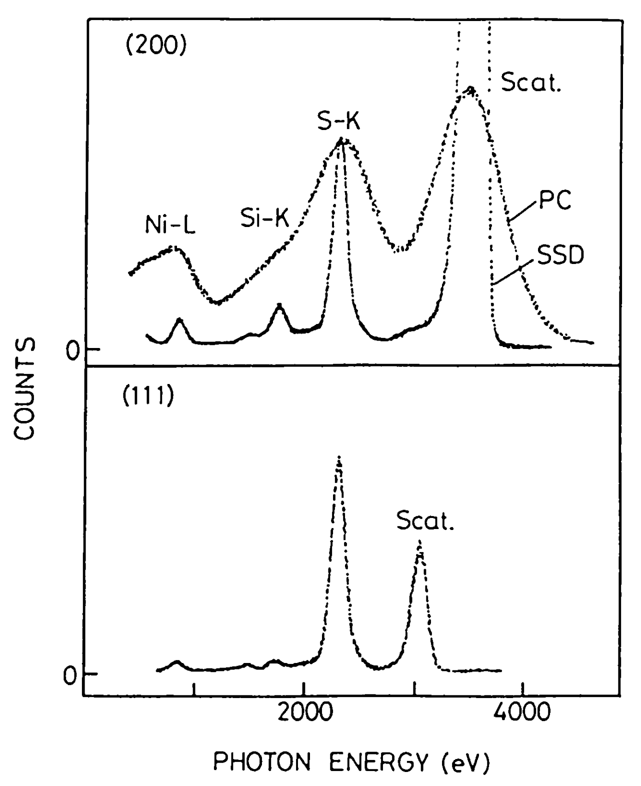

Fig. 20 Pulse-height spectra from c(2×2)S/Ni(100) at Ni 200 and 111 Bragg reflections.

Applications of an X-ray Phase Retarder

Dynamic X-ray diffraction theory leads to unequal dispersion relations for σ- and π-polarization components. This diffraction dichroism opened up the possibility of making an X-ray phase retarder using a perfect crystal, in which the dynamic diffraction is dominant. The first attempt in this direction was made by using the Laue geometry[1], but the great capability of the Bragg geometry was recently realized[2]. For the forward diffraction of a thin perfect crystal in Bragg geometry, the phase shift between both polarization components is a function of the deviation angle from the exact Bragg condition. The sign of the phase shift can be changed by changing the sign of the deviation.

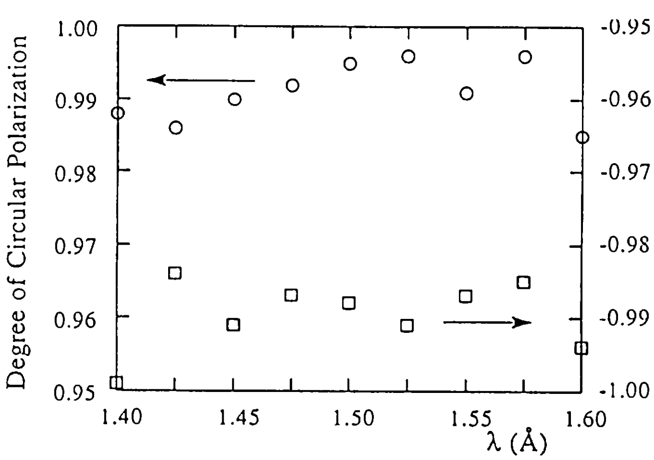

Fig. 21 Maximum values of the degree of circular polarization (P_C) obtained with the x-ray phase retarder. Open circles correspond to right-handed circular polarization and open rectangles to left-handed. Between 1.40 and 1.60 Å, absolute values of P_C's are more than 0.98 for both right- and left-handed circular polarizations.

A perfect crystal phase retarder based on this principle was fabricated from a silicon wafer by masked chemical etching. Right- and left-handed circularly polarized x-rays were at first produced and observed at a laboratory source using CuKα[2] radiation. The wavelength tunability of this phase retarder was shown at BL-15C using a newly constructed multi-axis diffractometer[3]. The observed absolute values of the degree of circular polarization, Pc, exceed 0.98 in the wavelength range of 1.40-1.60 Å, as shown in Fig. 21[4].

The phase retarder developed here was applied not only to the production of high-quality circular polarization in the x-ray region, but also to the complete determination of the polarization states in the hard x-ray region. Since the phase retardation is a function of the deviation angle from the exact Bragg condition, the polarization analyses of the beams produced by controlled retardation give a set of equations which contain the amplitudes of the electric vectors for both polarization components, as well as the phase shift between them. The polarization ellipses at three wavelength values thus determined at NE1 of AR are shown in Fig.22[3,5].

A remarkable feature of the Bragg-case phase retarder is the fast switching capability of the photon helicities[3]. A bistable crystal oscillator driven by PZT was constructed, which set the deviation angles to those giving right- and left-handed circular polarizations. Gate signals synchronized to the crystal oscillation distribute the signals corresponding to both helicities to two different scalers, the timing chart of which is shown in Fig. 23. A maximum frequency of 100 Hz was achieved with a duty ratio of 0.2 for the bistable switching. At 30 Hz, a duty ratio of 0.6 was achieved. The polarization ellipses for both helicities at 30 Hz are shown in Fig. 24.

T. Ishikawa

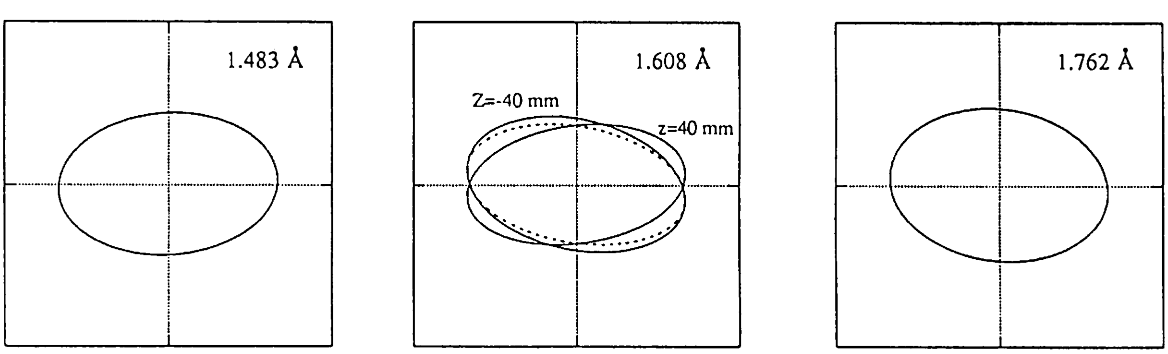

Fig.22 Polarization ellipses measured at the Elliptical Multipole Wiggler beamline of the TRISTAN Accumulation Ring. (a) λ=1.483 Å, (b) λ=1.608 Å; z=$\pm$40 mm correspond to phase differences of $\pm\pi/2$ between vertical and horizontal magnet arrays of the wiggler. The broken line shows a polarization ellipse when the helicity corresponding to z=40 mm is completely reversed. (c) λ=1.762 Å.

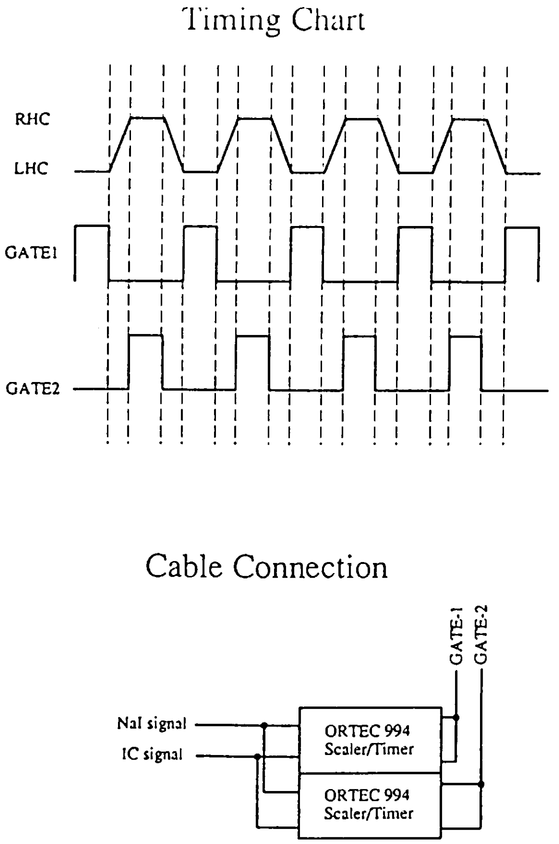

Fig. 23 Timing chart and data taking system for polarization switching diffractometry. Gate signals synchronized to right-handed circular polarization (RHC) and left-handed circular polarization (LHC) are supplied to scaler/timers.

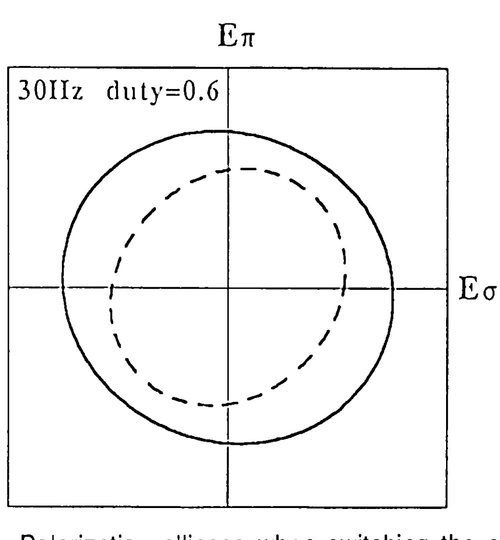

Fig. 24 Polarization ellipses when switching the photon helicities at 30 Hz. The solid and broken ellipses correspond to left- and right-handed circular polarizations, respectively. The X-ray wavelength was 1.463 Å. Estimated degrees of circular polarization are –0.996 and +0.989.

1) P.Skalicky and C.Malgrange; Acta Cryst., **A28** (1972) 501.
2) K.Hirano, K.Izumi, T.Ishikawa, S.Annaka and S.Kikuta; Jpn. J. Appl. Phys.,**30** (1991) L407.
3) T.Ishikawa, K.Hirano, K.Kanzaki and S.Kikuta; Rev. Sci. Instrum., **63** (1992) to be published.
4) T.Ishikawa, K.Hirano and S.Kikuta; J. Appl. Crystallogr., **24** (1991) 982.
5) K.Hirano, K.Kanzaki, M.Mikami, M.Miura, K.Tamasaku, T.Ishikawa and S.Kikuta; J. Appl. Crystallogr., **25** (1992) to be published.

Microcrystallography

It is essential to refine and to analyze the structure and/or texture of submicrometer-sized specimens in materials science. The smallest sample analyzed by X-ray diffraction was a fluorite (CaF_2) microcrystal with a volume of 2.2μm^3 at CHESS. A system for this purpose has been developed and it has been applied to some inorganic materials at PF by making use of synchrotron radiation employing the Laue method.

It is most important for analyzing a submicrometer-sized specimen to reduce the background to as low a level as possible. The use of a strong X-ray source such as SR is also indispensable. Because of the long time needed for collection of diffracted intensities and the differing diffraction geometries of the many kinds of apparatus in use, the Laue method with an imaging plate (Fuji Co., Ltd), a storage phosphor detector, was employed.

A new optical system, shown in Fig. 25, has been developed and installed in the Laue camera to reduce the background caused by the interaction of the polychromatic SR beam with the slit systems.

Software for reduction of the Laue reflection data and for structure refinement has been developed at PF and it has been applied to data from experiments on two molybdenum spheres (0.8μm in diameter, 0.27 μm^3 in volume, for both cases) and a 5μm chemical vapour deposited (CVD) diamond.

One of the molybdenum spheres was found to be twinned and the volume ratio of the twinned domains was determined based on fourteen Laue reflections. As well, the isotropic temperature factor (B) was found to be 0.08 (6)$Å^2$. This is to be compared with the value (B=0.07(4)$Å^2$) determined by the same powder chemicals by powder diffraction experiments. The refined volume of the smaller domain is 0.02 μm^3, which is beyond the resolution limit of an optical microscope.

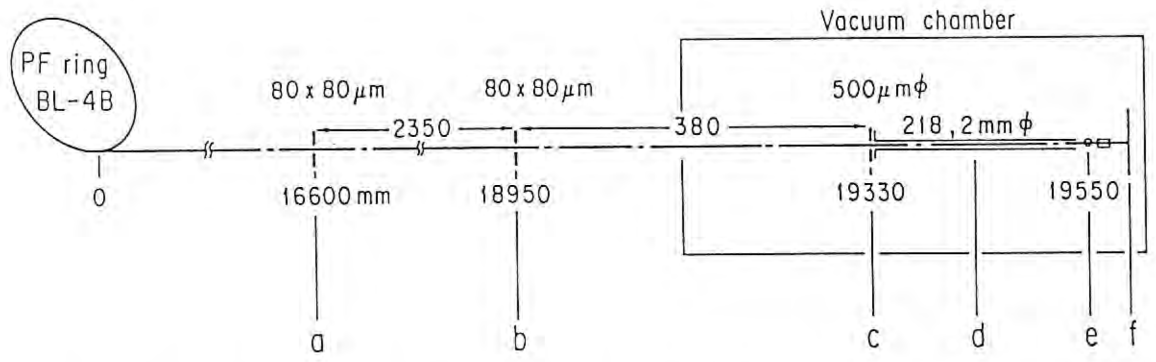

Fig. 25 Schematic drawing of the optical system to introduce white X-rays to the diffractometer. Letters a, b, c indicate first, and second slit, and pinhole, respectively. An aluminum tube is denoted by d. Sample and imaging plate are indicated by e and f, respectively. The numbers shown below the horizontal line are the distances from the source point.

The number of molybdenum atoms within the smaller domain is estimated to be less than 10^9. This experiment shows clearly that structure refinement of the twinned sample can be successfully carried out. The structure refinement of the other molybdenum sphere, whose scanning electron microscope image is shown in Fig. 26, was based on five Laue reflections and resulted in almost the same value (B=0.04Å^2).

A truncated icosahedral CVD diamond was found to be composed of 17 domains and the presence of the spinel twin type was confirmed in sixteen of the domains. The isotropic temperature factor was found to be 0.2(1)Å^2 by analysis of three Laue reflections from twin-free domains which had a volume of 0.08μm^3.

K. Ohsumi

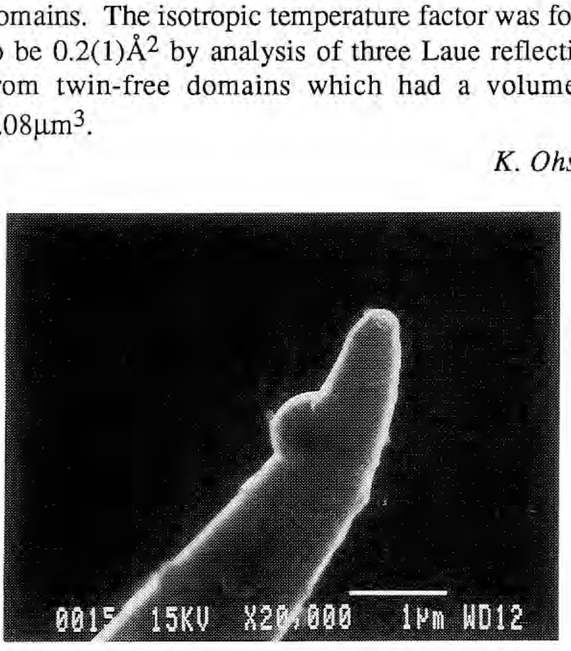

Fig. 26 SEM image of a Mo microcrystal attached to a thin glass fiber. The size of the sample is 0.8μm in diameter.

Dynamic Observation of the Secondary Recrystallization Process

The high brightness of synchrotron radiation makes possible the dynamic observation of changes in the microstructure of materials at elevated temperatures. Microstructural changes of silicon steel sheets in the secondary recrystallization process at 1233 K were observed by: (A) consecutive recording of the pole figure using a newly developed system consisting of a four-circle diffractometer and a translating Imaging Plate at BL-3A[1], and (B) real-time observation of Laue topographic pattern using two kinds of TV cameras at BL-15B [2].

Figure 27 shows schematically the experimental setup for the recording. Monochromatic X-radiation is used. The sample in the newly developed furnace is rotated by a certain angle, while an imaging plate moves synchronously with the sample rotation. A screen is placed such that reflected radiation from a specific crystallographic plane of the sample can reach the imaging plate. It takes only 40 s to record one pattern over an angle range of 10 deg in longitude of the surface of the sphere of poles. The change with time in the pole figure at high temperature is recorded by repeating the sample rotation while a long strip of the imaging plate is continuously translated.

Figure 28 shows that after a certain incubation period {110} <001> oriented grains grew at a burst. By applying tensile strain to the sample, growth of the {110} <001> oriented grains was appreciably delayed.

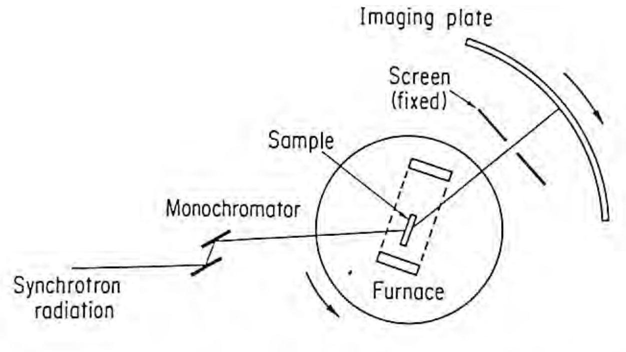

Fig. 27 Schematic layout showing the method of recording of a time change in the pole figure. The sample in the furnace repeats the rotation by a certain angle while a long strip of the Imaging Plate is continuously translated in the direction indicated by the arrow.

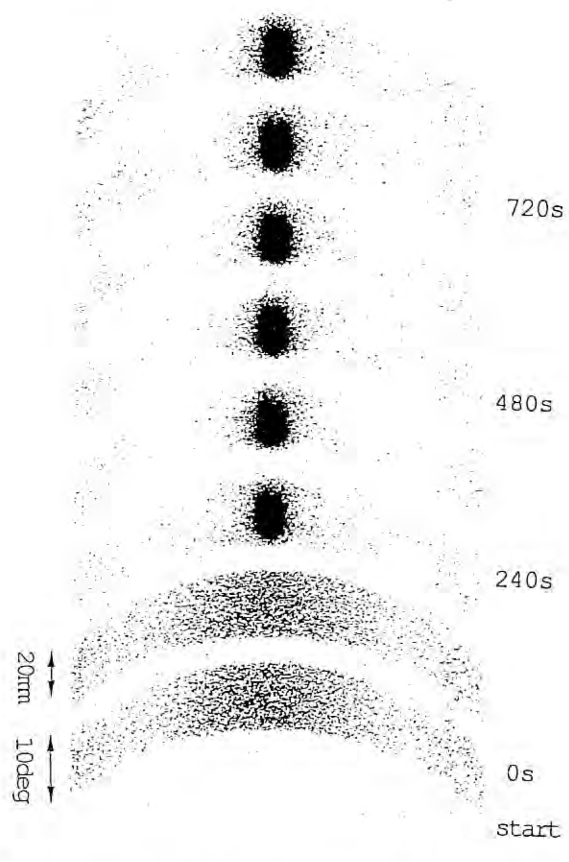

Fig. 28 Time change in the distribution of the [100] poles of the silicon steel sheet during the recrystallization at 1233 K. Each pattern shows the distribution over an angle range of 10 deg. around the North Pole of the sphere of poles. The time required to record one pattern was 40 s while the time interval between the patterns was 80s.

It was shown that synchrotron radiation combined with the imaging plate is a powerful tool for the dynamic observation of the microscopic mechanism of materials processing in industry.

By real-time observation of Laue topographic patterns, the time change in the size and shape of grains and competing processes of crystal grains were observed. In a magnified image employing the SATICON TV camera, the migration behavior of the recrystallization fronts was observed dynamically.

The method used here can be applied to the observation of, for example, a texture change in rolled sheets and extruded wires.

K. Kawasaki

1) K. Kawasaki, Y. Takagi, K. Nose, H. Morikawa, S. Yamazaki, T. Kikuchi and S. Sasaki; Rev. Sci. Instrum. **63** (1992) in press.
2) K. Kawasaki, H. Iwasaki, H. Kawata and K. Nose: Rev. Sci. Instrum. **63** (1992) in press.

E. SUMMARY OF EXPERIMENTAL STATIONS AND BEAMLINE OPTICS

Figure 29 is the latest plan view of the SR laboratory area of the PF experimental hall schematically showing the arrangement of the experimental stations now in operation or under construction. Table 3 summarizes the experimental stations in operation with the names of contact persons. The basic characters of X-ray beamlines are listed in Table 4. And the types of monochromators for VUV and soft X-ray beamlines are listed in Table 5.

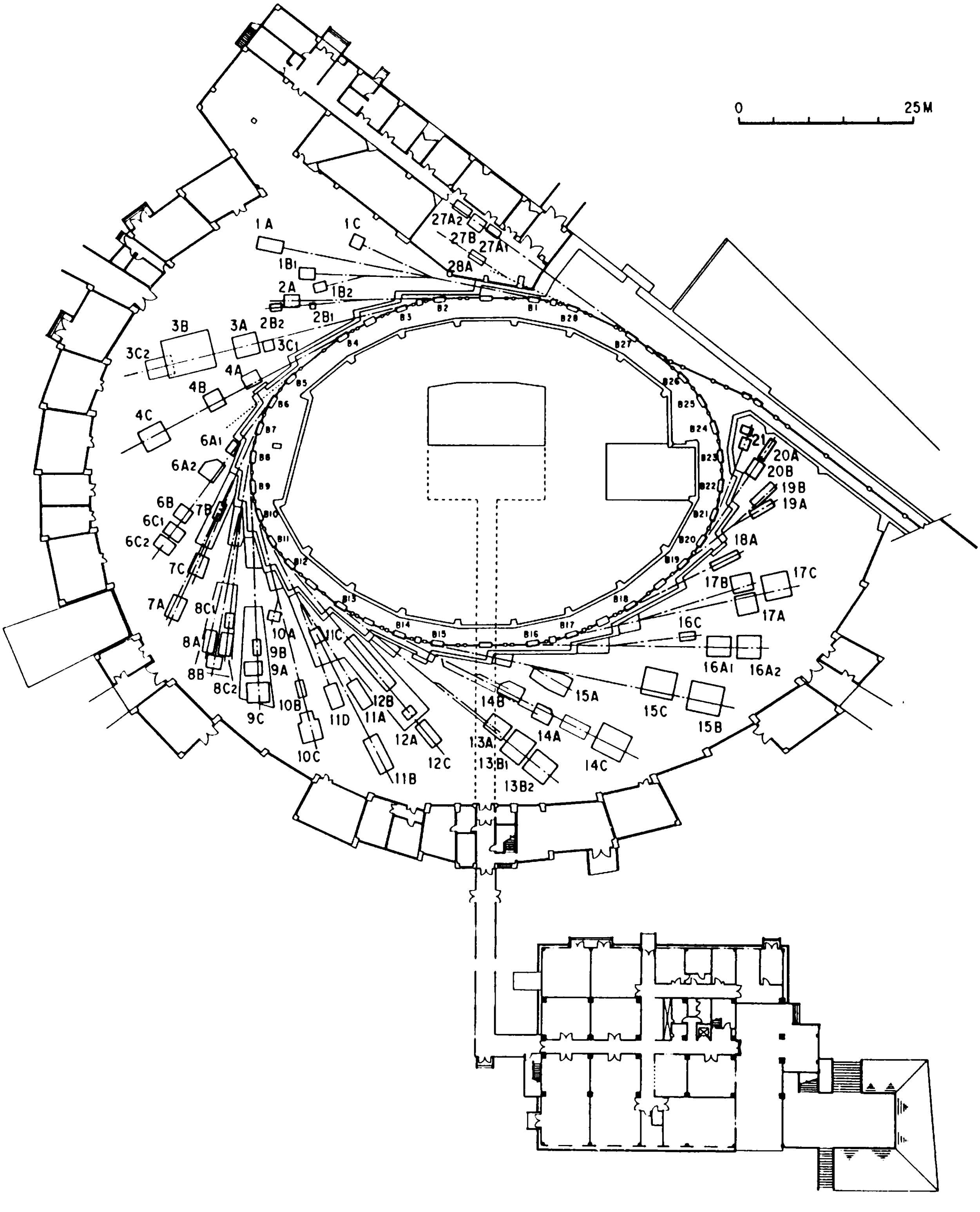

Fig. 29 Map of the experimental hall at the PF 2.5GeV storage ring.

Table 3. List of Experimental Stations

Experimental Station	Contact Person
BL-1 [NTT]	
A Solid surface analysis	M. Oshima
B X-ray lithography	H. Kinoshita
C Photochemical reaction	T. Urisu
BL-2 (Undulator)	
A Soft X-ray spectroscopy	Y. Kitajima
B1 Soft X-ray microscopy	A. Yagishita
B2 Soft X-ray spectroscopy	"
BL-3	
A X-ray diffraction and scattering	T. Matsushita
B VUV and soft X-ray spectroscopy	E. Shigemasa
C1 X-ray diffraction	T. Matsushita
C2 X-ray topography in milli-Kelvin region (for solid helium)	T. Nakajima
BL-4	
A Trace element analysis	A. Iida
B Liquid/melt structure analysis, powder diffraction, micro-crystal structure analysis	K. Ohsumi
C X-ray diffuse scattering, fluorescent EXAFS	S. Kishimoto
BL-6	
A1 Ultra small-angle X-ray scattering	M. Ando
A2 Macromolecular crystallography by Weissenberg camera	N. Sakabe
B X-ray spectroscopy and diffraction	M. Nomura
C1 X-ray diffraction at low temperatures	T. Nakajima
C2 Accurate lattice spacing measurement	M. Ando
BL-7 [The Research Center for Spectrochemistry, The Univ. of Tokyo]	
A Soft X-ray photoemission spectroscopy	H. Namba
B Surface photochemical reaction	"
[PF]	
C X-ray spectroscopy and diffraction	M. Nomura
BL-8 [Hitachi]	
A Soft X-ray spectroscopy	Y. Hirai
B EXAFS	A. Nakano
C1 X-ray lithography	K. Mochiji
C2 X-ray tomography and digital radiography	K. Usami
BL-9 [NEC]	
A X-ray lithography	K. Suzuki
B Photochemical reaction	I. Nishiyama
C EXAFS and X-ray topography/diffraction	J. Mizuki
BL-10	
A X-ray diffraction/scattering, crystal structure analysis	K. Ohsumi
B XAFS	M. Nomura
C Small-angle X-ray scattering of enzymes, surface diffraction	K. Kobayashi
BL-11	
A Soft X-ray spectroscopy	A. Yagishita
B Surface EXAFS, Soft X-ray spectroscopy	Y. Kitajima
C VUV spectroscopy (solid state)	H. Kato
D Angle-resolved photoelectron spectroscopy	"

Experimental Station	Contact Person
BL-12	
A VUV spectroscopy (gas phase)	K. Tanaka
B VUV high-resolution spectroscopy	K. Ito
C Photochemical reaction	K. Tanaka
BL-13 (Multipole wiggler/Undulator) [Research team for advanced materials*]	
A Accurate lattice parameter measurement	K. Nakayama
B1 Surface-sensitive XAFS, X-ray diffraction	H. Oyanagi
B2 High-pressure & high temperature X-ray diffraction	O. Shimomura
BL-14 (Vertical wiggler)	
A Crystal structure analysis of proteins, EXAFS	S. Kishimoto
B High-precision X-ray optics	X. Zhang
C General purpose (X-rays)	N. Watanabe
BL-15	
A Small-angle X-ray scattering of muscle and alloys	Y. Amemiya
B X-ray topography and interferometry	H. Kawata
C High-resolution X-ray diffraction	X. Zhang
BL-16 (Multipole wiggler/Undulator)	
X General purpose (X-rays)	T. Matsushita
U Soft X-ray spectroscopy	H. Kato
BL-17 [Fujitsu]	
A Characterization of crystals	S. Komiya
B Photochemical vapor deposition	Y. Nara
C X-ray lithography	S. Okamura
BL-18 [The Institute for Solid State Physics, The Univ. of Tokyo]	
A Angle-resolved photoelectron spectroscopy of surfaces and interfaces	A. Kakizaki
BL-19 (Revolver undulator) [The Institute for Solid State Physics, The Univ. of Tokyo]	
A Spin-polarized photoelectron spectroscopy	A. Kakizaki
B Photoelectron spectroscopy at various temperatures	"
BL-20	
A VUV spectroscopy	K. Ito
BL-21 [Light Source Division]	
Beam position monitoring	T. Katsura
BL-28 (Multipole wiggler/Undulator)	
U VUV and soft X-ray spectroscopy with circularly polarized undulator radiation	T. Miyahara

* National Laboratory of Metrology, National Institute for Research in Inorganic Materials, Electrotechnical Laboratory, National Chemical Laboratory, The Institute of Physics and Chemical Research

Table 4. X-Ray Beamline Optics

Beam Line	Acceptance Horiz. (mrad)	Beam Size (H × W) (mm)	Photon Flux at Sample Position	Type of Monochromator	Energy Resolution $(\Delta E/E)\times10^{-4}$	Photon Energy (keV)	Mirror
BL-3A	4	100 × 5 4 × 0.1		Double Crystal Si(111) Sagittal Focusing	~ 2	4 ~ 25	Collimating and Focusing Mirrors (Fused Quartz)
BL-3C1/C2	2	20 × 4		None		4 ~ 30	None
BL-4A	6	50 × 4 4 × 1		Double Crystal Sagittal Focusing	~ 2	4 ~ 20	None
BL-4B	4.5	50 × 5		Double Crystal Si(111)	~ 2	4 ~ 35	None
BL-4C	4	4 × 1		Double Crystal Si(111) Sagittal Focusing	~ 2	4 ~ 20	None
BL-6A1	0.1	10 × 3		Plane(111)	7.5	8 ~ 17	
BL-6A2	4	2.5 × 1		Bent Si(111) (a = 0, 6.0°, 7.8°, 9.5°, 11.4°, 13.7°, 16.5°)		5 ~ 25	Bent Plane Fused Quartz
BL-6B	4	8 × 1		Double Crystal Si(220), Si(111), Si(311) Sagittal Focusing with Si(111)	~ 2	4 ~ 25 (4 ~ 13)	None
BL-6C1	0.5	10 × 5		None		8 ~ 30	
BL-6C2	0.5	5 × 5		Channel-Cut Si (111)	7.5	8 ~ 12	None
BL-7C	4	8 × 1	1×10^{10}/6mm^2 (8 keV, 300 mA) (1×10^{11} when focused)	Double Crystal Si (111) Sagittal Focusing	~ 2	4 ~ 20 (4 ~ 13)	Double Mirror Fused Quartz Focusing
BL-8C1/C2	5	50 × 5	2×10^6/mA·mm^2 at 10 keV with Si (111)	Channel-Cut Si(220), Si(111), Si(400)	~ 2	5 ~ 40	None
BL-9A	5	25 × 25				1.2 ~ 3.1	SiC
BL-9C	5	150 × 5		Double Crystal Si(111) Sagittal Focusing	~ 2	5 ~ 25	None
BL-10A	1	10 × 3		Si(111), Si(220) Ge(111), InSb(111) Quartz(100), PG(002) Curved Si(111) (α ~ 4°, 8°)	50 ~ 5	5 ~ 25	None
BL-10B	2	8 × 1	1×10^9/7mm^2 (10 keV, 300 mA)	Channel-Cut Si(311)	1	6 ~ 30	None

Beam Line	Acceptance Horiz. (mrad)	Beam Size (H × W) (mm)	Photon Flux at Sample Position	Type of Monochromator	Energy Resolution $(\Delta E/E)\times10^{-4}$	Photon Energy (keV)	Mirror
BL-10C	4	6 × 1.5	~ 10^{10}/9mm^2 (8 keV, 100 mA)	Double Crystal Si(111)	2	4 ~ 10	Bent Cylinder
BL-13A	1			Double Crystal Si(220)	~ 0.1	4 ~ 30	None
BL-13B1/B2	4	4 × 1		Double Crystal Si(111), Si(331) Sagittal Focusing	~ 2	4 ~ 30	Bent plane Fused Quartz
BL-14A	1.28 (Vertical)	5 × 38		Double Crystal Si (111) Si (422) Si (553)	2	5.1 ~ 19.1 14.4 ~ 51.7 22.7 ~ 84.5	Bent Cylinder for Vertical Focusing, Pt-coated Fused Quartz
BL-14B	2.2	5 × 30		Double Crystal Si(111),Si(220),Si(311)	2	5.2 ~ 57	None
BL-14C	1.3	10 × 40		Double Crystal Si(111), Si(220)	2	5.5 ~ 69	None
BL-15A	2	0.7 × 0.8 at focus	9 × 10^{10}/6mm^2 (8.0 keV, 150 mA)	Curved Crystal Ge(111) ($\alpha = 8.0°$)	~ 10	5.6 ~ 12.4	Cylinder, Fused Quartz
BL-15B	0.14	5 × 5		None		3.5 ~ 34	None
BL-15C	2	60 × 6		Double Crystal Si(111)		4 ~ 30	None
BL-16A	4	4 × 1		Double Crystal Si(111) Sagittal Focusing	~ 2	4 ~ 35	Commissioned
BL-17A	4	100 × 10		Double Crystal Si(111)	~ 2	5 ~ 13	None
BL-17C	1	20 × 5		None		2	Quartz (plane)

Table 5. VUV and Soft X-ray Monochromators

Beamline	Acceptance Horiz./Vert. (mrad)	Type of Monochromator	Grating Groove density (l/mm)	Photon Energy (eV)	Beam Size (mm)	Typical Resolution ($\lambda/\Delta\lambda$)	Reference
BL-7B (RCS)	6 4	1m Seya-Namioka	1200 2400	5 ~ 45	1 × 1	1000	1
BL-11C	4.8 3	1m Seya-Namioka	1200 2400	4 ~ 30	~1 ϕ	1000	2
BL-12A	2.4 1.5	1m Seya-Namioka	1200 2400	4 ~ 35	~1 ϕ	1000	3
BL-12B	5 3.6	6.65 m Off-Plane Eagle	1200 4800	5 ~ 30	----	2.5×10^5	4, 5
BL-1A (NTT)	4 0.5	Grating/Crystal	1200 2400	50 ~ 900	4 × 1	500	6
BL-1B' (NTT)	1.2 4	Plane Grating	600 1200 2400	10 ~ 500	5 × 1	200	----
BL-1C' (NTT)	2 4	Plane Grating	600 1200	15 ~ 300		100	----
BL-2B2 Undulator	K = 0.55 ~ 2.2 λ_u = 6 cm	10 m Grazing Incidence α = 89°	1200 2400	250 ~ 1600	< 0.2 ϕ	500 ~ 5000	7, 8
BL-3B	10 2	Grazing Incidence R = 24 m $\alpha+\beta$ = 165°	200 600 1800	10 ~ 280	< 2 ϕ	200 ~ 3000	9
BL-7A (RCS)	6 1	Plane Grating	1200 2400	10 ~ 1000	2 × 1	500	10
BL-8A (Hitachi)	0.5 1	Varied-space Plane Grating	800 2400	40 ~ 1800	5 × 1	1000	11
BL-11A	1 0.5	2 m Grazing Incidence α = 88° Grasshopper Mark VII	600 1200 2400	40 ~ 1000	< 1 ϕ	200 ~ 2000	12
BL-11D	1.5 2	Grazing Incidence R = 2 m $\alpha+\beta$ = 154°	600 1200 2400	20 ~ 150	1.5 ϕ	100 ~ 1500	13
BL-12C'	3.8 1	Plane Grating	1200	50 ~ 690	7 × 15	100	----
BL-16U Undulator	K = 0.5 ~ 5.75 λ_u = 12 cm	2 m Grazing Incidence α = 87° Grazing Incidence	1200 2400 300	40 ~ 600	2 × 1	1400 ~ 2500	14

Beamline	Acceptance Horiz./Vert. (mrad)	Type of Monochromator	Grating Groove density (l/mm)	Photon Energy (eV)	Beam Size (mm)	Typical Resolution ($\lambda/\Delta\lambda$)	Reference
BL-18A (ISSP)	2 2	Grazing Incidence R = 3 m $\alpha+\beta = 152°$ R = 6.65 m $\alpha+\beta = 167.5°$	300 600 1200 500	7 ~ 150	< 1 ϕ	1000 ~ 2000	15
BL-19A Revolver Undulator (ISSP)	K = 1.0 ~ 9.0 λ_u = 16.4 cm	Grazing Incidence R = 2 m $\alpha+\beta = 160°$ R= 4 m $\alpha+\beta = 170°$	600 1200 600 1200	20 ~ 250	< 0.7 ϕ	1000	16
BL-19B Revolver Undulator (ISSP)	K = 0.5 ~ 1.25 λ_u = 5 cm K = 0.5 ~ 2.5 λ_u = 7.2 cm K = 1.0 ~ 5.0 λ_u = 10 cm	Varied-space Plane Grating	800 2400	10 ~ 1200	< 0.5 ϕ	1500	16
BL-28U Undulator	$K_x \simeq$ 0.5 ~ 3 $K_y \simeq$ 0.5 ~ 0.75 λ_u = 16 cm	Grazing Incidence R = 2 m $\alpha+\beta = 160°$ R = 4 m $\alpha+\beta = 170°$	600 1200 600 1200	15 ~ 280	< 0.5 ϕ	1000	----
BL-1A (NTT)	4 0.5	Grating/Crystal InSb (111), Si (111)	----	1800 ~ 4500	4 × 1	2000	6
BL-2A Undulator	K = 0.5 ~ 2.2 λ_u = 6 cm	Double Crystal InSb (111), Si (111)	----	1760 ~ 6000	< 0.5 ϕ	5000	8
BL-8B (Hitachi)	6 0.5	Double Crystal InSb (111), Si (111)	----	1700 ~ 14000	1.9 × 0.5	5000	----
BL-11B	4 0.6	Double Crystal InSb (111)	----	1760 ~ 3650	8 × 1	2000	17, 18
BL-1B (NTT)	1.2 4	Plane Mirror	----	----	5 × 1	----	----
BL-1C (NTT)	2 4	Toroidal Mirror	----	----	3 × 5	----	19
BL-2B1	K = 0.5 ~ 2.2 λ_u = 6 cm	Zone Plate	----	400 ~ 830	~ 0.01ϕ	50	20, 21
BL-9A (NEC)	5 0.3	Oscillating Mirror	----	----	----	----	22
BL-9B (NEC)	10	Plane + Toroidal Mirrors	----	----	15 × 20	----	22
BL-12C	3.8 1	Toroidal + Multilayer Mirrors	Rh - Si 21 Layers Rh - C 21 Layers	80 ~ 103 89 ~ 124	2 × 1	12 15	23
BL-17B (Fujitsu)	8 1	Toroidal Mirror	----	----	10 × 1	----	----

References

1. H. Namba et al., Rev. Sci. Instrum. **60**, 1917 (1989).
2. Photon Factory Activity Report 1982/1983, V-15 (1984).
3. Photon Factory Activity Report 1982/1983, V-17 (1984).
4. K. Ito et al., Appl. Opt. **25**, 837 (1986).
5. K. Ito et al., Appl. Opt. **28**, 1813 (1989).
6. T. Kawamura et al., Rev. Sci. Instrum. **60**, 1928 (1989).
7. H. Maezawa et al., Nucl. Instrum. and Meth. A**246**, 310 (1986).
8. H. Maezawa et al., Rev. Sci. Instrum. **60**, 1889 (1989).
9. A. Yagishita et al., Nucl. Instr. and Meth. A**306**, 578(1991).
10. H. Namba et al., Rev. Sci. Instrum. **60**, 1909 (1989).
11. M. Itou et al., Appl. Opt. **28**, 146 (1989).
12. M. Yanagihara et al., KEK Report 84-17 (1984).
13. T. Miyahara et al., Jpn. J. Appl. Phys. **24**, 293 (1985).
14. Y. Muramatsu and H. Maezawa, Rev. Sci. Instrum. **60**, 2078 (1989).
15. S. Suzuki et al., SRL-ISSP Activity Report 60 (1989).
16. A. Kakizaki et al., Rev. Sci. Instrum. **60**, 1893 (1989).
17. T. Ohta et al., Nucl. Instrum. and Meth. A**246**, 373 (1986).
18. M. Funabashi et al., Rev. Sci. Instrum. **60**, 1983 (1989).
19. T. Urisu et al., Rev. Sci. Instrum. **60**, 2157 (1989).
20. Y. Kagoshima et al., Jpn. J. Appl. Phys. **29**, L 172 (1989).
21. Y. Kagoshima et al., Rev. Sci. Instrum. **60**, 2448 (1989).
22. Photon Factory Activity Report 1988 # 6, I-13 (1989).
23. Photon Factory Activity Report 1988 # 6, I-11 (1989).

Super Light Source Project

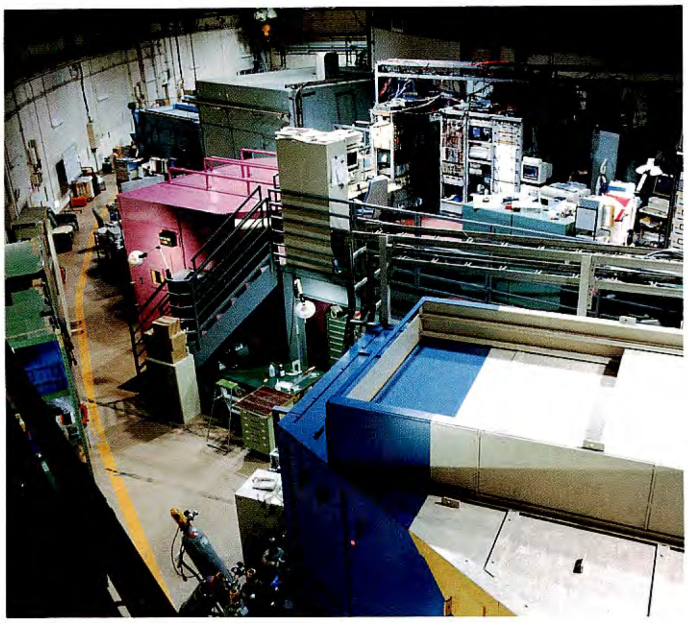

A complex of experimental stations in the SR utilization facility of the AR.

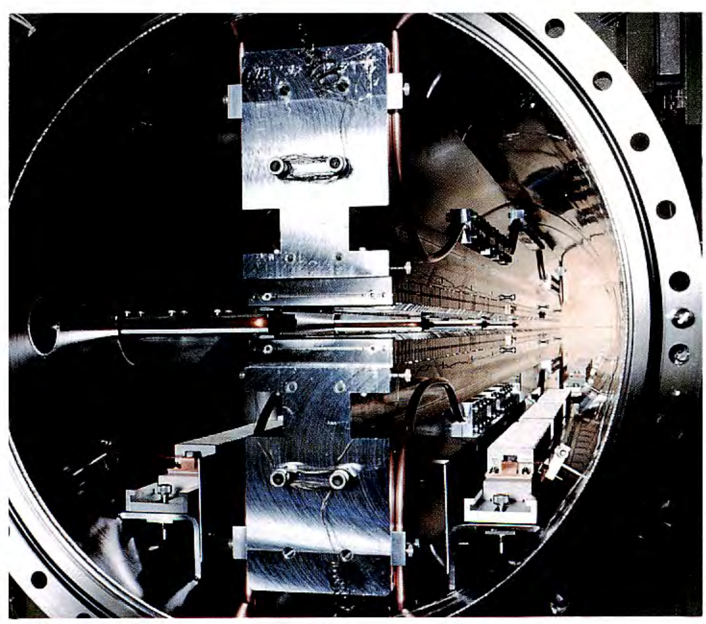

In side view of the in-vacuum type X-ray undulator for BL-NE3 in the AR.

You can jump to the article by clicking its title.

CONTENTS

SUPER LIGHT SOURCE PROJECT

A. INTRODUCTION

1. Present and Future SR Science to be Brought about by Utilizing the Tristan AR as a First-Generation Light Source and the Tristan MR as a Fourth-Generation Light Source

Owing to a foresighted decision made by leaders in the community of synchrotron radiation (SR) and the electron and positron accelerators in the early 80's at KEK, exploitation of the use of SR was ignited in 1985 as a joint programme between the Photon Factory (PF) and the Tristan Accelerator Department, when SR from the PF ring had not been long used. A quadrant of the circumference of the Tristan Accumulation Ring (AR) has been surrounded by an arc-shaped building which can accommodate five SR beamlines, at maximum. Its radiation shield wall has been designed so that SR from either electrons or positrons in the AR can be accepted and, further, two beamlines can be made which cross for photon-photon collision experiments at low photon energies if it is of great significance.

As a first step, a so-called test beamline (BL-NE5) was constructed in 1986. Because of the relatively narrow aperture of 10 mrad, two experimental stations have been built to share the machine time. Those were for an angiography project and for structure-change studies of a material embedded in a cubic anvil cell (called MAX80) for high-pressure, high-temperature environments. The typical machine parameters of the AR, such as 6.5 GeV as its accelerating energy and 22.3 m as the bending radius of its orbit, can provide a critical photon energy of 20 keV that is favourable for those both projects.

A budget approved in 1987 for two insertion device (ID) beamlines has resulted in a very progressive programme to use elliptically polarized SR (BL-NE1) at 40-70 keV, as well as a circularly polarized SR below 1 keV provided by a novel insertion device with not only a vertical, but also a horizontal, magnetic field which makes the electron orbit circular motion, and to use very brilliant quasi-monochromatic SR (BL-NE3) in the energy range 5-25 keV covered by the primary, third and fifth higher harmonics provided by another innovative in-vacuum ID. The former SR has now been in use since 1988 for the scientific programmes, such as magnetic Compton scattering, magnetic XAFS and magnetic circular dichroism (MCD), while the latter has been properly run since the very end of 1990 for a project involving Mössbauer nuclear Bragg scattering.

Further, after approval of an additional budget, a test beamline (BL-NE5) has been renewed, by which those stations can now be independently in operation and, thus, can virtually accommodate double scientific proposals. Another new bending magnet beamline (BL-NE9) for a pulse radiolysis experiment, characterization of x-ray optics elements under development and magnetic x-ray scattering experiments using linear polarized SR, is now under construction.

In order to help obtain higher energy x-ray photons, say above 25 keV, at the 2.5-GeV PF ring, a vertical superconducting wiggler had been invented to install, so that a spectrum with a critical photon energy of 20 keV would be available; the bending magnets can provide only 4 keV. The vertically fan-shaped SR beam of 9 mrad is shared among three equal aperture beamlines (protein crystallography, precision x-ray optics experiments and x-ray topography/high pressure experiments). An increased number of proposals regarding high-pressure experiments and a successful touch of imaging of a dog's coronary arteries by intravenous injection of a contrast material have accelerated the construction of the above-mentioned test beamline BL-NE5. The former requires high-energy x-ray photons to see high q-numbers, while the latter requires 10^{10}-10^{11} photons/sec/mm^2 at a heart with a beam size of 70 mm by 70 mm.

The very precious experiences in SR science, available exclusively at the AR which should belong to a first-generation ring, together with those available from the PF ring as a second-generation ring, had been planned to be transferred to a planned third-generation source --- a super PF ring at KEK; those are now to be brought by the PF users to another third-generation source in Japan --- SPring-8 in Harima which is now under construction.

Upon approval of its proposal, the PF promptly switched its future plan from construction of a new super PF to a conversion programme of the Tristan Main Ring (MR) into a fourth-generation light source without having incurred any delay. Owing to a great advance of the Tristan project for a high-energy physics programme, that community has made a decision that its physics programme will probably be finished in 1995 or 1996 at the latest, when the SR community will take over in order to start its conversion programme to welcome another advent of science by means of an extremely brilliant x-ray source. That generation will be defined in terms of an extremely brilliant source of the order of 10^{22} photons in a normal brilliance scale and a coherence which will be only completely produced by a free-electron laser. In order to achieve coherent radiation in the VUV and soft x-ray regions, and further in the far future in the x-ray region, the achievement of a very low emittance of the order of subnanometer radians should be an unavoidable factor to consider.

This Super Light Source Project was started as a part of the third phase of the Tristan Project in April 1991 to convert the MR into a fourth-generation light source. Further, that is in charge of managing the AR activity for SR utilization as well to perform a transfer of its associated technologies. In addition to one dedicated staff at present, four more new staffs will join that project in the near future. Both the groups and subgroups that are to be formed primarily on a voluntary basis to run the project will be assembled soon. The items to be developed by these people should be as follows: orbit analysis, magnets, electron monitors, RF cavities, vacuum engineering, beamline optics, optical axis monitors, control system, ID's, emittance measurement instrument, civil engineering etc. Naturally, budgetary and manpower request processes for the project are under way.

M. Ando

B. AR AS A SYNCHROTRON RADIATION SOURCE

1. Operation of AR for SR Experiments

The TRISTAN accumulation ring (AR), is a storage accelerator which accumulates electrons or positrons of 2.5 GeV and accelerates them to 8 GeV for transfer to the TRISTAN main colliding ring (MR). In the interval between the beam fillings in MR, AR is operated as an electron storage ring to provide SR to 3 beam lines (BL-NE1, -NE3 and -NE5). Two insertion devices, a multipole wiggler for circularly polarized SR for BL-NE1 and an in-vacuum X-ray undulator for BL-NE3, are installed in the ring. Table 1 shows the parameters of AR. Table 2 summarizes the operation statistics of AR during this year. A typical operation pattern of AR is shown in Fig. 1.

The operation energy for SR experiments was set at 6.5 and 5.8 GeV. Under 5.8 GeV operation, which accounts for about 15% of the total operation time, the vertical beam size was enlarged by putting the operating point near a coupling resonance for a coronary angiography animal experiment.

Table 1. Principal parameters of TRISTAN AR.

Energy	6.5 GeV, 5.8 GeV
Stored current	30 mA
Natural emittance	293 nm rad
Circumference	377 m
RF frequency	508.6 MHz
Bending radius	23.2 m
Energy loss per turn	6.66 MeV
Damping time	
horizontal	2.5 ms
vertical	2.5 ms
longitudinal	1.2 ms
Natural bunch length	18.6 mm
Momentum compaction factor	0.0129
Natural chromaticity	
horizontal	-14.3
vertical	-13.1

Table 2. Operation statistics of TRISTAN AR.

Ring operation time	3987.0 hr.
Net user time for SR use	2854.0 hr.
Time spend for MR injection & MR study	816.0 hr.
Others	194.5 hr.

The total current was limited to 30 mA at 6.5 GeV because some ceramic chambers were heated by SR to an intolerable level. They will be replaced during a short shutdown in January, 1992. The limit imposed on the total current will be relaxed to 60 mA at 6.5 GeV.

Through the whole operation period, AR was operated in the single-bunch mode since a current of 30 mA was easily stored in this mode.

After 30 ns from the main bucket a small number of electrons, 10^4 times less than those in the main bucket, were observed. Since these electrons produce serious noise signals in Mössbauer nuclear resonant scattering, they were removed by an RF kicker. The mechanism by which the electrons slip in is not yet understood.

The beam life was about 4-5 hours. A sudden shortening of beam life occurred about once or twice a day. It is speculated that this was caused by dust trapped by the electron beam.

A long-term-deviation of the position of SR beams was corrected by adjusting the closed orbit. The closed orbit immediately after tuning the beam position was stored in a file in the control computer. When the

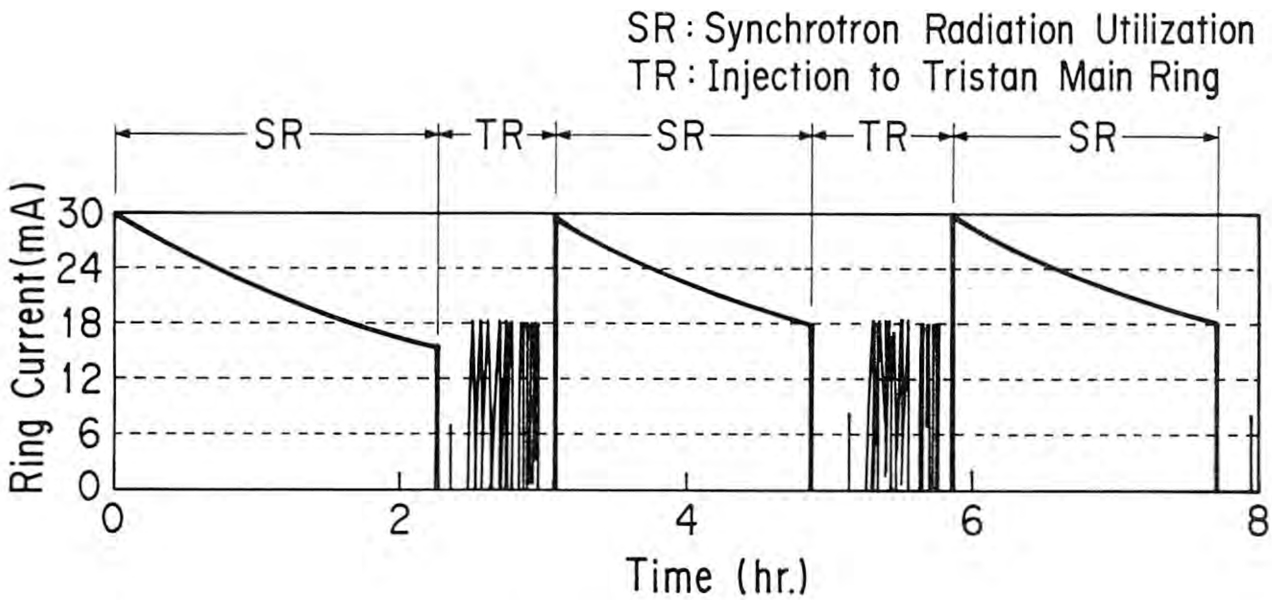

Fig. 1. Typical operation pattern of TRISTAN AR.

closed orbit deviated from the stored one, the difference between the deviated and stored orbits was corrected to restore the position of the SR beams.

H. Fukuma and K. Hyodo

2 Single-Bunch Purification

The study of Mössbauer nuclear resonant scattering (NRS) is under way in BL-NE3. In the incident photon spectrum, the band width of which is usually 10^{-1} eV in the hard X-ray region, only 10^{-7} eV contributes to NRS. Thus, the number of scattered photons through a nuclear process is 10^{6} times less than those through an atomic one. In spite of a large amount of background through atomic process, NRS can be separated from it by taking advantage of the different time response of the two processes to synchrotron radiation (SR) pulse. Photons scattered through the nuclear process appear in the range of several hundreds nanoseconds after an SR pulse, while those through the atomic process respond to it immediately. By measuring the photon spectrum in the time domain we can obtain all information concerning the hyperfine structures of matter, and determine the polarization of a photon or phase of a scattering amplitude from quantum beats.

AR is suitable for measurements of the time spectrum, since it is operated in the single-bunch

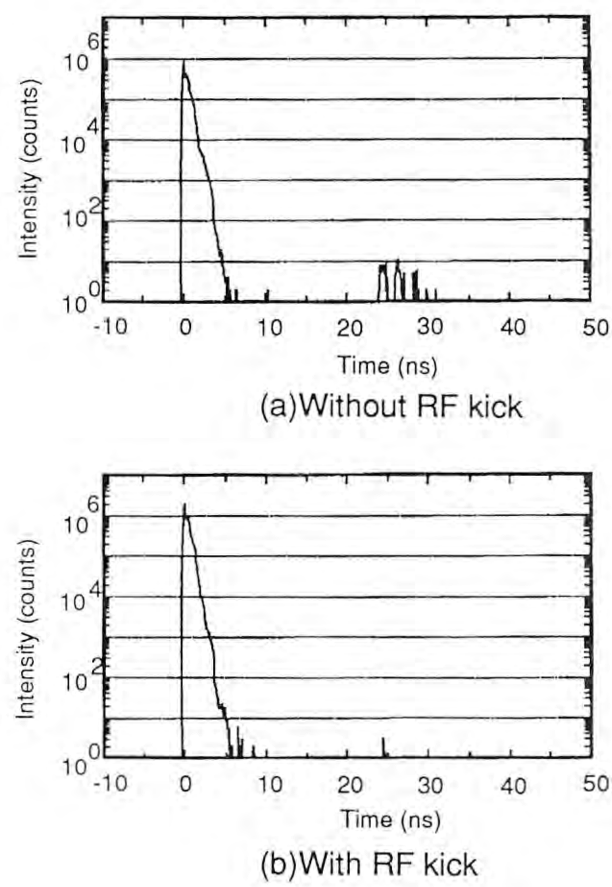

Fig. 2. Bunch profile with and without an RF kick.

mode. In an experiment at AR, since, the intensity of NRS photons in the time domain is about 10^5-times less than that of SR photons, electrons outside the main bucket should be 10^6-times fewer than those in the main bucket. A bunch profile was obtained from a distribution of the time difference between the RF and photon signals detected by an avalanche photodiode, which is located downstream of BL-NE3. One example of a bunch profile is shown in Fig. 2. The first bucket behind the main one contains electrons which amount to 1% of those in the main bucket; the second one is 0.001% of those. Furthermore, after 30 ns behind the main bucket there exist electrons, called satellite electrons, which amount to 0.01~0.001% of those in the main bucket. Among these electrons the satellite electrons are the most harmful, since they cause false signals.

To eliminate the satellite electrons we tried to kick them out using an RF kicker. If the frequency of the kicker is set to the betatron frequency of the electrons and the strength of the kick is large enough to overcome radiation damping, their oscillation amplitudes resonantly grow to the aperture of vacuum chambers and they are lost. As the raise time of the kicker is about 80 ns, it is difficult to adjust the timing to kick the satellite electrons without the loss of electrons in the main bucket. But, due to the wake field the coherent betatron frequency depends on the bunch current. If the frequency of the kicker is suitably selected, only cumbersome electrons are kicked out[1]. Figs. 2a and 2b are bunch profiles with and without an RF kick, respectively. These figures clearly show that the satellite electrons are removed by the RF kick. This method is being used in regular operation since this autumn.

H. Fukuma and X. Zhang

Reference
1) A. Hofmann, private communication.

3. Wide-Aperture Magnets for BL-NE9

Following BL-NE5, beamline BL-NE9 was under construction in 1991. A pair of a sextupole (SXD) and a steering (STV) magnets were replaced by new ones with a wider aperture so as to accept the synchrotron light from NE9.

The wide aperture sextupole magnet has the same bore radius as does the old one, but the coil slots are enlarged to make space for the synchrotron light orbit from NE9. As a result, the new sextupole magnet has a larger outer size than does the old one by about 80 mm. This sextupole, together with the other sextupoles, is connected to a power supply in series. The pole of the new sextupole was thus designed carefully so as to obtain the same field strength at each current. The mechanical and electrical parameters of the new sextupole magnet are listed in Table 3, and the mechanical dimension is shown in Fig. 3.

To accept a new vacuum chamber for NE9 line, the gap of the new vertical steering magnet was enlarged by 70 mm to 200 mm. The turn number of a coil is increased to 600 so as to keep as much field strength as the old one. The mechanical and electrical parameters and the mechanical dimension are shown in Table 4 and Fig. 4, respectively.

Field measurements of these magnets were achieved by a rotating coil. The old magnets were also measured as references. The output voltage from the probe was analyzed by an FFT device. The main field components are shown in Figs. 5 and 6, respectively, in comparison with the old ones. The results are satisfactory.

K.Egawa and K.Endo

Table 3. Sextupole Parameters (Design value)

Bore Radius (mm)	46
Core length (mm)	270
Weight (kg)	360
Conductor Size (mm^2)	6.5×6.5
Water Hole Diameter (mm)	3
Turns/Pole	32
Magnet Total Length (mm)	< 360
Max. Current (A)	100
Max. Field (T/m^2)	250
Resistance at 45°C (mΩ)	84.4
Inductance (mH)	22.1
Voltage (V)	8.4
Power (kW)	0.8
Water Flow (liter/min)	0.5
dT=30°C dP=5kg/cm^2	
No. of Water Circuit	2

Table 4. Steering Parameters (Design value)

Pole Gap (mm)	200
Pole Length (mm)	250
Turns/pole	600
Conductor (mm ϕ)	2.4
Max. Current (A)	10
Max. Field (Gauss)	> 350
Resistance at 75°C (Ω)	2.7
Weight (kg)	70

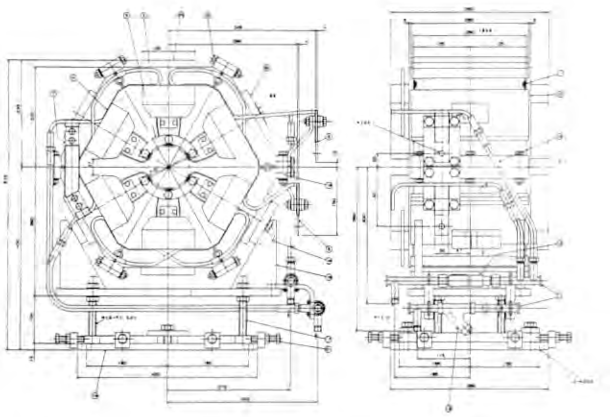

Fig. 3 Mechanical dimensions of the new sextupole magnet.

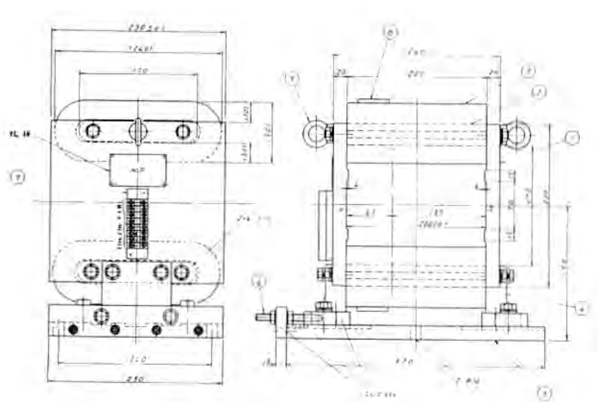

Fig. 4 Mechanical dimensions of the new steering magnet.

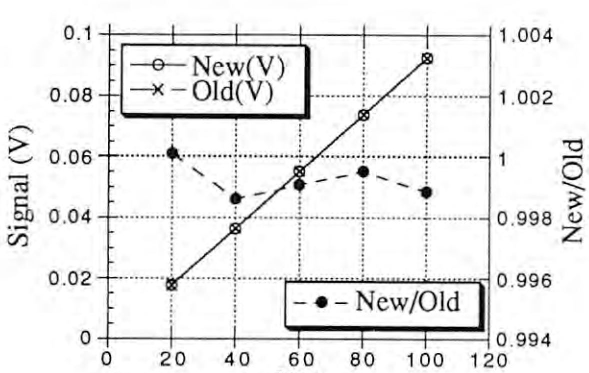

Fig. 5 Sextupole components of the new (wide aperture) and an old sextupole magnets are shown as a function of currents. The sextupole contents ratio of the new to the old is also shown.

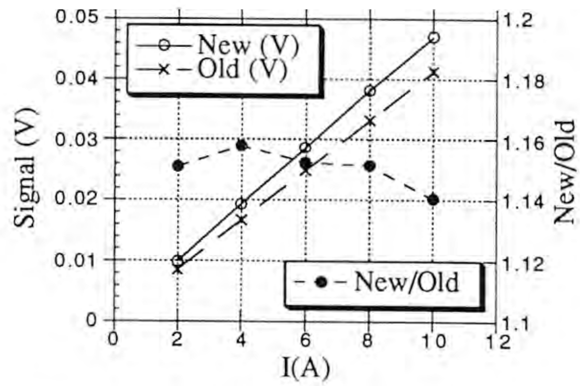

Fig. 6 Dipole components of the new (wide aperture) and an old steering magnets are shown. The ratio of the new to the old is also shown.

4. Test Trial of Low-Emittance Operation

There are two insertion device beamlines at the AR. One is for circularly polarized X-rays from EMPW#NE1, and the other is for undulator X-rays from U#NE3. The radiation properties of these insertion devices are largely benefited by low-emittance operation of the AR. We tried to reduce the emittance by reducing the dispersion function in normal cells, and to establish low-emittance operation.

Reduction of the dispersion function was achieved by increasing the horizontal phase advance from 90 to 145 degrees. The designed emittance at 6.5 GeV is 150 nm rad, which is 53% smaller than that in regular "normal optics" operation. The low injection rate was cured by increasing the horizontal beta function at the injection point. The maximum stored current was 33 mA, which is comparable to the current under regular operation. A beam of 30 mA was accelerated to 6.5 GeV without any beam loss. The measured dispersion function at 6.5 GeV agreed with the designed value.

The horizontal emittance (ε_X) has been estimated by a measurement of the horizontal source size (σ_S) of X rays from EMPW#NE1 at beamline BL-NE1. In a wiggler mode (K_y=15, and K_x=0), the horizontal source size can be expressed by

$$\sigma_s=(\varepsilon_x\beta_x)^{1/2}(1+L_1^2/4\beta_x^2)^{1/2}, \qquad (1)$$

where ε_x and β_x are the values of the horizontal emittance and β-function and L_1 is a length of EMPW#NE1 (L_1=3360 mm).

Figure 7 schematically shows the experimental arrangement used to measure the source size. Synchrotron radiation was limited by a horizontal slit

(0.2 mm wide), which was located at a distance of L_2 (L_2=38780 mm) from the center of EMPW#NE1. The angular spread of the incident X-rays through the slit (σ_b) is the convoluted value of the original angular divergence of the incident X-rays (σ_a) and the slit function (σ_{sl}). If we could measure the value of σ_b, we could estimate the value of σ_a, and finally obtain the value of the source size (σ_s) as follows:

$$\sigma_s = L_2 \cdot \sigma_a. \qquad (2)$$

In order to measure the angular divergence of X-rays, we used a double-crystal system, as show in Fig. 1. In the case of a (+,+) setting, the angular spread of the rocking curve gave the value of $2\sigma_b$. By taking the slit function into account, the final results are summarized in Table 5. The table shows the obtained values of the horizontal emittance at normal optics and under low-emittance operation at different β-functions. The obtained values are about 230 and 150 nmrad under normal and low-emittance operations, respectively; these are in a good agreement with those described before. Furthermore, we tried to measure the spectral profiles at an undulator mode in the normal optics and under low-emittance operation. The observed peak intensity of the first harmonic in the low-emittance operation is about three-times the high as that in the normal optics. This indicates the effectiveness and importance of low-emittance operation.

H. Kawata and H. Fukuma

Table 5. Result of an emittance measurement

	σ_s (nm)	β_x (m)	observed emittance (nm rad)
normal emittance operation	1.061	3.81	232
low emittance operation	1.022	6.38	149
	0.920	4.5	157

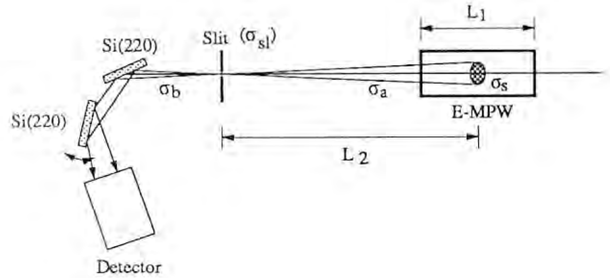

Fig. 7 Experimental arrangement used to measure the source size.

5. New In-vacuum Undulator for BL-NE3

A new undulator for the production of highly brilliant and quasi-monochromatic hard x-rays in the 5-25 keV region has been completed and installed[1] in the AR. This undulator (called U#NE3) was constructed for beamline BL-NE3,[4] in which Mössbauer experiments and interface/surface experiments were designed as primary subjects. We brought vacuum-sealed magnets into the vacuum chamber of the undulator. The aperture of this in-vacuum undulator for an electron beam in the AR can be changed so as to satisfy various requirements of AR operation. Thus, only when undulator x-rays are used, the desired strength of the magnetic field is obtained by closing the magnet gap.

The undulator consists of a pair of permanent-magnet arrays (the pure configuration; period length λ_u=4cm, a number of periods N=90), a vacuum chamber containing the arrays and a mechanical frame which controls the gap through bellows couplings (See the front page of this division). As a magnet material, we used Nd-Fe-B alloy with the remanent field of B_r=12kG and the coercivity of iH_c=21kOe (NEOMAX33SH manufactured by Sumitomo Special Metals Co. Ltd.), because of its magnetic performance and endurance against high temperatures for heating evacuation. Magnet blocks made of the above-mentiond porous material were plated with Ni (25μm thick) for a vacuum sealing. The available region of the magnet gap ranges from 5 to 1cm. The aperture of the undulator with the present vacuum-sealing method is almost equal to the magnet gap. This point is another advantage of the in-vacuum undulator. The magnetic field of U#NE3 ranges from 0.36G (when gap=5cm) to 8.2kG (when gap=1cm).

The vacuum chamber of U#NE3 (60cm (inner diameter)×410cm (length)) is evacuated with non-evaporable getter pumps and sputter ion pumps having a total speed of 4500 liter/s. The total surface area of the inside and of the contents in the chamber amounts to about 30×10^4cm^2, including the surface area of the magnets (3.7×10^4cm^2). In order to avoid problems caused from parasitic mode loss and to keep the wall current path continuous, we installed laminar sheets of stainless steel on both opposed faces of the magnet arrays, and placed contactors comprising many strips of stainless steel, which flexibly connect the end of the laminar sheet to the Q-duct of the AR.[1]

By adopting preparatory treatments for the magnets[1,3] the vacuum system of the undulator could be evacuated down to 7×10^{-11} Torr without any significant degradation of the undulator field during a bake-out (115°C) for an ultra-high-vacuum, as shown in Figs. 8 and 9. These are: (1) 200-°C baking (36hrs.) of the plated magnets before magnetization for degassing molecules adsorbed on the surface of the magnets during plating process and (2) 125-°C baking (48hrs.) of the magnets for "magnetic stabilization". Magnetic degradation under high temperature is inevitable,[4] even though the present magnets are highly durable against temperature. However, it can be negligibly small by a treatment carried out in advance at the same or higher temperature.

The undulator x-rays from U#NE3 were extracted successfully. More than 1.4×10^4 Mössbauer photons at 14.4keV per second have been produced[5] using the third-harmonic radiation from U#NE3 with K=1.47 and with 6.5-GeV and 30-mA operation of the AR. Figure 10 shows the result of a spectral characterization of the radiation from U#NE3 (K=1.47 and 0.3mA). The observed spectrum well compared with a theoretical calculation in an arbitrary scale, as shown in Fig. 10. In the calculation, taken into accounts are: the effects of the emittance and the energy spread an electron beam in the AR, and the absorption in the optical path. The discrepancy below 5keV is caused by absorption due to impurities in the graphite absorber and Be window.

S. Yamamoto

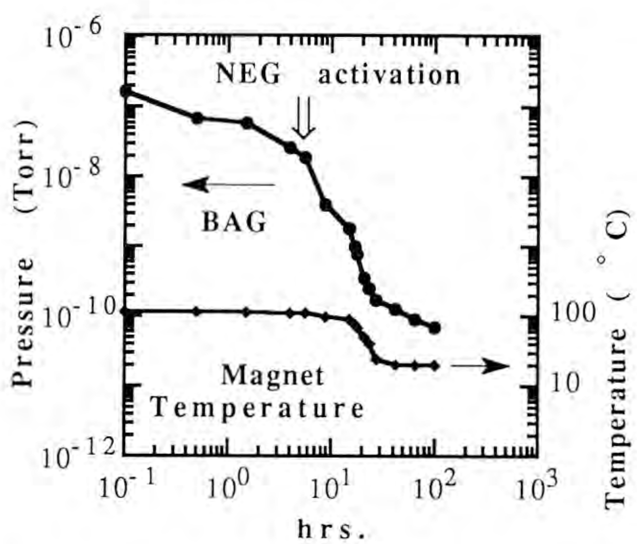

Fig. 8 Evacuation curve of U#NE3. NEG stands for non-evaporable getter pumps, and BAG does for a Bayard-Alpert gauge for pressure measurements. The temperature of the magnets is also shown.

References

1) S.Yamamoto et al., Rev. Sci. Instrum., to be published.
2) X.Zhang et al., Rev. Sci. Instrum., to be published.
3) S.Yamamoto, Photon Factory Activity Report 1989.
4) E.Hoyer et al., SPIE Proc. **582**, 84 (1985).
5) S.Yamamoto et al., in preparation.

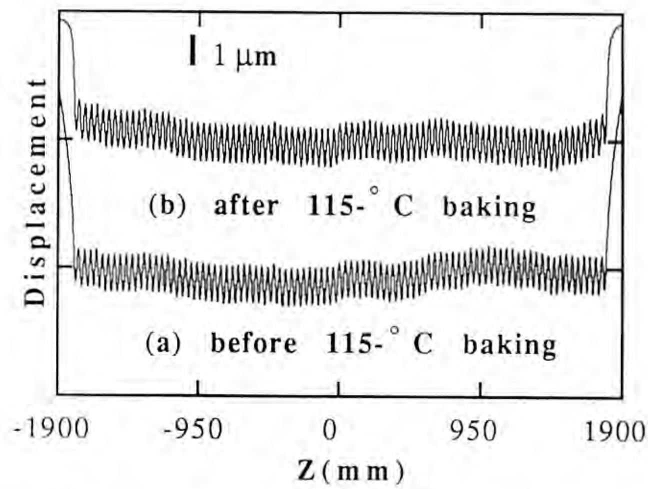

Fig. 9 Electron orbits (a) before and (b) after the 115-°C baking for ultra-high vacuum. The degradation of the undulator field which is expressed as a variation in the orbits is very small. Vertical bar represents 1mm of displacement.

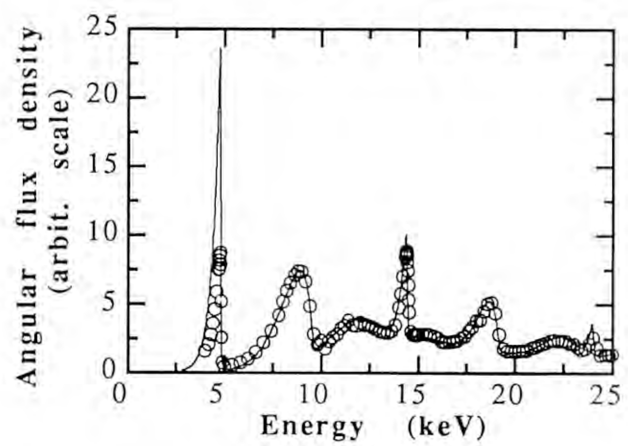

Fig. 10 A result of an on-axis observation of the undulator x-rays from U#NE3. The observation (circles) is compared with the calculated spectrum.

6. Specifications of the TRISTAN Accumulation Ring

This section summarizes principal parameters of a bend source and insertion devices and their calculated spectral performance.

Table 6. Calculated spectral performance of the bend source and insertion devices at the TRISTAN Accumulation Ring. E/I: beam energy and current, λ_u: period length, N: number of periods, L: length of undulator or wiggler, G_y (G_x): minimum vertical (horizontal) gap, B_y (B_x): maximum vertical (horizontal) magnetic field, P: pure configuration, H: hybrid configuration, $\sigma_{x,y}$: horizontal and vertical beam size, $\sigma_{x',y'}$: horizontal and vertical beam divergence, K_y (K_x): horizontal (vertical) deflection parameter, $\varepsilon_1/\varepsilon_c$: photon energy of the first harmonic (critical energy in the case of bend source or wiggler), $\Delta\varepsilon/\varepsilon$: relative bandwidth, Pc: degree of circular polarization, $\mathcal{D}$: photon flux in a unit solid angle (photons /s · mrad^2 · 0.1%b.w.), $\mathcal{B}$: brilliance (photons/s · mm^2 · mrad^2 · 0.1%b.w.), P_T: total radiated power, dP/d Ω: power in a unit solid angle. Different operation modes of a helical undulator and a wiggler are denoted by -H and -W, respectively

Name	Bend-NE5	EMPW#NE1	-W	-H	U#NE3	
E/I GeV/mA	6.5/50	6.5/50			6.5/50	
λ_u cm		16.0			4.0	
N		21			90	
L m		3.4			3.6	
G_y (G_x)		3 (11)			1.0	
B_y (B_x)		1 (0.2)			0.83	
Type of magnet		P (NdFeB)			P (NdFeB)	
σ_x mm	0.8	1.14			1.24	
σ_y mm	0.15	0.079			0.121	
$\sigma_{x'}$ mrad	0.45	0.14			1.24	
$\sigma_{y'}$ mrad	0.023	0.021			0.018	
K_y (K_x)			15 (1)	1 (1)	1.5	3.1
$\varepsilon_1/\varepsilon_c$ keV	26.3		28 (Pc=83%)	1.2 (Pc=97%)	4.68	
$\Delta\varepsilon/\varepsilon$				0.12	0.064	
$\mathcal{D}$	3.5×10^{13}		5.3×10^{14}	5.4×10^{15}	1.4×10^{16}	
$\mathcal{B}$	4.7×10^{13}		8.8×10^{14}	9.5×10^{15}	1.5×10^{16}	
P_T kW			4.5	0.04	0.78	3.3
dP/d Ω kW/mrad^2	0.38		5.6	0.49	8.95	35

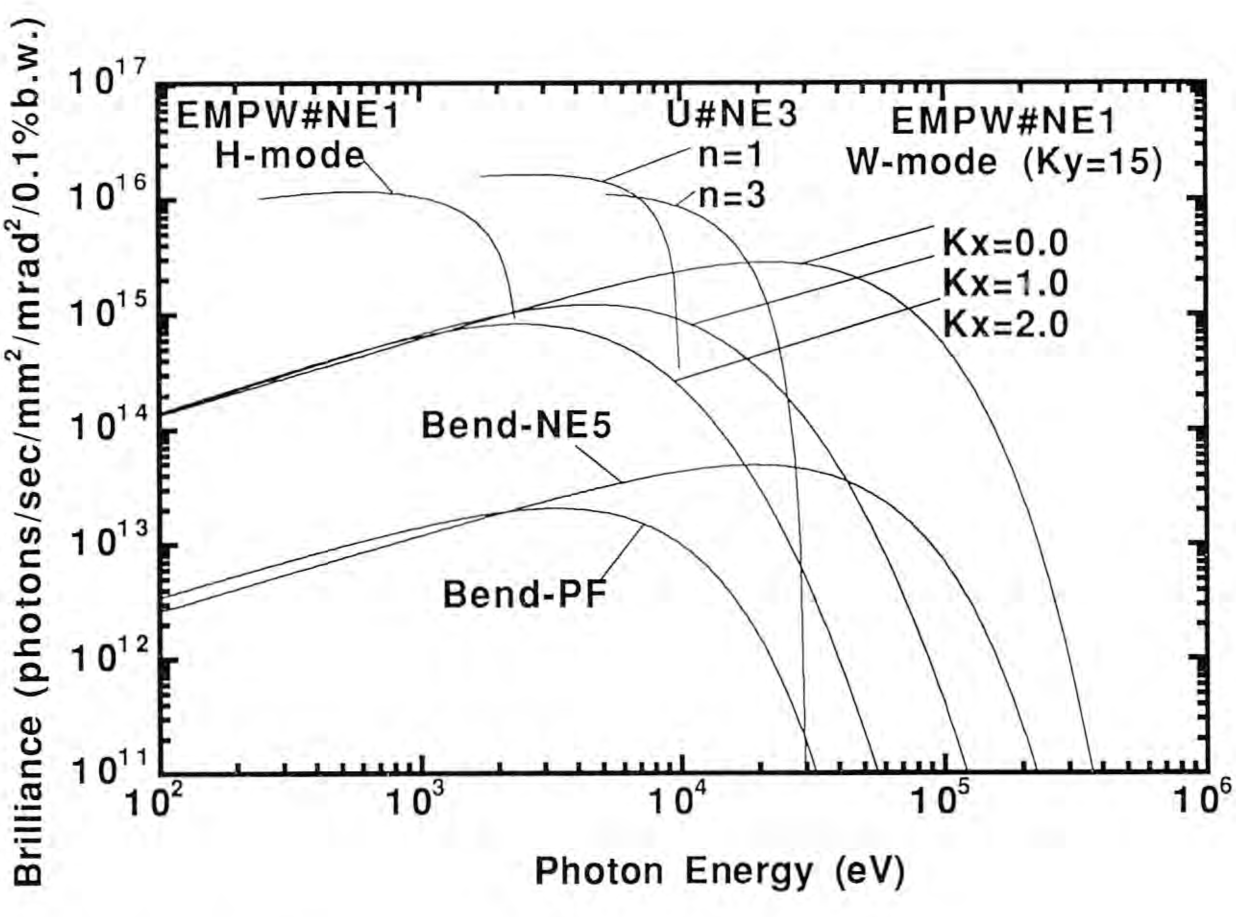

Fig. 11. Synchrotron radiation spectra.
Brilliance of radiation vs. photon energy for the insertion devices (EMPW#NE1 and U#NE3) and the bending magnet (Bend-NE5) of the AR. The name of each source is assigned in Table 6. EMPW#NE1 has both a helical undulator and a wiggler modes, which are denoted by H or W, respectively. The spectral curve of each undulator (or a helical undulator mode of EMPW) is a locus of the peak of the harmonics within the allowable range of K-parameter.

C. INSTRUMENTATION FOR SR EXPERIMENTS

1. Improvements of BL-NE1A2

The direct application of high-critical-energy synchrotron radiation to a double-crystal monochromator generates serious thermal problems not only in the first crystal. Since Compton scattered X-rays are divergent as 2π steradian from the first crystal, the second crystal and adjusting mechanisms must be cooled in order to avoid any degradation of the performance of the monochromator.

The double-crystal monochromator installed in BL-NE1 is located at the 32 m point from the multipole wiggler, EMPW#NE1. A holder of the second crystal has a bending system for sagittal focusing. We use a second crystal that is similar to that of the CHESS group.[1] A triangular shaped plate (1.2 mm thick of phosphor bronze) is backed by the second crystal; they are mounted on a water-cooled crystal holder. The second crystal, phosphar plate and crystal holder are in thermal contact with each other using a liquid Ga-In

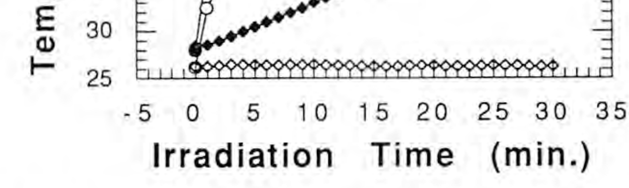

Fig. 12 Irradiation time dependence of the temperature of the second crystal.

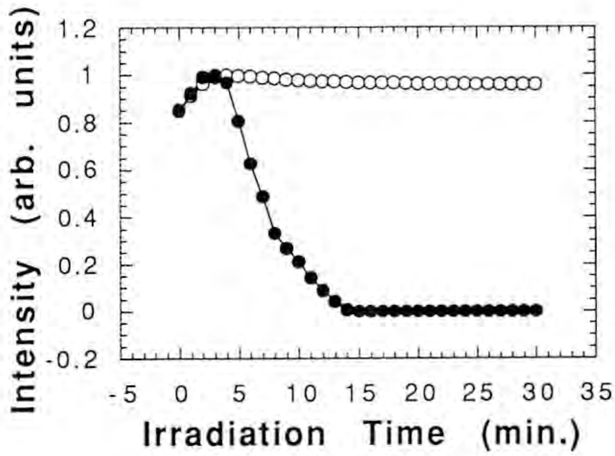

Fig. 13 Irradiation time dependence of the intensity of output beam normalized by the stored current. The open and closed circles are the normalized intensity in the case of cooling and without cooling, respectively.

alloy. The adjusting mechanisms of the second crystal are cooled indirectly by the water, and lead plates backed by water-cooled copper plates are placed between the mechanisms and the first crystal.

Figure 12 shows the irradiation time dependence of the temperatures of the second crystal (circles) and the adjusting mechanisms (squares) in the case of cooling (open marks) and without cooling (closed marks). Though the measuring point was far from the water-cooled holder, the increase in the temperature of the second crystal was stopped within 20 minutes in the case of cooling. The variation in the temperature in the adjusting mechanisms near the water tube was less than 0.3 degree with cooling.

The stability of parallelism between the two crystals can be estimated by the irradiation time dependence of the output beam intensity. Figure 13 shows the Si(111) diffraction intensity at θ_B=19° as a function of the irradiation time. The angle shift due to thermal expansion of the adjusting mechanisms in the case without cooling was larger than 20 arcsec, because Si(111) diffraction disappeared perfectly. That in the case of cooling was less than 2 arcsec. As a result, a highly stable monochromatized beam has presently been obtained.

T. Iwazumi

Reference

1) D. M. Mills, C. Henderson, and B. W. Batterman: Nucl. Instrum. Methods A**246**, 356 (1986).

2. Commissioning of BL-NE1B

An elliptically polarized synchrotron radiation source, EMPW#NE1, produces circularly polarized soft x-rays ranging from 250 to 1500 eV in its helical undulator mode. A beamline, NE1B, connected to the undulator was designed and built in 1988 to perform spectroscopic studies using circular polarization.

The optical layout of NE1B, including a monochromator, is shown in Fig. 14. It has two pre-mirrors, one of which is a water-cooled SiC plane mirror, M0, with platinum coating; the other is a variably bendable cylindrical SiO_2 mirror, M1, with a platinum coating. The grazing incident angle on the mirrors is 1.5°. A sagittal radius of curvature of M1 is 485 mm, which corresponds to a vertical focal length of 9.3 m.

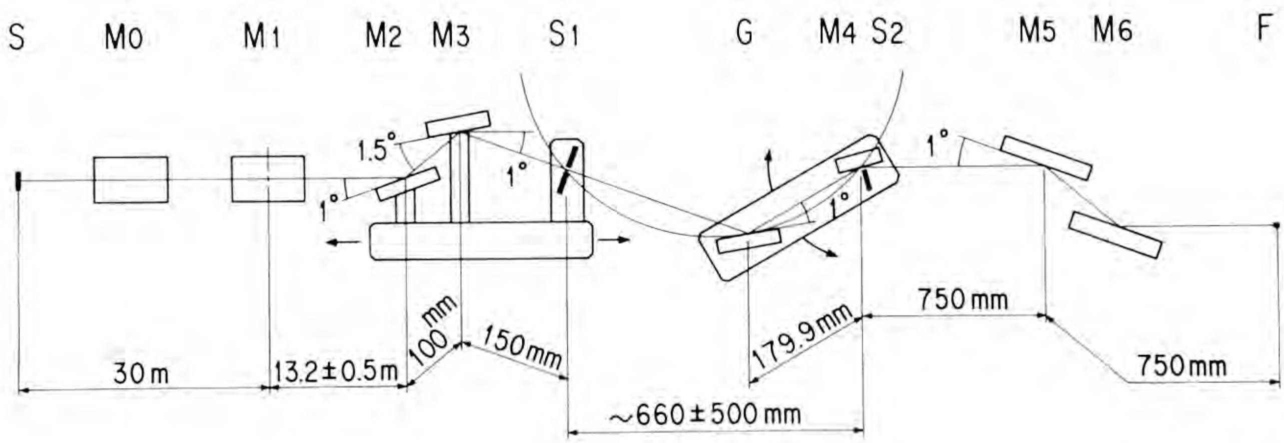

Fig. 14 Entire optical arrangement of beamline NE1B for circularly polarized soft x-ray undulator radiation.

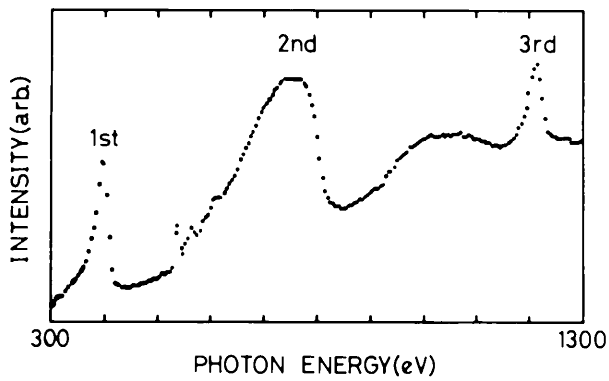

Fig. 15 Obtained spectrum of the elliptical undulator, where K_x=0.44 and K_y=3.14, respectively.

The monochromator takes a vertical dispersion and forms an inverse Vodar configuration. It has two pre-focusing concave mirrors, M2 and M3, with radii of curvature of 78 m, and a Codling mirror, M4, working as an exit slit. We have two spherical gratings with different groove densities, one of which is 1200 *lines/mm* and the other is 2400 *lines/mm*. They can be exchanged *in situ*. A radius of curvature of the gratings is 10.3 m. A negative first-order diffraction is employed with a constant exit angle of β=1°. The pre-focusing system is mounted in vacuum on a high-precision linear stage that is movable along the optical axis. Since the linear motion of the stage and the rotary motion of the grating can be made independently, Rowland's mounting can be easily realized by the tuning position of the stage and the angle of the grating by using a personal computer. A toroidal mirror, M5, is employed for post-focusing. An adjustable plane mirror, M6, is introduced for easy positioning of the output beam onto a sample.

A measured undulator spectrum from EMPW#NE1 is shown in Fig. 15. A characteristic profile of the undulator radiation is obtained, although the intensity of the first harmonic is weaker than expected from a calculation. Since an off-axis observation remarkably impairs important properties of the undulator radiation, such as brilliance and polarization, a determination of the beam axis must be made carefully. By using four-dimensional variable slits equipped just in front of M1, the relation between the observation angle and the undulator spectrum has been examined. A resolution test will be made by measurements of the absorption spectra of inert gases. Experiments to study the magnetic circular dichroism (MCD) of magnetic metals will also be made.

Y. Kagoshima

3. Improvements of BL-NE3

We have improved the monochromator crystal which was used in the beamline. As reported at SRI '91(Chaster, UK), we had not been able to obtain a sufficient photon flux from an in-vacuum undulator U#NE3, because of a mechanical deformation of the first crystal in the monochromator. The deformation was caused by the pressure of the water used for crystal cooling.

To prevent the deformation, we designed a new type of silicon crystal, as shown in Fig. 16. It is expected that the deformation would be decreased because of the reinforced rigidness of the crystal. We made off-line measurements of the rocking curves of Si (333) diffraction with Mo $K\alpha_1$ for both the old and new crystals, giving static air pressure in the water flow channel of the crystals instead of water pressure. The results are shown in Figs. 17 (a) and (b). When we increase the air pressure in the water flow channel, the Bragg angle of the diffraction shifts to the higher angle side. This means that the d-spacing of the silicon decreases with the pressure in the water channel. The newly designed crystal has exhibited better behavior in the angle shifts, reflexivities and rocking curve widths versus the pressure increase up to 2.5kg/cm^2.

We installed a new crystal in the monochromator for BL-NE3 and evaluated the ability of the improved monochromator using the X-ray optics of nuclear Bragg scattering (NBS). The obtained NBS signals (within a band width of $\Delta E \sim 10^{-7}$eV at 14.4keV) amounted to 1.85×10^4 cps with a storage current of

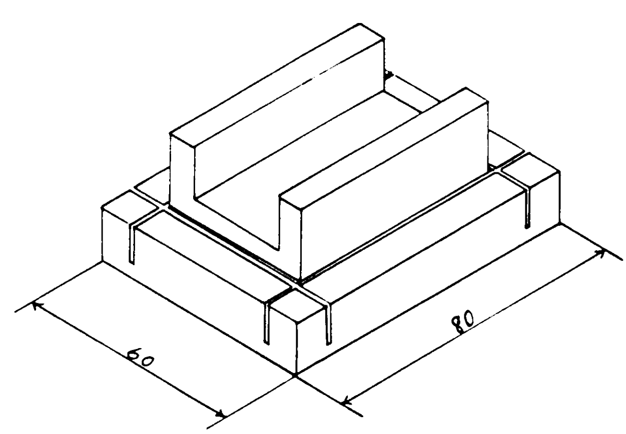

Fig.16 Newly designed first crystal of the monochromator. There are ten water flow channels in the rear of the crystal. Two ribs placed on the top of the crystal, prevent the deformation caused by the pressure in the water channels.

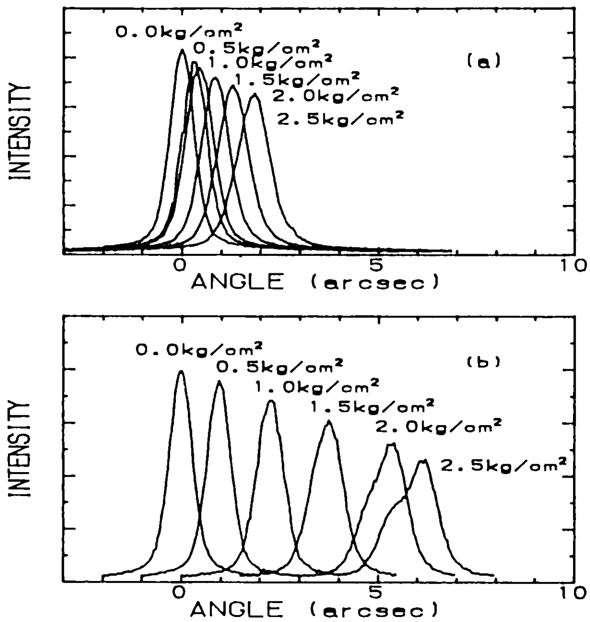

Fig.17 Rocking curves of silicon (333) with Mo $K\alpha_1$ vs. air pressures; (a) results for the new type, and (b) results for the old type.

22mA, which overcame the old champion data of 1.4×10^4cps with a current of 30mA.

For higher ability of the monochromator, we have started to design a cryogenic system for cooling the silicon first crystal of the monochromator.

X. Zhang

4. Construction of BL-NE9

Beamline BL-NE9 was built during the starting year of AR operation in 1983, and various vacuum experiments such as gas desorption from a vacuum chamber or a cold bore due to synchrotron radiation (SR) irradiation have been undertaken, mainly by the accelerator physicists at the Tristan Accerelator Group as well as by the graduate students in the course of Accelerator Science. Its beam aperture is around 10 mrad.

During the summer of 1991, a new radiation shield for its beamline was constructed to replace a slightly inconvenient and partly insufficient old one. The new one on a railway is removable as well as movable along the beamline so that one can change a sample chamber easily.

The bending vacuum chamber for this beamline was also changed into a new one similar to that at BL-NE5. This should be able to accommodate two beamlines, if needed, such as one with an aperture of 11.5 mrad at its center of 25.25 mrad, and the other with an aperture of 10 mrad at its center of 48.5 mrad. The present one is located at 24.4 mrad instead.

The layout of the present BL-NE9 is shown in Fig 18. That and its arrangement is different from a normal standard PF model. At the end flange for the 25.25 mrad line of the bending chamber, we have connected an off-center end flange to a vacuum pipe in order to fit it to the 24.4 mrad line. That flange is followed by a 10 cm thick lead block in a water-cooled aluminum container as a beam stop, an all-metal gate valve and a long vacuum beamline having NEG (non-evaporable getter) pumps and ion pumps.

Inside the experimental hall we have installed an adjustable collimator by which we can change both the width and height of collimated SR. Downstream this, we have also installed a manual all-metal gate valve for vacuum isolation, which is required while changing samples. At the very end of the beamline a chamber having a TMP (turbo molecular pump) with magnetic bearings, can accommodate sample pieces, and can be connected to a test chamber through an orifice. In front of and behind the orifice, two extractor gages are provided in order to measure the flow rate of desorbed gas through the orifice together with a quadrupole mass spectrometer.

In order to operate two branch beamlines simultaneously at BL-NE9, the design of a new beamline is under way as a joint project between the Tristan Accelerator Group and the Photon Factory. That fabrication will be completed some time in 1992; however, that will not be installed before the current study programme has been completed.

K. Kanazawa and M. Ando

5. Pulsed High-Field Magnet for Magnetic Scattering

It is interesting to investigate first- and second-order phase transitions in a spin structure induced by a high magnetic field. When we try to use a high magnetic field above 10 T for an X-ray magnetic scattering experiment, a superconducting magnet does not always fit for the purpose, because X-ray scattering experiments require a wide scattering angle geometry.

One of the promising solutions will be to use a pulsed high magnetic field under a repetition mode. The technique of a pulsed high magnetic field is well developed, and some applications have been reported in the field of neutron scattering experiments, using, for example, a 20-T magnetic field having a sinusoidal wave form with a 1-ms duration. An intense circularly

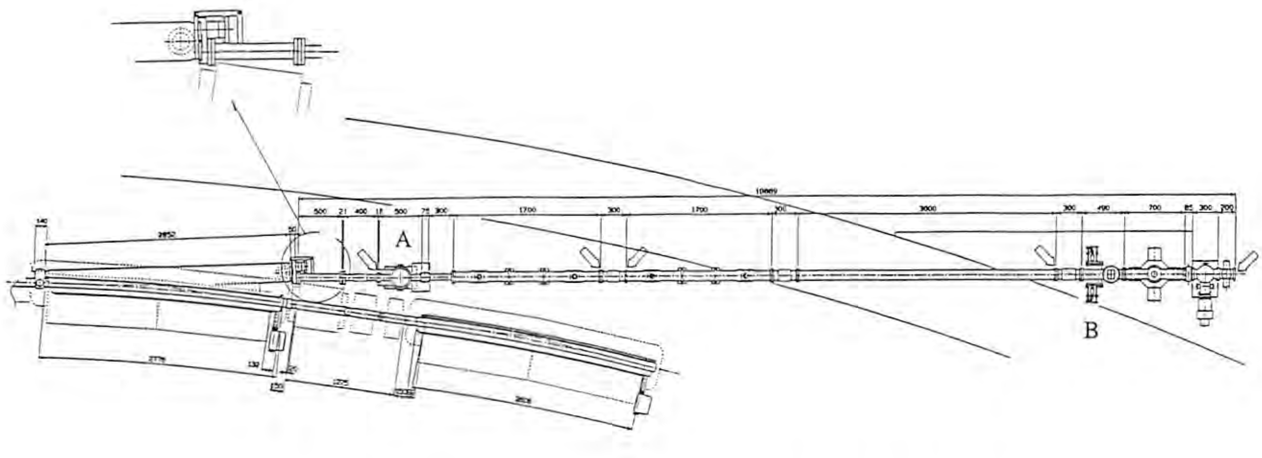

A : BEAM STOP B : ADJUSTABLE COLLIMATOR

Fig. 18 Layout of beamline BL-NE9

polarized X-ray flux of 10^{11} photons/s at the beam line of NE-1 of the AR synchrotron-radiation facility allows the use of such a pulsed magnetic field, in spite of the low yield rate of accumulation time. A magnet system has been designed for magnetic X-ray scattering experiments. It consists of a coil and a capacitor bank, whose specifications are given in Table 7.

The direction of the sequential pulsed current can be altered by a computer. The bank will be put outside of the AR building. The coil system placed at the beam line is connected to the bank through cables that are less than 20 m in length.

The intensity of scattered X-rays will be accumulated with a multichannel analyzer in the multiscale mode, in which the intensity is recorded as a function of time in coincidence with each start of a pulsed magnetic field. The facility will start operation next spring.

N. Sakai

Table 7. Specifications of the capacitor bank for the pulsed high field magnet.

Power	50 KJ, 1.2 mF
Wave from	half sinusoidal
Duration	1 ms
Repetition	1 Hz
Total inductance	less than 84 mH
Total resistance	less than 50 mW

6. Specifications of Experimental Stations

This section summarizes the experimental stations with the names of the contact persons (Table 8) and the beamline optics (Table 9). Figure 19 shows a plan view of the experimental hall of the Accumulation Ring (AR).

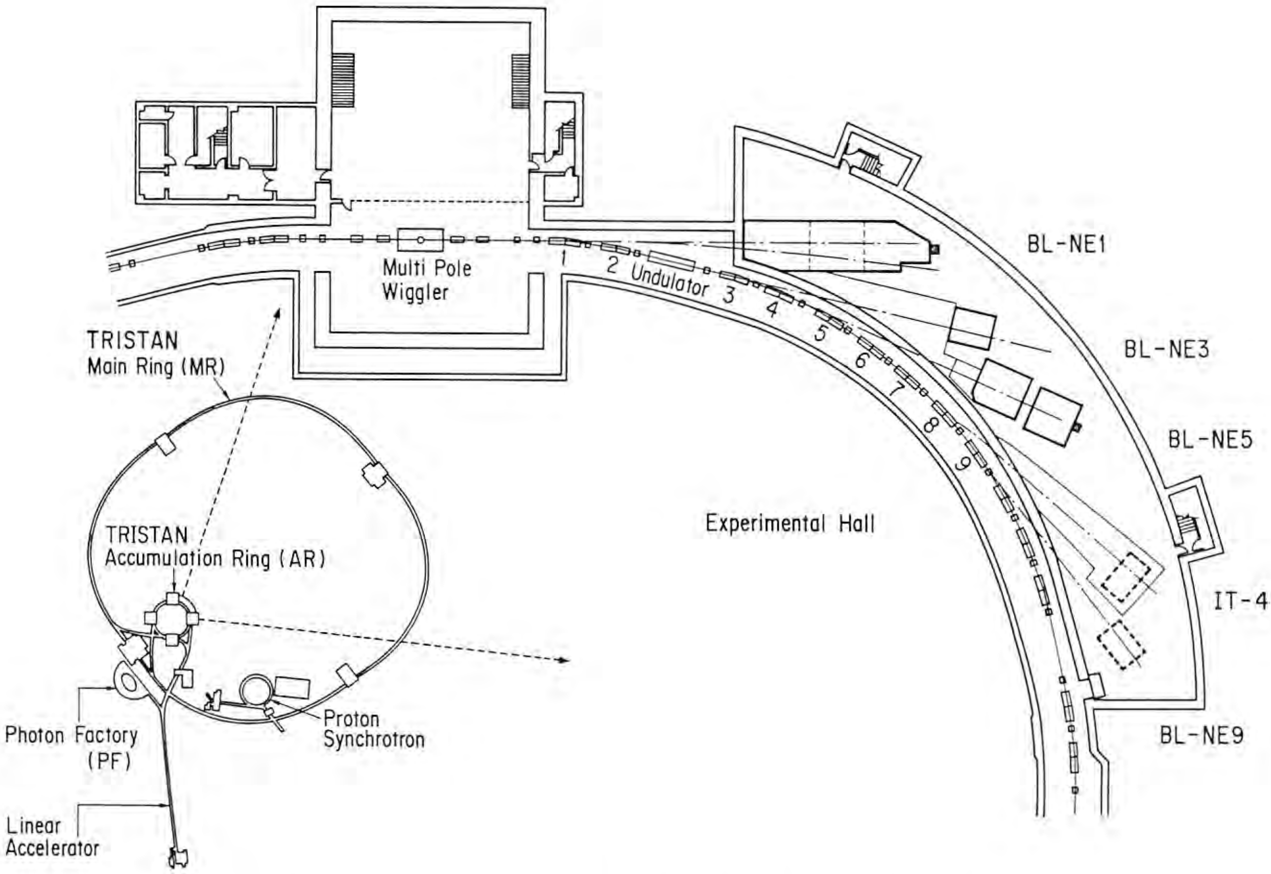

Fig. 19 Plan view of the experimental hall of the TRISTAN Accumulation Ring.

Table 8 List of Experimental Stations

Experimental station		Source	Typical Experiments	Contact Person
AR-NE1		EMPW#NE1		
	A1		Precision Compton and magnetic Compton scattering	H. Kawata
	A2		Spectroscopy and scattering with circularly polarized x-rays	T. Iwazumi
	B		Spectroscopy with circularly polarized soft x-rays	Y. Kagoshima
AR-NE3		Undulator#NE3		
			Nuclear Bragg scattering and surface diffraction	X. Zhang
AR-NE5		Bending-NE5		
	A		Angiography. X-ray tomography	K. Hyodo
	C		High pressure and high temperature x-ray diffraction	T. Kikegawa

Table 9. List of Beamline Optics

Experimental Station	Horizontal Angular Acceptance (mrad)	Typical Beam Size (hor.×ver.) (mm^2)	Photon Flux at Sample Position (mm^2/s/mA)	Monochromator System	Energy Resolution ($\Delta E/E$)	Energy Range (keV)
NE1-A1	2	8×3	1×10^{10} (60.0keV)	Single Crystal Si(111) Double Bent Crystal Si(111)	1.5×10^{-3}	40~70
NE1-A2	2	80×4 4×4		Double Crystal Si(111) Sagittal Focusing Si(111)	2×10^{-4}	6~28
NE1-B	~0.2 [0.02(ver.)]	~0.3×0.1	~1×10^{11} (400eV)	10m Grazing Incidence Grating (1200 or 2400*lines*/mm) β=89°	2×10^{-3}	0.25~1.8
NE-3	0.5	10×31	8×10^{2} (14.4keV)	Double Crystal Si(111) with Single Crystal $^{57}Fe_2O_3$(777)	1×10^{-12}	5~25
NE5-A	10	150×10	5×10^{7} (33.2keV)	Asymmetrically Cut Single Crystal Si(311) (α=4°~6°)	6×10^{-3}	20~40
NE5-C	3	60×5		Double Crystal Si(111) (Sagittal Focusing)	1×10^{-3}	30~100

D. NEW RESULTS OF EXPERIMENTS

1. Burst of Magnetic Compton Profiles in BL-NE1

One of the useful applications of circularly polarized hard X rays is the measurement of magnetic Compton profiles (MCP), which provide direct information concerning the momentum density of electron spins in solids. There has been, however, difficulty in achieving high statistical accuracy and high momentum resolution of MCP, because of (1) a weak interaction between a photon and an electron spin, and (2) a lack of flux of circularly polarized photons. Recently, the latter was overcome by EMPW#NE1, a quasi doubly bent monochromator and a segmented Ge solid-state detector. Although the equivalent momentum resolution (0.75 atomic units (a.u.)) of the solid-state detector is not completely satisfactory, it is sufficient, as shown below, to investigate the characteristic feature of magnetic electrons in ferromagnetic materials.

So far, MCPs of Fe, Ni, FeNi alloy, amorphous FeB, Gd, amorphous FeGd, NdFeB alloy have been measured. Among them, the following two results demonstrate the unique application of the MCP method to studies of magnetism. One is the first reconstruction of the three-dimensional momentum density of magnetic electrons of Fe from fourteen experimental directional MCPs. The accumulation time for one MCP was about 8 hours. Without the present setup, it is hard to perform measurements within a practical accumulation time. The determined spin momentum density of Fe (+3% Si) in the p_z=0 plane is shown in Fig. 20. The reconstruction was carried out using a simple Fourier-transform method. The negative spin density around the Γ point

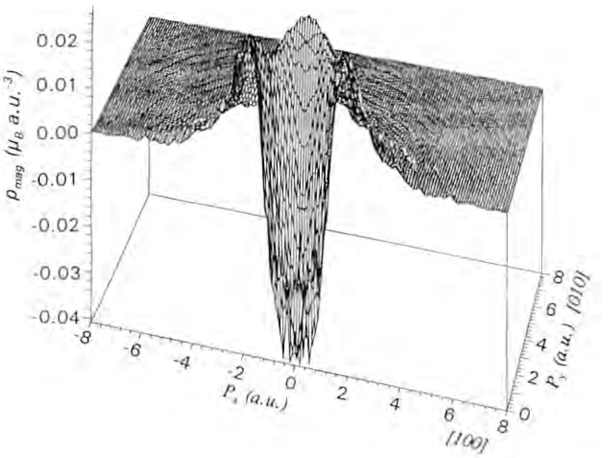

Fig. 20 Three dimensional momentum density of magnetic electrons in Fe+3%Si reconstructed from magnetic Compton profiles.

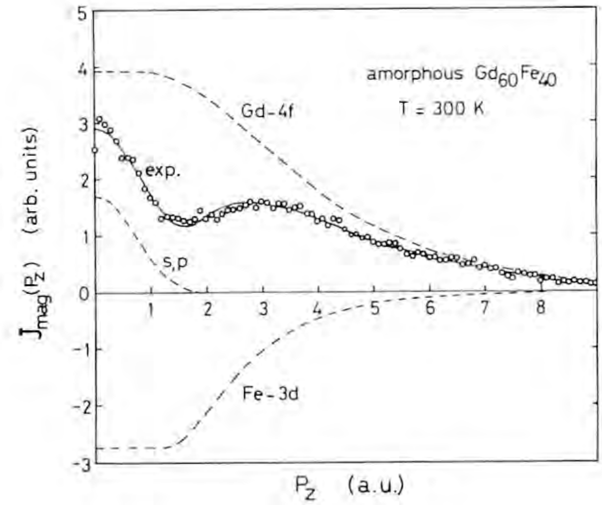

Fig. 21 Separation to individual magnetic Compton profiles of Fe-3d, Gd-4f and s,p-like electrons in amorphous $Gd_{60}Fe_{40}$ alloy.

corresponds to the s,p-like itinerant electron spin polarization induced by the hybridization between s,p- and 3d-band electrons. The anisotropic momentum density of 3d electrons is clearly observed as different heights of the peaks surrounding the central deep hollow. A theoretical calculation based on band theory has been found to be in good agreement with the present experimental result.

Another new application of the MCP method is the determination of individual magnetic moments of 3d- and 4f-electron components in alloys. This is based on the fact that the area of MCP of 3d (or 4f) is proportional to the magnetic moment of 3d (or 4f) electrons. Figure 21 shows the MCP of an amorphous FeGd alloy, where the magnetic moments of the 3d and 4f components can be identified based on their different momentum distributions: the MCP of 4f electrons has a larger component in the region of p_z>4a.u. than does that of the 3d electrons. The analysis clarifies the ferrimagnetic ordering of Fe and Gd atoms, as well as the different temperature dependence of 3d and 4f magnetic moment in this alloy.

Beside the above results, the following information has been obtained: (1) the MCP of amorphous FeB supports the theoretical prediction of the spin polarization of s,p-like electrons from B atoms, and (2) the MCPs of FeNi alloys show a suppression of the anisotropic momentum distribution, compared with pure Ni.

N.Sakai

2. Experiments in BL-NE3

The pulsed intense x-rays (pulse width of ~0.2nsec and interval of 1.28msec) from in-vacuum undulator U#NE3 installed in the AR are quite suitable to study research fields related to the Mössbauer effect. The so-called quantum beats measured in the time domain using pulsed x-rays have many advantages compared with standard Mössbauer spectroscopy (i.e. measurement in energy domain). Quantum beats do not only correspond to the energy property of the scattering process, but also contain information concerning the phase, polarization and other properties of the scattering.

This year over ten kinds of the experiments of Mössbauer nuclear resonant scattering have been carried out at AR-NE3. Most of them were the first attempts in the world. These have developed a new field of applications of the Mössbauer effect using synchrotron radiation.

A typical example of experiments is to use Mössbauer photons in an x-ray interferometer system. The experimental set-up is shown in Fig. 22(a). The results are shown in Fig. 23. We observed that time-delayed Mössbauer photons showed interference oscillations in an x-ray interferometer in the same way as do prompt photons scattered by electrons.[1]

Further more, we made measurements of the quantum beats which were caused by two objects containing ^{57}Fe placed in the ray paths of the interferometer. The set-up of this experiment is shown in Fig. 22(b). Figs. 24.(a) and (b) show the calculated

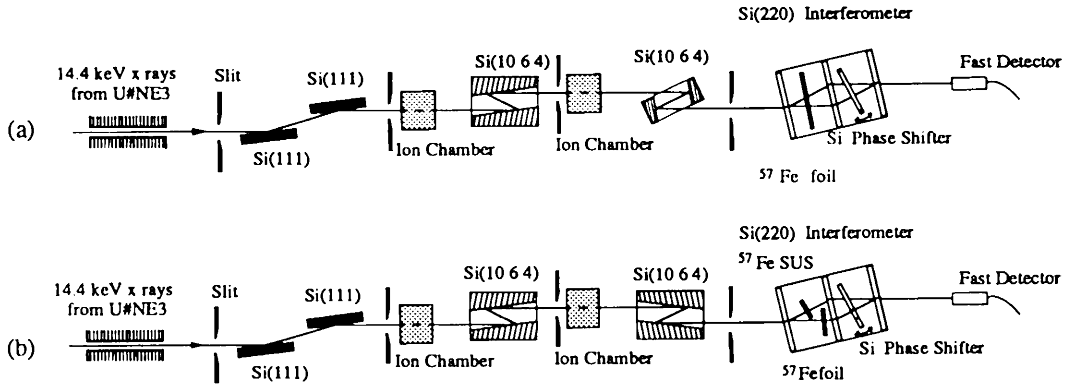

Fig. 22 Set-up of an LLL type x-ray interferometer: (a) the same ^{57}Fe-enriched iron foils in both ray paths, and (b) the ^{57}Fe-enriched iron foil and ^{57}Fe- enriched stainless steel foil in each ray path.

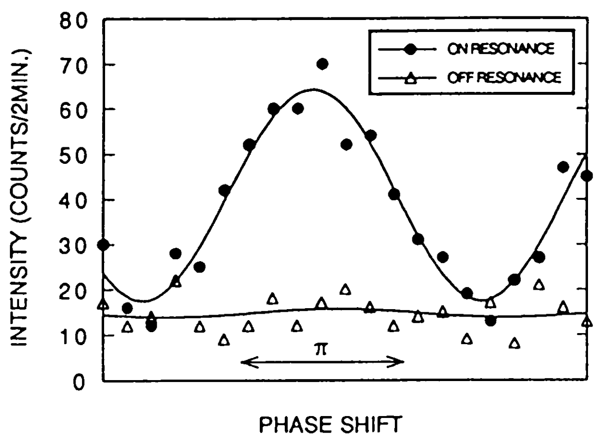

Fig. 23 Interference oscillations of time delayed Mössbauer photons (circles). Background is shown by triangular.

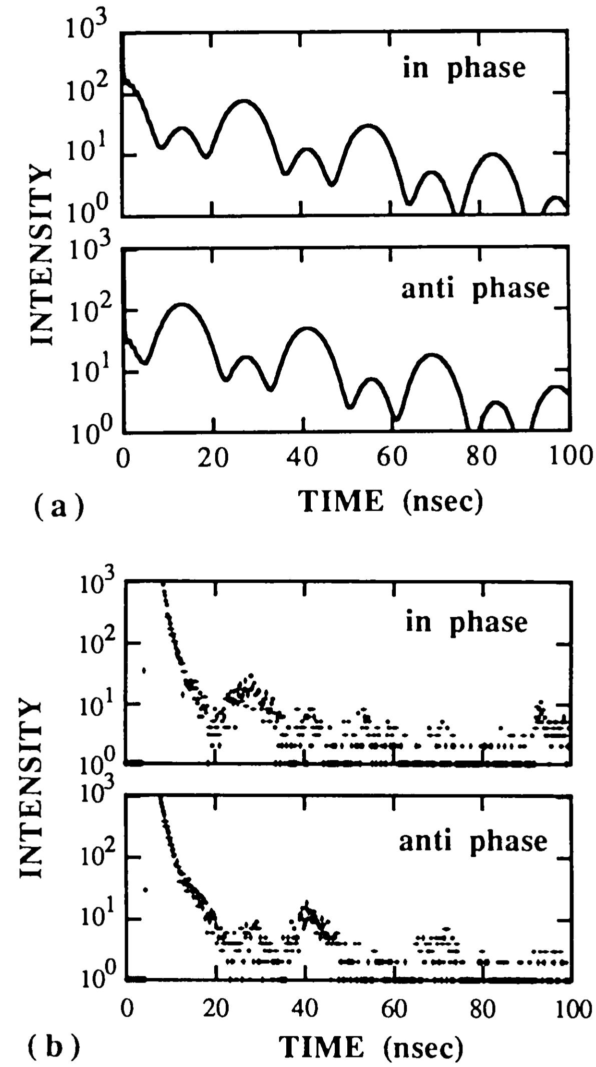

Fig. 24 Quantum beats with in-phase (bottom of (a) and (b)) and anti-phase (top of (a) and (b)) conditions: (a) calculated quantum beats of iron and stainless steel foils in an LLL type x-ray interferometer. (b) those observed in 0~100nsec time region.

and observed quantum beats, respectively. The tops of Figs. 24 (a) and (b) correspond to the anti-phase condition of the interferometer, and the bottoms to the in-phase condition. The phase conditions were selected according to the rotation of a silicon wafer. This result means that quantum beats are not only a information carrier of hyperfine structures of matter in this experiment, but can also provide information concerning the phase directly. We can extract information concerning the phase by observing the changes of quantum beats.

X. Zhang

Reference

1) S. Kikuta et al. ICAME'91, Nanjing, to be published in the Hyperfine interactions.

3. Use of Dual-Beam Produced by an EMPW#NE1 for Angiography

We have been developing a two-dimensional imaging system for K-edge subtraction angiography with a large-size monochromatic Synchrotron Radiation (SR) beam by using asymmetrical reflection from a crystal and a two-dimensional detector system (Image intensifier-TV system). The advantages of this two-dimensional imaging system with TV-rate image acquisition were confirmed through our preliminary experiments. However, taking account of medical applications, a faster and more stable energy-switching system is required, and the incident photon intensity onto a patient should be more than 10^{11} photons/mm^2/s in order to attain an image with a high signal-to-noise ratio.

We propose a totally new two-dimensional imaging system for angiography using very intense dual-beam of linearly polarized SR produced by the EMPW#NE1, which was primarily constructed so as to produce elliptically polarized SR for BL-NE1 at the Accumulation Ring (AR). The angular separation between the two linearly polarized SR is described as

$$\Psi=2K_x/\gamma,$$

where $K_x=0.934B_{x0}\lambda_u$. B_{x0} is the peak value of the horizontal magnetic field, λ_u is the periodicity of the magnetic field. In the case of the current device, the maximum separation is about 0.48 mrad. If we would use the dual-beam from EMPW#NE1, we could overcome the above two problems simultaneously.

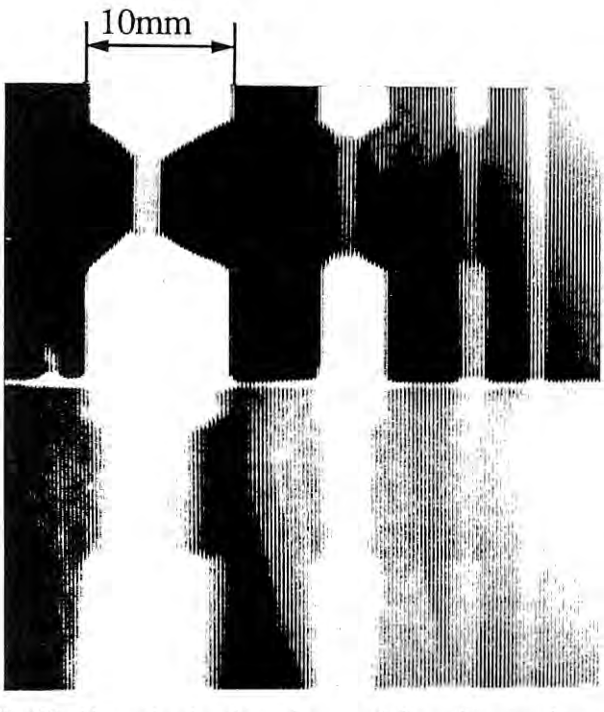

Fig. 25 Vessel phantom image taken by an image intensifier-TV system using the dual linearly polarized beams produced by the EMPW

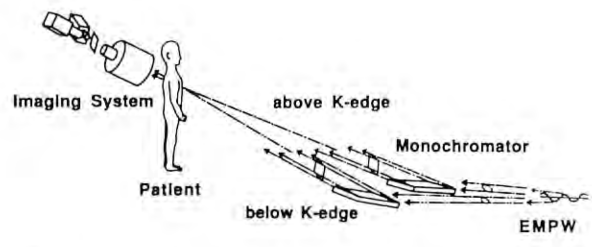

Fig. 26 K-edge subtraction angiography system using the dual- beam produced by an EMPW

A vessel phantom was used in an experiment to evaluate the possibility of this new imaging method. The phantom, made of 30 mm thick lucite, consisted of channels with diameters of 10, 5, 2 and 1mm. These channels were filled with a contrast material with an iodine concentration of 15% in weight. Two asymmetrically cut Si(311) crystals were set so as to attain each linearly polarized SR beam, which corresponds to the X-ray energy above and below the K-edge of iodine, respectively. Figure 25 shows one TV frame image taken within 2 msec using an image-intensifier TV system. The upper and lower regions of this figure correspond to images taken above and below the K-edge energy, respectively. The photon intensity amounted to about 10^{11} photons/mm^2/s.

The possibility of a new imaging method for angiography using dual linearly polarized SR by EMPW#NE1 was successfully demonstrated. Figure 26 shows one possible future system using a dual-beam produced by EMPW#NE1 and a two-dimensional detector system.

K.Hyodo

E. SUPER LIGHT-SOURCE PROJECT ON TRISTAN MR

1. Conversion of the TRISTAN Main Ring to a Very Low-Emittance SR Machine.

Status of TRISTAN

At present, the TRISTAN Main Ring (MR) is working in its second stage to pursue higher luminosity, rather than higher energy, since the successful completion in 1990 of first stage operation to survey high-energy frontiers.

The TRISTAN MR will be converted into a light source of ultra-high brilliance after the second stage of operation, which aims to integrate the luminosity up to $300pb^{-1}$. The conversion work is expected to take place within 3~4 years, since the integration rate of the luminosity reached $1pb^{-1}$/day in 1991's operation with mini-β optics.

Merits of high-energy machine as a light source[1]

There exist some merits in using a high-energy machine as a light source, compared with a dedicated light source lattice of the third generation, e.g. Chasmann-Green and TBA.

In the operation of a high-energy machine at low energy, a low emittance beam can be achieved with reasonably weak sextupole magnets for chromaticity correction. This makes the beam robust against fluctuation of the machine parameters and allows a large dynamic aperture, even if long straight sections interrupt the periodic structure of a machine.

The TRISTAN MR is equipped with four 200m long straight sections for beam collision experiments, rf cavities and injection tools. They will provide space for the installation of very long undulators used to produce synchrotron light of ultra-high brilliance and damping wigglers to make the beam parameters flexible over a wide range.

Utilization plan of MR

Figure 27 shows a schematic layout of the MR light source now under consideration. It is planned to modify the long straight sections for the installation of damping wigglers and undulators, as well as rf cavities and injection tools. The damping wigglers are used to reduce the beam emittance further at the cost of an enlarged spread of the beam energy, which helps to suppress the occurrence of beam instabilities, but reduces the gain of FEL amplification.

Figure 28 shows one octant of the MR light source lattice designed for installation of a short undulator and a 70m long undulator. To maintain the overlap between the light and electron(or positron) beams, no magnets are placed in the straight sections used for undulators. The effect of the undulator field could be corrected if necessary.

Table 10 summarizes the principal parameters of the MR light source.

Subjects studied[2]

In 1990, an orbit sub-group was organized to study relevant problems concerning the MR light source project, especially in the field of beam dynamics, as described briefly in the following.

A dynamic aperture survey by particle tracking was conducted through a wide range of horizontal phase advances of a normal cell. The provisional result says that the dynamic aperture necessary for beam injection from the AR is not satisfied by the 145 degree lattice of the original plan,[1] but is satisfied by a 90 degree lattice in which the emittance can be made very low by using damping wigglers.

The effect of orbit distortion was estimated for both the arc section and the straight section where damping

Table 10. Principal parameters of the MR light source

circumference	3018	m
nominal beam energy	10	GeV
nominal beam current	100	mA
total length of damping wiggler	110	m
field strength of damping wiggler	1.2	T
phase advance in a normal cell		
horizontal	90	degree
vertical	60	degree
betatron tune		
horizontal	46.20	
vertical	37.25	
momentum compaction	0.000691	
natural chromaticity		
horizontal	-72.8	
vertical	-53.6	
rf voltage	90	MV
radiated energy per turn	20.7	MeV
energy spread	0.0015	
natural bunch length	0.71	cm
natural emittance	1.6	nm

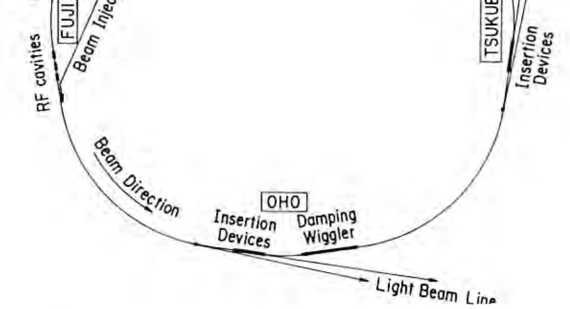

Fig. 27 Schematic Layout of the TRISTAN MR Light Source

wigglers are placed. The error dispersion in the arc is tolerable by factor of 7, compared with that in the damping wiggler section.

The effects of intra-beam scattering on the beam emittance and lifetime were evaluated. It is not serious for nominal energy beams, but will become quite serious when the beam energy is lowered.

An rf system based on APS-type cavities were studied, especially in connection with excitation of multi bunch beam instabilities. The result seems to be quite serious, and further study is essential.

The synchrotron radiation from the damping wigglers was investigated from the view point of damage to the vacuum system. It can be solved by a careful design of vacuum system.

These surveys are only the beginning. Many questions, problems and ideas are still open to discussion.

S. Kamada

References
1) KEK Report 88-16
2) KEK Report 91-5

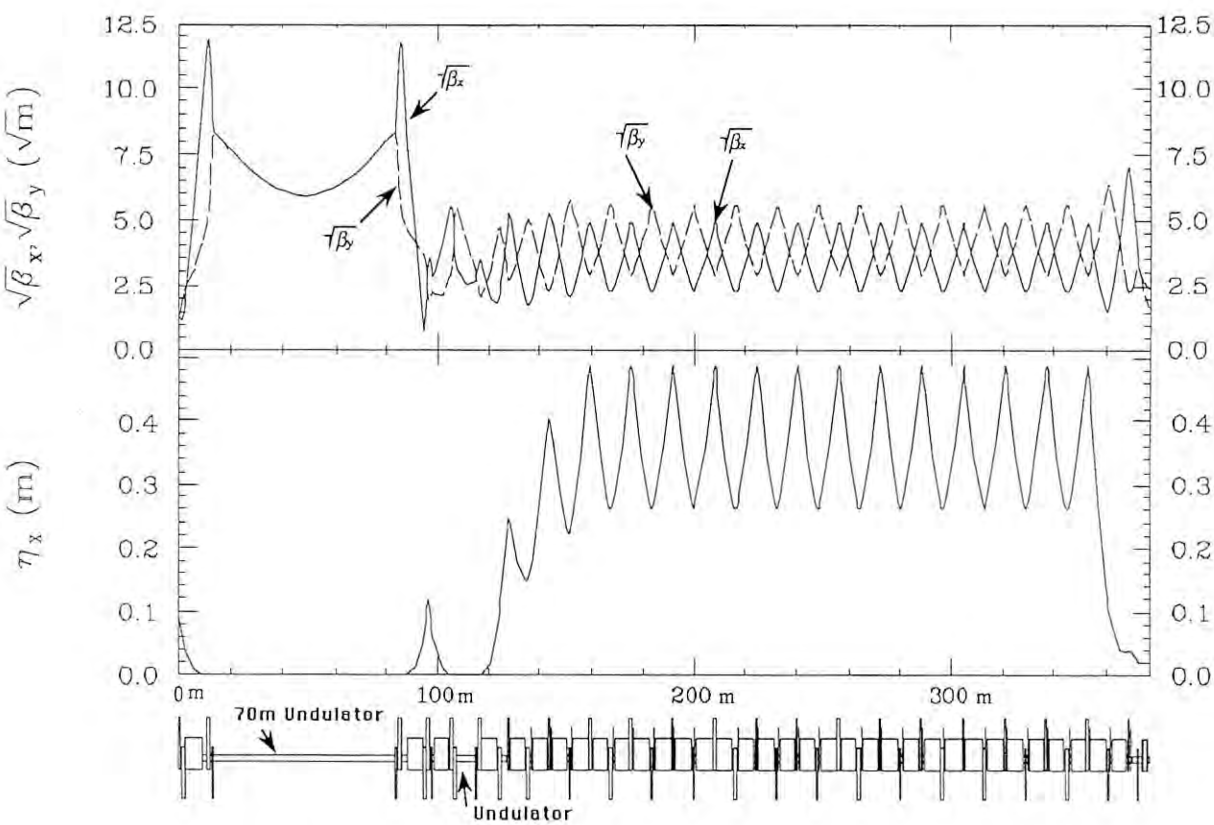

Fig. 28 The TRISTAN MR Light Source Optics in an octant for installation of undulators

PHOTON FACTORY ACTIVITY REPORT 1991

#9

ISSN 0912-1803

PHOTON FACTORY ACTIVITY REPORT

1991

#9